

May 2015

Virtual Droop Control Framework and Stability Analyses for Microgrids with High Penetration of Renewables

Ashishkumar Kanubhai Solanki
University of Wisconsin-Milwaukee

Follow this and additional works at: <https://dc.uwm.edu/etd>

 Part of the [Electrical and Electronics Commons](#), and the [Oil, Gas, and Energy Commons](#)

Recommended Citation

Solanki, Ashishkumar Kanubhai, "Virtual Droop Control Framework and Stability Analyses for Microgrids with High Penetration of Renewables" (2015). *Theses and Dissertations*. 928.
<https://dc.uwm.edu/etd/928>

This Dissertation is brought to you for free and open access by UWM Digital Commons. It has been accepted for inclusion in Theses and Dissertations by an authorized administrator of UWM Digital Commons. For more information, please contact open-access@uwm.edu.

VIRTUAL DROOP CONTROL FRAMEWORK AND STABILITY
ANALYSES FOR MICROGRIDS WITH HIGH PENETRATION OF
RENEWABLES

by

Ashishkumar K Solanki

A Dissertation Submitted in
Partial Fulfillment of the
Requirements for the Degree of

Doctor of Philosophy
in Engineering

at

The University of Wisconsin-Milwaukee

May 2015

ABSTRACT

VIRTUAL DROOP CONTROL FRAMEWORK AND STABILITY ANALYSES FOR MICROGRIDS WITH HIGH PENETRATION OF RENEWABLES

by

Ashishkumar K Solanki

The University of Wisconsin-Milwaukee, 2015
Under the Supervision of Professor Adel Nasiri

Microgrids can provide the most promising means of integrating large amounts of distributed sources into the power grid and can supply reliable power to critical loads. However, managing distributed sources and loads within a microgrid during island and grid-tie modes and during transitions is a challenge. Stable operation of a microgrid is a concern specifically during the starting of motor loads, switching of large loads, and in presence of high penetration of renewable resources. Hence, a generalized control framework is required to regulate microgrid voltage and frequency, maintain power quality, manage Distributed Generations (DG) and ensure microgrid stability. Several control methods have been developed for microgrid control. Majority of these techniques are based on natural droop control or modified natural droop control, which rely on voltage and frequency variations as inputs to control algorithms. At present, there are no methods available for sizing the capacities needed to ensure reliable operation and stability. A new microgrid control framework, Virtual Droop Control (VDC), for power management as well as for voltage and frequency regulation is proposed in this thesis. The proposed control method analyzes the effect of intermittent resources and dispatches the power commands to individual generation assets ensuring stable operation of the microgrid. The proposed method is described, formulated and

compared with existing natural droop control technique in this dissertation. The unit commitment algorithm has also been implemented to manage non-renewable sources to improve system efficiency. The proposed technique operates the microgrid at a constant voltage and frequency and uses communications for power sharing. It also provides the means to operate the microgrid in case of lost communication or sabotage on the communication network. The modeling results of the Virtual VDC technique have been compared with existing microgrid control methods including natural droop control technique. A laboratory setup, that consists of a 100kW natural gas generator, a 56 kWh Li-ion battery with a 250kW inverter, and a 100kW load bank, has been built and tested. The results of the setup have been provided, confirming the viability of the proposed technique. Detailed analysis for intentional islanding, unintentional islanding, and reconnection are presented. The state space model has been developed for the Fort Sill microgrid and the stability analysis has been performed to verify stability of a microgrid in various scenarios. The proposed method has been applied to the Fort Sill microgrid and examined for effectiveness and viability.

A modified control technique is also proposed to regulate the voltage and frequency for high penetration of renewable energy, which can be used with VDC framework. This technique allows the improvement of efficiency and power quality indexes for critical loads while reducing greenhouse gas emissions. The standard IEEE 34 bus system is modified and adapted to function as a microgrid test bed. Three different cases were studied and analyzed. The CO₂ emission, efficiency, and power quality indexes have been calculated and compared for all three cases in order to verify the performance of the proposed control technique.

© Copyright by Ashishkumar Solanki, 2015

All Rights Reserved

Dedicated to my wife and my parents for their support

ACKNOWLEDGMENT

Foremost, I would like to express my sincere gratitude to my advisor Prof. Adel Nasiri for his continuous support, motivation, and patience throughout my PhD study and research. His guidance and advices always helped me to do innovative research. Without his excellent knowledge in my research field, it would have not been possible to make a strong contribution in the field of microgrid. I would like to thank Dr. Vijay Bhavaraju of Eaton Corporation for his constant guidance and support and also for letting me use Eaton Corporation's labs and resources to perform practical tests during my research. His innovative ideas and great knowledge helped a lot to learn new things during my research. I would like thank Prof. David Yu from bottom of my heart for recognizing my potential and for his tremendous help during initial phase of my PhD. I would also like to thank my other committee members Prof. Brian Armstrong and Prof. Jugal Ghorai for their valuable suggestions and discussions.

I would like to thank all my colleagues and friends for sharing their ideas and healthy discussion on various subjects. I would like to express my special gratitude to Bora Novakovic, Zeljko Jankovic, Dr. Qiang Fu, Chun Ju Huang and Dr. Yakov Familiant.

Finally I would like to thank my wife and my parents for their unconditional love and support. I would not have been able to complete my dissertation without their continuous love and encouragement.

TABLE OF CONTENTS

TABLE OF CONTENTS.....	vi
LIST OF FIGURES	viii
Chapter 1 Introduction.....	1
1.1 Background.....	1
1.2 Microgrid Concept.....	4
1.2.1 Microgrid Definition.....	4
1.2.2 Importance of Microgrid.....	5
1.2.3 Microgrid Projects under Research and Development	6
1.3 Research Review.....	9
1.3.1 Microgrid Control Methods.....	9
1.3.2 Stability Assessment.....	10
1.4 Problem Statement.....	12
Chapter 2 Microgrid Configuration and Component Modeling	14
2.1 Microgrid Configuration.....	14
2.1.1 Fort Sill Microgrid Configuration.....	14
2.1.2 IEEE 34 Bus Microgrid Configuration.....	16
2.2 Natural Gas Generator Modeling.....	17
2.2.1 Synchronous generator rating.....	18
2.2.2 Exciter Modeling.....	19
2.2.3 Natural Gas Turbine Modeling.....	23
2.2.4 Synchronization of generator.....	25
2.2.5 Results and Model Verification.....	26
2.3 Voltage Source Converter System.....	29
2.3.1 State Space Vector Modulation Technique.....	29
2.3.2 Current Mode Voltage Source Converter.....	34
2.3.3 Voltage Mode Voltage Source Converter.....	37
2.4 Energy storage System.....	41
2.4.1 Lithium-ion Battery Storage System	42
2.4.2 Zinc Bromide Energy storage system.....	46
2.5 Wind Turbine Generator.....	50
2.6 Solar PV Generator.....	52
Chapter 3 Virtual Droop Control Framework.....	55
3.1 Introduction.....	55
3.2 Unit Commitment Algorithm.....	56
3.3 Virtual Droop Control.....	59
3.4 Comparisons between VDC and Natural Droop Control	66
3.3 Operation without Communication.....	78

3.4 Experimental Setup for the VDC concept	84
3.5 Deployment of VDC technique in Actual Fort Sill Microgrid	87
Chapter 4 Islanding and Reconnection Operations of Microgrid	90
4.1 Unintentional Islanding.....	90
4.2 Intentional Islanding	93
4.3 Reconnection.....	95
Chapter 5 State Space Modeling and Stability Analysis of Fort Sill Microgrid.....	99
5.1 State space modelling of Current Mode Inverter	100
5.2 State space modeling of Voltage Mode Inverter.....	110
5.3 Natural gas generator state space modelling.....	120
5.3.1 Mechanical system state space modeling	120
5.3.2 Exciter state space modeling.....	130
5.3.3 Synchronous generator representation	136
5.4 State space modeling of transmission line/Cable.....	143
5.5 Microgrid state space modeling	150
5.6 Stability Analysis for Proposed VDC method.	154
Chapter 6 Modified Control Technique for CO ₂ Reduction, Improve Efficiency and Power Quality in a Microgrid	158
6.1 Introduction.....	158
6.2 Renewables and Energy storage system sizing.....	160
6.3 Control Algorithm.....	163
6.4 Results.....	167
Chapter 7 Conclusion.....	178
References.....	180

LIST OF FIGURES

Figure 1-1. The microgrid concept	4
Figure 2-1. Schematic of the Fort Sill microgrid studied.	15
Figure 2-2. The configuration of the IEEE 34 bus microgrid.....	16
Figure 2-3. Block diagram of a natural gas generator connected to a grid/microgrid.	17
Figure 2-4. Basic block diagram of an excitation control system.....	20
Figure 2-5. Block diagram of AC8B: Alternator-rectifier excitation system with digital control.....	20
Figure 2-6. The Matlab simulink model used to tune a PID controller.	23
Figure 2-7. Step response of a closed-loop excitation system.	23
Figure 2-8. Basic arrangement of a single shaft gas turbine.....	24
Figure 2-9. The detailed control system of a gas engine system.	24
Figure 2-10. Control logic behind the synchronization breaker.	25
Figure 2-11. Frequency response to a 50% step change load, test result (above), simulation result (below).	27
Figure 2-12. Active and reactive power dynamics of the natural gas generator.....	28
Figure 2-13. Topology of a three-phase VSC system.....	30
Figure 2-14. Possible switching state topologies of a voltage source inverter	31
Figure 2-15. Space vector representation.....	32
Figure 2-16. The phase gating signal in the symmetric SVM technique.	34
Figure 2-17. Schematic diagram of the current mode VSC system.....	35
Figure 2-18. Active and reactive power simulation test results for a 500 kVA current mode VSC system, when a step active power command from 10% to 100% and to 10% is applied.	36
Figure 2-19. Active and reactive power simulation test results for a 500 kVA current mode VSC system, when a step reactive power command from 10% to 100% and to 10 % is applied.	36
Figure 2-20. Active and reactive power simulation test results for a 500 kVA current mode VSC system, when a step active and reactive power command from 10% to 100% and to 10 % is applied.....	37
Figure 2-21. Active and reactive power simulation test results for a 500 kVA current mode VSC system, when a step active and reactive power command from 10% to -100% and to 10 % is applied.....	37
Figure 2-22. Schematic diagram of voltage mode VSC system	38
Figure 2-23. Simulation result; transition from grid-tie mode to island mode	39
Figure 2-24. Experimental test result; transition from grid-tie mode to island mode..	39
Figure 2-25. Equivalent circuit of the battery system.....	42
Figure 2-26. Discharging curve of one PowerRack 320.....	44
Figure 2-27. Charging curve of one PowerRack 320.	44
Figure 2-28. SOC of 60 Ah Li-ion battery system simulation model while discharging by 60 A for 1 hour.	45
Figure 2-29. Battery voltage of 60 Ah Li-ion battery system simulation model while discharging by 60 A for 1 hour.	45

Figure 2-30. SOC of a 60 Ah Li-ion battery system simulation model while charging by 60 A for 1 hour.	46
Figure 2-31. Battery voltage of 60 Ah Li-ion battery system simulation model, while charging by 60 A for 1 hour.	46
Figure 2-32. Discharging curve of 500 kWhr ZBB energy storage system.....	47
Figure 2-33. Charging curve of 500 kWhr ZBB energy storage system	47
Figure 2-34. SOC of a ZBB battery system simulation model while discharging by 462.5 A for 2 hours.	48
Figure 2-35. Battery voltage of a ZBB battery system simulation model while discharging by 60 A for 2 hours.	48
Figure 2-36. SOC of a ZBB battery system simulation model while charging by 462.5 A for 2 hours.	49
Figure 2-37. Battery voltage of a ZBB battery system simulation model while charging by 462.5 A for 2 hours.	49
Figure 2-38. Wind turbine with full scale converter connected to the grid/microgrid.	50
Figure 2-39. Sample wind speed (above) and wind power profile (below).....	51
Figure 2-40. Solar PV system with inverter connected to the grid/microgrid	52
Figure 2-41. PV cell equivalent circuit.....	52
Figure 2-42. PV cell typical I-V characteristic	53
Figure 2-43. 90 kW solar PV power day profile for a bright day, cloudy day, and the worst power fluctuation during a one-month period.	54
Figure 3-1. Unit commitment algorithm as part of virtual droop control to increase efficiency.	56
Figure 3-2. Generalized droop curve between active power load and virtual frequency.	60
Figure 3-3. Generalized droop curve between reactive power load and virtual voltage.	60
Figure 3-4. Control flow diagram of microgrid controller in island mode	62
Figure 3-5. Virtual frequency and voltage droop curves for mode 1, when only energy storage provides power in island mode for the Fort Sill microgrid.	63
Figure 3-6. Virtual Frequency and voltage droop curves for mode 2, when energy storage and one generator provide power in island mode for the Fort Sill microgrid.....	64
Figure 3-7. Virtual Frequency and voltage droop curves for mode 3, when energy storage and both generators provide power in island mode for the Fort Sill microgrid.....	65
Figure 3-8. Active load profile for the microgrid.	66
Figure 3-9. Extrapolated fuel consumption curve of 190 kW generator.	67
Figure 3-10. Frequency and voltage droop curves for natural droop method.	67
Figure 3-11. Active power at energy storage, natural gas generator 1 and 2, solar PV and wind; when natural droop control method is applied.....	68
Figure 3-12. Reactive power at energy storage, natural gas generator 1 and 2; when natural droop control method is applied.	68
Figure 3-13. Voltage at energy storage device, natural gas generators, solar PV and wind; when natural droop control method is applied	69

Figure 3-14. The Fort Sill microgrid frequency, when natural droop control method is applied.....	70
Figure 3-15. Energy output of natural gas generators; when natural droop control method is applied.....	70
Figure 3-16. Charging/discharging energy of energy storage; when natural droop control method is applied.....	71
Figure 3-17. Fuel consumption of both natural gas generator; when natural droop control method is applied.....	71
Figure 3-18. Microgrid load and active power at energy storage device, natural gas generator 1 and 2, solar PV and wind turbine; when VDC control method is applied.....	72
Figure 3-19. SOC of the energy storage system.	72
Figure 3-20. Reactive power at energy storage, natural gas generator 1 and 2; when VDC control method is applied.	74
Figure 3-21. Voltage at energy storage device, natural gas generators, solar PV and wind; when VDC control method is applied.	74
Figure 3-22. Microgrid frequency; when VDC control method is applied.....	75
Figure 3-23. Energy output of natural gas generators; when VDC control method is applied.....	76
Figure 3-24. Charging/discharging energy of energy storage; when VDC control method is applied.....	76
Figure 3-25. Fuel consumption of both natural gas generator; while natural droop control method is applied.....	77
Figure 3-26. Control flow diagram of “Control Transfer Process” (a) at energy storage inverter (b) at Natural gas generators.....	79
Figure 3-27. Transfer controls from VDC to natural droop control for Fort sill microgrid.....	81
Figure 3-28. Microgrid frequency (above), Active power at PCC, energy storage, natural gas generator 1 and 2(below); during the transition from VDC to natural droop.....	82
Figure 3-29. The schematic of the experimental test setup.	84
Figure 3-30. (a) SEL 849 rely to measure total load and send data to microgrid inverter using MODBUS TCP/IP (b) WT1600 power meter to measure the powers, frequency and voltages (c) 100 kW load bank (d) Altairnano energy storage (e) SMAX inverter connected to energy storage (f) 100 kW natural gas generator.....	85
Figure 3-31. Active Power at Natural gas generator, Energy storage and load; experiment results.....	86
Figure 3-32. Microgrid frequency (above), Microgrid voltage (below); experiment results.....	86
Figure 3-33. Active Power of utility, energy storage inverter, generator 1, generator 2 and renewables; successful test of generator 2 synchronization (Courtesy: Eaton Corporation).	87
Figure 3-34. Frequency at utility, energy storage inverter, generator 1, generator 2 and renewable source (Courtesy: Eaton Corporation).....	88

Figure 3-35. RMS voltage at utility, energy storage inverter, generator 1, generator 2 and renewables (Courtesy: Eaton Corporation).....	88
Figure 4-1. Active power at PCC point and of the energy storage for Fort Sill microgrid; when unintentional islanding is occurred.	91
Figure 4-2. Reactive power at PCC point and of the energy storage for Fort Sill; when unintentional islanding is occurred.	91
Figure 4-3. RMS voltage at PCC point and of the energy storage for Fort Sill microgrid; when unintentional islanding is occurred.	91
Figure 4-4. Microgrid frequency Fort Sill microgrid systems; when unintentional islanding is occurred.	92
Figure 4-5. Active power at PCC point and of the energy storage for Fort Sill microgrid; when intentional islanding is occurred.	94
Figure 4-6. Reactive power at PCC point and of the energy storage for Fort Sill microgrid; when intentional islanding is occurred.	94
Figure 4-7. RMS voltage at PCC point and of the energy storage for Fort Sill microgrid; when intentional islanding is occurred.....	94
Figure 4-8. Microgrid frequency of Fort Sill microgrid systems; when intentional islanding is occurred.....	95
Figure 4-9 Active power at PCC terminal, energy storage device, natural gas generator 1, and natural gas generator during reconnection event; when natural droop control method is applied to Fort Sill microgrid in island mode.	96
Figure 4-10. Microgrid frequency and grid frequency during reconnection event; when natural droop control method is applied to Fort Sill microgrid in island mode.....	96
Figure 4-11. Active power at PCC terminal, energy storage device, natural gas generator 1 and 2 at the time of reconnection event; when VDC method is applied to Fort Sill Microgrid.	97
Figure 4-12. Reactive power at PCC terminal, energy storage device, natural gas generator 1 and 2 at the time of reconnection event; when VDC method is applied to Fort Sill Microgrid.	97
Figure 4-13. . Voltage at PCC terminal, energy storage device, natural gas generator 1 and 2 at the time of reconnection event; when VDC method is applied to Fort Sill Microgrid.....	97
Figure 4-14. Microgrid frequency and grid frequency during reconnection event; when VDC method is applied to Fort Sill Microgrid.	98
Figure 5-1 Schematic diagram of current mode inverter	100
Figure 5-2. Poles and zeros map of current mode inverter state space model.....	108
Figure 5-3. Step response from i_{dref} to i_{ren_id}	109
Figure 5-4. Step response from i_{dref} to i_{ren_id}	109
Figure 5-5. Schematic diagram of voltage mode inverter.....	110
Figure 5-6. Poles and zeros map of voltage mode inverter state space model.	118
Figure 5-7. Step response from v_{dref} to v_{es_cd}	119
Figure 5-8. Step response from v_{qref} to v_{es_cq}	119
Figure 5-9. The complete mechanical system.....	122
Figure 5-10. Poles and zeros map of mechanical system of natural gas generator. ..	129

Figure 5-11. Step response from ω_{dref} to ω	130
Figure 5-12. Block diagram of excitation system.....	130
Figure 5-13. Poles and zeros map of excitation system of natural gas generator.	136
Figure 5-14. Step response from V_{dref} to V_{cref}	136
Figure 5-15. Equivalent PI representation of transmission line/Cable	143
Figure 5-16. Cascaded transmission line/cable representation.....	145
Figure 5-17. Line configuration of the fort Sill microgrid system.	146
Figure 5-18. Pole-zero map for microgrid, when only energy storage is connected.	154
Figure 5-19. Pole-zero map for microgrid, when energy storage and solar PV are connected.	155
Figure 5-20. Pole-zero map for microgrid, when energy storage and renewables are connected.	156
Figure 5-21. Pole-zero map for microgrid, when energy storage, renewables and generator 1 are connected.	156
Figure 5-22. Pole-zero map for microgrid, when energy storage, renewables and both natural gas generators are connected.	157
Figure 6-1. Active load profile of small island energy network	160
Figure 6-2. Predefined droop curve for frequency support power reference for solar PV energy storage system versus the system frequency	164
Figure 6-3. Droop curve for 1.5 MW natural gas generator.	167
Figure 6-4. Typical load v/s efficiency curve	168
Figure 6-5. Energy network frequency; case1.	168
Figure 6-6. Active power output of generator 1 and 2; case1.....	169
Figure 6-7. Reactive power output of generator 1 and 2; case1.	169
Figure 6-8. Voltage output of generator 1 and 2; case 1.....	170
Figure 6-9. Active power output of generator 1, generator 2, wind turbine 1, wind turbine 2 and solar PV; case2.	171
Figure 6-10. Energy network frequency; case2.....	172
Figure 6-11. Voltage output of generator 1 and 2; case 2.....	172
Figure 6-12. Reactive power output of generator 1, generator 2, wind turbine 1, wind turbine 2 and solar PV; case2.	173
Figure 6-13. Active power output of generator 1 and 2; case3.....	174
Figure 6-14. Active power output of wind turbine 1, active power of associate energy storage system and active power at POI of wind turbine 1.	174
Figure 6-15. Active power output of wind turbine 2, active power of associate energy storage system and active power at POI of wind turbine 2.	175
Figure 6-16. Active power output of solar PV, active power of associate energy storage system and active power at POI of solar PV.....	175
Figure 6-17. Energy network frequency; case3.	176
Figure 6-18. Reactive power at generator 1, generator 2, wind turbine 1 POI, wind turbine 2 POI and solar PV POI; case3.	176
Figure 6-19. Voltage at generator 1, generator 2; case3.....	177

LIST OF TABLES

Table 2-1. Key parameters of a 190 kW synchronous generator.....	18
Table 2-2. Key parameters of a 1.2 MW synchronous generator	19
Table 2-3. Key parameters of 250 kW, 56 kW Li-ion battery system.....	43
Table 3-1. Unit commitment algorithm parameters for the Fort Sill microgrid	58
Table 3-2. Time sequence of the test	89
Table 5-1. LCL filter parameters of current mode inverter.	108
Table 5-2. LCL filter parameters of voltage mode inverter.	118
Table 5-3. Parameters of mechanical system of natural gas generator.....	129
Table 5-4. Parameters of excitation system of natural gas generator.	135

Chapter 1 Introduction

1.1 Background

The greatest scientific achievement of the nineteenth century was the discovery of electricity. During the past decades, electricity has played a progressively more essential role in technological development and economic growth [1-4]. Modern society depends critically on a secure supply of energy and it would not be an exaggeration to say that it has become the backbone of development. Any prolonged power outage or blackout could potentially play a devastating role in our life and economy. The global electrical energy demand has consistently increased in recent years and it is expected to double within the next two decades [5, 6]. Fossil fuel resources that have been used as a main source of energy to generate electricity to date are rapidly depleting [7, 8]. The usage of fossil fuel resources has a significant effect on the global environment [9-11]. The gradual depletion of fossil fuels and environmental pollution have led us to look toward alternative sources of energy.

Wind and solar PV are two of the major alternative sources of energy being utilized in many parts of the world [12]. According to the American Wind Energy Association (AWEA), at the end of 2012, the total installed wind power capacity was at 60,007 MW and at the end of 2013, 1300 MW of wind energy projects were under construction in the U.S. [13]. The U.S. government has a vision to generate 20% of electricity using wind energy by 2030 [14]. Solar PV is also a large source of renewable energy and the U.S. now has over 10,250 MW of installed solar electric capacity, which is enough to power more than 1.7 million average American households [15].

However, on the other hand, the U.S. relies on an aging electrical grid and distribution systems, some of which originated in the 1880s. The U.S. grid was graded

a low score of D+ by the American Council of Civil Engineers in 2013[16]. There are three major problems associated with the current centralized electric power system: low energy efficiency, low reliability and low power quality [17, 18]. It is estimated that the current power grid has an average efficiency of approximately 33%. The rest of the energy is wasted in generation, transmission, and distribution systems to unrecoverable heat. The efficiency of generation is typically low and is about 30-35% for traditional coal plants [12]. In addition, the transmission and distribution system generally accounts for 6-8% of total energy loss. Recent power black outs have proven the vulnerability of the power grid and the need for a major overhaul to improve the reliability. Furthermore, with the increasing of non-linear loads in electric power systems, power quality distortion has become a serious issue in recent years. Power distortions such as power interruptions, voltage sags and swells, voltage spikes, and voltage harmonics can cause severe effects on the loads in the electrical systems. Ongoing generation, transmission and distribution permitting issues, weather related events such as Hurricanes Sandy and Katrina, and limited maintenance have contributed to an increasing number of failures and power interruptions[16, 19-21].

Integration of renewable energy and DG will support better utilization of the existing systems and can provide a variety of benefits if they are properly operated in the electrical distribution system [22]. DG has the potential to reduce consumption of fossil based fuels, reduce transmission and distribution losses, reduce the effects of electricity price fluctuations, improve system efficiency, and improve voltage quality [23, 24]. However, higher penetration of DG creates technical and non-technical issues which include power quality, power surety, reliability, power management, overall system efficiency, interconnection of grid and regulation [25-27]. A microgrid concept provides a solution to manage DG and renewable energy and it has the ability to

maximize the overall system efficiency, power quality and power surety to critical loads [28, 29]. Transmission constraints requiring supplies closer to loads, lower cost of solar PV installations, energy storage and natural gas, and military demand for more energy surety and security are several other motivation factors [30]. Government incentives for energy efficiency and renewable power generations stimulate the research in microgrid technology [31, 32]. Advanced technology in data acquisition, communication, and microcontroller further enhanced the microgrid concept [33].

1.2 Microgrid Concept

1.2.1 Microgrid Definition

The U.S. Department of Energy (DOE) defines a microgrid as a group of interconnected loads and DG within clearly defined electrical boundaries that act as a single controllable entity with respect to the grid [34]. There are many other definitions of microgrid, but all of them involve a collection of DG and loads connected with the utility grid. Figure 1-1 shows a definition of the microgrid concept.

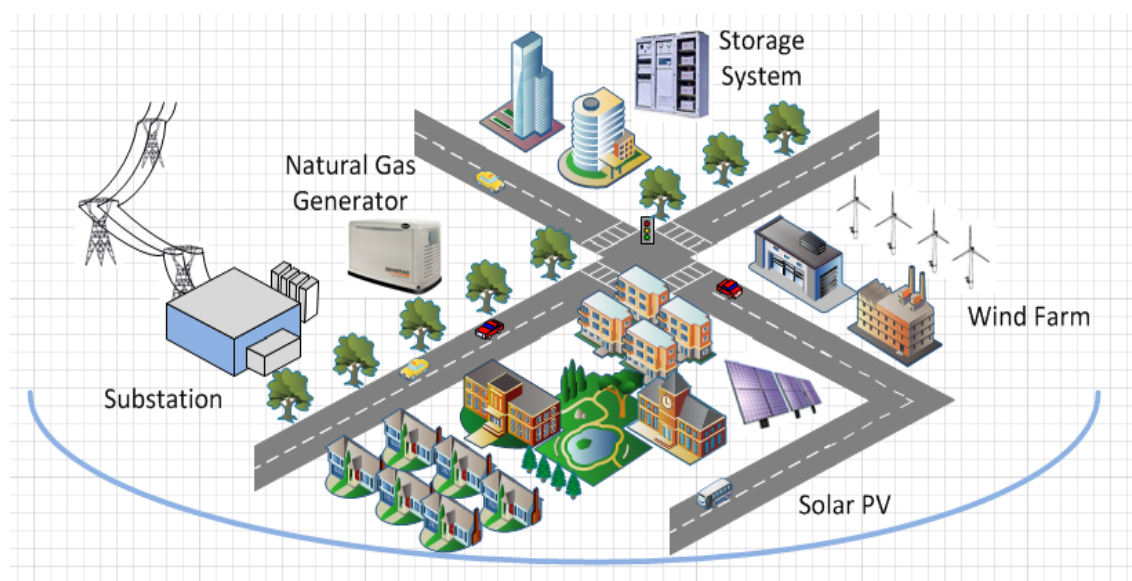


Figure 1-1. The microgrid concept

A microgrid can operate in parallel to the grid or as an island. The most compelling feature of a microgrid is the ability to separate and isolate itself from the utility's distribution system unintentionally during events (i.e., faults, voltage collapses, black-outs) [32, 35]. It may also intentionally disconnect during grid maintenance and also when the quality of power from the grid falls below certain standards. During the islanding procedure it is mandatory to preserve the reliability of a critical load and a noncritical load may need to disconnect unless sufficient generations are provided in the microgrid to cover all needs [36, 37]. Microgrids can be reconnected to the utility grid without any interruption to critical load once the utility is recovered.

1.2.2 Importance of Microgrid

Microgrids provide the most promising means of integrating large amounts of distributed resources into the power grid [38]. Particularly, it is important for renewable energy resources to improve sustainability, since a growing number of organizations and governments place a higher value on renewable energy generation [39, 40]. The deep penetration of renewables also reduces emissions. The U.S. Department of Defense (DOD) has identified reliability on the utility grid as a significant vulnerability to their mission because of growing threats to power control and utility systems [41]. A microgrid can provide higher reliability against such a threat. Hospitals, universities, refineries, pharmaceutical manufacturing, data centers and research labs have a critical need for constant power and cannot afford brownouts or blackouts. Today, these organizations have backup generators for emergencies. A microgrid can better utilize these backup generators with automated controls in a microgrid and provide a reliable power system.

In addition, they offer energy security and surety to critical loads. Moreover, they open the door to significant system efficiency improvements using Combined Heating and Power (CHP). Unlike electricity, heat is usually in the form of steam or hot water and cannot be easily or economically transported a long distance. CHP implies an integrated energy system that delivers both electricity and useful heat from an energy source such as natural gas. Microgrids can also provide additional benefits to the local utility by providing dispatchable power for use during peak power conditions. They create opportunity for electricity market players in terms of ancillary services. Consumers and businesses can supply valuable services including demand response, real time price response, and voltage support to the grid in return for payments from the serving utility or independent system operator [32, 41].

1.2.3 Microgrid Projects under Research and Development

Due to government enlightenment and initiatives there are several microgrid projects currently under research and development and many more microgrid research projects have been announced by the government as well as private firms. More than 50 U.S. military bases and communities now operate, plan, or test microgrids, according to fourth-quarter 2013 data by Navigant Consulting, a research group that has compiled a microgrid database. Some of the important microgrid projects are listed as follows.

- The 100kW Consortium for Electric Reliability Technology Solutions (CERTS) microgrid test bed near Columbus, Ohio is an advance approach for enabling integration of DG into the electric utility grid [42]. The key feature of the CERTS microgrid is its ability to separate and isolate itself from the utility system during grid disturbance. The islanding and reconnection is accomplished via an intelligent power electronics interface switch. The CERTS microgrid also offers plug and play and autonomous control for DG.
- The 3 MW Santa Rita correctional facility test site in Alameda County, CA, the main goal of this project is to ensure a successful integration of multiple renewables, energy storage, and distributed generation systems within the CERTS environment [43].
- The vision of Smart Power Infrastructure Demonstration for Energy Reliability and Security (SPIDERS) microgrids is to create fully independent and secure microgrids that are resilient to power disruption, protected against cyber-attack, integrate more sustainable energy and greater efficiency [44].
- In the Fort Sill microgrid project, the objective is to demonstrate a field-scale, renewables-focused, intelligent microgrid that serves critical mission power requirements in a sustainable, reliable, and secure manner. This microgrid includes two

natural gas generators, one 500kWh energy storage element, small wind and solar PV systems, various loads, and a static switch [45].

- The Energy Department and Sandia National Laboratories will work with NJ Transit and the Board of Public Utilities to design a dynamic microgrid to power the transit system, critical stations and maintenance facilities. After Hurricane Sandy, Hurricane Irene, and other natural disasters have exposed the vulnerability of the transit system to power outage, NJ Transit microgrid project's main goal is to enhance the reliability and resiliency of electricity used for rail and system operation [46].
- The Twentynine Palms, CA Marine base, microgrid project is one of the initiatives of the US Department of Defense (DOD) to meet criteria for cyber security [30].
- The Fort Bragg, North Carolina microgrid project is one of the world's largest microgrid projects by integrating a variety of distributed generation technologies that work in conjunction with the facility's utility infrastructure [30].
- The Borrego Springs Microgrid Demonstration Project's main objective is to conduct a pilot scale "proof of concept" demonstration of how advanced information-based technologies and distributed energy resources may increase asset utilization and reliability of the power grid in support of the national agenda [47].
- The Fort Bliss grid-tied microgrid is designed to reduce overall greenhouse gas emissions and energy costs while providing the capability to operate independent of the electric utility grid when needed to provide energy security. The Fort Bliss microgrid consists of onsite backup generation, a 120 kW solar PV, and a 300 kW energy storage system [48].
- The Illinois Institute of Technology's Perfect Power System concept is also the initiative to develop the self-sustaining infrastructure [49].

- Howard University has taken an initiative with Pareto energy to construct an independent power system on the school's campus. The idea behind this project is to reduce the school's carbon footprint and also to meet energy requirements.
- The Los Alamos microgrid test bed's principal goal is to solve the nations overburdened power grid and to provide a residential microgrid, which includes 1 MW solar PV, a large energy storage system. This microgrid project is a joint collaboration of US-Japan on microgrid demonstration [50].
- The Energy Independence District (EID) concept and framework is the first of many communities microgrid project. The main goal is to enable, organize and finance EID that optimally deploy energy saving technologies, renewables, and other onsite power generation [51].
- The Marin County microgrid project is funded by the Department of Energy to optimize large scale renewable energy in a community setting. This project involves five municipal buildings on the Marin County Civil Center Campus [52].
- The Pecan Street Project in Austin, TX has stimulated technology and policy regarding how electricity will be generated and distributed in the future to take advantage of renewable energy sources. The mission is to develop advances in energy usage and delivery that give consumers more control of their electricity usage and utility bills and increased energy efficiency [53, 54].
- The Sacramento Municipal Utility District, Sacramento, CA microgrid project will demonstrate a multi-facility scale microgrid. Major investigations in this microgrid project are: improve customer and system reliability at reduced cost, reduce peak load, reduce emission through more efficient use of Natural gas and develop and deploy cost effective, clean distributed generation [55].

1.3 Research Review

1.3.1 Microgrid Control Methods

There are several control methods proposed previously for power management and to control voltage and frequency within a microgrid in island mode. The CERTS microgrid concept proposes an autonomous controller and plug and play concept [42]. The static switch has the ability to autonomously island the microgrid from disturbances such as faults and poor power quality events. The key concept includes controllers based on local terminal quantities. In island mode, each DG can seamlessly balance the power on the islanded microgrid using a power vs. frequency droop controller. The coordination between sources and loads is through frequency. The voltage vs. reactive power droop controller is also provided so that, as the reactive power generated by the sources becomes more capacitive, the local voltage set point is reduced based on the preset slope. Contrarily, as reactive power becomes more inductive, the voltage set point is increased. Thus, voltage and frequency stability are achieved by drooping the voltage and frequency according to active and reactive power requirements [29, 56]. The natural droop method is not suitable when the microgrid has nonlinear loads due to harmonic currents. Moreover, all of the resources in the microgrid contribute power to the load and operate autonomously; opportunities to optimize the system and improve efficiencies are limited.

The virtual impedance droop control method was proposed to modify the output impedance for better power sharing in a natural droop framework. Errors in estimation of this virtual impedance can affect the power sharing method [57]. In the angle droop control method, voltage angle for the sources droops instead of frequency for power sharing to limit frequency variations [58]. However, angle measurement with a common-reference is needed and fast communication is required with this method. In

all of these methods, system voltage and frequency vary to achieve stability in island mode. There are three layers of controls in a hierarchical control method for microgrids. Primary control uses the natural droop with or without a virtual impedance droop loop. In secondary control, based on the frequency and voltage deviation, power adjustment is made to the sources or unit commitment is performed. The third layer is used in grid-connected mode to adjust active and reactive power and ancillary services to the grid [59, 60].

1.3.2 Stability Assessment

In a traditional large power system, frequency can be maintained by inertia of large synchronous generators, while the voltage can be maintained by maintaining reactive power [61-64]. The major sources of reactive power are synchronous generator, synchronous condenser and capacitor banks. The regulating transformer also contributes to regulate the system voltage [64]. In a microgrid, a large numbers of inverters are integrated with renewables and energy storage. Hence, during island mode of operation, a microgrid has little inertia or it may not have any inertia if none of the synchronous generators are connected. Depending on the structure of the microgrid and sources connected into the microgrid, the stability aspect differs [65].

One of the most important concerns in the reliable operation of any power system is stability. When two or more synchronous machines are interconnected, the stator voltages and currents of all the machines must have the same frequency and the rotor mechanical speed of each is synchronized to this frequency. The electrical power output of the generator is changed only by changing the mechanical power. The effect of increasing the mechanical power is to advance the rotor to a new position relative to the stator. Under steady state conditions, there is equilibrium between the input mechanical torque and the output electrical torque of each machine. Any changes in the

system upset this equilibrium, resulting in acceleration or deceleration of the rotors of the machines. If one generator temporarily runs faster than the other, the angular position of its rotor relative to that of the slower machine will advance. The resulting angular difference transfers part of the load from the slow machine to the fast machine depending on the power angle relationship. Since the power angle relationship is highly nonlinear, beyond a certain limit; an increase in angular separation is accompanied by a decrease in power transfer, this increases angular separation further and leads to instability [64]. Moreover, the voltage stability is equally important in any power system. Voltage instability mainly occurs due to inability of the power system to meet the demand for reactive power which leads to an uncontrollable drop in voltage. The core of the problem is the voltage drop that occurs when active power and reactive power flow through inductive reactance associated with the transmission lines and cable.

In a conventional power system, stability analysis is well established and for the different frequency ranges of possible concern there are models that include the appropriate features. However, detailed generalized dynamic models for a microgrid are not available. Previous dynamic analysis of microgrid system considered inverters as an ideal source [66], which are not appropriate to study the stability of the microgrid and are not useful to analyze the robustness of microgrid controls.

1.4 Problem Statement

Managing DGs (i.e., renewables, conventional, and storage) and loads within microgrid during island and grid-tie modes and transitions is a challenge. Some of the key microgrid control scheme concerns are: (i) maintaining stability, (ii) regulating voltage and frequency, (iii) active and reactive load sharing, and (iv) easier and faster islanding and reconnection [29, 56, 67, 68]. The angle droop control and virtual impedance droop control methods are not completely reliable, while in the natural droop control method, voltage and frequency vary a lot to achieve stability in island mode. In the CERTS microgrid concept, all of the resources contribute power to the load and operate autonomously. As a result, opportunities to optimize the system and to improve efficiency are limited. Since, the active and reactive power output of natural gas generators, natural gas generators and energy storage are dependent on microgrid load and present power output of renewables, natural gas generators and natural gas generators might not operate at their rated power. At the same time, the State of Charge (SOC) of energy storage might not be sufficient due to longer period of operation in an island mode. In such a scenario, the autonomous controller might be proved vulnerable.

The main objective of this dissertation is to introduce a new framework for microgrid control, power management, and reducing voltage and frequency variations. The proposed control framework also offers improved efficiency, better utilization of renewable energy and minimization of the natural gas generator by using a unit commitment algorithm. Secure communication is used to improve efficiency, power quality and power management. The proposed control will provide the capability to operate a microgrid in case of lost communication or any sabotage on the communication network. It provides flexibility to integrate more DGs in the future. A detailed comparison between the proposed VDC and natural droop control has been

performed in this dissertation. A modified power management technique is proposed to improve power quality indexes, reduce Co₂ emission and improve energy efficiency for high penetration of renewable in a microgrid.

Control of microgrids especially in island mode of operation, is generally more difficult than a traditional power system due to (a) limited energy storage capacity and lack of inertia, (b) fast dynamics and short response time of inverter-based distributed resources, and (c) a high degree of parametric and topological uncertainties. Hence studying the stability of the proposed VDC control is required to analyze the robustness of the controls. To study stability, the state space model has been developed for microgrid. Detailed dynamic characteristic of each inverter based and machine bases DG, network dynamics and load dynamics are included into state space model. The stability analysis of the proposed control strategy has been done, which investigates the effect of the changes in microgrid and controller parameters on the trajectories of the closed loop system modes and verify the stability of the microgrid.

Chapter 2 Microgrid Configuration and Component Modeling

2.1 Microgrid Configuration

The proposed state of art has been applied to the Fort Sill microgrid under construction, and also to the IEEE 34 bus system which is adopted as a microgrid, to examine the effectiveness of the proposed technology. The microgrid systems studied in this dissertation are modeled based on the real system data and are simulated using PSCAD software. PSCAD has been chosen since it offers the capabilities to model both power systems and power electronics setups, including distribution and transmission systems, drives, switches, machines, etc. In addition, it provides control tools in order to model the controls for microgrids. Furthermore, it enables both cycle-by-cycle and average modeling.

2.1.1 Fort Sill Microgrid Configuration

The configuration of the Fort Sill microgrid studied is shown in Figure 2-1. The Fort Sill microgrid is rated at 480V, 60 Hz, and 630kW. It is connected to the utility grid through a 480V/13.20kV transformer and a static switch.

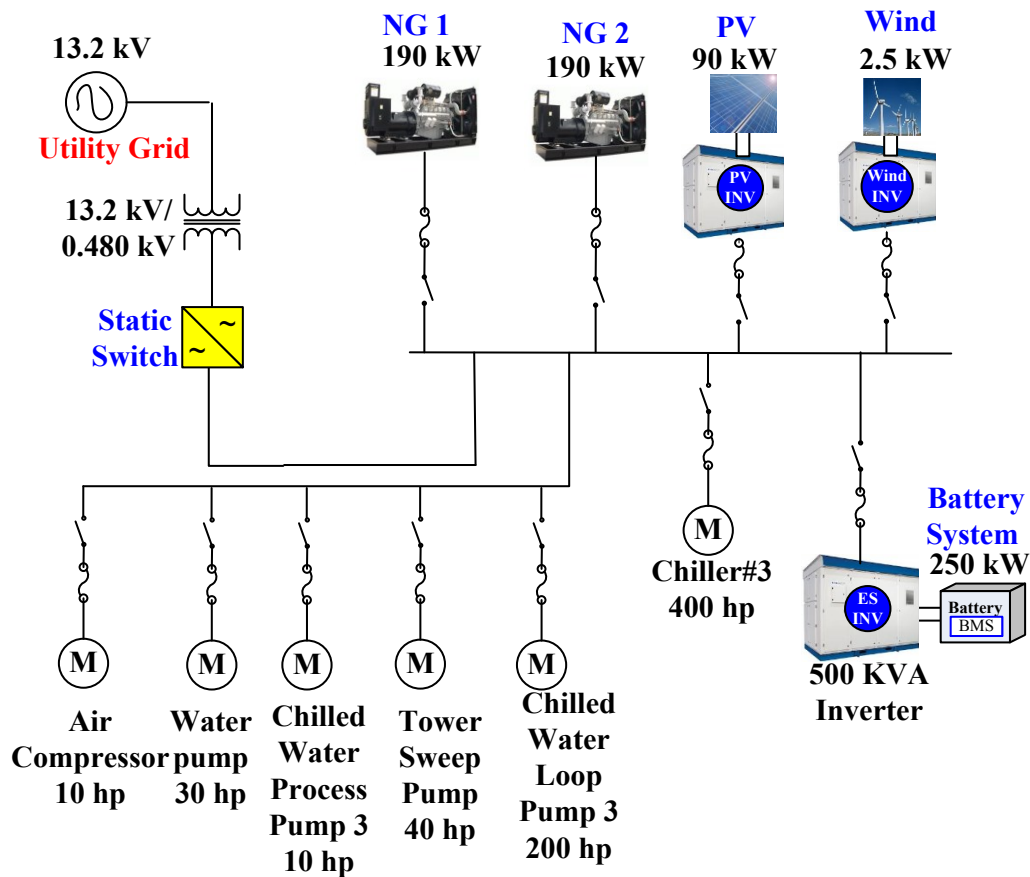


Figure 2-1. Schematic of the Fort Sill microgrid studied.

The generations in this microgrid include two natural gas generators each rated at 190 kW, one 90 kW solar PV system, a 2.5 kW wind turbine and a 250 kW energy storage device. The solar PV and wind turbine generators are connected to the system through inverters operating in current mode and the energy storage inverter is operated in voltage mode. The system also includes various motor loads and variable loads. Motor loads mainly include chillers, water pumps and air compressors. This microgrid can operate in a grid-tie mode or island mode. An energy storage inverter is always connected to the system. During grid-tie operation, natural gas generators are turned off. In an island mode of operation, natural gas generators are brought into the system according to the developed unit commitment algorithm.

2.1.2 IEEE 34 Bus Microgrid Configuration

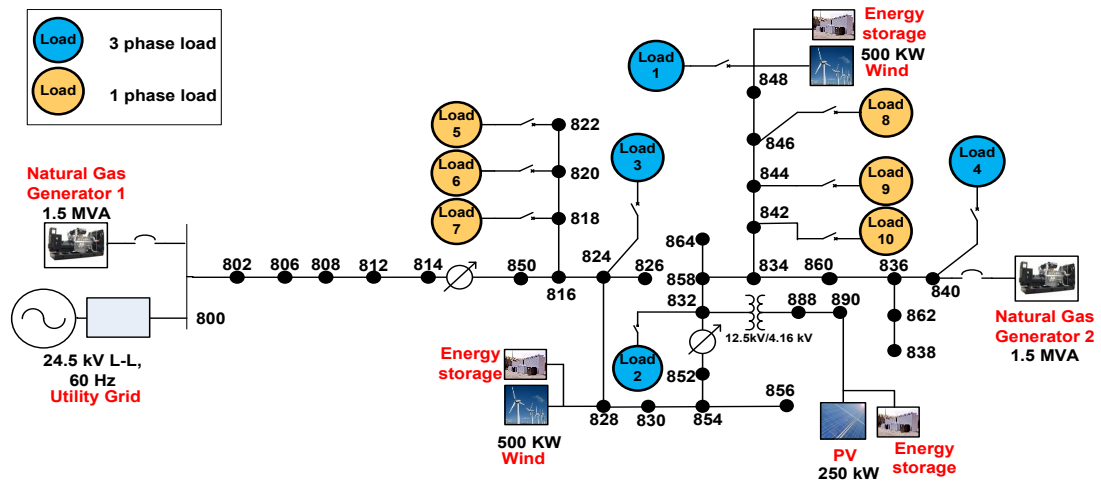


Figure 2-2. The configuration of the IEEE 34 bus microgrid.

The original IEEE 34 bus system is 24.9 kV, 60 Hz, 6 MVA with different fixed loads. It is connected to the utility and it has no Distributed Resources (DRs). It includes constant three-phase and single phase active/reactive power loads and constant impedance loads. The system has significant amount of line losses due to long transmission lines. Hence, it includes two regulators at bus 814 and 832 [69-71].

Figure 2-2 shows the modified IEEE 34 bus distribution system used as a microgrid system modeling. During island mode of operation, in base case, the utility connection is opened and two large traditional natural gas generators, each rated at 1.875 MVA, are added at buses 800 and 840. System includes constant and variable loads. Total ten variables loads are added and considered as critical loads. They are located at various buses as shown in Figure 2-2. In the case 2, two 0.5 MW of wind turbine and one 0.25 MW solar PV have been added at buses 828, 848 and 890 respectively. In case 3, the energy storage systems have been integrated with renewables and the modified control technique has been applied.

2.2 Natural Gas Generator Modeling

The natural gas generator plays a very important role in the microgrid. There are many benefits of using a natural gas generator for power production in a microgrid when a utility fails. Compared to coal, gasoline, and oil, natural gas is the cleanest fossil fuel. It causes far less environmental pollution than some other generators in the market. Greenhouse gas emission of CO₂ is minimal with a natural gas generator. The price reduction on a natural gas generator and easy transportation via pipelines motivates the use of a natural gas generator [72].

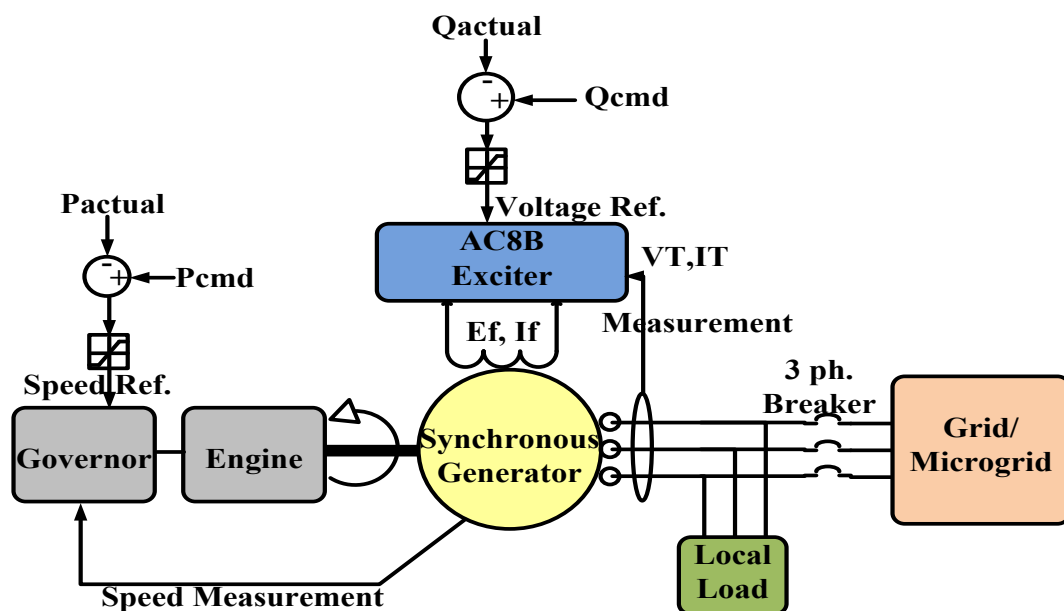


Figure 2-3. Block diagram of a natural gas generator connected to a grid/microgrid.

The exciter of a natural gas generator is in charge of reactive power and a governor adjusts the active power. By supplying active and reactive power to the system, it helps to maintain the voltage and frequency of a microgrid to a constant value. Figure 2-3 shows the basic block diagram of a natural generator connected to a grid or microgrid. To accurately study the behavior of a natural gas generator, it is required to model a synchronous generator, excitation, an Automatic Voltage Regulator (AVR) system, a gas engine, and a governor system with sufficient details [73].

The detailed modeling of all the components of a natural gas generator is described in this chapter. A synchronization scheme and active-reactive power control have been implemented for the synchronous generator. In addition, load testing has been done on the developed simulation model and has been validated using real system load testing data.

2.2.1 Synchronous generator rating

Table 2-1. Key parameters of a 190 kW synchronous generator

Rated RMS line to neutral voltage	0.277 [KV]
Rated RMS line current	0.360.8 [KA]
Frequency	60 Hz
Inertia constant	0.1619 [s]
Armature time constant [T_a]	0.0212 [p.u]
Unsaturated reactance[X_d]	2.7730 [p.u]
Unsaturated transient reactance[X_d']	0.2611 [p.u]
Unsaturated transient reactance time(open)[T_{d0}']	1.7410 [s]
Unsaturated sub transient reactance[X_d'']	0.1478 [p.u]
Unsaturated sub transient reactance time(open)[T_{d0}'']	0.0044 [s]
Unsaturated reactance[X_q]	1.6440 [p.u]
Unsaturated sub transient reactance[X_q'']	0.1710 [p.u]
Unsaturated sub transient reactance time(open)[T_{q0}'']	0.0046 [s]

In the Fort Sill microgrid, two gas generators (Caterpillar G3406 generator set), each rated at 190 kW continuous and 240 kW standbys have been integrated. The key parameters of 190 kW continuous synchronous generators are given in Table 2-1.

Table 2-2. Key parameters of a 1.2 MW synchronous generator

Rated RMS line to neutral voltage	0.277 [KV]
Rated RMS line current	2.26 [KA]
Frequency	60 Hz
Inertia constant	1 [s]
Armature time constant[T_a]	0.032 [s]
Unsaturated reactance[X_d]	2.65 [p.u]
Unsaturated transient reactance[X_d']	0.282 [p.u]
Unsaturated transient reactance time(open)[T_{d0}']	2.6 [s]
Unsaturated sub transient reactance[X_d'']	0.134 [p.u]
Unsaturated sub transient reactance time(open)[T_{d0}'']	0.014 [s]
Unsaturated reactance[X_q]	1.45 [p.u]
Unsaturated sub transient reactance[X_q'']	0.136 [p.u]
Unsaturated sub transient reactance time(open)[T_{q0}'']	0.008 [s]

In the IEEE 34 bus microgrid, two synchronous generators, each rated at 1.2 MW continuous and 1.5 MW standbys have been added and the key parameters of a 1.5 MW synchronous generators are given in Table 2-2.

2.2.2 Exciter Modeling

The basic function of an excitation system is to provide direct current to the synchronous machine field winding. The excitation system must be able to automatically adjust the field current to maintain the required terminal voltage/reactive power. To study the behavior of a synchronous machine for the power system stability studies, it is essential that the excitation system of the machine is modeled with sufficient detail [74]. The developed model must be suitable for representing the actual

excitation equipment performance for large, severe disturbances as well as for small perturbations. The basic block diagram of an excitation control system is given in Figure 2-4.

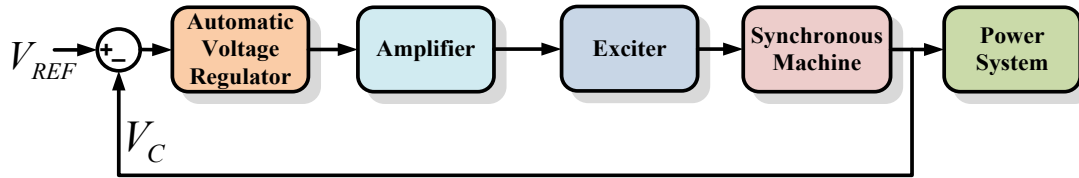


Figure 2-4. Basic block diagram of an excitation control system

On the basis of an excitation power source, IEEE Standard 421.5 recommends three distinctive types of excitation systems: DC type excitation systems, AC type excitation systems and static type excitation systems [74-77]. Due to the fairly small size of the machines used in both microgrids studied, the alternator supplied rectifier exciter (AC8B) has been chosen.

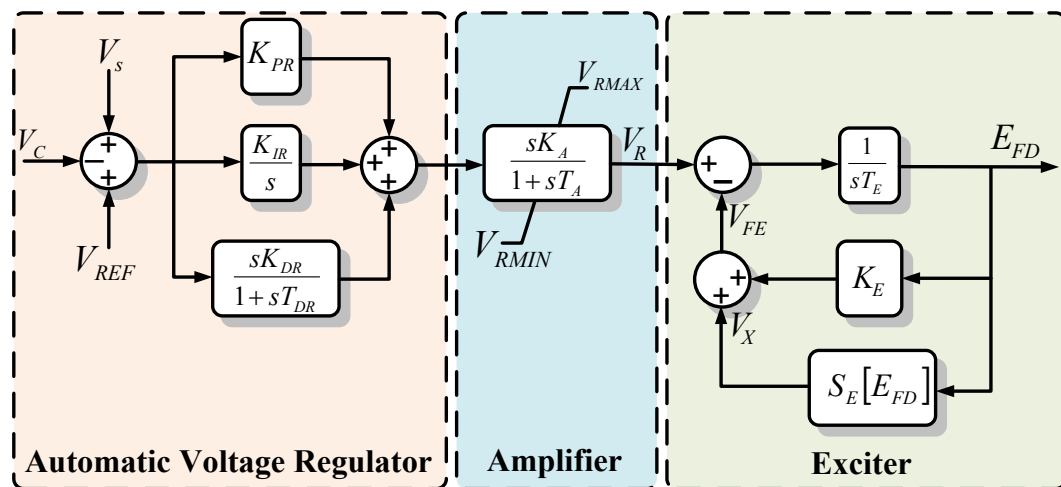


Figure 2-5. Block diagram of AC8B: Alternator-rectifier excitation system with digital control

The block diagram of the AC8B model with AVR system is shown in Figure 2-5. The AVR in this model consists of a PID control, with separate constants for proportional, integral and derivative gains. The values of constants are chosen for the best performance for each particular generator excitation system. The amplifier amplifies the control signal from the AVR system to exciter level where, K_A is the

amplifier gain. In reality, the amplifier will have a time delay that can be represented by time constant T_A and usually it will be in the range of 0.02 to 0.1 second.

It is also required to derive the transfer function of exciter field to complete the excitation system model. If R_E and L_E represent the resistance and inductance of the exciter field, then the exciter current equation can be written as follows:

$$V_R = R_E I_E + L_E \frac{d}{dt} I_E \quad (2-1)$$

The exciter field current (I_{ED}) produces voltage (E_{FD}), which is the rectified armature voltage of the exciter given as follows:

$$E_{FD} = K_1 I_{ED} \quad (2-2)$$

By replacing the field voltage in equation (2-1), the following equation can be written.

$$V_R = R_E \frac{E_{FD}}{K_1} + L_E \frac{d}{dt} \left(\frac{E_{FD}}{K_1} \right) \quad (2-3)$$

$$E_{FD} = \frac{K_E}{1 + sT_E} V_R \quad (2-4)$$

Where,

$$K_E = \frac{K_1}{R_E} \text{ and } T_E = \frac{L_E}{R_E}$$

The exciter time T_E is in the range of 0.5 to 1.0 second. In Figure 2-5, $S_E[E_{FD}]$ represent exciter saturation function value at the corresponding exciter voltage E_{FD} .

To get the closed-loop transfer function and design the exciter, it is necessary to establish a dynamic link between the field voltage and synchronous generator terminal voltage. It is also required to define the per unit system for exciter to connect them to per unit synchronous machine model. The obvious choice is to have 1.00 per unit exciter output voltage equal to the field voltage required to produce a rated synchronous machine armature terminal voltage on the air-gap line and 1.0 per unit exciter output

current is the corresponding synchronous machine field current. Under steady state conditions, per unit values of E_{FD} and I_{ED} are equal. During a transient condition, however, E_{FD} and I_{ED} differ. E_{FD} is determined by the excitation system and I_{ED} is determined by the dynamics of the field circuit. The open circuit transfer function of the generator is given by equation as follows:

$$V_t = \frac{1}{1 + sT'_{d0}} E_{FD} \quad (2-5)$$

According to IEEE standards and guide, it is requisite to meet certain dynamic performance criteria of an exciter control system. Small signal performance measures provides a means of evaluating the response to the closed-loop excitation control systems to incremental changes in system conditions. In addition, a small signal performance characteristic provides a convenient means for determining or verifying system model parameters for system studies. The major performance indices associated with time response are rise time, overshoot, and settling time, while indices associated with open-loop frequency response are the low frequency gain G, cross over frequency, phase margin and gain margin. However, the indices of interest associated with the closed-loop frequency response are the bandwidth and peak value. Generally accepted values of performance indices characterizing good feedback control system performance are given as follows:

Gain margin ≥ 6 dB

Phase margin ≥ 40 degrees

Overshoot = 5-15%

Peak magnitude=1.1-1.6

A Matlab simulink and PID tuner available in Matlab has been used to design the AVR. However time constants of exciter and amplifiers are known. The Matlab simulink model used to tune the PID controller is shown in Figure 2-6. Based on the

controller performance benchmark and using the PID tuner, the parameters of the AVR system have been achieved and used to model the exciter system in PSCAD software. The step response of the exciter system including AVR system has been plotted in Figure 2-7. The achieved PID parameters are given as follows:

$$K_{PR}=1.0129,$$

$$K_{IR}=2.270138$$

$$K_{DR}=1.266049 \text{ and}$$

$$T_{DR}=0.0020111.$$

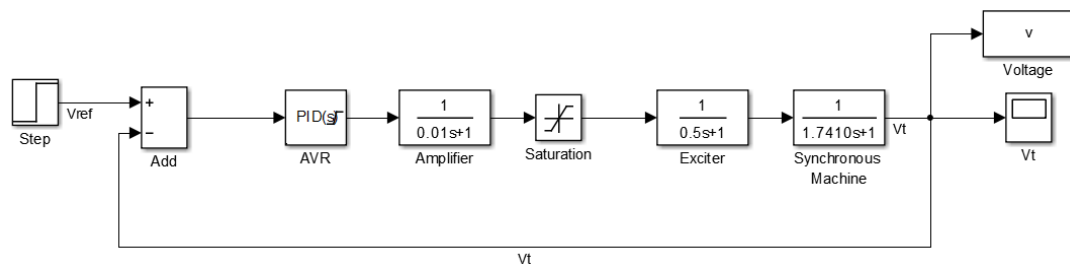


Figure 2-6. The Matlab simulink model used to tune a PID controller.

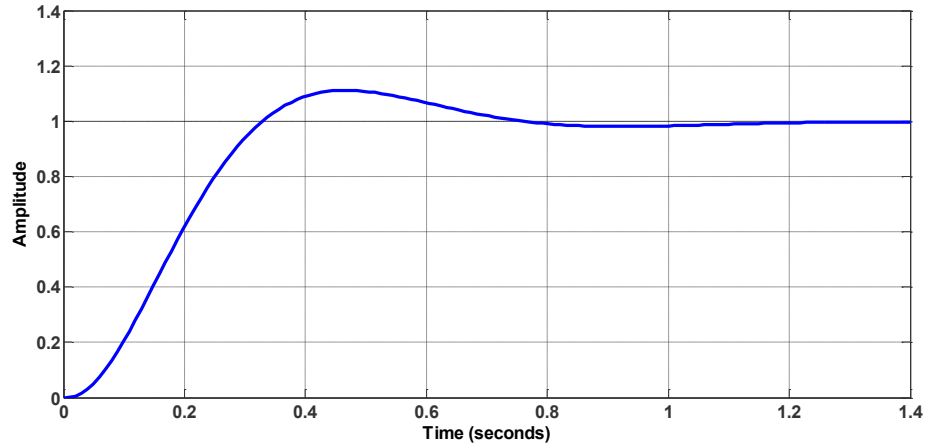


Figure 2-7. Step response of a closed-loop excitation system.

2.2.3 Natural Gas Turbine Modeling

Gas turbines can be classified in the following three categories:

- (1) Aero derivative gas turbines: Power output from approximately 8 MW up to approximately 25 MW.
- (2) Light industrial gas turbines: Power output less than 10 MW

(3) Heavy industrial gas turbines: Power output greater than 25 MW.

There are two gas turbine driving methods known as ‘single-shaft’ and ‘two shaft’ drives. In a single-shaft gas turbine, all of the rotating elements share a common shaft. The common elements between the two types of gas turbines are the air compressor, the compressor turbine and the power turbine. In the studied microgrid systems, single-shaft light industrial gas turbines are used as distributed resources [72]. The basic arrangement of a single-shaft gas turbine is shown in Figure 2-8.

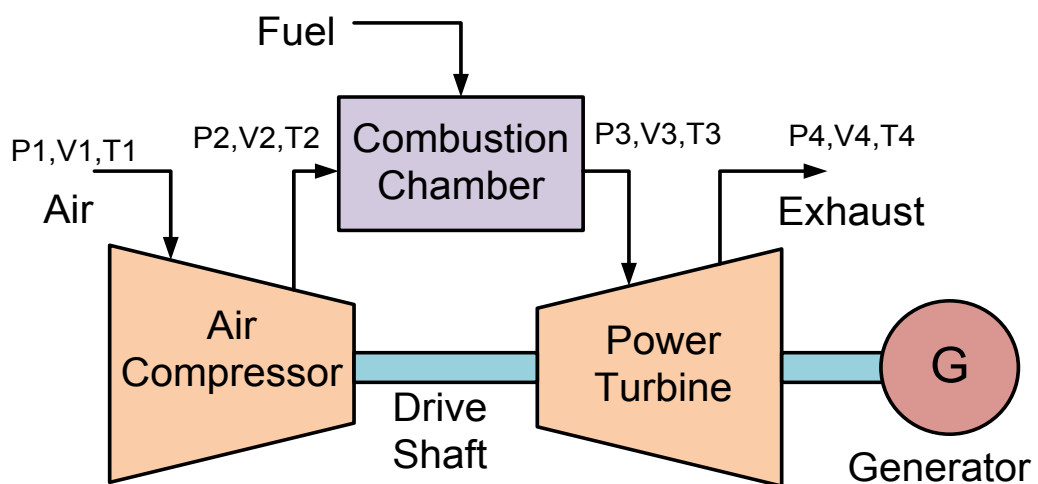


Figure 2-8. Basic arrangement of a single shaft gas turbine

The basic control block diagram of a natural gas engine and the governor system is shown in Figure 2-9.

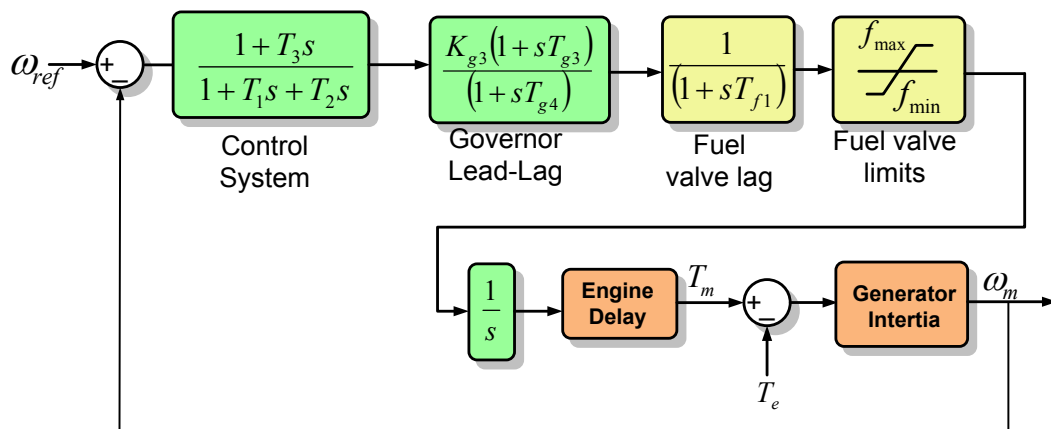


Figure 2-9. The detailed control system of a gas engine system.

The natural gas engine must be controlled in order to convert the power to useful work. The essential device called a governor, controls the speed or power output. To improve the speed response, an electronic control system is employed in the governor control system. The governor senses the speed of a prime mover and sends an electrical signal to the actuator to control the fuel to the engine to maintain its speed/load at the desired level. The gas engine, governor, and actuator are modeled with sufficient details and the governor controls are adjusted to meet the typical performance of the engine. The gain and time constant used in the governor model were adjusted until a reasonable response was obtained [78, 79].

2.2.4 Synchronization of generator

The synchronization scheme has been implemented for a natural gas generator.

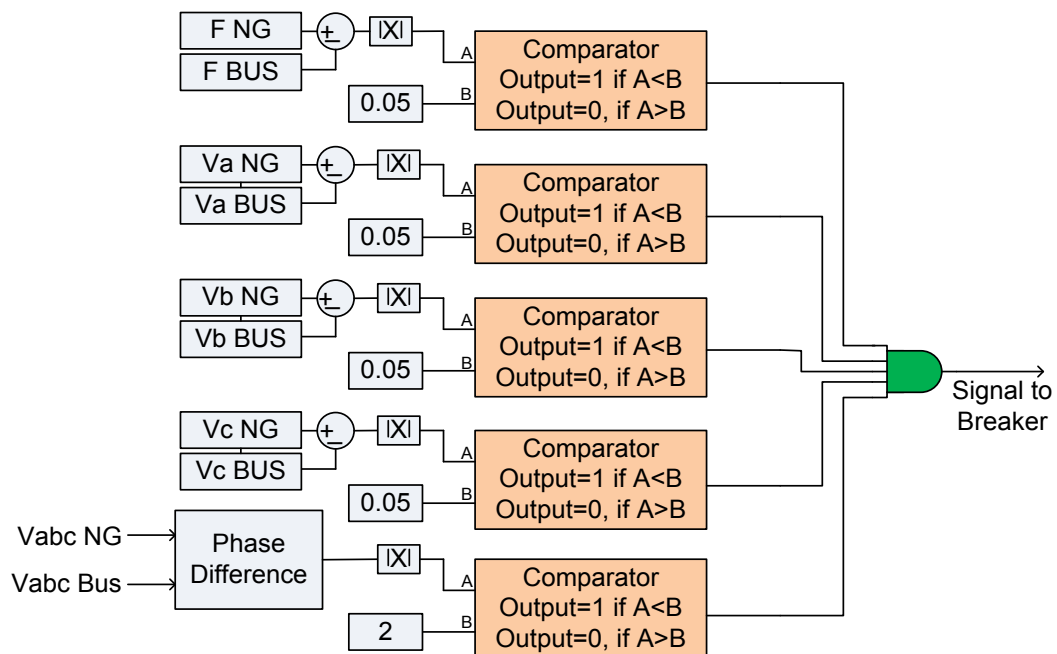


Figure 2-10. Control logic behind the synchronization breaker.

Figure 2-10 shows the controller logic behind a synchronization scheme. The three-phase instantaneous voltage has been measured on the generator side as well as the grid/microgrid side. From instantaneous voltage, rms voltage, frequency and phase angle have been calculated. The reference voltage of the exciter is set to the

grid/microgrid voltage and the frequency of the generator is set in such a way that the frequency and phase angle of the generator match to the grid/microgrid frequency and phase angle. When the frequency difference is less than 0.1%, the voltage difference is less than 0.01 p.u and the phase angle difference is less than 2 degree, the breaker will be closed. Once, the breaker is closed, the generator will follow the active and reactive power references and set the power output.

2.2.5 Results and Model Verification

To verify the developed model, a load test has been done. In standalone mode, the step load has been applied to verify the dynamic behavior of the natural gas generator. Figure 2-11 shows the experimental and simulation frequency responses. A step load change of 50% of rated generator capacity is applied and reference frequency is set to 59.7 Hz. The test result is for a 100 kW natural gas generator, which is used in the test setup explained in later in this dissertation. However, the simulation result is for a 190 kW natural gas generator. ISO 8528 is the industry standards that has set transient response standard requirements for the generator sets. These standards specify a detailed description of load and unload steps and frequency deviations. The simulation response of a 190 kW generator meets the ISO 8528 standard and its response is similar to a 100 kW natural gas generator. However, due to difference in inertia constant and rated power, the frequency deviation in the case of 190 kW generators is slightly higher compared to a 100 kW natural gas generator. As shown in the experimental result, using a 100 kW generator, for 50% step load change, the frequency deviates approximately by 1.35 Hz and settling time is nearly 1.65 seconds. As shown in the simulation result, using a 190 kW generator, the frequency deviation is approximately 1.8 Hz and the settling time is nearly 2 seconds.

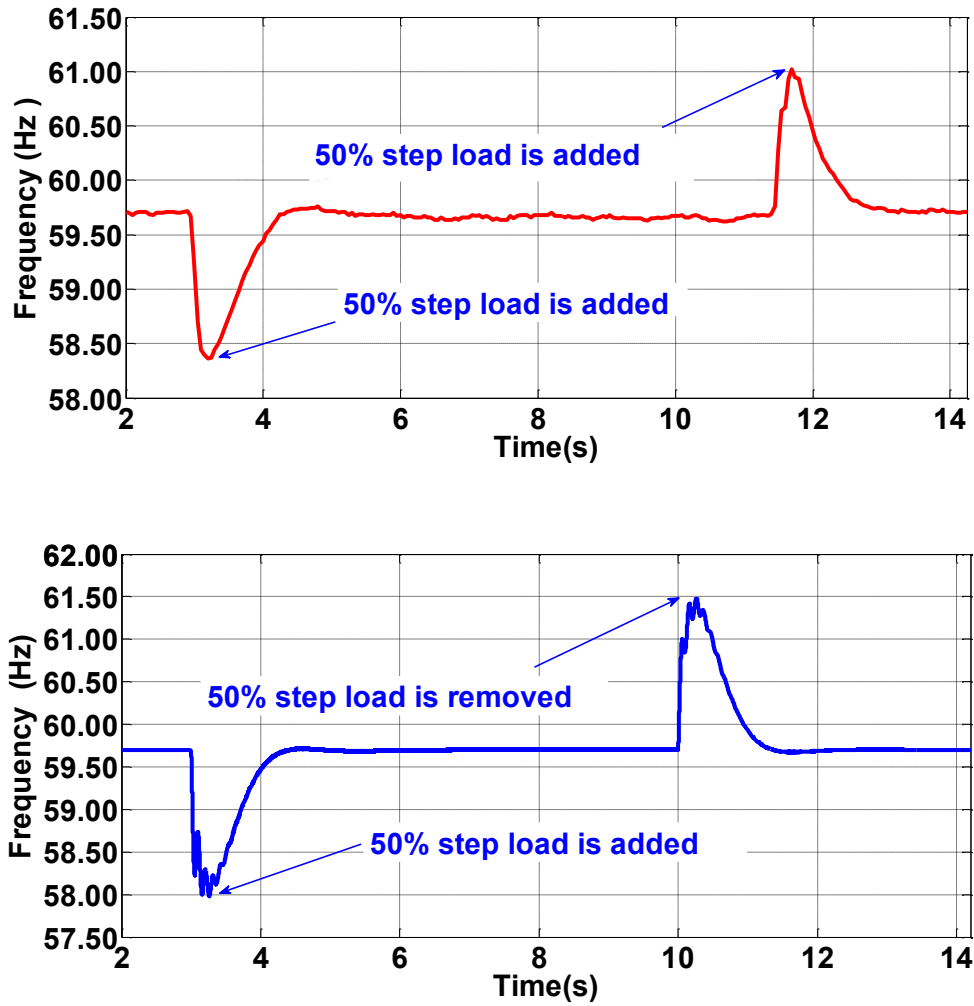


Figure 2-11. Frequency response to a 50% step change load, test result (above), simulation result (below).

Figure 2-12 shows the active and reactive power dynamics when the active-reactive power control for the generator is applied. At 13th second, 100% power command with a power factor of 0.8 is applied. At 30th second, power command changes from 100% to 10%.

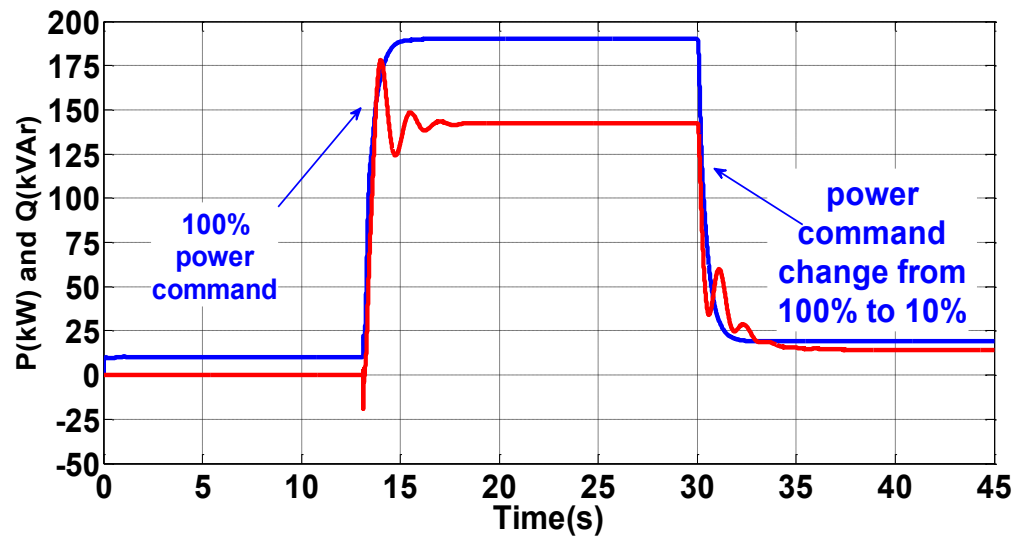


Figure 2-12. Active and reactive power dynamics of the natural gas generator.

2.3 Voltage Source Converter System

In recent years, the field of power electronics has experienced significant growth due to advancement in semiconductor fabrication technology and revolutionary advances in digital signal processors. The power converter system facilitates the exchange of energy between two subsystems in a desired manner based on predefined performance criteria. The subsystems often have different voltage and current forms, different frequency, phase angle, and magnitude and it is not possible to directly interface with each other. A power electronics converter system provides an interface link between two different subsystems.

The renewable energy and energy storage system utilize the Voltage Source Converter (VSC) system to interface them with a grid/microgrid. There are mainly two modes of operation, current mode and voltage mode. A current mode VSC system is important to extract maximum power from renewable energy resources. However, for an energy storage system, voltage mode is utilized in island mode operation and current mode is used in grid-tie mode as well as during loss of communication. The state vector modulation (SVM) technique has been implemented for the VSC system to provide the switching signal [80]. The details of the SVM technique, current mode VSC system, and voltage mode VSC system are given in the following sections.

2.3.1 State Space Vector Modulation Technique

The PWM switching signals for the VSC system can be generated by analogue or digital control electronics [81-84]. The major advantages of digital controls are stability, precision, flexibility and less computing time. By using the SVM technique, the calculation process can be simplified. In turn, computing time can be reduced; therefore better performance can be obtained.

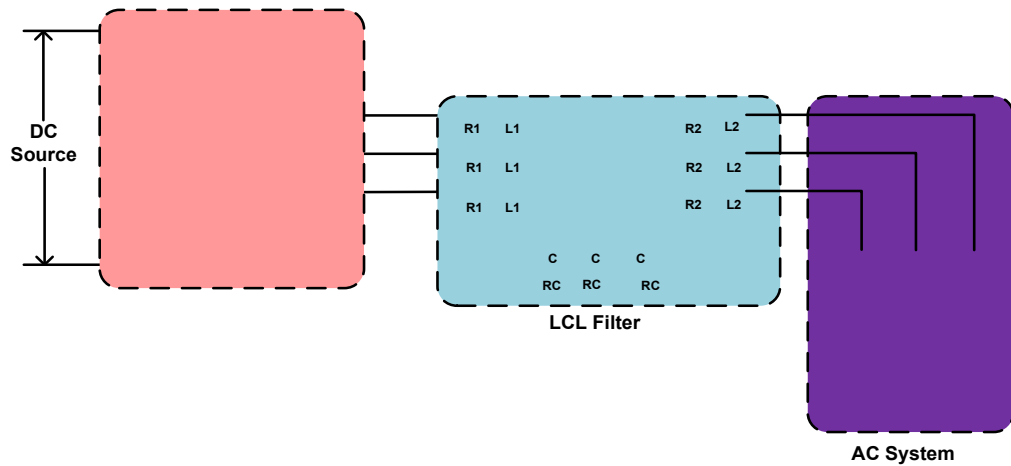


Figure 2-13. Topology of a three-phase VSC system

The topology of a three-phase two-level VSC system is shown in Figure 2-13. In the three-phase VSC system, the major constraint is that the switches of the same leg cannot be turned on together. This is to avoid short circuit of the input DC source. According to the given constraint, there are only eight possible switching patterns, which are shown in Figure 2-14. Six of eight topologies produce a non-zero output voltage and are known as non-zero switching states and the remaining two topologies produce zero output voltage and are known as zero switching states.

Any three phase set of variables that add up to zero in the stationary a-b-c frame can be represented in a complex plane by a complex vector that contains a real and an imaginary component. The coordinate transformation from a-b-c to α - β is given by following equation (2-6).

$$\begin{bmatrix} v_\alpha \\ v_\beta \end{bmatrix} = \sqrt{\frac{2}{3}} \begin{bmatrix} 1 & -\frac{1}{2} & -\frac{1}{2} \\ 0 & \frac{\sqrt{3}}{2} & -\frac{\sqrt{3}}{2} \end{bmatrix} * \begin{bmatrix} v_a \\ v_b \\ v_c \end{bmatrix} \quad (2-6)$$

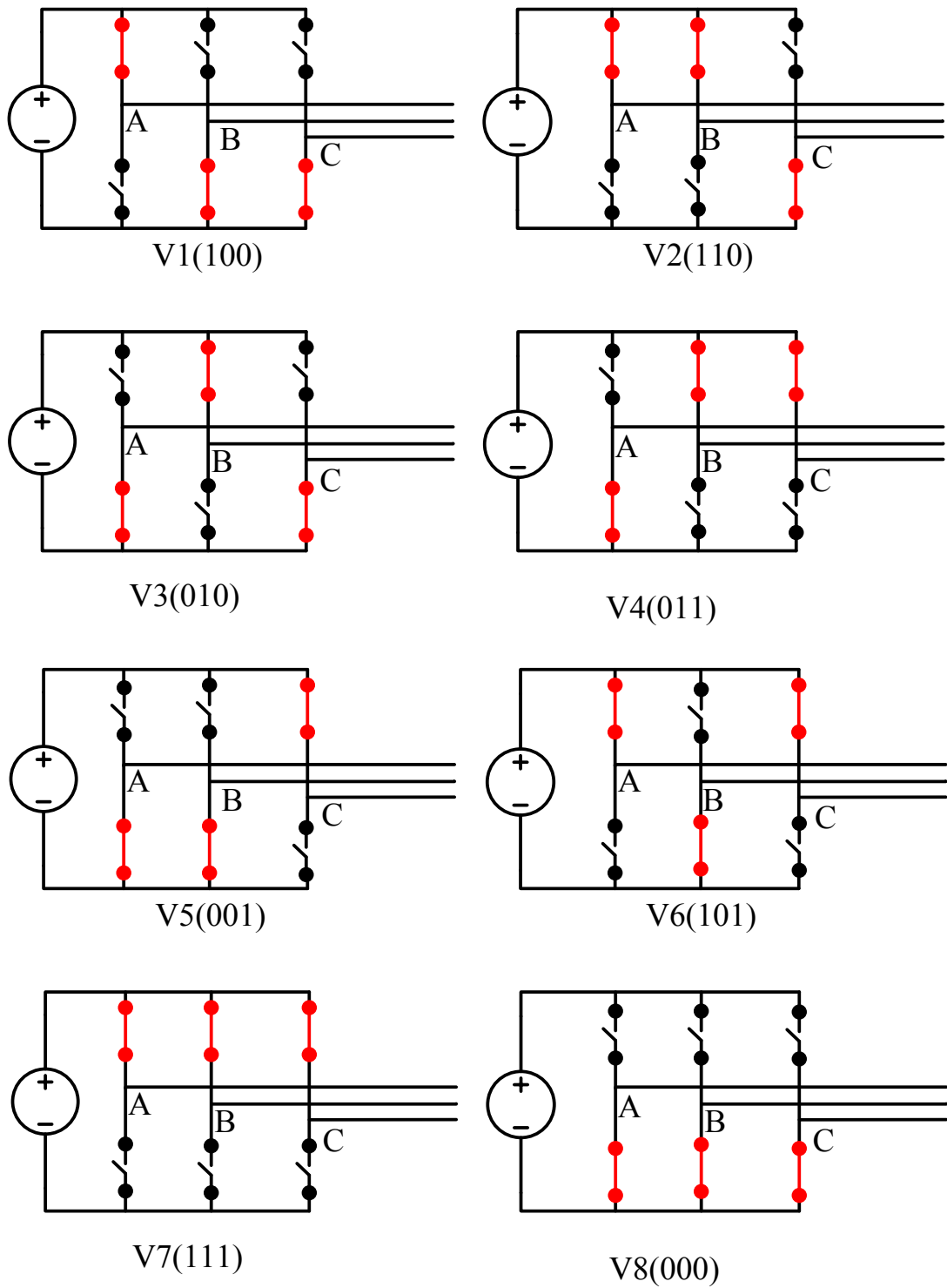


Figure 2-14. Possible switching state topologies of a voltage source inverter

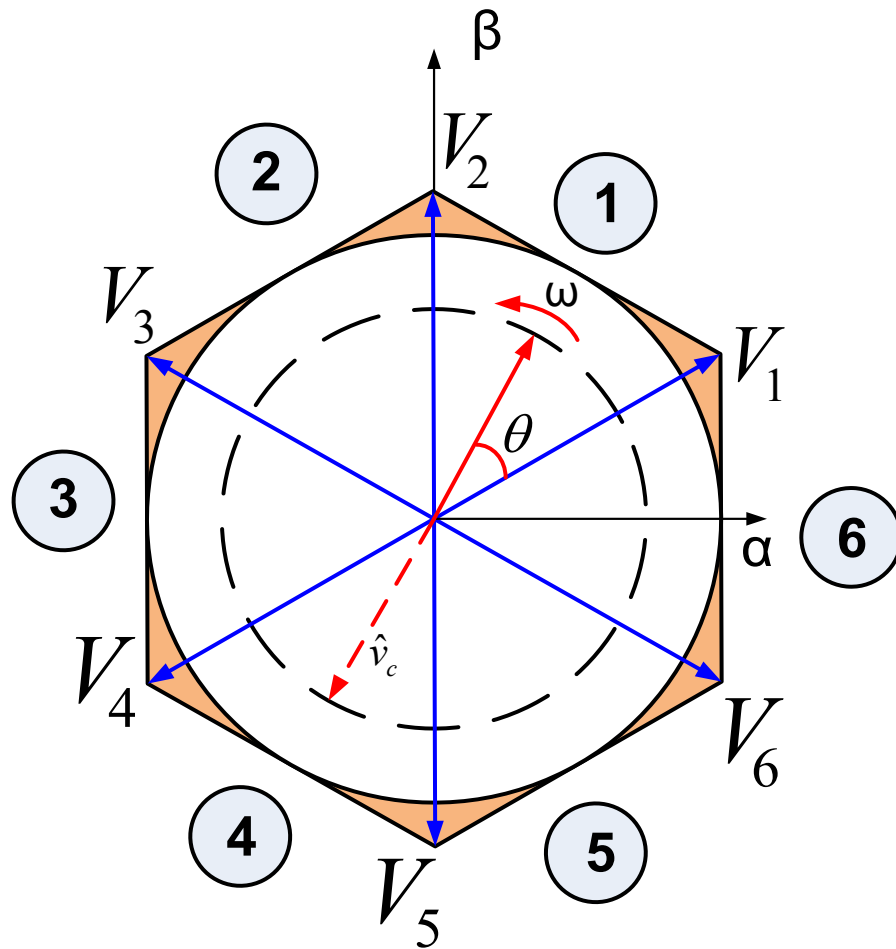


Figure 2-15. Space vector representation

The three-phase line modulating signal (v_c^{abc}) is received from the control system which controls the active and reactive power, or DC bus voltage or converter's terminal voltage and frequency. The three-phase line modulating signal (v_c^{abc}) is transformed into an α - β reference frame and can be represented by the complex vector $\vec{v}_c = v_c^{\alpha\beta}$. For instance, if the line modulating signals are three-phase balanced sinusoidal waveforms with an amplitude equal to \hat{v}_c and angular frequency ω , the resulting modulating signals in the α - β reference frame become a vector of fixed amplitude equal to \hat{v}_c that rotates at frequency ω . Similar space vector transformation is also applied to the line voltages of eight states, which generate eight space vectors shown in Figure 2-15.

The objective of the SVM is to approximate the sinusoidal line modulating signal \vec{v}_c with eight space vectors. In addition, if the modulating signal \vec{v}_c is laying between two arbitrary vectors, only the nearest two nonzero vectors and one zero space vectors should be used to obtain the maximum load line voltage and to minimize the switching frequency. For instance, if the modulating vector \vec{v}_c is in section 1, it can be realized by \vec{v}_1 and \vec{v}_2 vectors and one zero vector \vec{v}_z (\vec{v}_7 and \vec{v}_8). If vector \vec{v}_1 is active for time T_1 , \vec{v}_2 is active for T_2 and zero vector \vec{v}_z for T_z time, then the vector \vec{v}_c is active for T_s sampling time. The sampling time can be determined from the switching frequency. For sufficiently high switching frequency, \vec{v}_c can be assumed constant during one switching period. Based on the discussion the following equation (2-7) should be true.

$$\vec{v}_c * T_s = \vec{v}_1 * T_1 + \vec{v}_2 * T_2 + \vec{v}_z * T_z \quad (2-7)$$

Expressing the space vectors in equation (2-7) into rectangular coordinates, comparing real and imaginary parts on both sides and solving for T_1 and T_2 , equations should be written as follows:

$$T_1 = T_s * \hat{v}_c * \sin\left(\frac{\pi}{3} - \theta\right) \quad (2-8)$$

$$T_2 = T_s * \hat{v}_c * \sin(\theta) \quad (2-9)$$

$$T_z = T_s - T_1 - T_2 \quad (2-10)$$

Based on the selection of zero vectors and space vector sequences, there are different SVM algorithms available. The space vector sequence to be used should ensure load line voltages that feature quarter wave symmetry in order to reduce unwanted harmonics in their spectra. Zero vectors section should be done in order to reduce the switching frequency. To have the lowest Total Harmonic Distortion (THD),

the symmetric sequence SVM technique had been used. The switching waveform of the symmetric sequence SVM technique is shown in Figure 2-16.

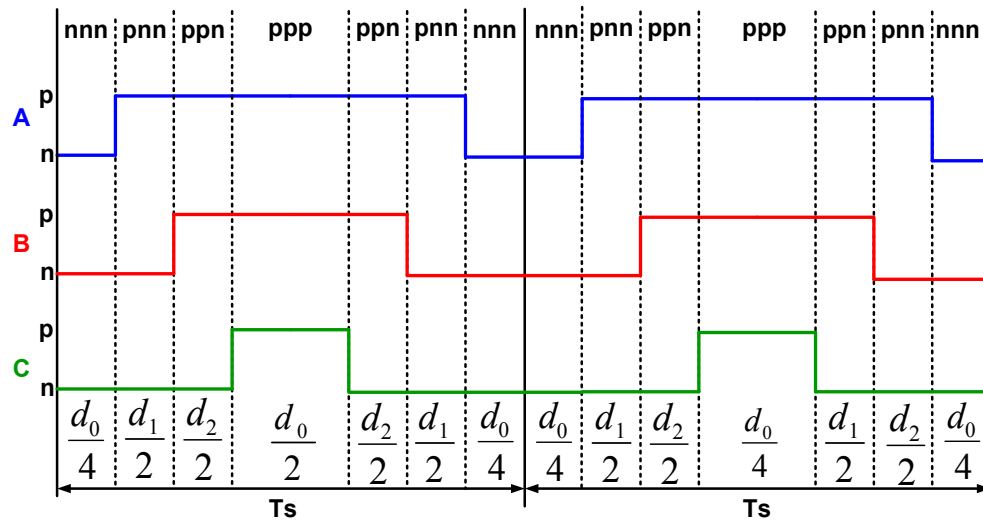


Figure 2-16. The phase gating signal in the symmetric SVM technique.

2.3.2 Current Mode Voltage Source Converter

The controlled objective of the current mode VSC system is to regulate the output active and reactive power of a converter. This class of VSC system has been utilized in renewable energy applications mainly with solar PV and full conversion topology of the wind energy system. The active and reactive power reference can be obtained from MPPT to extract maximum power from renewable energy resources [80, 85-87].

In this mode of operation, the VSC line current is tightly regulated by a dedicated current control scheme through the VSC AC-side terminal voltage. Due to the current regulation scheme, the VSC is protected against over current conditions. Other advantages of the current mode control include robustness against variations in parameters of the VSC system and the AC system, better dynamic performance, and higher precision. The d-q reference frame is used for a control system due to the following features. The number of plants to be controlled is reduced from three to two. The decoupled control of the active and reactive power output of the converter is

possible. In addition, all of the control variables are DC quantities in the steady state. This feature very remarkably facilitates the compensator design.

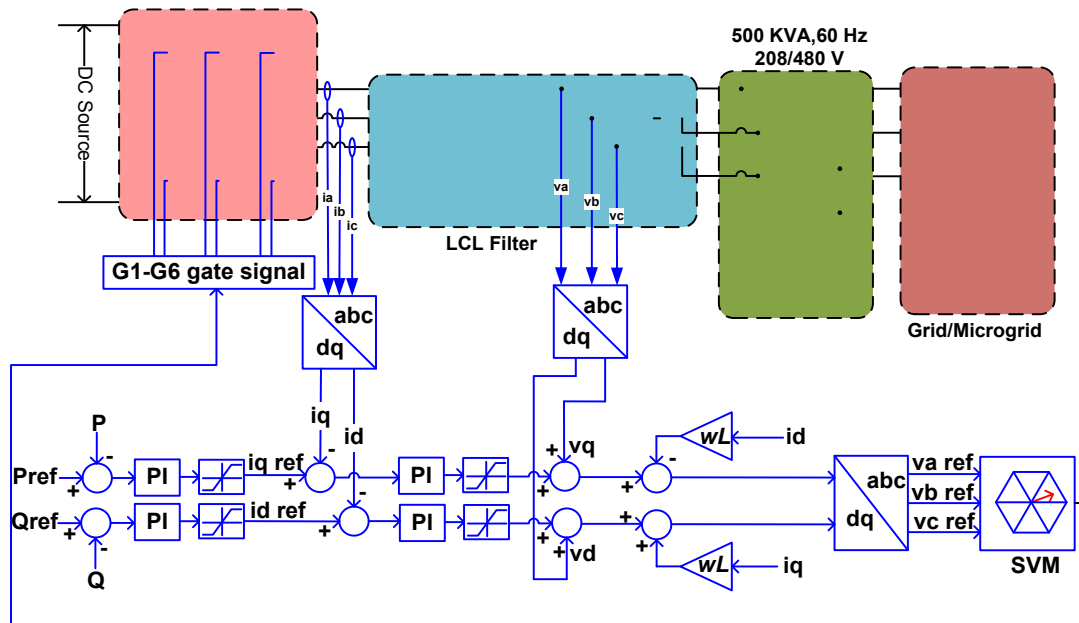


Figure 2-17. Schematic diagram of the current mode VSC system.

The schematic diagram of the current mode VSC system is shown in Figure 2-17. In the current mode VSC system, the line current is tightly regulated by a dedicated current control scheme, through the converter side AC voltage. The real and reactive powers are controlled by the angle and magnitude of the line current with respect to the terminal voltage. The VSC system is protected against over current because of this control scheme. The terminal voltage and line current are first transformed to the d-q frame. The active and reactive error signals are processed by a proportional-integral controller to generate the d-q reference current signals. The current error signals in d-q frame are processed by a PI controller to produce the control signals in the d-q frame. Finally, the control signals are transformed to the a-b-c frame and fed to the VSC system through the PWM technique. The SVM technique is used to generate the gating signals for switches [88].

Simulation tests have been conducted on an energy storage inverter in a current mode of operation. Figure 2-18 to Figure 2-21 show the active and reactive power of the energy storage inverter in the current mode. At 5th and 10th second, step change is applied in the power command.

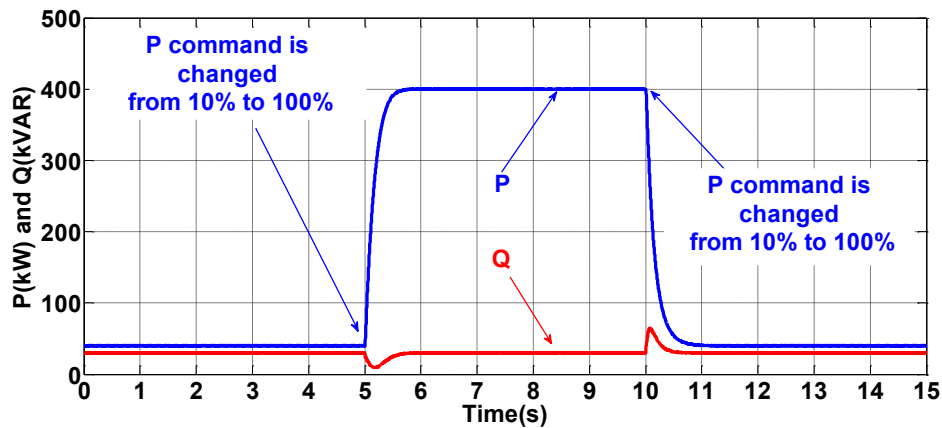


Figure 2-18. Active and reactive power simulation test results for a 500 kVA current mode VSC system, when a step active power command from 10% to 100% and to 10% is applied.

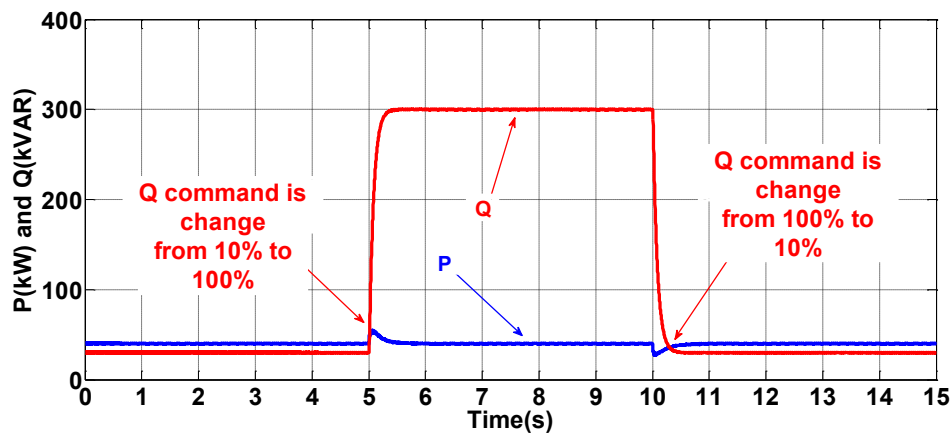


Figure 2-19. Active and reactive power simulation test results for a 500 kVA current mode VSC system, when a step reactive power command from 10% to 100% and to 10 % is applied.

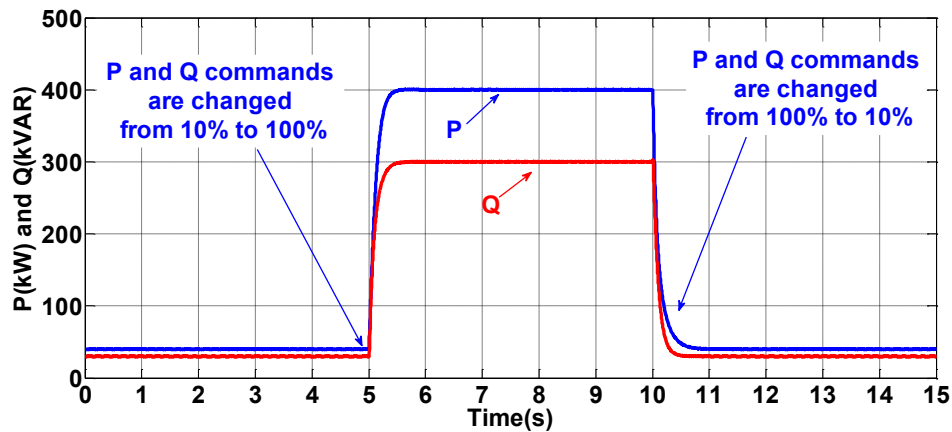


Figure 2-20. Active and reactive power simulation test results for a 500 kVA current mode VSC system, when a step active and reactive power command from 10% to 100% and to 10% is applied.

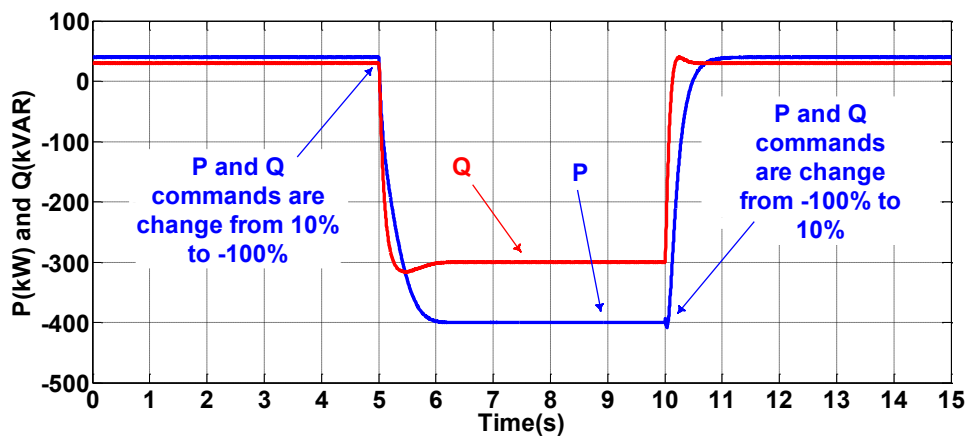


Figure 2-21. Active and reactive power simulation test results for a 500 kVA current mode VSC system, when a step active and reactive power command from 10% to -100% and to 10% is applied.

2.3.3 Voltage Mode Voltage Source Converter

The controlled objective of the voltage mode VSC system is to regulate the amplitude and the frequency of the AC system. Unlike the current mode VSC system, the operating frequency and voltage are not imposed by the AC system, but are controlled by the VSC system itself. Hence, this class of VSC system is referred to as the voltage mode. It is assumed that the net DC side voltage is supported by a DC voltage source. In studied microgrid systems the energy storage system is used as a DC voltage source.

synchronize with this voltage to deliver power. A simulation test and experimental test have been conducted on the energy storage inverter during transition from current mode to voltage mode and the results are shown in Figure 2-23 and Figure 2-24.

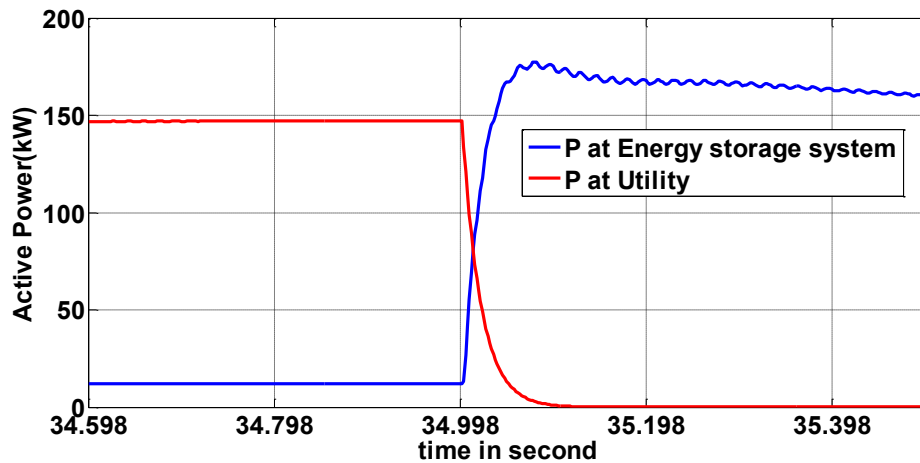


Figure 2-23. Simulation result; transition from grid-tie mode to island mode

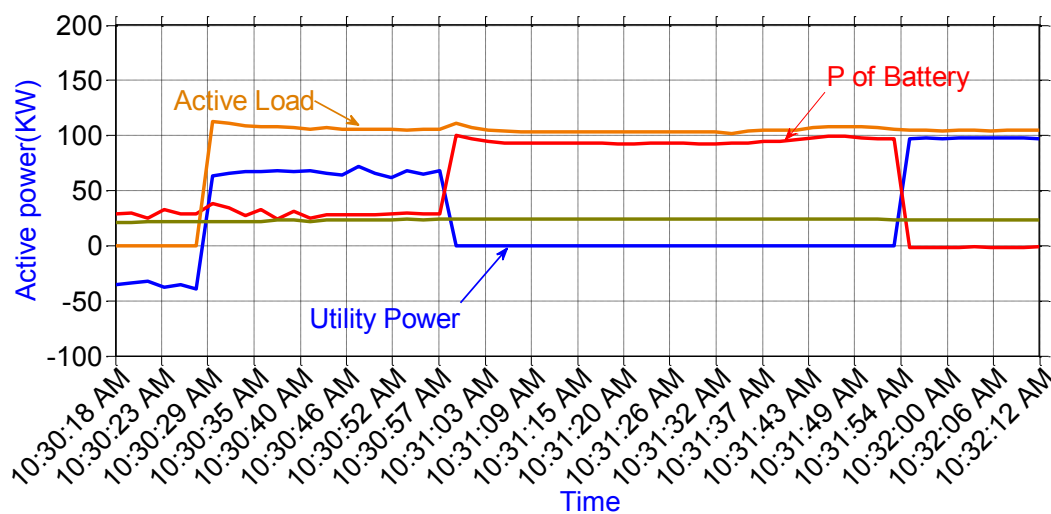


Figure 2-24. Experimental test result; transition from grid-tie mode to island mode

As shown in Figure 2-23, at 34.998th second, the microgrid is islanded from the grid and the energy storage inverter is switched from current mode to voltage mode. The power from the grid becomes zero after the breaker is opened and the energy storage inverter picks up the microgrid load. The simulation result has been verified using experimental result. As shown in Figure 2-24, around 10:30:29 AM, 100 kW load has been added. Before 10:30:57 AM, the energy storage inverter is operated in current

mode and the active power command given to the energy storage system is 50 kW. At 10:30:57 AM, the microgrid is islanded and the energy storage inverter is switched from current mode to voltage mode and takes the entire load except a small amount of power generated from renewable resources.

2.4 Energy storage System

An energy storage system is a rapidly emerging approach to managing grid/microgrid systems [91]. Energy storage systems have the ability to provide multiple services such as electric supply capacity and energy time shift, ancillary services, distribution system support, customer cost management and higher renewable energy integration into an energy network. The integration of an energy storage system into a microgrid enhances the power security for critical loads by reducing the vulnerability of the local distribution system. The energy storage system enables higher penetration of renewables by protecting the stability of the energy network. An energy storage system is an essential device in a microgrid due to all of the benefits as described. Hence, it is very important to model the energy storage system with all key dynamics [92]. 250kW, 56kWh Li-ion battery storage is used for the Fort Sill microgrid system and a 250 kW, 500 kWh zinc bromide energy storage system have been added to the IEEE 34 bus microgrid system.

The energy storage system is modeled using a simple controlled source in series with an internal resistance which is shown in Figure 2-25. The voltage of the controlled voltage source determined by SOC versus open circuit voltage (OCV) is given by the manufacturer for a specific battery or it can be derived from testing. The relationship between OCV and SOC can be represented by an n^{th} order polynomial function in equation or can be represented into lookup table into simulation model [93-95]. In PSCAD software, a piece-wise linear look-up table can be defined, where the XY coordinate points can be specified. The input to this component will be the SOC of the energy storage system and the output will be the OCV, which is the voltage of controlled voltage source. Based on the output current from the energy storage system SOC is calculated as follows:

$$SOC = \frac{Q - i_t}{Q} * 100 \quad (2-11)$$

Where,

Q = battery capacity (Ah)

i_{out} = battery current (A)

$$i_t = \frac{1}{3600} \int_0^{Q*3600} i_{out} = \text{actual battery charge(Ah)}$$

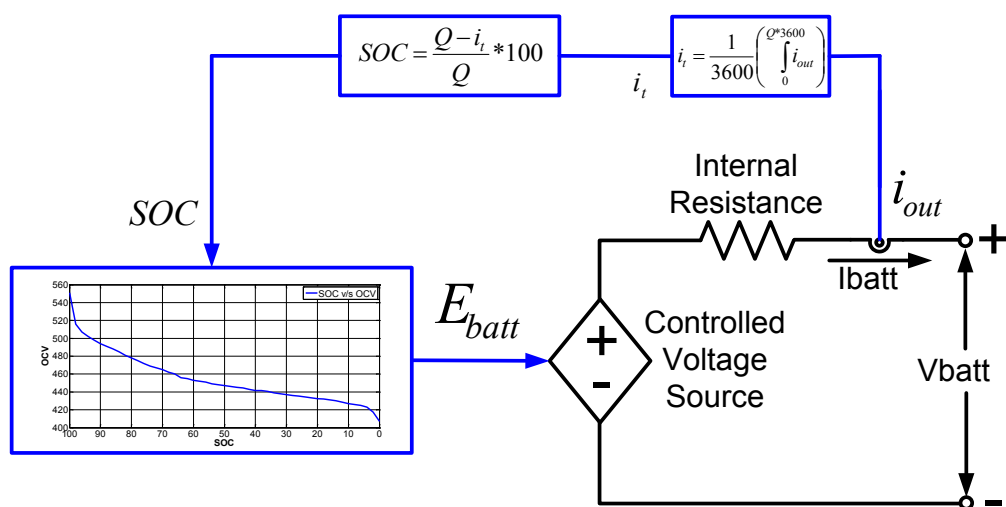


Figure 2-25. Equivalent circuit of the battery system

2.4.1 Lithium-ion Battery Storage System

A lithium-ion battery system is reliable and has high power performance, symmetrical charge and discharge capability, wider operational temperature capabilities, longer cycle life, and higher safety aspects [93]. The 250 kW, 56 kWh Altairnano battery storage system (PowerRack 320) has two parallel units and each unit has twenty 24 V 60 Ah battery modules in series. There are 10 battery cells in series in each battery module.

The battery management system includes the Master Battery Monitoring Unit (BMU) which resides inside the Connection and Control Unit (CCU). The BMU monitors the battery system health and status of the system via the Local Battery

Management Units (LMU). The BMU controls cooling fans and contactors to operate the system in a coordinated and optimal manner. In addition the BMU communicates battery system status, alarms, and SOC to the energy storage inverter. Each battery module is supplied with a Local Monitoring Unit (LMU) that reports, to the BMU, each cell's voltage and the module's temperature. This accurately determines the module's health and capacity for charging and discharging. In addition, at the direction of the BMU, the LMU balances the individual cells to maintain the best operating characteristics of the battery module. The key parameters of the battery system are shown below.

Table 2-3. Key parameters of 250 kW, 56 kW Li-ion battery system

Units in parallel	2
Cells in series each unit	200
Maximum voltage for system, V	580
Maximum current for system, A	1200
Maximum power for system, KW	417
Maximum energy for system, KWh	56
Cell charge capacity (Ah)	60
Cells in series for a module	10
Modules in series per string	20
Strings of modules in parallel	2

Figure 2-26 and Figure 2-27 show the experimental discharging and charging curves of Power Rack 320 for a single unit. The discharge and charge rates are 100 kW at 30⁰ C temperature. The charging and discharging curves are the same for the Li-ion battery system.

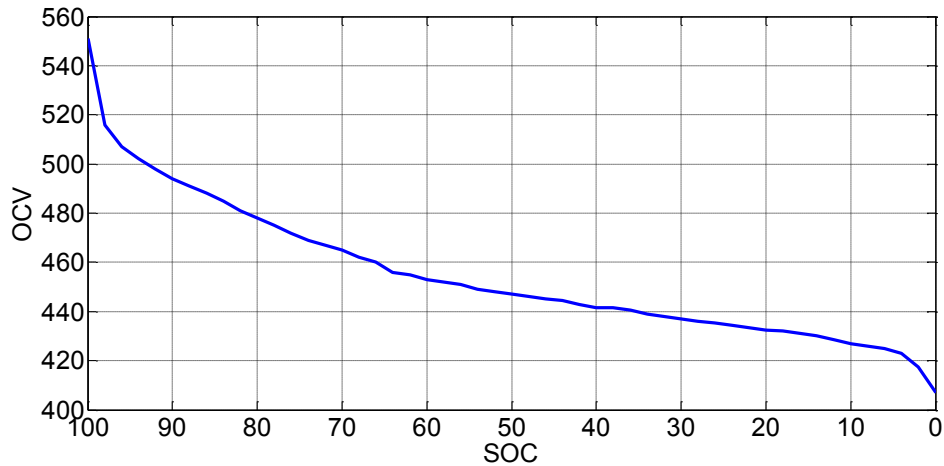


Figure 2-26. Discharging curve of one PowerRack 320.

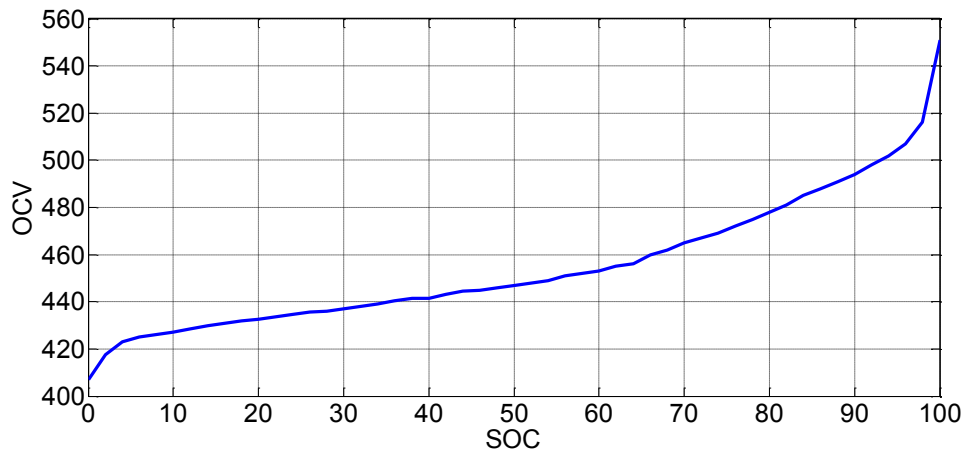


Figure 2-27. Charging curve of one PowerRack 320.

From the experimental charging and discharging curves a look-up is derived for the model and is used to derive the battery OCV. To verify the simulation model, the simulation model has been run for 3600 second (i.e. 1 hour). The initial SOC of the battery is considered to be 100. The battery is continuously discharged by 60 A. Since the battery capacity is 60 Ah, battery must be completely discharged in 1 hours. Figure 2-28 and Figure 2-29 show the simulation results while discharging the Li-ion battery by 60 A for 1 hour.

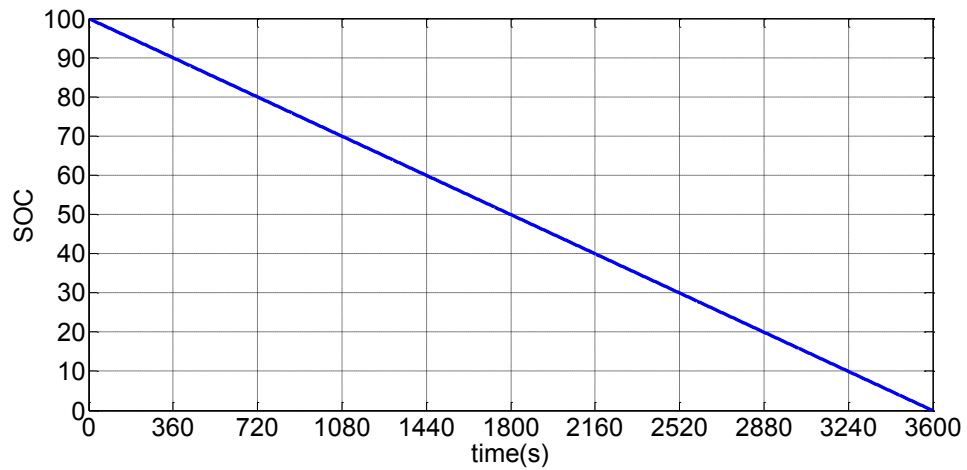


Figure 2-28. SOC of 60 Ah Li-ion battery system simulation model while discharging by 60 A for 1 hour.

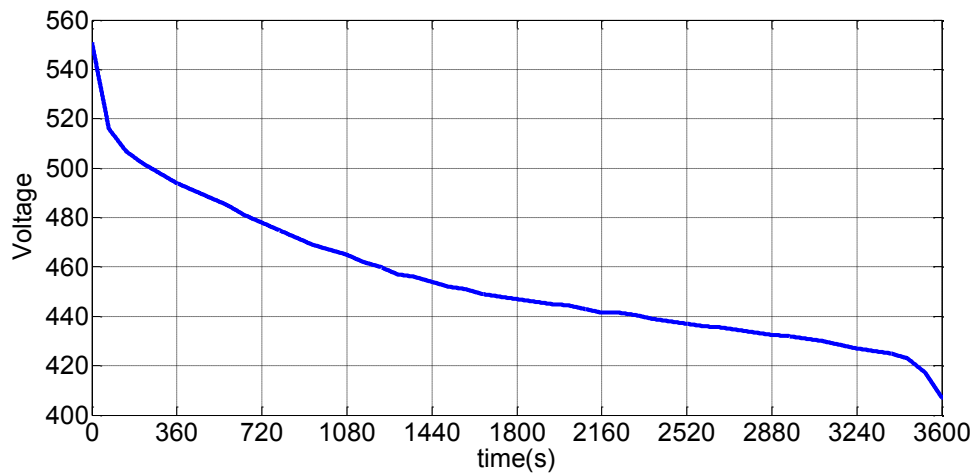


Figure 2-29. Battery voltage of 60 Ah Li-ion battery system simulation model while discharging by 60 A for 1 hour.

Similarly, for a charging test, the battery is considered to be fully discharged and is charged by 60 A for 1 hour. Figure 2-30 and Figure 2-31 show the simulation results while discharging the Li-ion battery by 60 A for 1 hour.

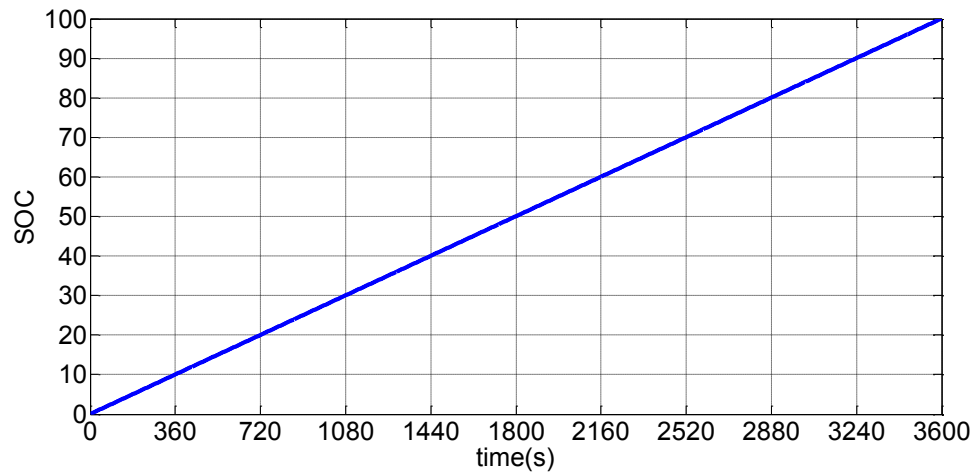


Figure 2-30. SOC of a 60 Ah Li-ion battery system simulation model while charging by 60 A for 1 hour.

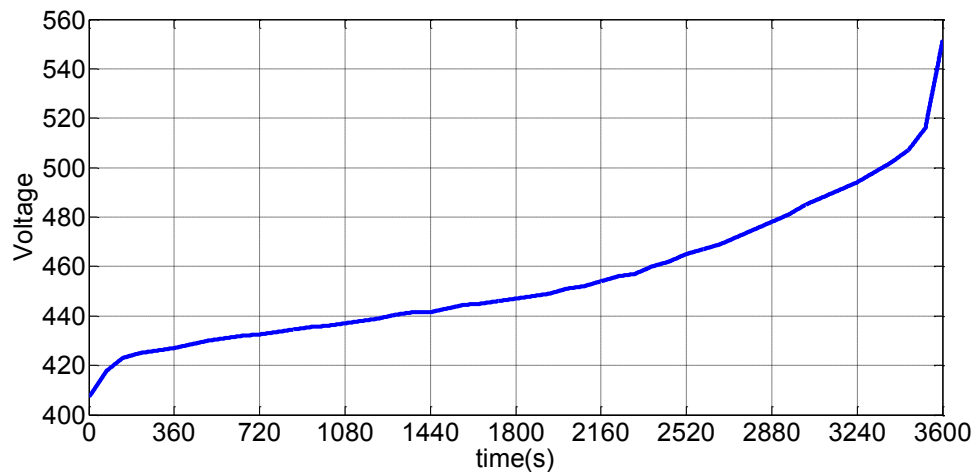


Figure 2-31. Battery voltage of 60 Ah Li-ion battery system simulation model, while charging by 60 A for 1 hour.

2.4.2 Zinc Bromide Energy storage system

A zinc bromide energy storage system has high energy and power density, high efficiency and long life. A 250 kW, 500 kWh ZBB energy storage has been modelled. The energy storage can be discharged 250 KW continuously and 500 KW for 3 minutes.

ZBB energy storage is modeled using actual system performance. A 25 kW, 50 kWh zinc bromide energy storage system manufactured by the “ZBB Energy Corporation” has undergone a series of charging and discharging tests in order to find the SOC versus OCV curves [94, 96]. 10 modules of 50 kWh are used for a 500 kWh

energy storage system. Two parallel strings of five 50 kWh modules are connected in series. Hence, from the testing data of a 50 kWh module, the charging and discharging curves for a 250 kW, 500 kWh energy storage system are derived, these are shown in Figure 2-32 and Figure 2-33.

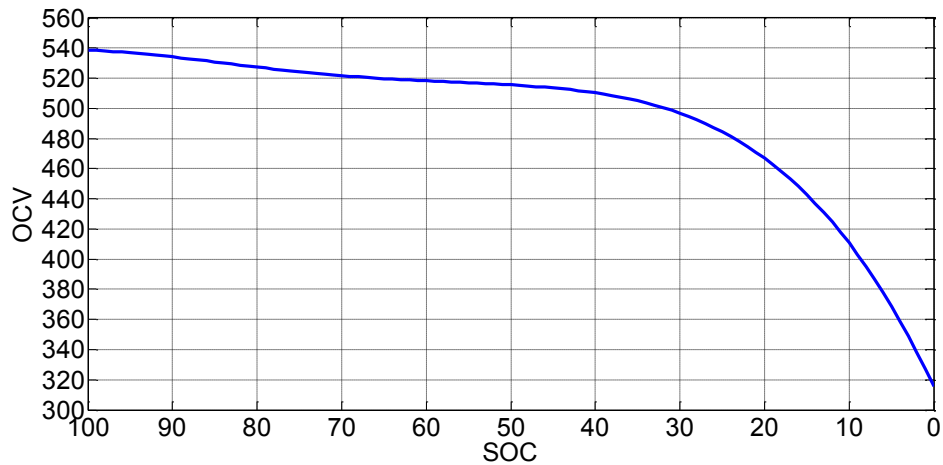


Figure 2-32. Discharging curve of 500 kWhr ZBB energy storage system

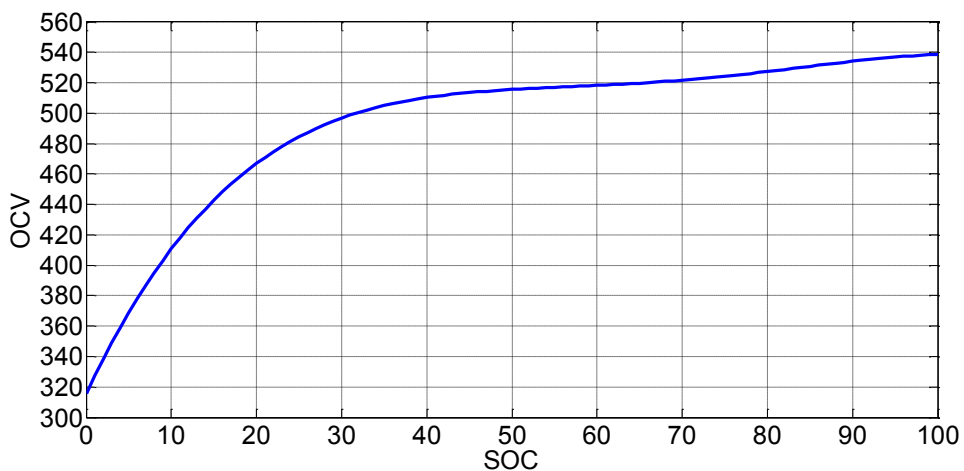


Figure 2-33. Charging curve of 500 kWhr ZBB energy storage system

The current capacity of a ZBB energy storage system is 925 Ah and it can be discharged by 250 kW, which is approximately 462.5 A at nominal voltage. To verify the simulation model, the simulation model has been run for 7200 second (2 hours). The initial SOC of the battery is considered to be 100. The battery is continuously

discharged by 462.5 A. Since the battery capacity is 925 Ah, the battery must be completely discharged in 2 hours.

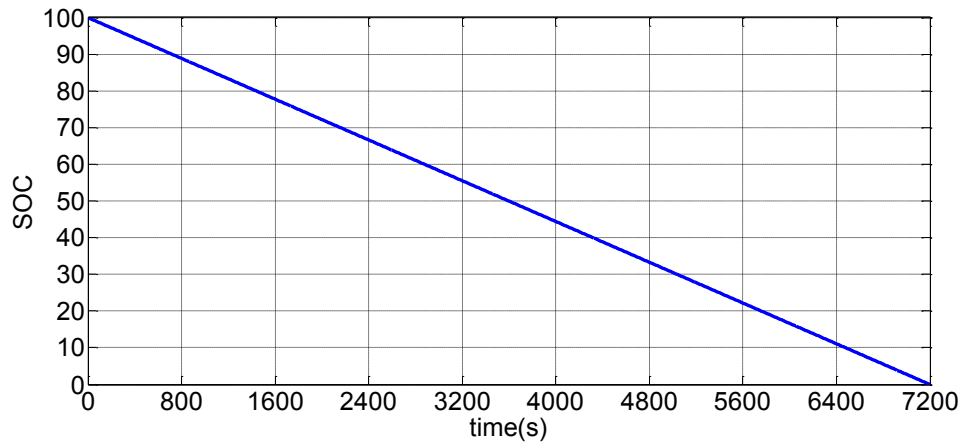


Figure 2-34. SOC of a ZBB battery system simulation model while discharging by 462.5 A for 2 hours.

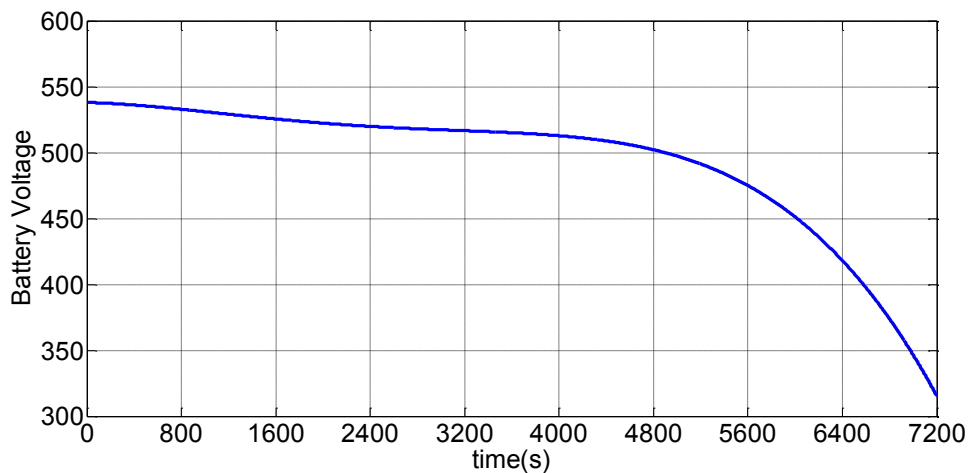


Figure 2-35. Battery voltage of a ZBB battery system simulation model while discharging by 60 A for 2 hours.

Figure 2-34 and Figure 2-35 shows the simulation results while discharging the ZBB battery by 462.5 A for 2 hours. Similarly, for a charging test, the battery is considered to be fully discharged and is charged by 462.5 A for 2 hours. Figure 2-36 and Figure 2-37 show the simulation results while discharging the ZBB battery by 462.5 A for 2 hours.

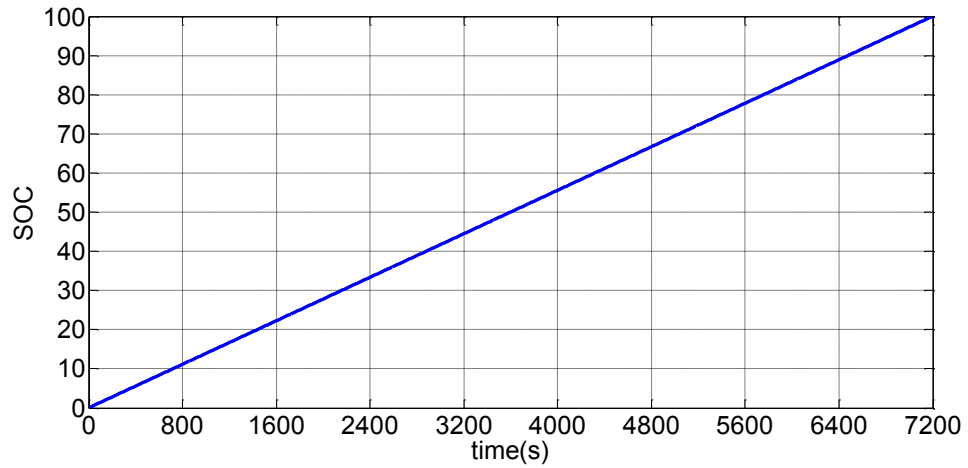


Figure 2-36. SOC of a ZBB battery system simulation model while charging by 462.5 A for 2 hours.

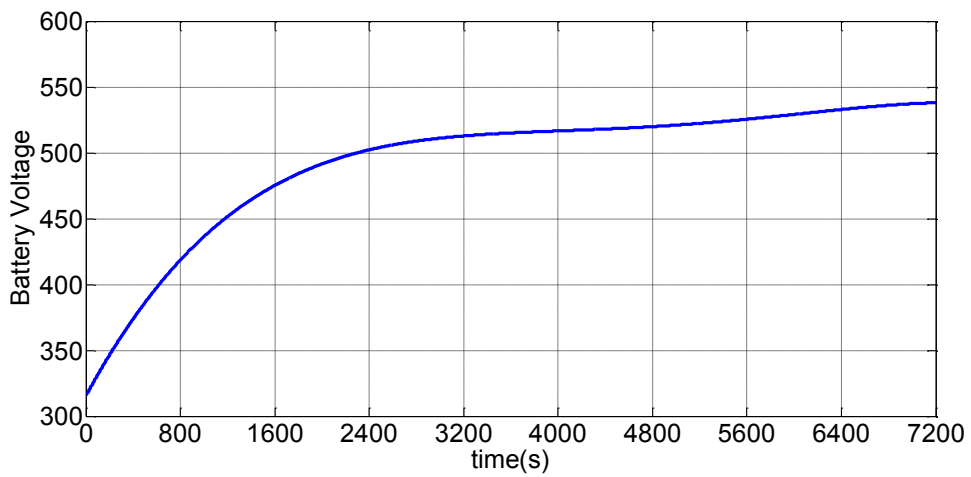


Figure 2-37. Battery voltage of a ZBB battery system simulation model while charging by 462.5 A for 2 hours.

2.5 Wind Turbine Generator

The wind energy system with full conversion configuration is modeled in PSCAD [97, 98]. The topology of the turbine is shown in Figure 2-38.

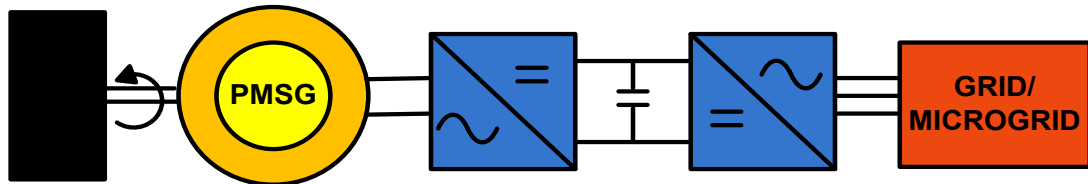


Figure 2-38. Wind turbine with full scale converter connected to the grid/microgrid.

The converter is operated in current mode and is configured to provide flexible active and reactive power [99, 100]. A wind turbine extracts kinetic energy from the swept area of the blades. The power in the wind can be described as follows:

$$P_w = \frac{1}{2}(\rho Av)v^2 = \frac{1}{2}\rho Av^3 \quad (2-12)$$

Where,

P_w (Watts): Power in the wind

ρ (kg/m³): Air density (1.225kg/m³ at 15°C and 1 atm.)

A (m²): The swept area of the turbine blades

v (m/s): Wind speed normal to A

Although equation (2-12) provides the available power in the wind, the power captured by the wind turbine is less due to a power coefficient of C_p [101-103]. Power extracted by the blades is given by the equation (2-13) and the power coefficient of C_p is provided by equation (2-14).

$$P_b = \frac{1}{2}\rho Av^3.C_p \quad (2-13)$$

$$C_p = 1/2(1 + \lambda)(1 - \lambda^2) \quad (2-14)$$

Where, λ is the ratio of down wind speed over upwind and is given by $\lambda = v_d / v$.

The above equations have been implemented in PSCAD software to model a wind turbine. Measured wind speed data near city of Milwaukee has been used to calculate the wind power [104]. A Maximum Power Point Tracking (MPPT) algorithm has been implemented. The sample wind speed and wind turbine power for a period of 24 hours for a 2.5 kW wind turbine generator are shown in Figure 2-39.

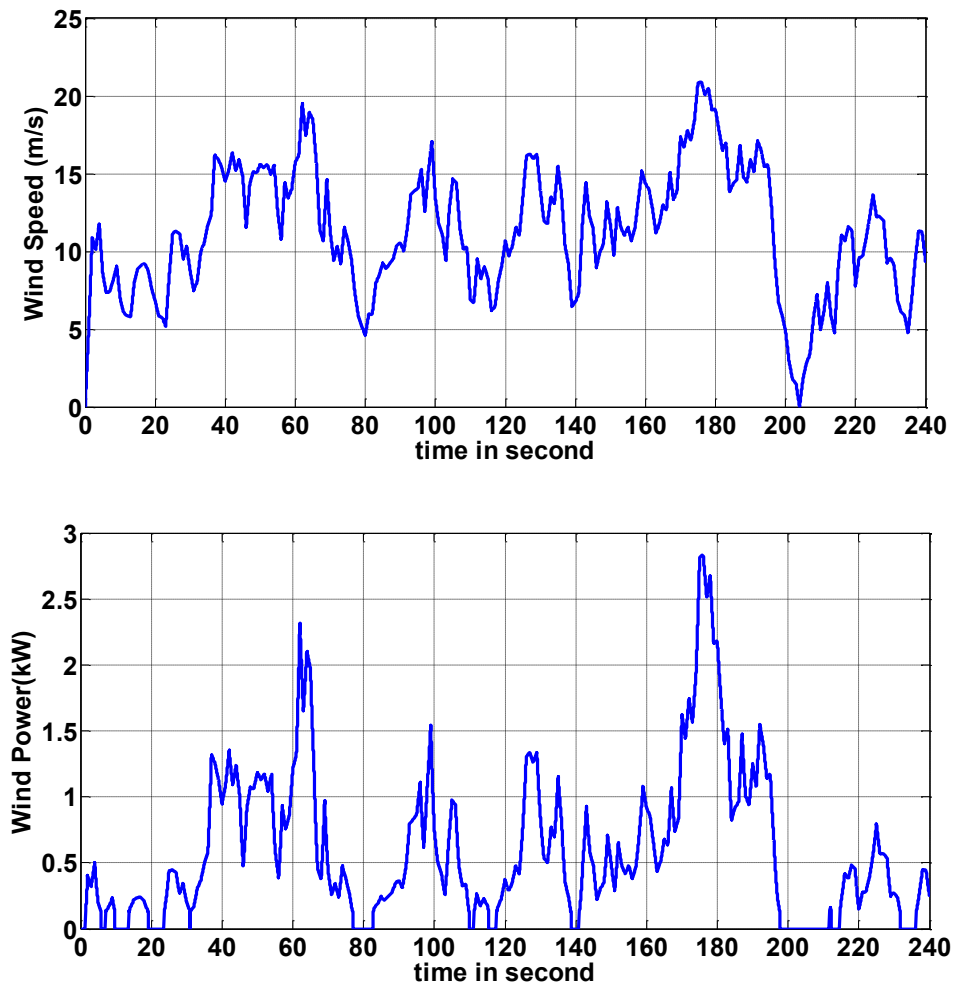


Figure 2-39. Sample wind speed (above) and wind power profile (below).

2.6 Solar PV Generator

Solar PV distributed generation systems are one of the fastest growing types of renewable energy sources being integrated worldwide. To integrate such solar farms with the grid/microgrid, a thorough technical study is required in terms of their effects on system voltage, power quality, response to faults and short circuit contributions. Hence, solar PV must be modelled with sufficient details [105].

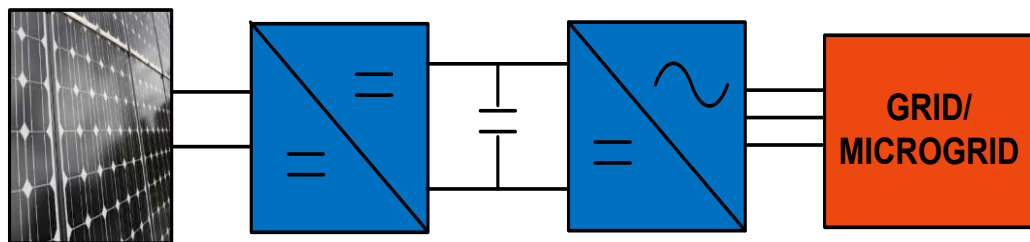


Figure 2-40. Solar PV system with inverter connected to the grid/microgrid

Figure 2-40 shows the schematic diagram of a solar PV generator. The inverter is modeled as a current source connected to the microgrid/grid. Maximum Power Point Tracking (MPPT) for the panels was developed and simulated [106, 107]. The solar PV array is modelled using an electrical equivalent circuit as shown in Figure 2-41.

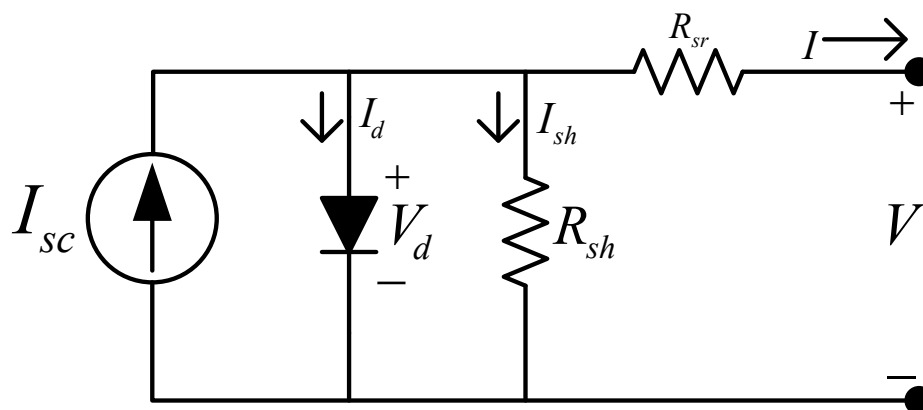


Figure 2-41. PV cell equivalent circuit

An electrical equivalent circuit contains a current source anti-parallel with a diode, a shunt resistance and a series resistance [108]. The DC current I , generated when the cell is exposed to light, varies linearly with solar irradiance. The current I_d through the

anti-parallel diode is responsible for nonlinear I-V characteristics of the PV cell which is shown in Figure 2-42.

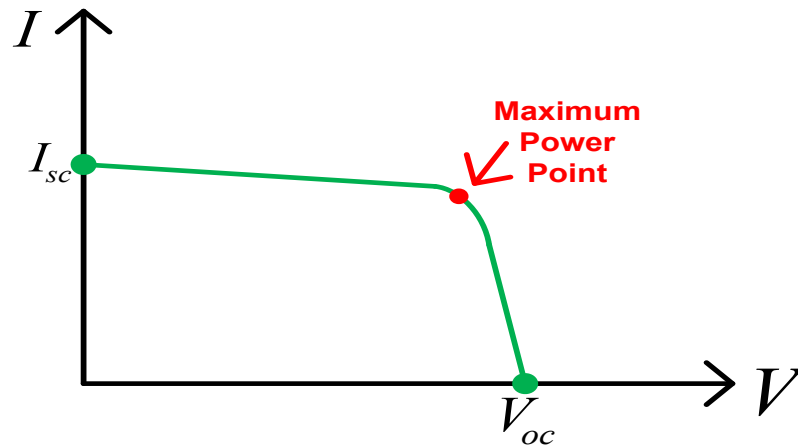


Figure 2-42. PV cell typical I-V characteristic

The basic equation that characterizes the solar cell I-V relationship can be derived from the equivalent circuit shown in Figure 2-41. Kirchhoff's current equation for a PV cell equivalent circuit is given by the following equation (2-15).

$$I = I_{sc} - I_d - I_{sh} \quad (2-15)$$

After substituting relevant expressions for the diode current I_d and the shunt resistance current I_{sh} into equation (2-15), DC current I is represented by following equation.

$$I = I_{sc} - I_0 \left[\exp \left(\frac{V + IR_{sr}}{\eta k T_c / q} \right) - 1 \right] - \left(\frac{V + IR_{sr}}{R_{sh}} \right) \quad (2-16)$$

Where,

η = diode ideality factor

k = Boltzmann constant

q = electron charge

I_{sc} is the photo current and it is a function of solar radiation on the plan of the solar cell G and the cell temperature T_c , which is given by the following equation (2-17).

$$I_{sc} = I_{scR} \frac{G}{G_R} [1 + \alpha_T (T_c - T_{cR})] \quad (2-17)$$

In equation (2-17), I_{scR} is the short circuit current at the reference solar radiation G_R and the reference cell temperature T_{cR} . In equation (2-16), the current I_0 is called the dark current and is a function of cell temperature and given by the following equation (2-18).

$$I_0 = I_{0R} \left(\frac{T_c^3}{T_{cR}^3} \right) \exp \left[\left(\frac{1}{T_{cR}} - \frac{1}{T_c} \right) \frac{q e_g}{nk} \right] \quad (2-18)$$

Where,

e_g = band gap energy of the solar cell material

I_{0R} = dark current at the reference temperature

All of the constants can be determined from the manufacture's specifications of the PV modules and from the I-V curves. A PV array is composed of series and parallel connected modules and the single cell circuit can be scaled up to represent any series/parallel combination. Based on the above equations, PV cell model has been implemented [104]. Figure 2-43 shows 90 kW solar PV power profile for a bright day, cloudy day and the worst power fluctuation during a one-month period.

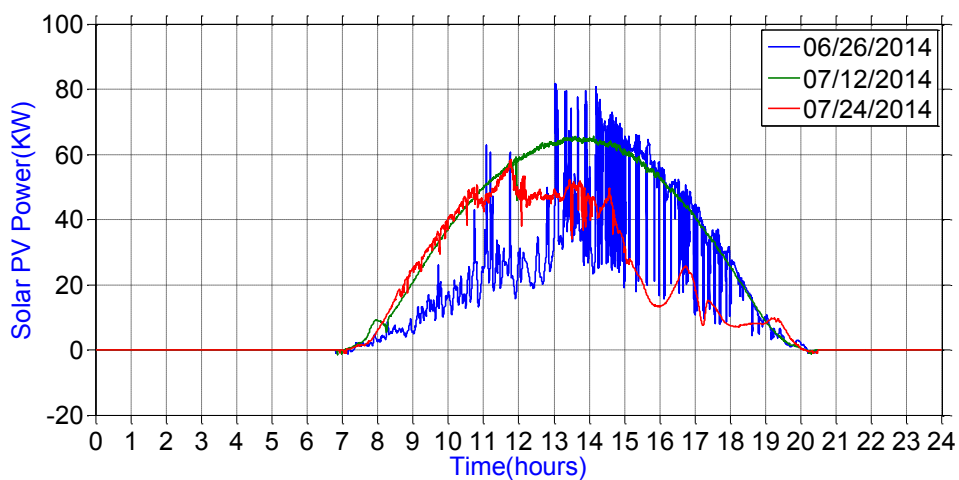


Figure 2-43. 90 kW solar PV power day profile for a bright day, cloudy day, and the worst power fluctuation during a one-month period.

Chapter 3 Virtual Droop Control Framework

3.1 Introduction

Natural droop control method has been proposed in many literatures to regulate the voltage and frequency in a microgrid in an island mode of operation. The voltage and frequency are drooped naturally to contribute active and reactive power to the load. A new framework for microgrid control and power management is proposed. In the proposed VDC framework, the power sharing is performed between various sources while the system frequency and voltage remain constant. By tightly regulating voltage and frequency, the reconnection mechanism to grid, from an island mode, becomes easier and faster. The proposed framework offers improved efficiency, better utilization of renewable energy and minimization of natural gas generator use by unit commitment method. The proposed control will provide the capability to operate a microgrid in case of lost communication or any sabotage on communication network.

During island mode of operation, in a virtual droop control, the energy storage inverter is operated in a voltage mode and the natural gas generators are operated in active/reactive power control mode. However, wind and PV inverters are operated in a current mode. This means that energy storage inverter provides a voltage with a magnitude of 1 p.u. and frequency of 60Hz. Other sources, including natural gas generators and renewables must synchronize with this voltage to deliver power. All the sources in a microgrid communicate with each other using TCP/IP Modbus secure communication protocol.

3.2 Unit Commitment Algorithm

A unit commitment strategy is applied for the natural gas generators to increase the efficiency, reduce the carbon dioxide emission and reduce the fuel consumption. For various levels of loads and the SOC of the energy storage, none, one, or both of the generators are synchronized to supply power.

In the developed unit commitment algorithm, there are two levels of priority. The primary level of priority is SOC of energy storage and the secondary level of priority is microgrid load. The primary decision is made based on the SOC of the energy storage. If the SOC of the energy storage is in the defined range then the secondary decision is made based on the microgrid load to improve overall efficiency.

There are total three modes of operation in unit commitment algorithm as shown below.

Mode 1: Only energy storage provides power to the system.

Mode 2: Energy storage and natural gas generator 1 provide power to the system.

Mode 3: Energy storage and both natural gas generators provide power to the system.

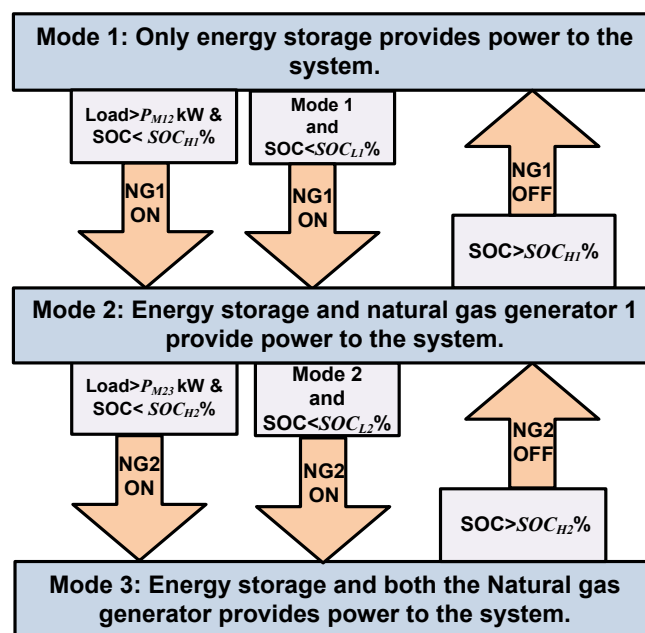


Figure 3-1. Unit commitment algorithm as part of virtual droop control to increase efficiency.

Details of the unit commitment procedure are shown in Figure 3-1. As mentioned earlier, all the sources in a microgrid communicate with each other using TCP/IP Modbus secure communication protocol. The active and reactive power output of all the source are measured and are broadcasted over TCP/IP Modbus. The energy storage inverter is received all the measured active and reactive power. Energy storage inverter also receives the SOC measurement from the energy storage. From all measured powers, the system active load has been calculated based on the following equation.

$$P_{load} = P_{NG1} + P_{NG2} + P_{ES} \quad (3-1)$$

If the system load is less than P_{M12} kW and the SOC of energy storage is greater than SOC_{H1} %, then the energy storage supplies the total microgrid load and natural gas generators are off to improve efficiency and reduce the chances to overcharge the energy storage. In this mode, if the system load exceeds P_{M12} kW and if the SOC of energy storage is less than SOC_{H1} %, natural gas generator 1 is turned on to provide power. However, if the system load is less than P_{M12} kW but the SOC of energy storage is less than SOC_{L1} %, then in order to charge the energy storage, the natural gas generator 1 is connected, and the system moves to mode 2. Once the system is in mode 2, it can move to mode 1 only if the SOC is increased to above SOC_{H1} %.

While in mode 2, if the system load is increased to above P_{M23} kW and SOC of the energy storage is less than SOC_{H2} %, then generator 2 will turn on and moves the system to mode 3. In addition, when the total load is less than P_{M23} kW but the SOC is less than SOC_{L2} %, then the system still moves from mode 2 to 3. Once the system is in mode 3, it can move to mode 2 only if the SOC is increased to above SOC_{H2} %.

The parameters of the unit commitment algorithms are selected based on the past load profiles, weather forecasting and size and type of energy storage used in a microgrid. To increase the life of energy storage it is necessary to operate it into linear

operating region of OCV-SOC curve of energy storage. It is also required to consider the generator starting and synchronization time and miss sync while selecting the unit commitment parameters.

Based on all these criteria, the parameters selected for unit commitment algorithm for the Fort Sill microgrid system is given in Table 3-1.

Table 3-1. Unit commitment algorithm parameters for the Fort Sill microgrid

P_{M12}	80 kW
SOC_{L1}	50%
SOC_{H1}	90%
P_{M23}	270 kW
SOC_{L2}	40%
SOC_{H2}	80%

3.3 Virtual Droop Control

To regulate the active and reactive power output of the sources, a virtual frequency and voltage are created. The active power load of the microgrid determines the virtual frequency from virtual droop curve. The droop curve is defined between microgrid active power load and virtual frequency. The virtual frequency will determine the active power commands for natural gas generators from a droop relationship, defined between the virtual frequency and active power command of each source. The same concept applies to system voltage. A virtual voltage is determined according to reactive power load. The virtual voltage will determine the reactive power command for natural gas generators from a droop relationship, defined between the virtual voltage of the system and reactive power command of each source.

It should be noted that since energy storage inverter is placed in a voltage mode, it supplies the difference between load active and reactive power and other sources in the microgrid. It behaves as a slack bus in a power system concept. Power commands of natural gas generators are updated only when load variation is greater than defined value. Load variation less than defined value is taken care of by the energy storage inverter.

Virtual frequency and voltage slopes can be define for different modes by user for different microgrid architecture. Figure 3-2 and Figure 3-3 shows the slope curve for mode n and m generator. P_{Lmax} and Q_{Lmax} are the total active power load and reactive power load of a microgrid. For mode n and generator m, the parameters $P1$ to $P4$ and $Q1$ to $Q4$ are defined by the user.

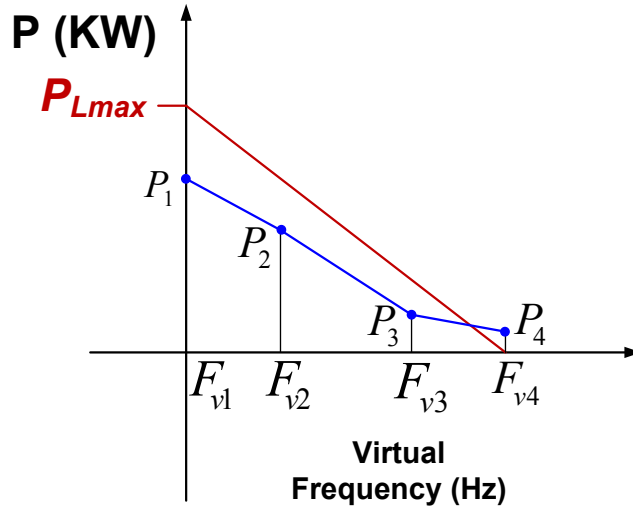


Figure 3-2. Generalized droop curve between active power load and virtual frequency.

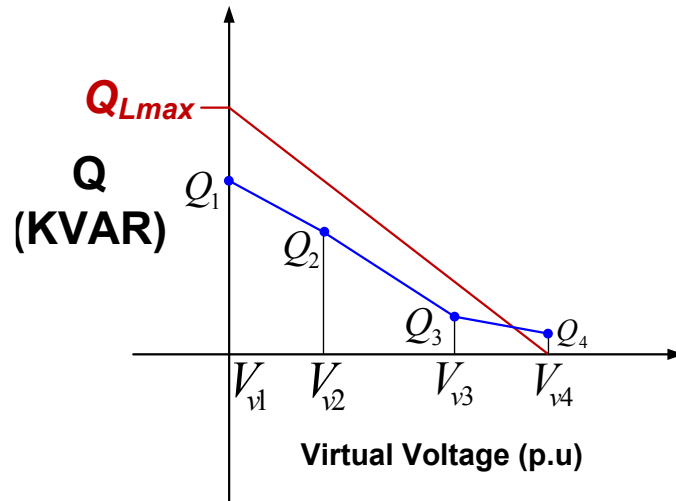


Figure 3-3. Generalized droop curve between reactive power load and virtual voltage.

The virtual frequency and virtual voltage has been calculated based on microgrid load at any instance during microgrid operation, which are shown in equation (3-2) and (3-3).

$$F_{virtual} = (F_{v1} - F_{v4}) * \left(\frac{P_{L_measured}}{P_{Lmax}} \right) + F_{v4} \quad (3-2)$$

$$V_{virtual} = (V_{v1} - V_{v4}) * \left(\frac{Q_{L_measured}}{Q_{Lmax}} \right) + V_{v4} \quad (3-3)$$

The slope between virtual frequency versus generator active power command and virtual voltage versus generator reactive power command are predefined by the user and generalized slopes are shown in Figure 3-2 and Figure 3-3. From virtual frequency and voltage, the power command for generator m in mode n are calculated as shown in equation (3-4) and (3-5).

$$\begin{aligned} & \text{For } F_{v1} < F_{virtual} < F_{v2} \\ & P_{NG_CMD} = \left(\frac{P_2 - P_1}{F_{v1} - F_{v2}} \right) (F_{virtual} - F_{v2}) + P_1 \\ & \text{For } F_{v2} < F_{virtual} < F_{v3} \end{aligned} \quad (3-4)$$

$$P_{NG_CMD} = \left(\frac{P_3 - P_2}{F_{v2} - F_{v3}} \right) (F_{virtual} - F_{v3}) + P_2$$

$$\begin{aligned} & \text{For } F_{v3} < F_{virtual} < F_{v4} \\ & P_{NG_CMD} = \left(\frac{P_4 - P_3}{F_{v3} - F_{v4}} \right) (F_{virtual} - F_{v4}) + P_3 \end{aligned}$$

$$\begin{aligned} & \text{For } V_{v1} < V_{virtual} < V_{v2} \\ & Q_{NG_CMD} = \left(\frac{Q_2 - Q_1}{V_{v1} - V_{v2}} \right) (V_{virtual} - V_{v2}) + Q_1 \end{aligned}$$

$$\begin{aligned} & \text{For } V_{v2} < V_{virtual} < V_{v3} \end{aligned} \quad (3-5)$$

$$Q_{NG_CMD} = \left(\frac{Q_3 - Q_2}{V_{v2} - V_{v3}} \right) (V_{virtual} - V_{v3}) + Q_2$$

$$\begin{aligned} & \text{For } V_{v3} < V_{virtual} < V_{v4} \\ & Q_{NG_CMD} = \left(\frac{Q_4 - Q_3}{V_{v3} - V_{v4}} \right) (V_{virtual} - V_{v4}) + Q_3 \end{aligned}$$

Figure 3-4 shows the control flow diagram of microgrid controller during island mode and when communication presents.

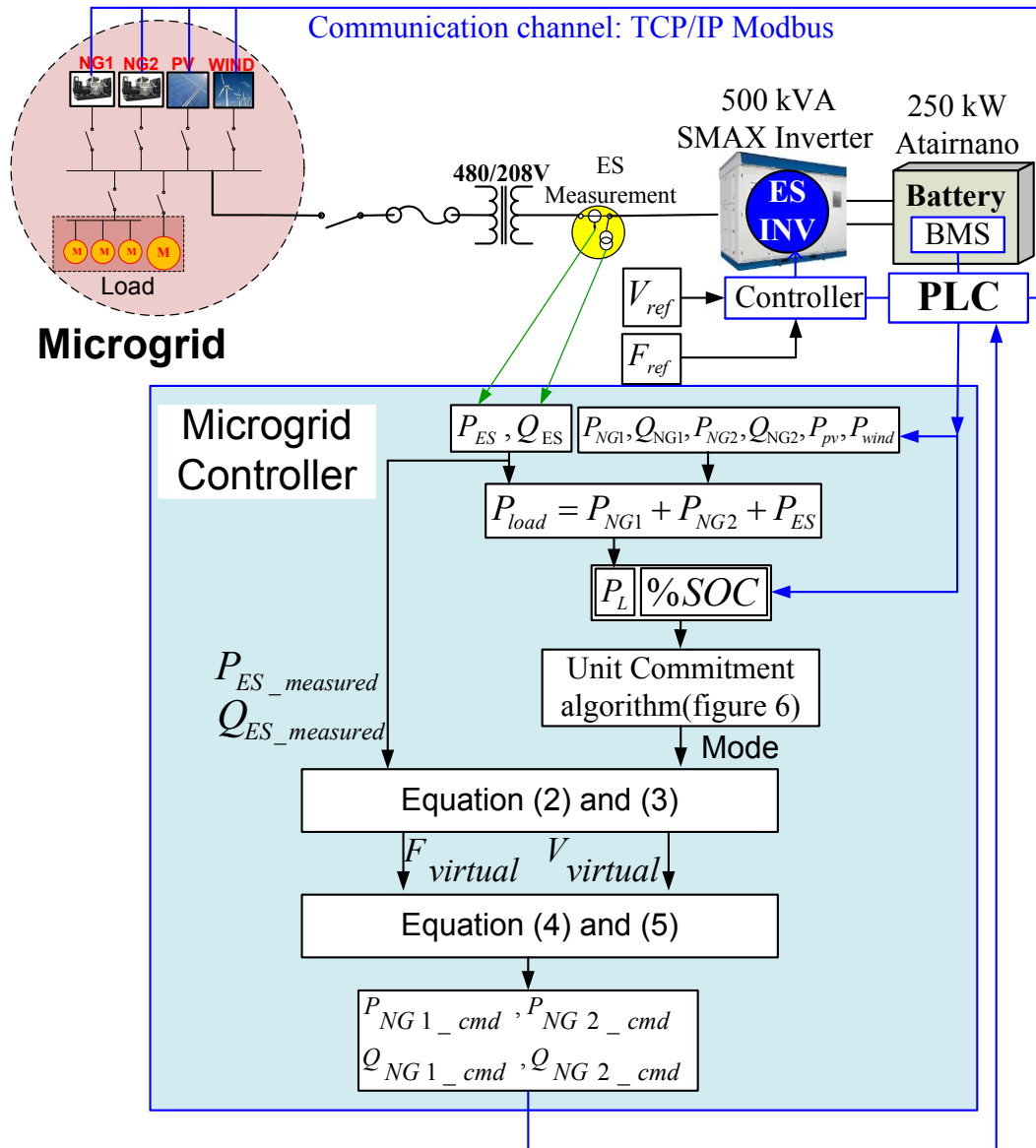


Figure 3-4. Control flow diagram of microgrid controller in island mode

Since there are two natural gas generators in the Fort Sill microgrid configuration, the total unit commitment mode of operations are three. In mode 1, both generators are off, so the power command for both generators are zero. In virtual frequency and voltage droop curves (Figure 3-2 and Figure 3-3), for mode 2 and 3, P_1 to P_4 , Q_1 to Q_4 , F_{v1} to F_{v2} and V_{v1} to V_{v4} are required to define based on the generator and energy storage system ratings. Figure 3-5, Figure 3-6 and Figure 3-7 shows the voltage and frequency curves for mode 1, 2 and 3 respectively for the fort sill microgrid. The selected virtual droop curve parameters are mentioned in the droop curves.

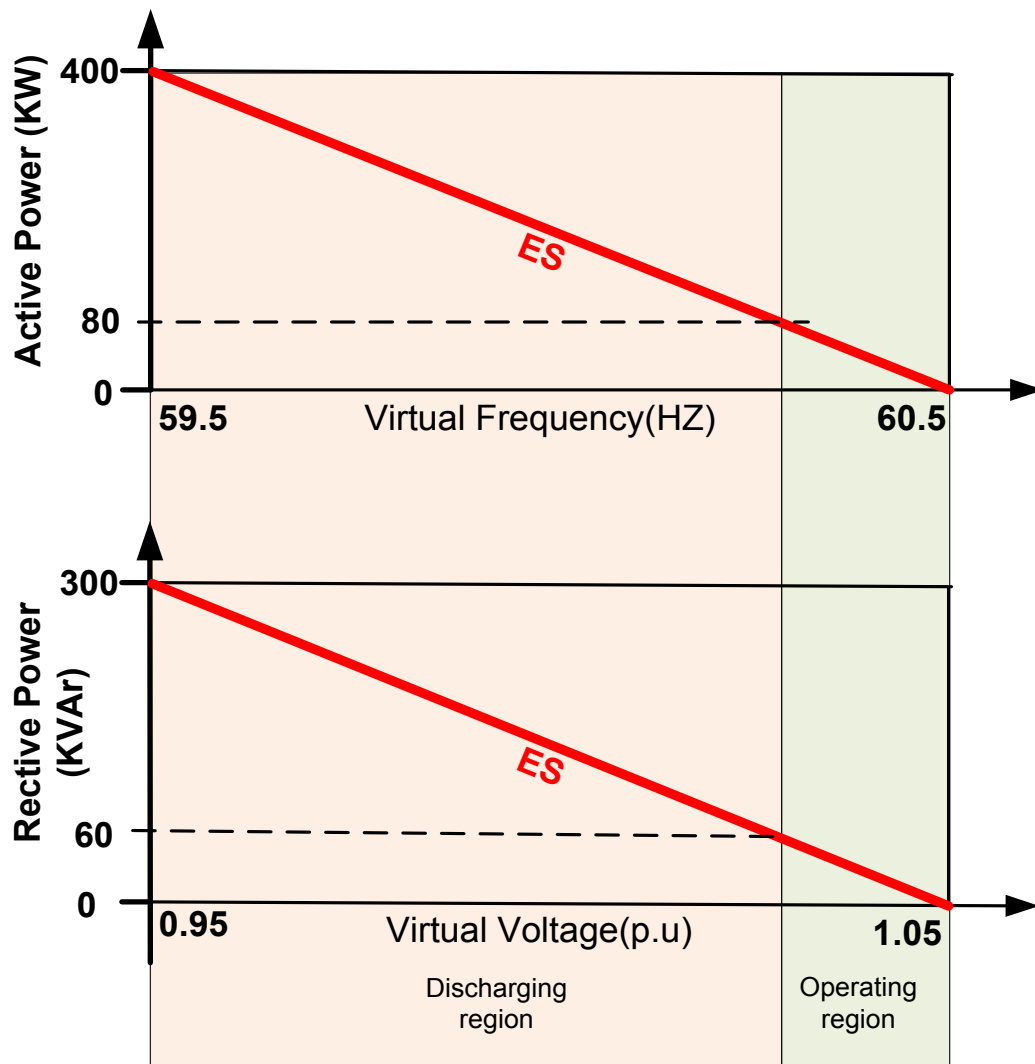


Figure 3-5. Virtual frequency and voltage droop curves for mode 1, when only energy storage provides power in island mode for the Fort Sill microgrid.

As shown in Figure 3-5, in mode 1 only energy storage provides power. According to the unit commitment algorithm, if the microgrid load is greater than 80 kW but the SOC of energy storage is also greater than 90% then the microgrid operates into discharging region of mode 1. However, if the SOC of energy storage is less than 90% but greater than 40% and the microgrid load is less than 80 kW then the microgrid operates in operating region of mode 1.

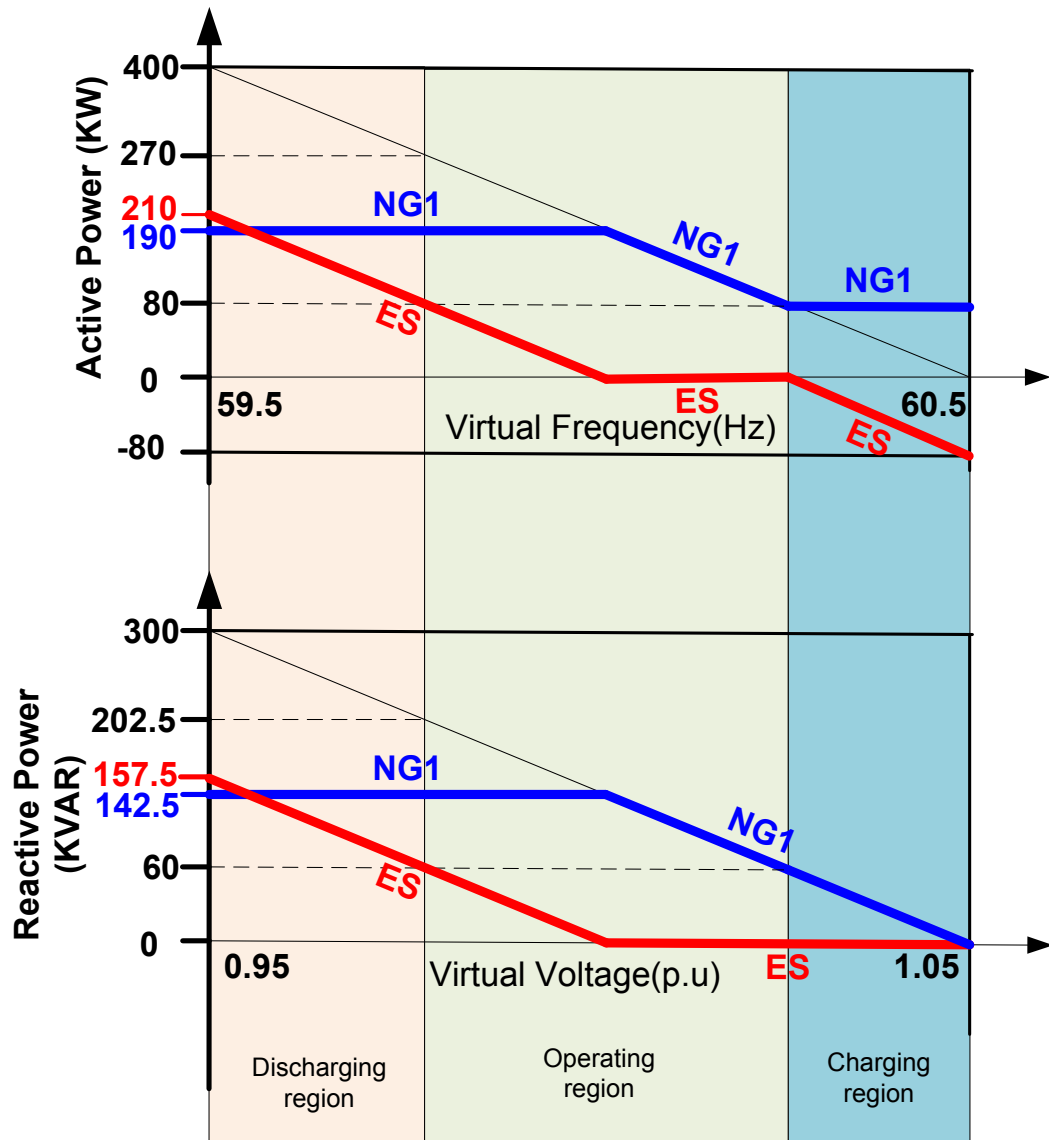


Figure 3-6. Virtual Frequency and voltage droop curves for mode 2, when energy storage and one generator provide power in island mode for the Fort Sill microgrid.

As shown in Figure 3-6, in mode 2, there are total three region: charging region, operating region and discharging region. If the microgrid load is above 80 kW and the SOC of the energy storage is between 40-90%, then microgrid operates into operating region of mode 2. If microgrid load becomes less than 80 kW but SOC is less than 90% then microgrid operates into charging region. The microgrid operates into discharging region of mode 2, if microgrid load is greater than 270 kW, but SOC of the energy storage greater than 80%.

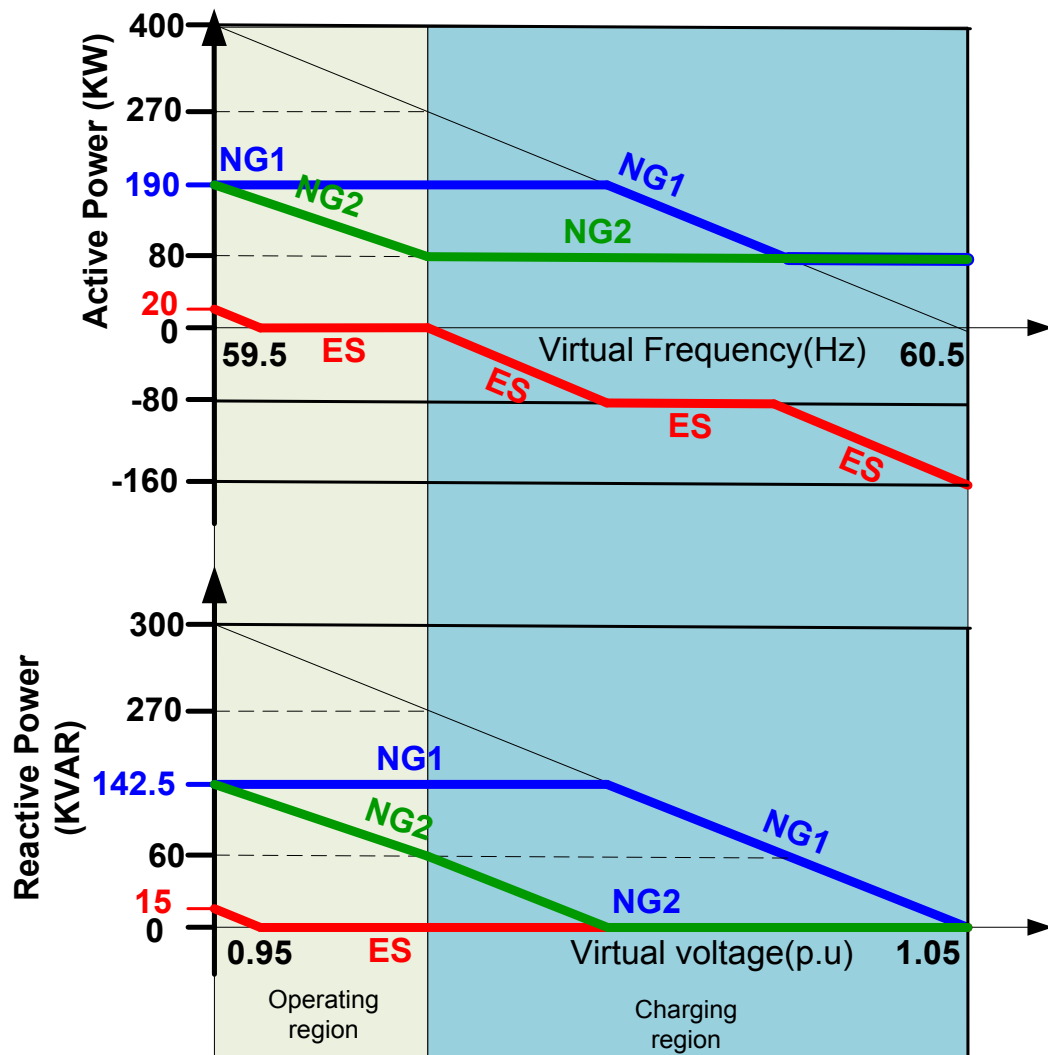


Figure 3-7. Virtual Frequency and voltage droop curves for mode 3, when energy storage and both generators provide power in island mode for the Fort Sill microgrid.

Figure 3-7 shows the virtual frequency and voltage droop curves for mode 3 of unit commitment. Mode 3 is divided into two region: operating region and charging region. The microgrid operated into operating region of mode 3 if SOC of energy storage in less than 80% and microgrid load is greater than 270 kW. Once the microgrid moves into case 3, it can transit to move 2 only if SOC of the energy storage becomes greater than 80%. If the load is less than 270 kW and SOC is less than 40% than microgrid operates into charging region of mode 3.

3.4 Comparisons between VDC and Natural Droop Control

Detailed comparison between proposed VDC and natural droop control for the Fort Sill microgrid system has been performed in this section. In the system modeling, 24 hours load profile, wind profile and solar PV radiation profile are scaled down to 2400 simulation second. Hence, each 100 simulation second represents 1 hour. Same profiles are used in simulation of VDC and natural droop control method. The active power outputs, the reactive power outputs and voltages of all the sources and frequency of microgrid are plotted for comparison. The energy output of both generators and energy storage are also plotted for efficiency comparison. In addition, the fuel usages of natural gas (cubic-feet) are also calculated for both methods.

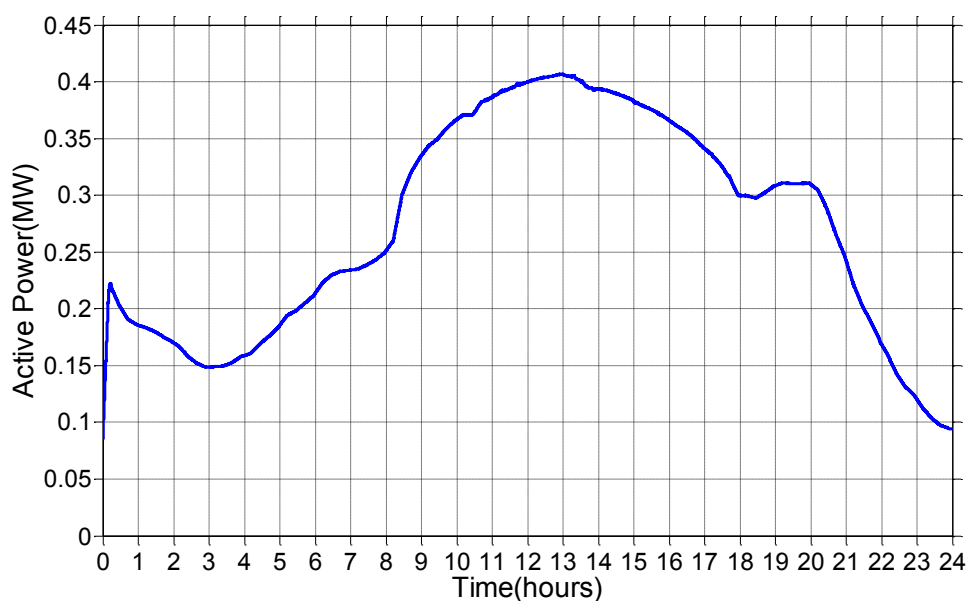


Figure 3-8. Active load profile for the microgrid.

Figure 3-8 shows the active load profile of the fort sill microgrid used for analysis. Fuel Consumption for engine G3406 is given in the data sheet for 100%, 75% and 50% load. The data is extrapolated and fuel consumption v/s load curve is derived to calculate the fuel consumption, which is shown in Figure 3-9.

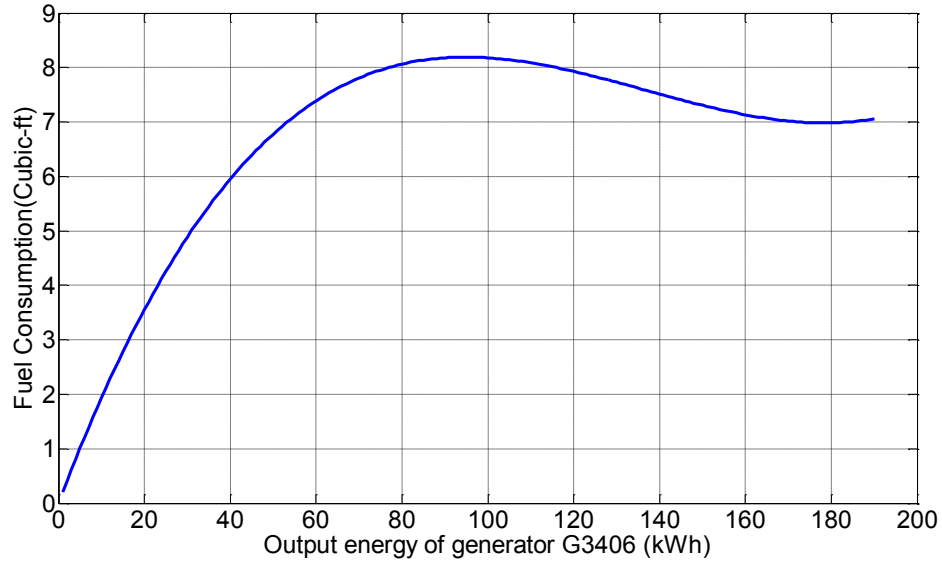


Figure 3-9. Extrapolated fuel consumption curve of 190 kW generator.

a. Natural droop control method

The droop curves for natural droop control method are provided in Figure 3-10. In natural droop control, the energy storage system's active and reactive power are adjusted based on the system voltage and frequency. However, generator's voltage and frequency are adjusted according to their active and reactive power.

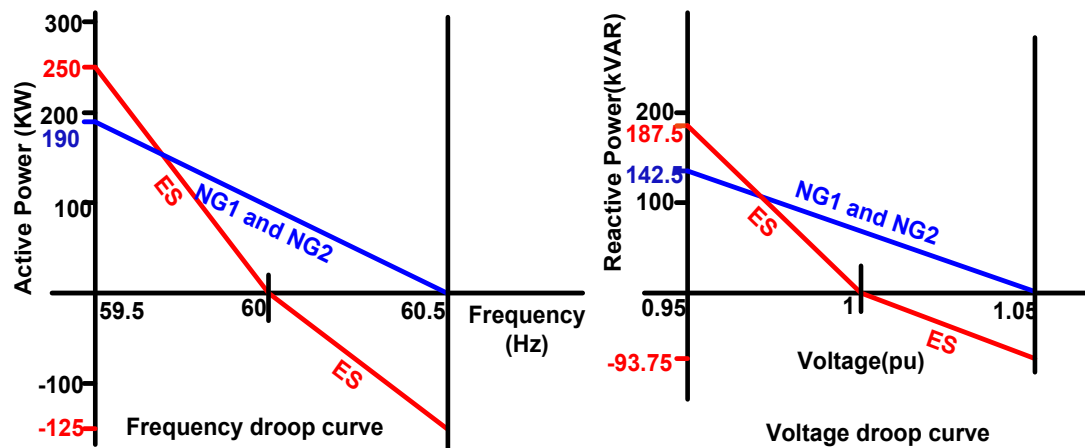


Figure 3-10. Frequency and voltage droop curves for natural droop method.

For 24 hours, the active power at energy storage, natural gas generators, solar PV and wind are shown in Figure 3-11. The reactive power at energy storage and natural gas generators are also shown in Figure 3-12.

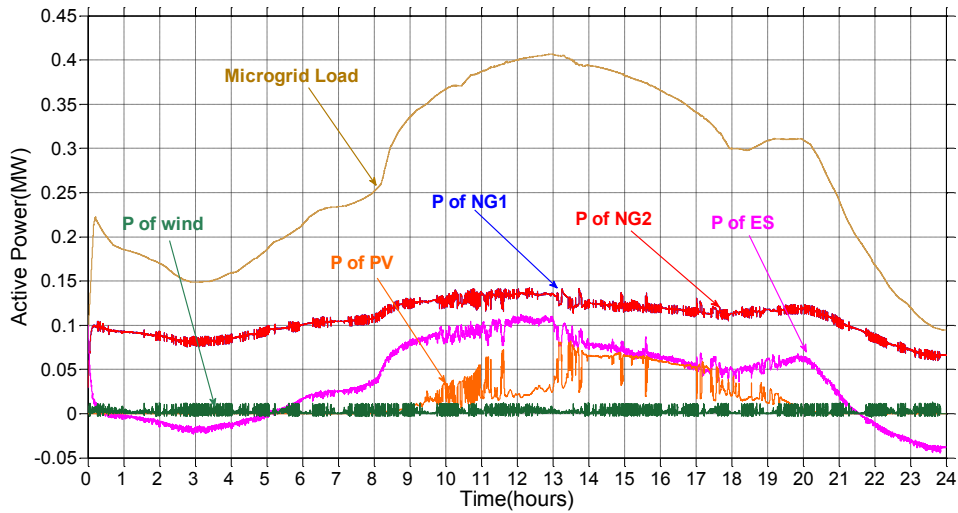


Figure 3-11. Active power at energy storage, natural gas generator 1 and 2, solar PV and wind; when natural droop control method is applied.

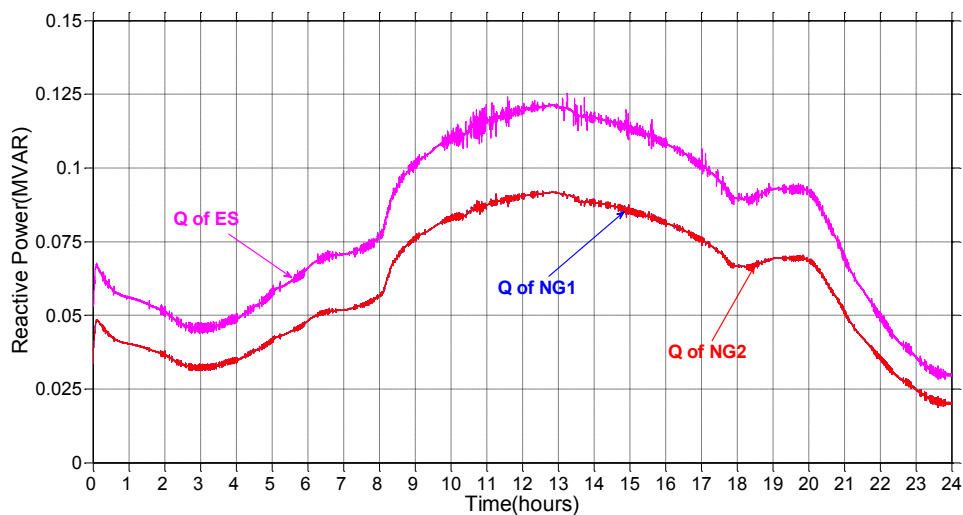


Figure 3-12. Reactive power at energy storage, natural gas generator 1 and 2; when natural droop control method is applied.

As shown in Figure 3-11 and Figure 3-12, after at 0 hour the islanding occurred and energy storage inverter picks up the system load. After few seconds, both generators are started and synchronized and droop control is active. Once the droop mode is activated, both the natural gas generators and energy storage inverter adjust the voltage and frequency based on their output power and predefined curves. Since the droop curves and rating of both generators are the same, they share equal amount of active and reactive power. The maximum active and reactive power output from both

generators are 136 kW and 92.00 kVAR respectively and the minimum active and reactive power output from both generators are 60 kW and 30 kVAR which is quite less than their power rating. Hence, they are operating at lower efficiency compared with their nominal efficiency.

As shown in Figure 3-13, the voltages vary between 0.95 p.u. to 1.05 p.u based on the system reactive load. In the afternoon, the solar PV power increases, which keeps the voltages little higher, otherwise it would have been lower than showed in graph.

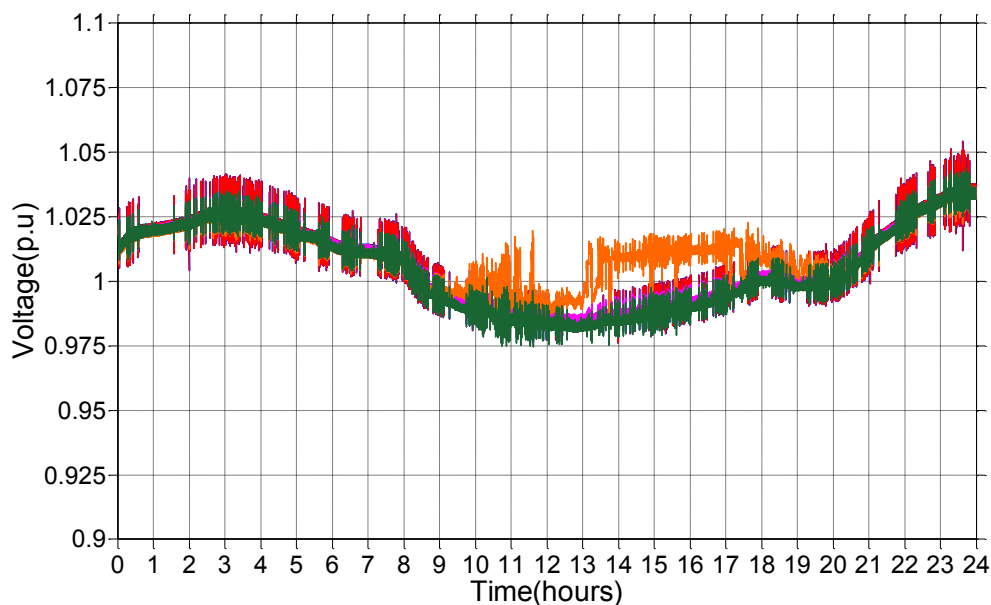


Figure 3-13. Voltage at energy storage device, natural gas generators, solar PV and wind; when natural droop control method is applied

Figure 3-14 shows that the frequency of the Fort Sill microgrid while operated in natural droop control in an island mode. Due to the large fluctuations in power output of renewables, the frequency cannot be in the specific range (59.5 to 60.5 Hz) defined by IEEE 1547. For the given solar PV, wind and load profiles, the frequency varies between 59 HZ to 60.5 HZ. The power sharing is based on the system frequency, so the power output of natural gas generators constantly changes.

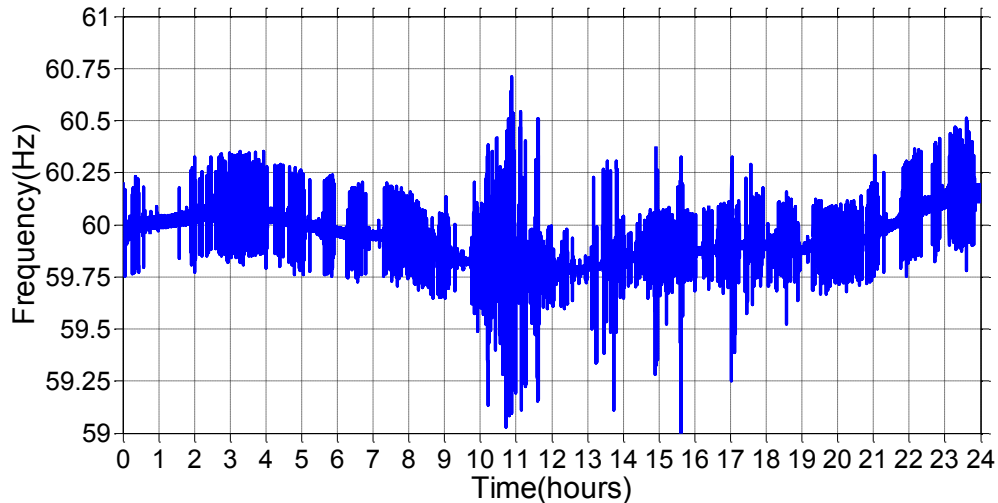


Figure 3-14. The Fort Sill microgrid frequency, when natural droop control method is applied.

The energy outputs of both generators are shown in Figure 3-15 and charging/discharging energy at energy storage is shown in Figure 3-16. It is observed that the discharging energy from the energy storage at one instance reaches to almost 1 MWh. It means the selected 56 kWh energy storage is too small for natural droop control method and the microgrid operation fails. For selected droop curve of energy storage, the required size of the energy storage is near 1 MWh, which is way higher than 56 kWh. In addition, the energy provided by each natural gas generator after 24 hours of microgrid operation in island mode is 2.6 MWh.

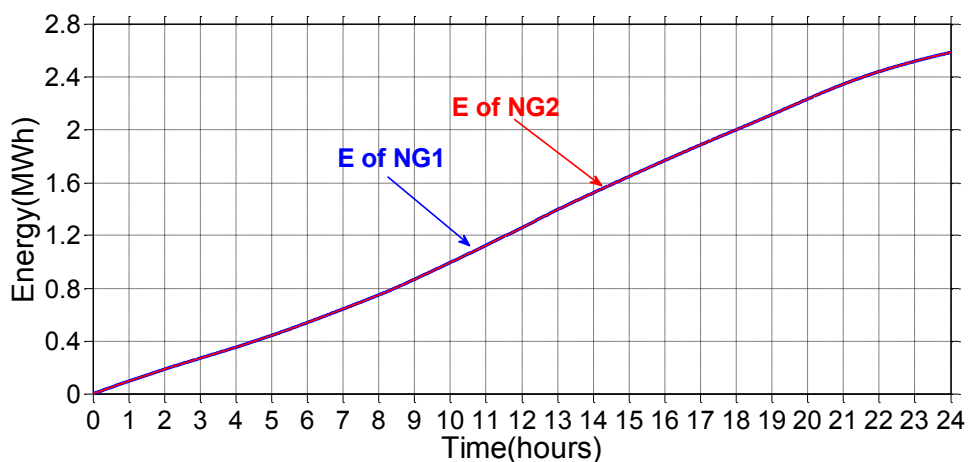


Figure 3-15. Energy output of natural gas generators; when natural droop control method is applied

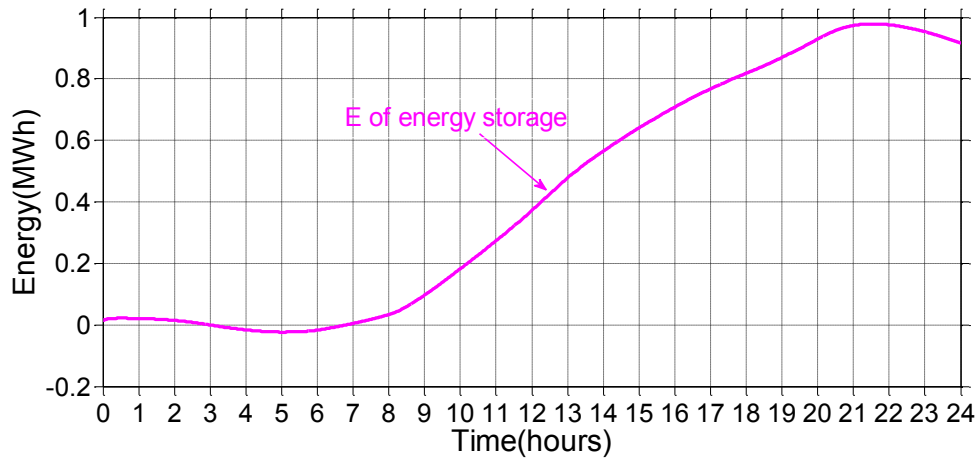


Figure 3-16. Charging/discharging energy of energy storage; when natural droop control method is applied.

The fuel consumption of both natural gas generators are shown in Figure 3-17. After 24 hours of operation in an island mode, while natural droop control method is applied, the natural gas consumption of each natural gas generator is 139.2 cubic-feet. Since both generators are of same rating and share equal power, the fuel consumptions are same. The total fuel consumption in 24 hours is 278.4 cubic-feet.

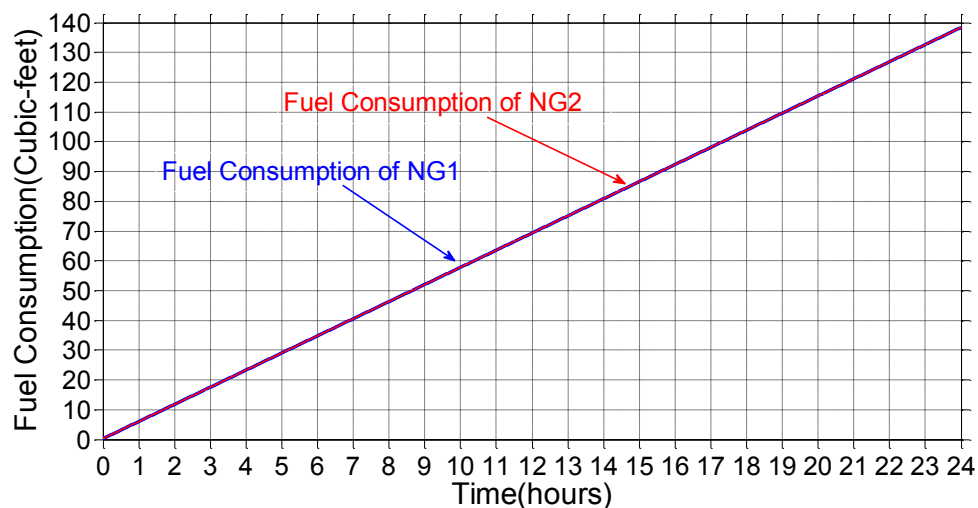


Figure 3-17. Fuel consumption of both natural gas generator; when natural droop control method is applied.

b. Virtual droop control method

In case of VDC method, as soon as the PCC breaker opens, unit commitment algorithm activates and decides the turn on-off operation of the natural gas generators based on the SOC of the energy storage and the microgrid load. Figure 3-18 shows the microgrid load profile and active power at energy storage device, at natural gas generators, at solar PV and at wind turbine. Figure 3-19 shows the SOC of the energy storage system.

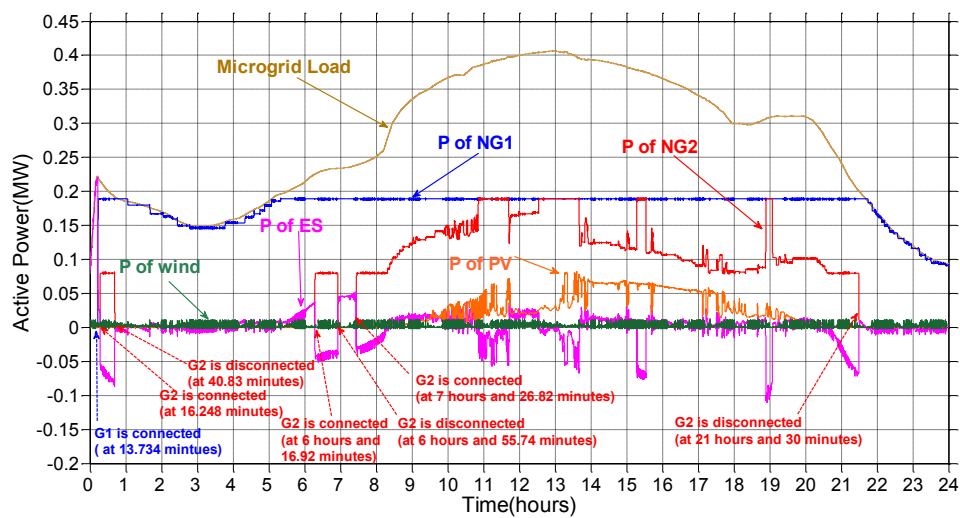


Figure 3-18. Microgrid load and active power at energy storage device, natural gas generator 1 and 2, solar PV and wind turbine; when VDC control method is applied.

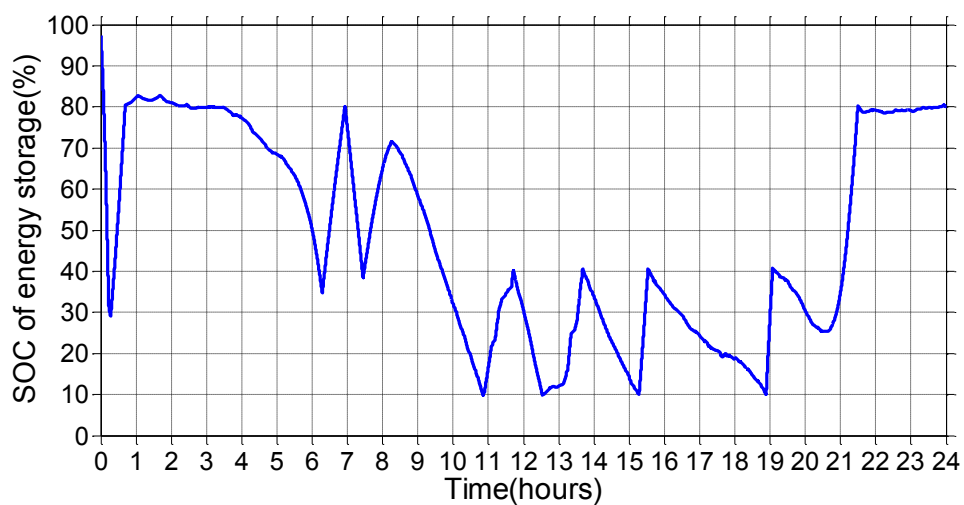


Figure 3-19. SOC of the energy storage system.

As shown in Figure 3-18, the PCC breaker has been opened at 0 hours and energy storage provided almost entire microgrid load, except power generated from renewables. Hence, the SOC of the energy storage has been dropped quickly. Since, the microgrid load is above 80 kW and also the SOC has been dropped below 50%, the natural gas generator 1 is turned on. As shown in Figure 3-18, at 13.734th minutes, at generator 1 is synchronized and the system operated in operated region of mode 2. Since the SOC of energy storage is dropped below 40%, at 16.248th minutes, the second generator is synchronized and microgrid enters in case 3. However, the microgrid load is below 270 kW, hence microgrid operates into charging region of mode 3. The generator 2 is disconnected at 40.83th minute, as SOC of the energy storage reaches 80% and microgrid again enters in mode 2.

At 6 hours and 16.92th minute, the generator 2 is again connected to charge energy storage as the SOC of energy storage dropped below 40%. After the energy storage charge up to 80%, the generator 2 is disconnected at 6 hours and 55.74 minutes. At 7 hours and 26.82th minute, the generator 2 is again connected to charge energy storage as the SOC of energy storage dropped below 40%. Since the energy storage is small, sometimes, it is quickly discharges, so generator 2 is required to connect to charge the energy storage. However, after 8 hours, the microgrid load is above 270 kW, hence generator 2 remained connected. From 8 hour and 19 minute to 21 hours and 30 minute, microgrid operated in various region of mode 3. At 21 hour and 30 minute, generator 2 is disconnected and microgrid moves to mode 1 and remained in mode 2 till 24th hours.

Figure 3-20 shows the reactive power at energy storage system and generator 1 and 2; when VDC control method is applied. When generator is connected, it provides the reactive power according to predefined virtual droop curves.

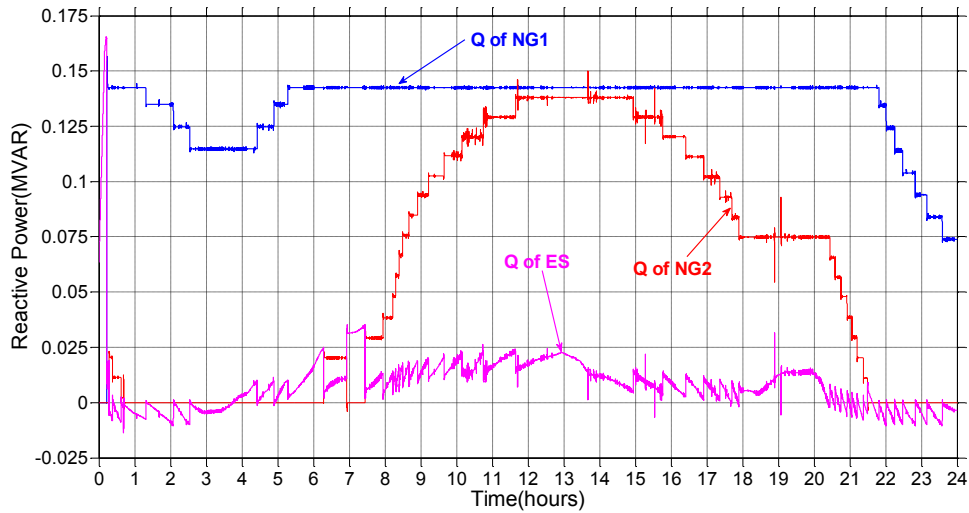


Figure 3-20. Reactive power at energy storage, natural gas generator 1 and 2; when VDC control method is applied.

Natural gas generators are operated very close to the rated active and reactive power. The maximum active and reactive power of the natural gas generator 1 are 190 kW and 142.5 kVAR, respectively, while for natural gas generator 2, the maximum output power is at 190 kW and 138 kVAR. The minimum active power output from of generator 1 is 90 kW for very short period of time. However, the minimum active power output of generator 2 is 80 kW.

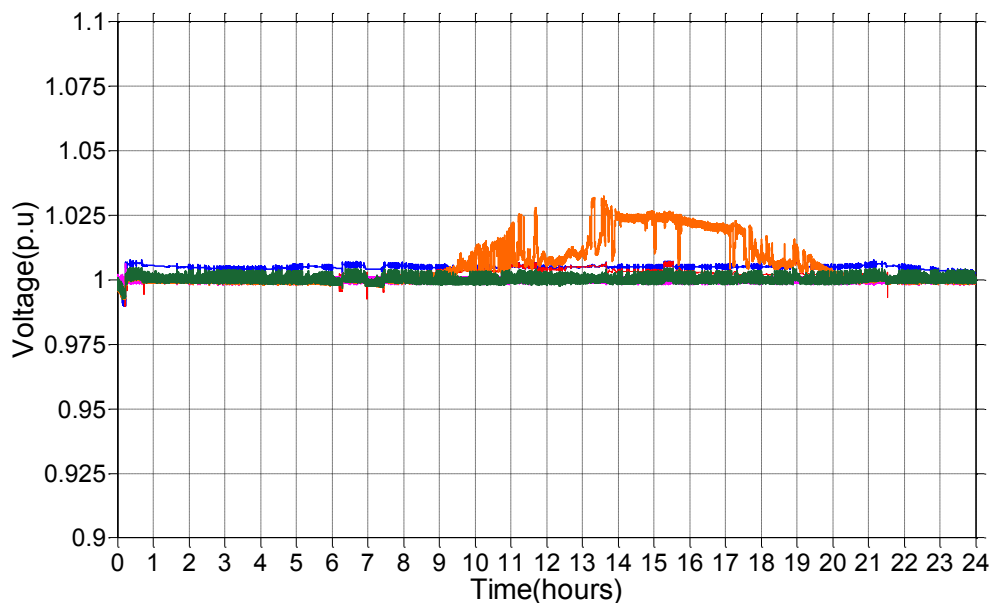


Figure 3-21. Voltage at energy storage device, natural gas generators, solar PV and wind; when VDC control method is applied.

Figure 3-21 shows the system voltages at energy storage, natural gas generators, solar PV and wind turbine; when VDC control method is applied. The voltages at DGs and energy storage remain very close to 1 p.u. The solar PV terminal voltage is little higher when it produces the power. However, the voltages at all DGs and energy storage are within specific range defined by IEEE 1547. Microgrid frequency remains at 60 Hz during island mode for VDC method, as shown in Figure 3-22.

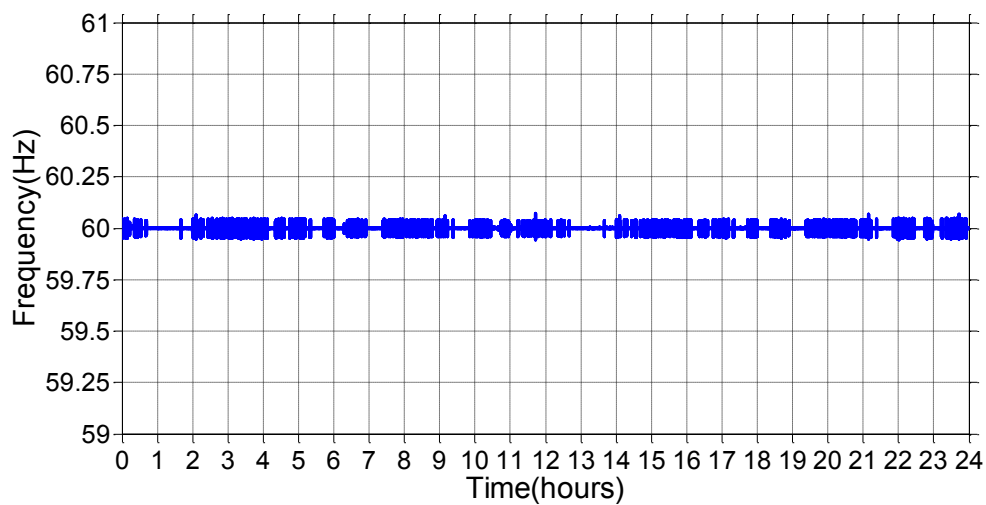


Figure 3-22. Microgrid frequency; when VDC control method is applied.

The energy outputs of both generators are shown in Figure 3-23 and charging/discharging energy at energy storage is shown in Figure 3-24. The energy provided by natural gas generator 1 and 2 after 24 hours of microgrid operation in island mode are 4.259 MWh and 1.829 MWh. It is observed that the discharging energy from the energy storage never cross 0.056 MWh. It means the selected 56 kWh energy storage is sufficient for microgrid operation in island mode; when VDC control method is applied.

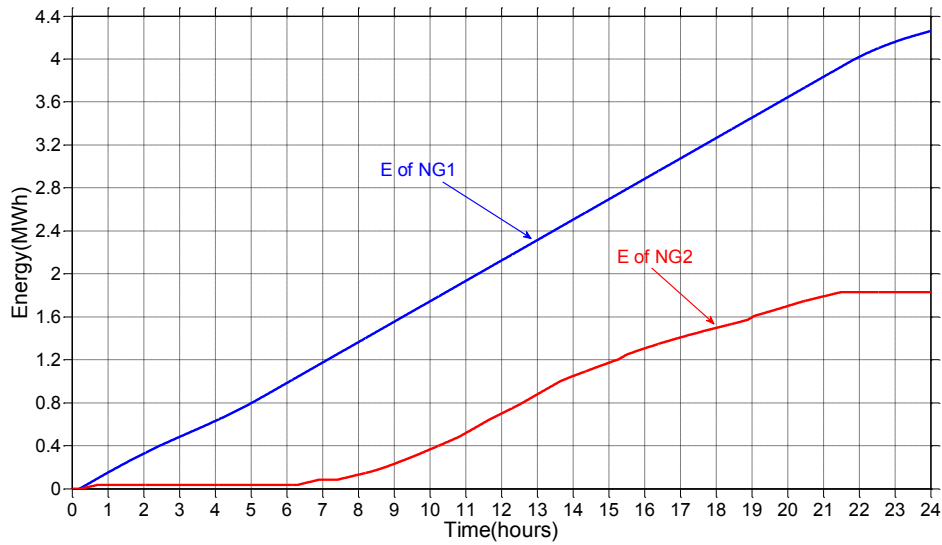


Figure 3-23. Energy output of natural gas generators; when VDC control method is applied

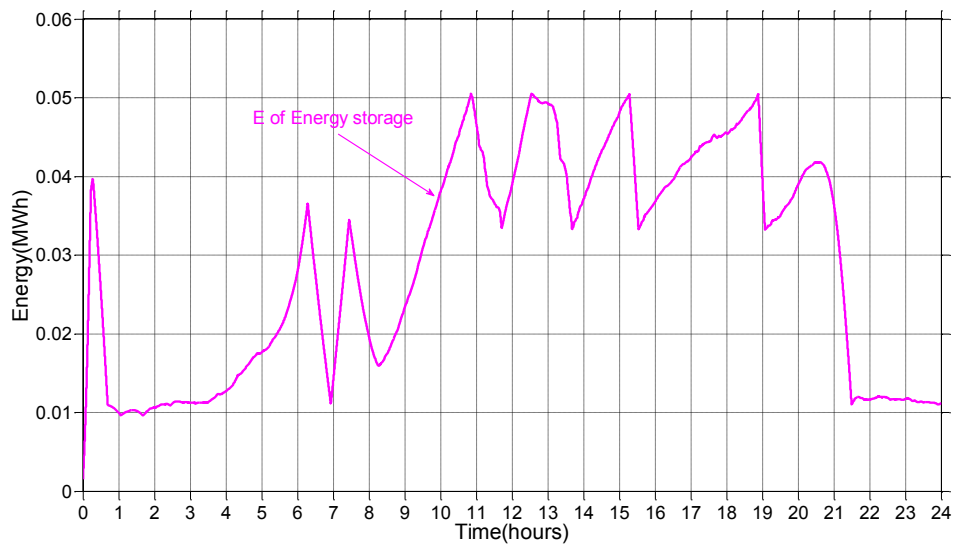


Figure 3-24. Charging/discharging energy of energy storage; when VDC control method is applied.

The fuel consumption of both natural gas generators are shown in Figure 3-25. After 24 hours of operation in an island mode; when VDC control method is applied, the natural gas consumption of natural gas generator 1 and 2 are 136.9 cubic-feet and 87.44 cubic-feet respectively. The total fuel consumption in VDC control method for 24 hours load profile is 224.34 cubic-feet. The total fuel saved in 24 hours in VDC

control method compare to natural droop control method is 54.06 cubic-feet, which proves that the VDC control method improves the microgrid efficiency.

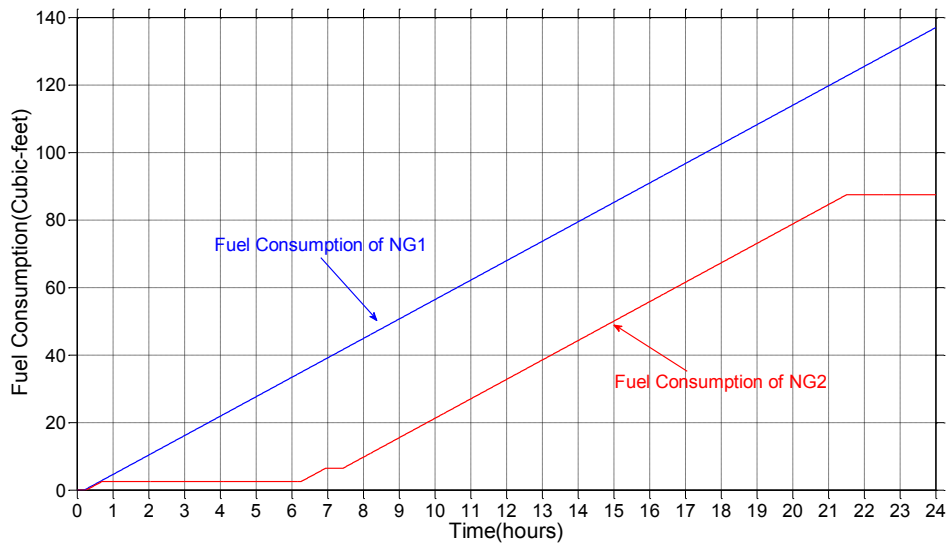


Figure 3-25. Fuel consumption of both natural gas generator; while natural droop control method is applied.

3.3 Operation without Communication

Even though the proposed control methodology uses secure communication, it is necessary to study the microgrid in case of lost communication. The proposed control framework provides the means to transfer the control from VDC to natural droop and operate without the communication. Energy storage inverter plays very important role in this control transfer. Figure 3-26 shows the control flow diagram of control transfer process.

During normal operation, microgrid operates according to VDC control method and unit commitment algorithm. Once communication loss is detected, each DG including the energy storage, operate according to the last image of the system. For instance, natural gas generator 1 has the last power output information of generator 2 and energy storage inverter. From the last information on all the sources, each generator decides their ID based on predefined criteria. The same criteria are used for all the generators to avoid any conflict between the generators' ID numbers. Each DGs and ES inverter have real time clock, which provides a tick signal at every 2 second.

In communication lost event, based on a tick signal the system control transfer process can be initialized. Before starting the transfer process, each source, hold till next tick signal to avoid any undesired situation. All the sources check frequency and voltage and if they are at rated values, the generator with ID number 1 becomes the master and it will switch its control from active/reactive power control mode to voltage/frequency control. At the same tick signal, the energy storage inverter will switch to current mode from voltage mode. The other generator remains in the active/reactive power control mode.

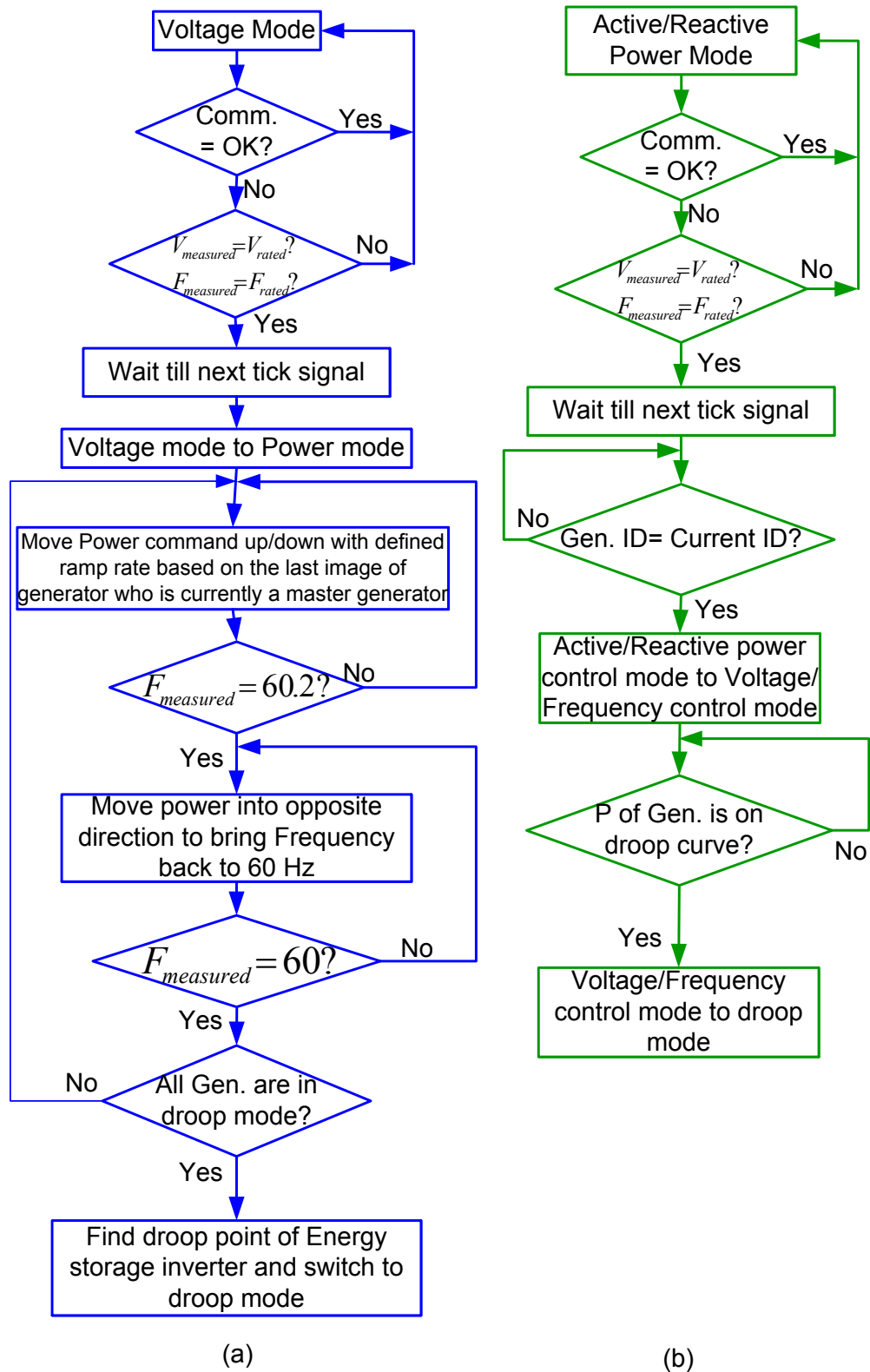


Figure 3-26. Control flow diagram of “Control Transfer Process” (a) at energy storage inverter (b) at Natural gas generators.

Based on the current generator ID and the corresponding last power output of that generator, energy storage will move its power up or down with a predefined slope. As the power from the energy storage inverter changes, the output power of master generator will also change because the master generator is in voltage/frequency control mode and moves towards the natural droop operating point. Once the master generator reaches this point, it will switch its control from voltage/frequency control to droop control. Since the other generator and energy storage inverter does not know the status of the master generator, energy storage inverter keeps moving up or down. Since the master generator is already in droop mode, the frequency and voltage will change. When frequency changes 0.2 Hz from nominal frequency of 60 Hz, the second generator and energy storage will come to know that master generator is in droop mode. Energy storage inverter moves its power in reverse direction and brings the frequency back to 60 Hz and wait for the next tick signal.

At the next tick signal, the generator with ID number 2 becomes master and switches its control from active/reactive power control to voltage/frequency control. Energy storage inverter repeats the same procedure to move the second generator to its droop curve operating point. Once all the generators switch their controls to droop control, energy storage slowly moves its power up/down and finds its own droop curve. The changes in load during control transfer process can delay the process. However it will not impact the operation of the microgrid, since at least one source will be in voltage mode during the entire process.

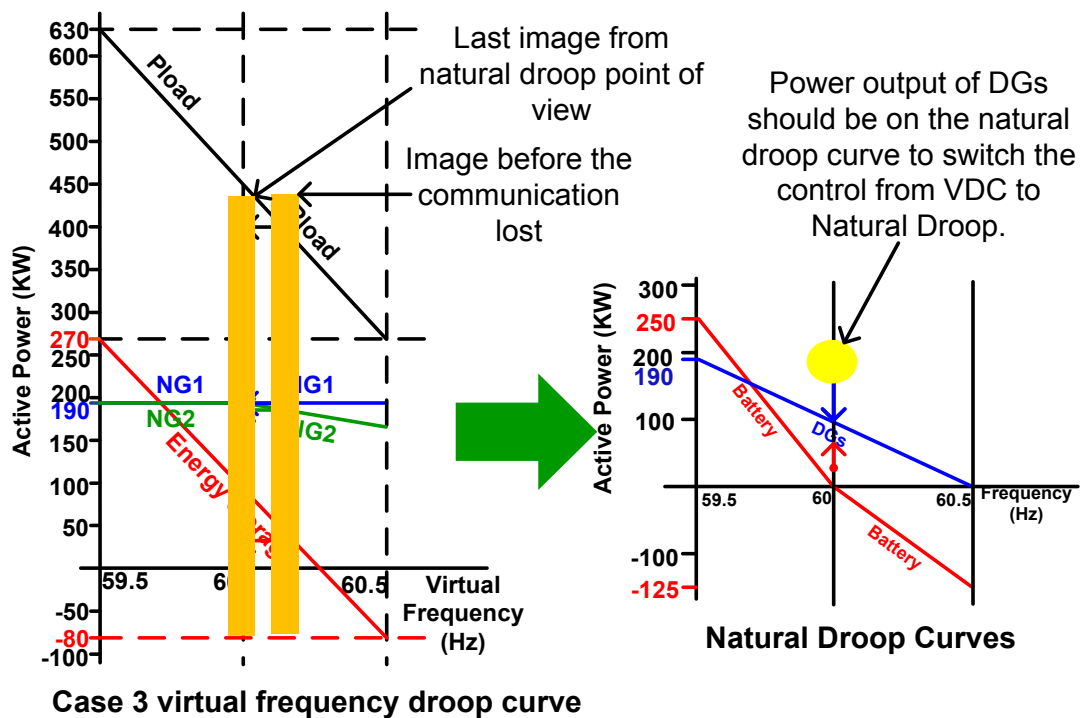


Figure 3-27. Transfer controls from VDC to natural droop control for Fort Sill microgrid

An example of the operation can be described for Fort Sill microgrid when considering that the microgrid load is 400 kW and the communication is lost between the sources. As shown in Figure 3-27, the last image is that the generator 1 provides 190 kW, generator 2 provides 180 kW and energy storage provides 30 kW. Since both generators' powers are above the natural droop curves, energy storage inverter has to increase its power output in order to bring the generators to the natural droop curves. Natural gas generator 1 is assigned ID 1 and generator 2 is assigned ID 2. Figure 3-28 shows the frequency and active powers of energy storage and generators during control transfer process.

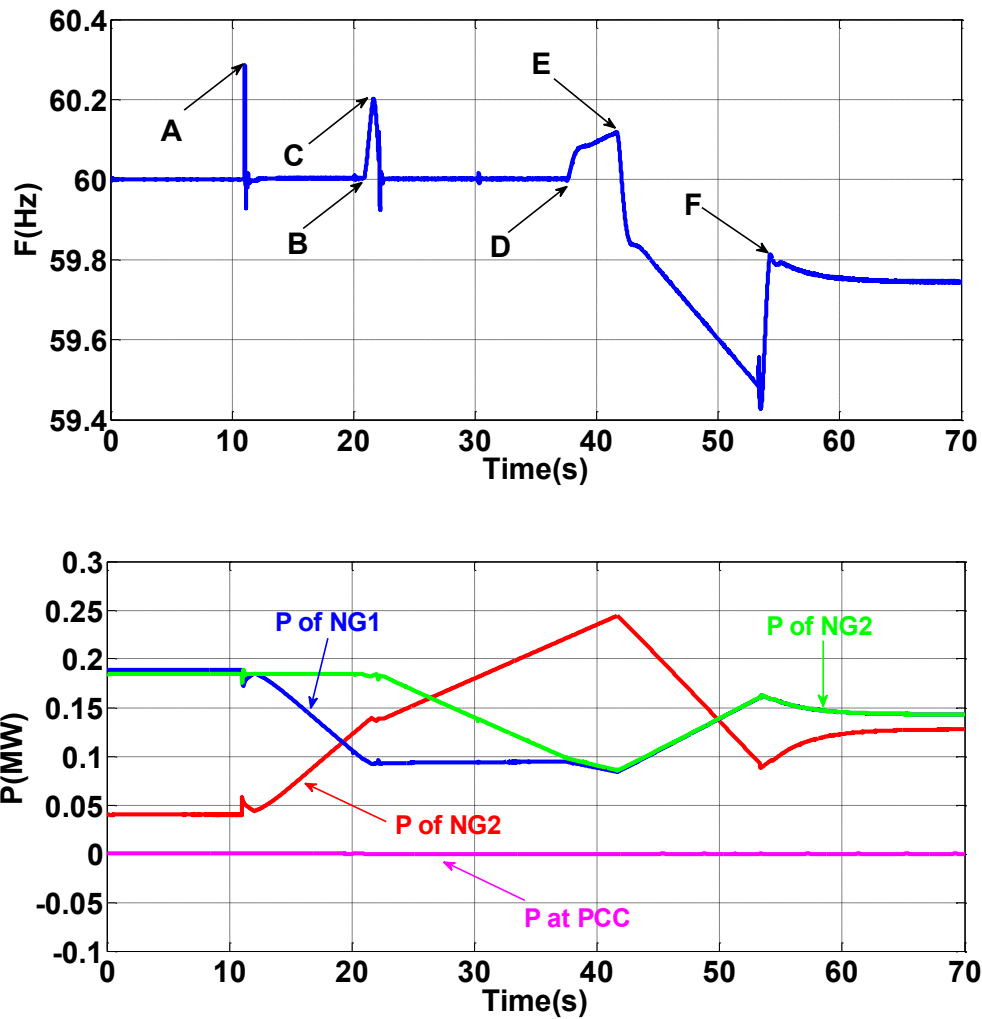


Figure 3-28. Microgrid frequency (above), Active power at PCC, energy storage, natural gas generator 1 and 2(below); during the transition from VDC to natural droop.

At point A, generator 1 switches its control from active/reactive power control to voltage/frequency control and energy storage switches to current mode. Energy storage inverter increases its power output to bring the generator 1 to the droop curve. At point B, generator 1 reaches at the droop curve and switches its control to natural droop control. At point C, frequency changes by 0.2 Hz and the second generator and energy storage come to realize that generator 1 is switched to droop control. At point C, the second generator becomes master and moves its control from active/reactive power control to voltage/frequency control. At point D, the second generator also reaches at the droop curve operating point and switches its control to droop control. At point E,

all other sources come to know that generator 2 is operating in the droop mode. Then energy storage inverter changes its power output and at point F it switches its control to droop control. After all the sources switch to droop control, the microgrid can operate autonomously without communication.

3.4 Experimental Setup for the VDC concept

In order to experimentally verify the techniques developed in this paper, an experimental test setup has been built. The schematic of the setup is shown in Figure 3-29 and pictures of component used for the experiment are shown in Figure 3-30.

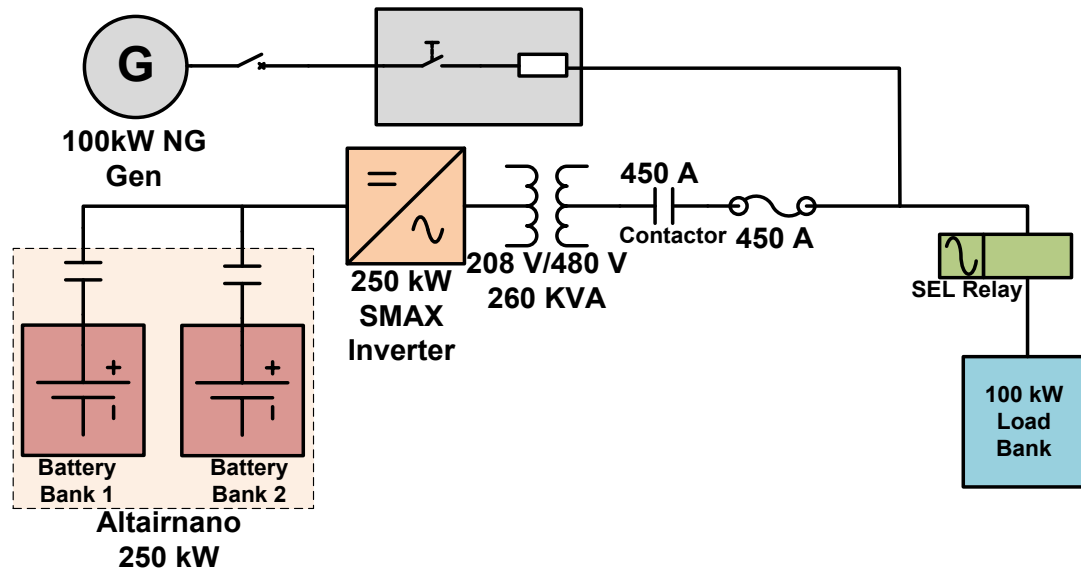


Figure 3-29. The schematic of the experimental test setup.

A SEL 849 relay has been used to measure the microgrid load and send data to storage inverter using TCP/IP Modbus secure communication protocol. WT1600 power meter is used to measure power, voltage and frequency. A 100 kW natural gas generator and a 250 kW storage inverter are used for the experimental setup. The rating of each unit of Altairnano power battery is 125 kW and one of the units is used at a time.

Once the generator is synchronized with the microgrid inverter, a 35 kW power command is given to the generator. Any change in the load is taken care of by the energy storage inverter since the inverter is operating in a voltage mode. Figure 3-31 shows the load, active power of natural gas generator and energy storage. Figure 3-32 shows the microgrid voltage and frequency when VDC is applied. Larger variations in

frequency compared with the modeling results occur due to existence of a low pass filter on the slew rate of the energy storage inverter.



(a)



(b)



(c)



(d)



(e)



(f)

Figure 3-30. (a) SEL 849 relay to measure total load and send data to microgrid inverter using MODBUS TCP/IP (b) WT1600 power meter to measure the powers, frequency and voltages (c) 100 kW load bank (d) Altairnano energy storage (e) SMAX inverter connected to energy storage (f) 100 kW natural gas generator

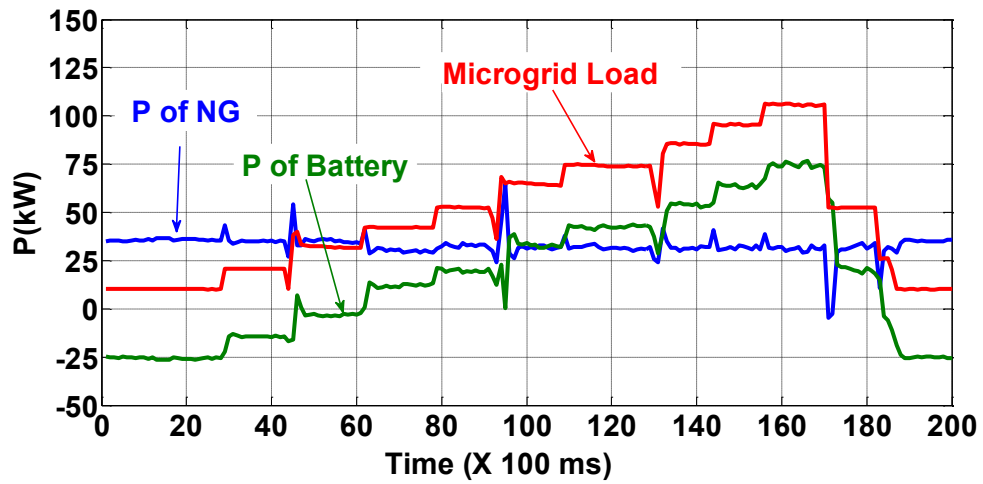


Figure 3-31. Active Power at Natural gas generator, Energy storage and load; experiment results

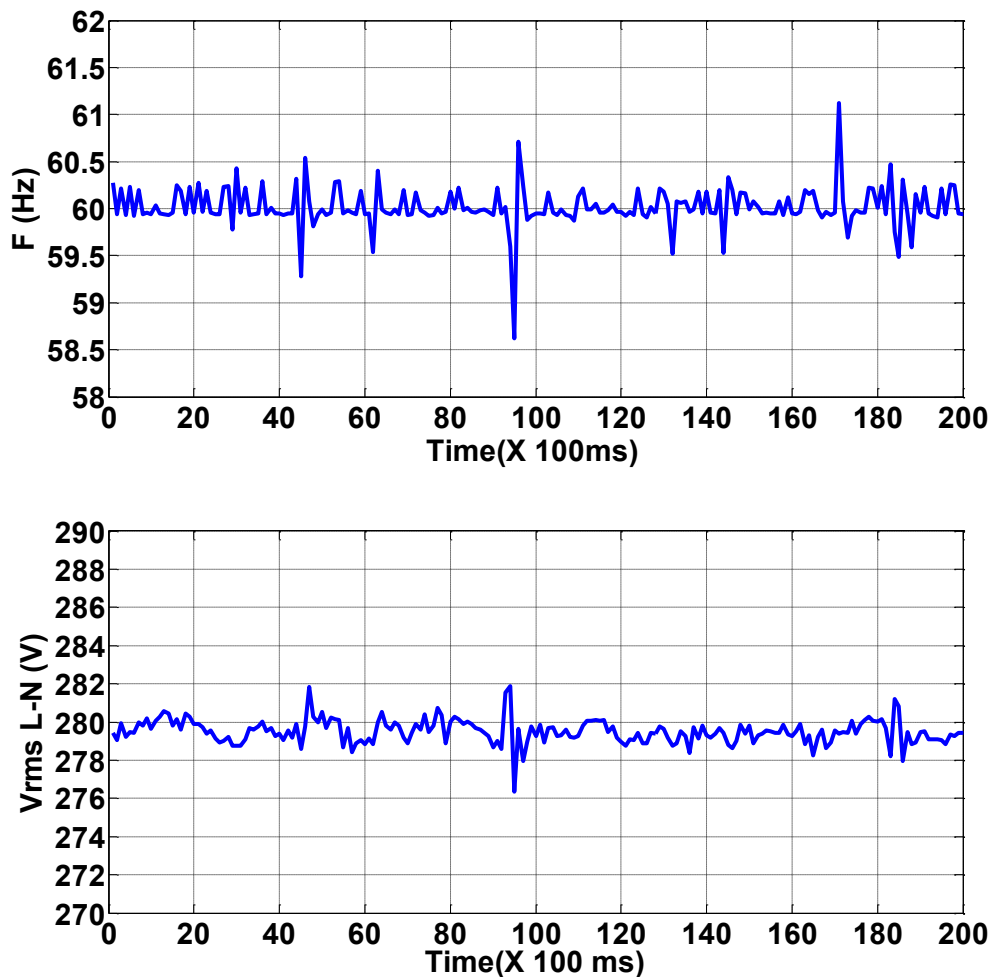


Figure 3-32. Microgrid frequency (above), Microgrid voltage (below); experiment results.

3.5 Deployment of VDC technique in Actual Fort Sill

Microgrid

The proposed VDC technique has been deployed to the actual fort sill microgrid in Oklahoma and successfully tested. In the field, Red Lion meter monitors the voltage, frequency and active power output of utility, energy storage, generator 1, generator 2, and renewables. Figure 3-33 shows active power of utility, energy storage inverter, generator 1, generator 2 and renewables. Figure 3-34 shows the measured frequency at utility, energy storage inverter, generator 1, generator 2 and renewables. Figure 3-35 shows the measured RMS voltage at utility, energy storage inverter, generator 1, generator 2 and renewables.

Figure 3-35 shows the measured RMS voltage at utility, energy storage inverter, generator 1, generator 2 and renewables.

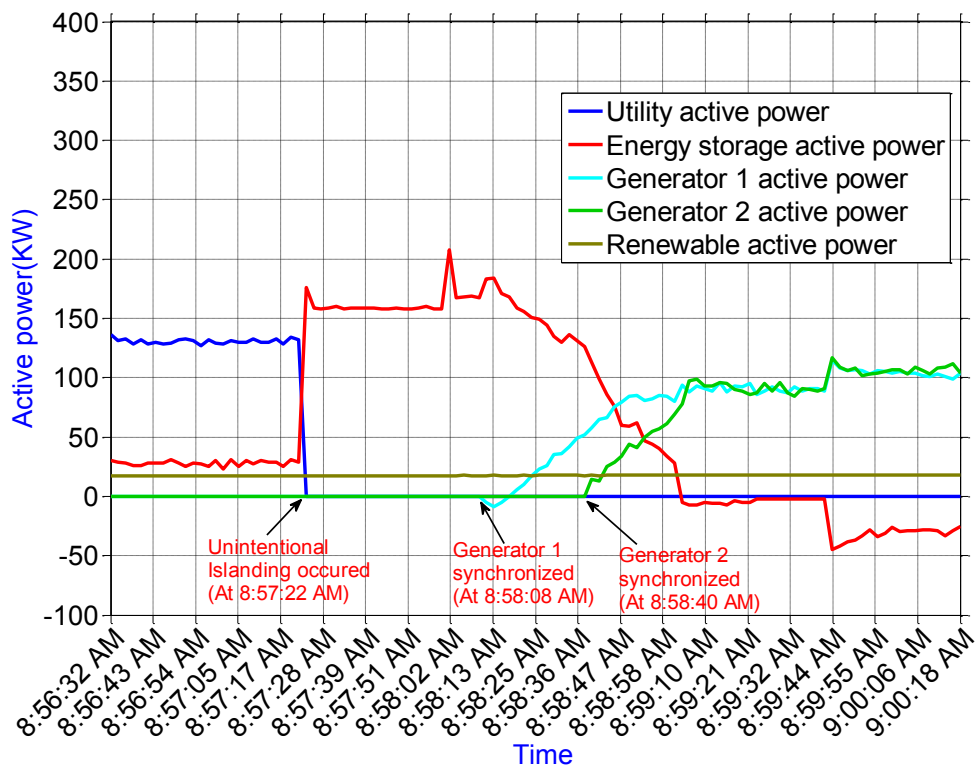


Figure 3-33. Active Power of utility, energy storage inverter, generator 1, generator 2 and renewables; successful test of generator 2 synchronization (Courtesy: Eaton Corporation).

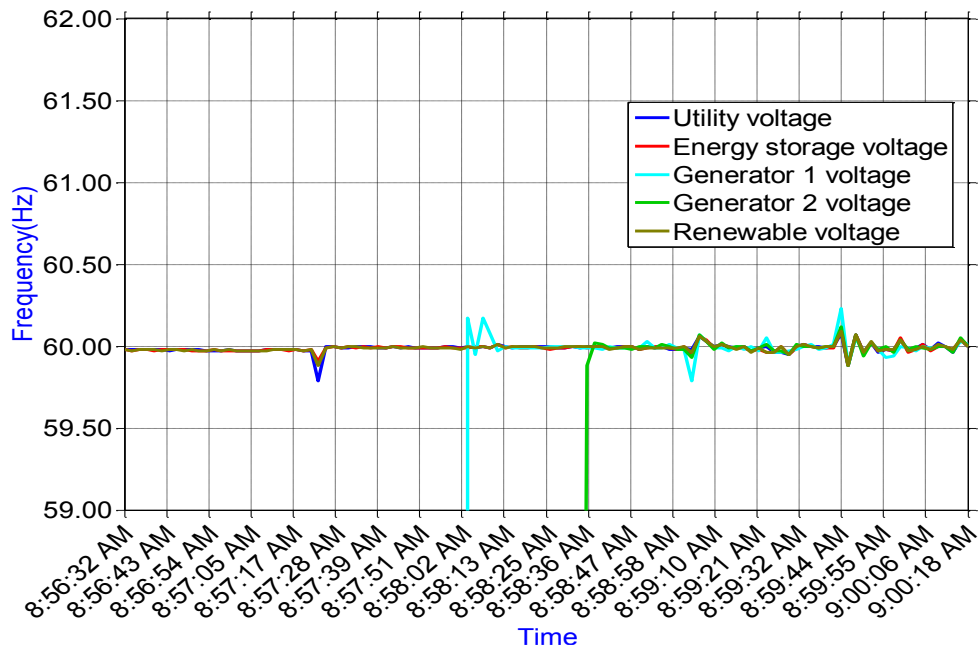


Figure 3-34. Frequency at utility, energy storage inverter, generator 1, generator 2 and renewable source (Courtesy: Eaton Corporation).

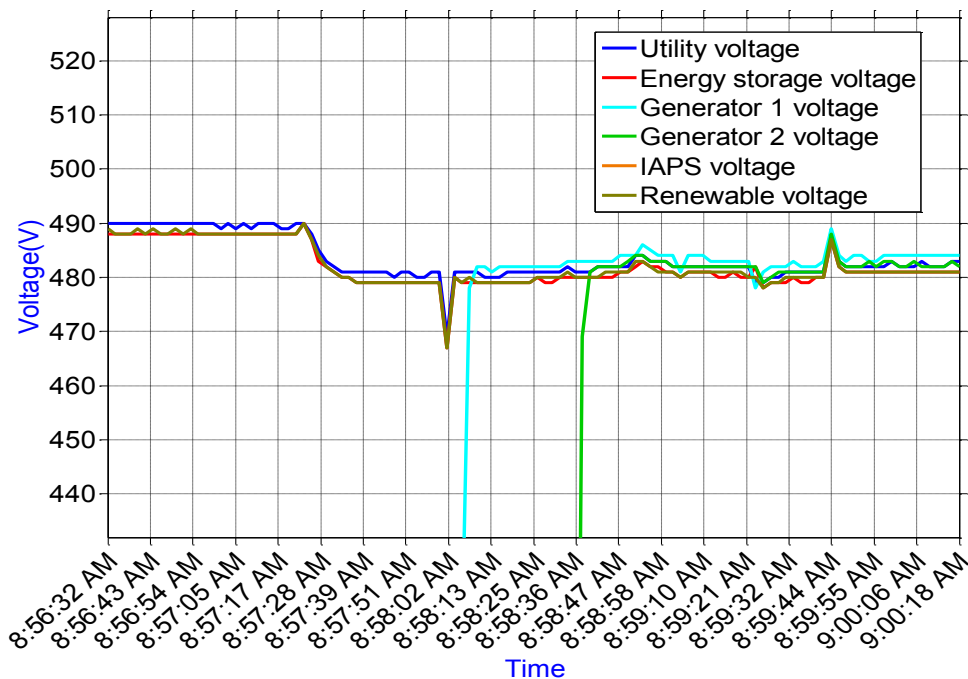


Figure 3-35. RMS voltage at utility, energy storage inverter, generator 1, generator 2 and renewables (Courtesy: Eaton Corporation).

As shown in Figure 3-33, initially, the microgrid is operated in grid connected mode. And chiller load is on. The unintentional islanding is occurred at 5:57:22 AM and the energy storage inverter is switched from current mode to voltage mode of

operation. The energy storage system supports almost entire chiller load except small power generated by solar PV after islanding. Generator 1 is commanded to start after 30 second of islanding. Once the generator 1 is synchronized and the breaker is closed. The power command is determined from predefined virtual droop curves. Generator 2 is commanded to start after 60 second of islanding. Generator 2 is successfully synchronized and started providing power according to the power command. The time sequence of the test is shown in Table 3-2.

Table 3-2. Time sequence of the test

Time	Event
8:57:22 AM	Unintentional islanding occurred.
8:57:52 AM	Generator 1 is commanded to start.
8:58:02 AM	Generator 1 is synchronized and started delivering power.
8:58:22 AM	Generator 2 is commanded to start
8:58:40 AM	Generator 2 is synchronized and started delivering power.

Chapter 4 Islanding and Reconnection

Operations of Microgrid

Both types of microgrid islanding, intentional and unintentional, are studied in this chapter. Intentional islanding may occur due to scheduled grid outage or maintenance issues. Unintentional islanding is a more complex case and may be required due to grid faults, unscheduled outages, and voltage or/and frequency transients [65, 67, 68, 109]. Since Energy storage inverter is always connected to the system, it is playing key role during islanding. Simulation results are provided for the Fort Sill microgrid system.

4.1 Unintentional Islanding

When the main grid is lost or breaker at the PCC opens to prevent DGs from the faults at main grid, the unintentional islanding occurs, and the microgrid is exposed to voltage and frequency variations. To prevent large voltage and frequency transients during unintentional islanding, power has to supply immediately to microgrid load by the dispatchable power sources, which requires them to operate in voltage control mode. Since the natural gas generators are off-line during grid-connected and also renewables are in current mode, the energy storage system becomes the only power source to adjust the power flow during unintentional islanding.

Figure 4-1 to Figure 4-3 shows active power, reactive power and voltage at PCC terminal and at the energy storage during the transition from grid tie mode to island mode. Figure 4-4 shows the microgrid frequency during the transition. In grid tie mode, energy storage power is zero and natural gas generators are off. For instance, at 10th second the PCC breaker opens due to unintentional islanding. As soon as PCC breaker opens energy storage control is switched from power reference mode to voltage

reference mode and it pick up the microgrid load. Since energy storage picked up the system load, voltage and frequency will see small transient.

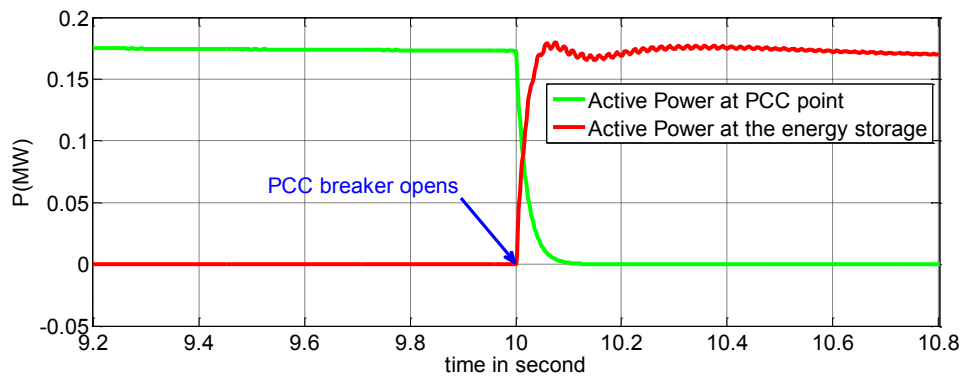


Figure 4-1. Active power at PCC point and of the energy storage for Fort Sill microgrid; when unintentional islanding is occurred.

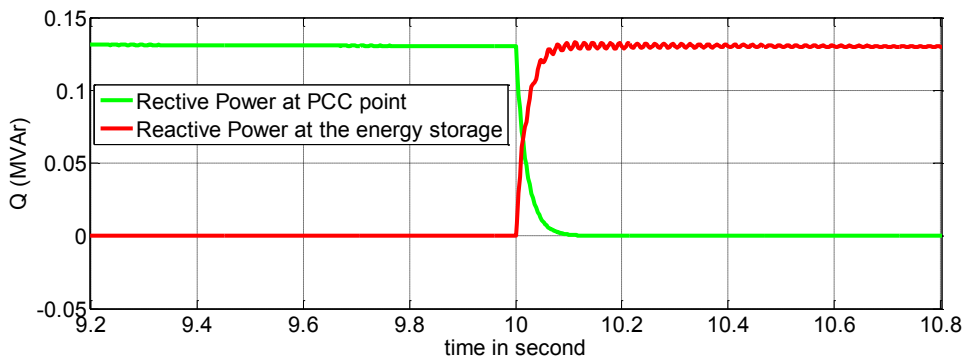


Figure 4-2. Reactive power at PCC point and of the energy storage for Fort Sill; when unintentional islanding is occurred.

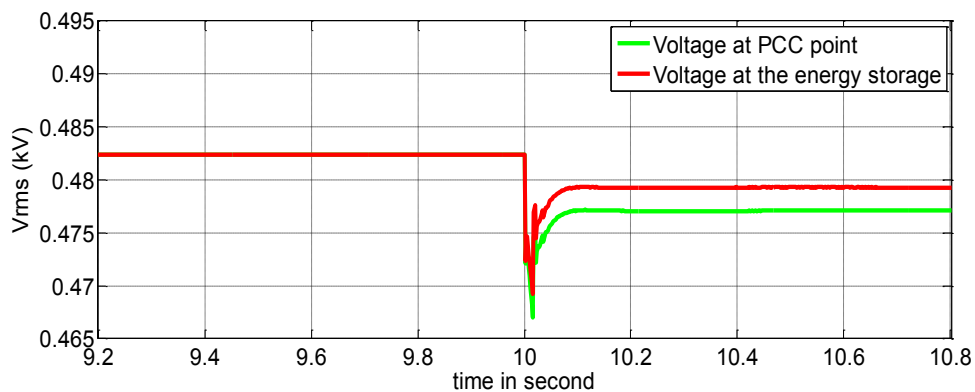


Figure 4-3. RMS voltage at PCC point and of the energy storage for Fort Sill microgrid; when unintentional islanding is occurred.

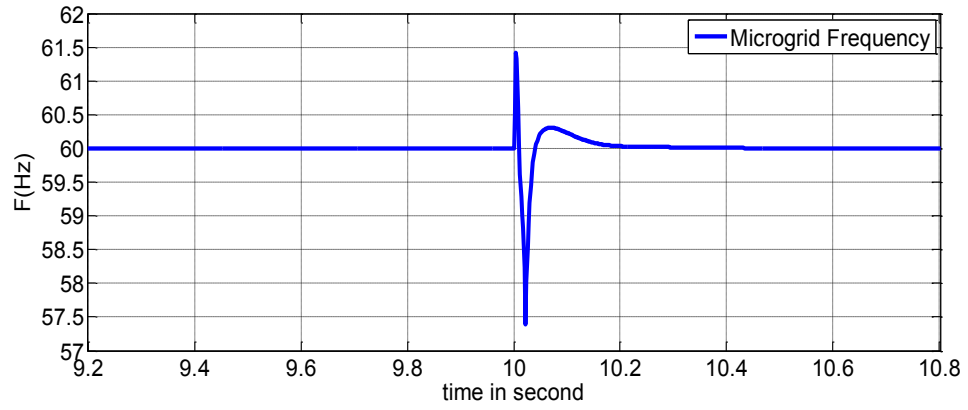


Figure 4-4. Microgrid frequency Fort Sill microgrid systems; when unintentional islanding is occurred.

4.2 Intentional Islanding

Intentional islanding, which provides the capability for the microgrid to manually separate from the bulk grid, leads to potential issues of power balancing, voltage sag, and frequency oscillation. To prevent the large transient, the power at PCC terminal must be close to zero. Since the intentional islanding is predetermined, the power at the PCC terminal can be made zero by increasing the power from the DGs. The DGs within microgrid must be preplanned to switch their controls and share the local loads to minimize the impact of disconnection from the host utility.

Figure 4-5 to Figure 4-8 shows the simulation results during intentional islanding for Fort Sill microgrid. As soon as intentional islanding command is given, energy storage active and reactive power command is changed. Energy storage brings the active and reactive power at PCC point close to zero and simultaneously, commands are sent to DGs based on the unit commitment to turn them on. Once the active and reactive power at PCC becomes zero, PCC breaker opens and energy storage controls change to voltage mode. In Fort Sill microgrid system, the energy storage inverter is capable to take entire microgrid load. So in order to island the microgrid, additional resources are not required during transition. However, in some cases where the energy storage cannot supply total microgrid load, the generators are required to turn on to bring the PCC power to zero. The voltage and frequency will not deviate too much during the intentional islanding due to zero or negligible power transfer at PCC. As shown in Figure 4-5 at 10th second the intentional islanding command is given and at 10.90th second PCC breaker is opened.

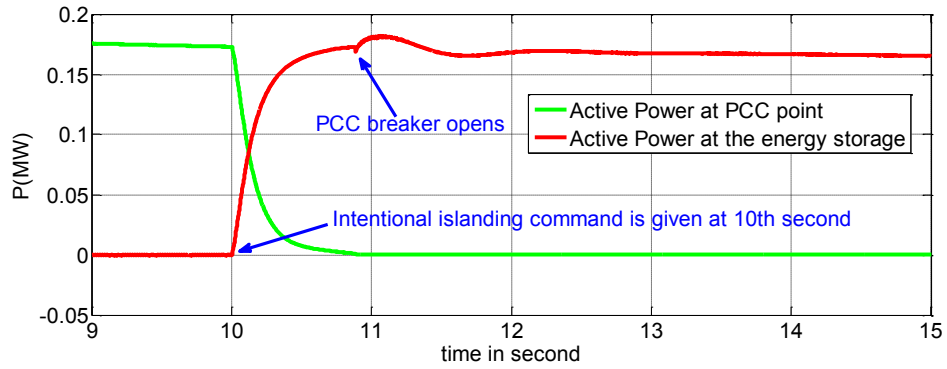


Figure 4-5. Active power at PCC point and of the energy storage for Fort Sill microgrid; when intentional islanding is occurred.

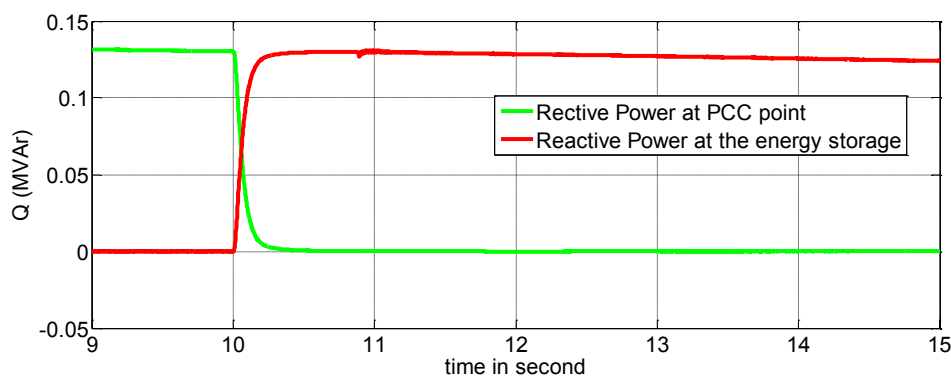


Figure 4-6. Reactive power at PCC point and of the energy storage for Fort Sill microgrid; when intentional islanding is occurred.

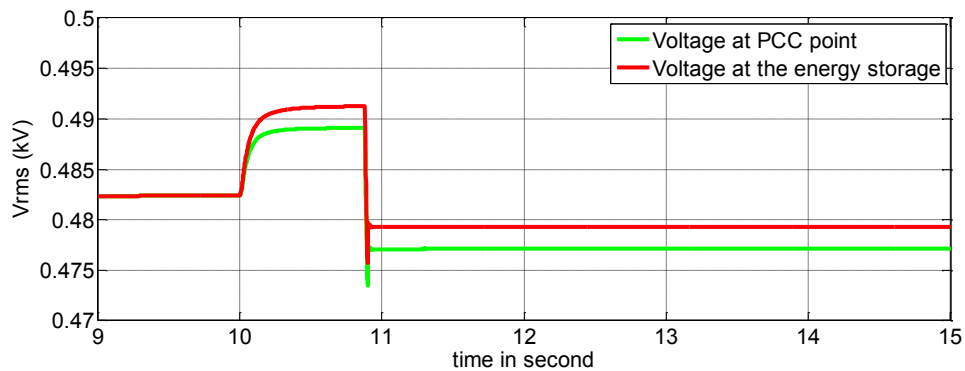


Figure 4-7. RMS voltage at PCC point and of the energy storage for Fort Sill microgrid; when intentional islanding is occurred.

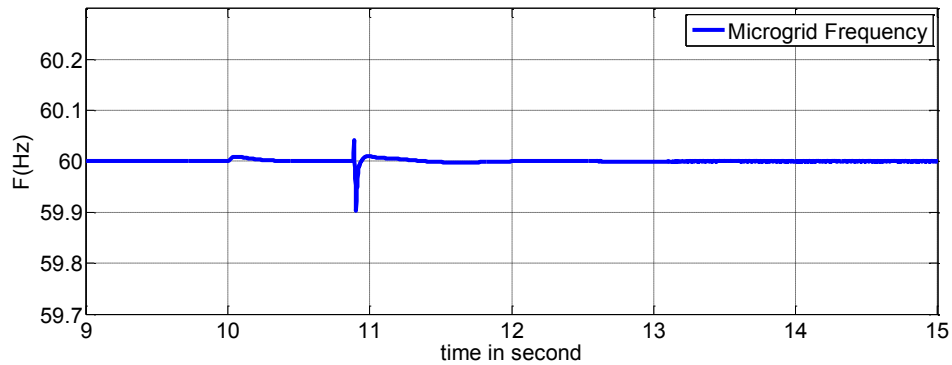


Figure 4-8. Microgrid frequency of Fort Sill microgrid systems; when intentional islanding is occurred.

4.3 Reconnection

Before reconnecting microgrid to the grid, the frequencies, voltages and phases at both side of the PCC must be the same to minimize the transients and avoid disturbance. Since a microgrid consists of more than one generation, adjusting system frequency and voltage becomes challenging.

In case of traditional droop control methods, operating voltage and frequency vary based on the active and reactive power output. Microgrid control has to change microgrid operating voltage and frequency to match with the main grid in order to reconnect the system with minimum transient. Once the reconnection command is given, the voltage and frequency reference at all DGs are changed to grid voltage and frequency. The microgrid frequency is set at 0.01Hz above the grid frequency to adjust the phase angle. However this method is time consuming since matching phase on both sides is time consuming. Reconnection method for traditional droop control method is implemented for both Fort Sill microgrid and IEEE 34 bus microgrid system and comparison has been made with the reconnection results for VDC method.

In proposed VDC method, reconnection is very quick, since voltage and frequency are very tightly regulating during islanding mode. The angle is regulating and keep very close to grid angle, to make the reconnection faster and easier. As soon as the

reconnection command is received, the reconnection mechanism make sure all three parameters on both side of PCC breaker and close the PCC breaker. Once the reconnection transient is disappeared, the active and reactive power at natural gas generators are brought to zero and disconnected from the system if any of the generators are in operation during that time.

Figure 4-9 shows the active powers and Figure 4-10 shows the frequency on both side of PCC breaker at the time of reconnection, when natural droop control is applied during islanded mode of operation. At 155th second reconnection command is given and around 169th second PCC breaker gets open.

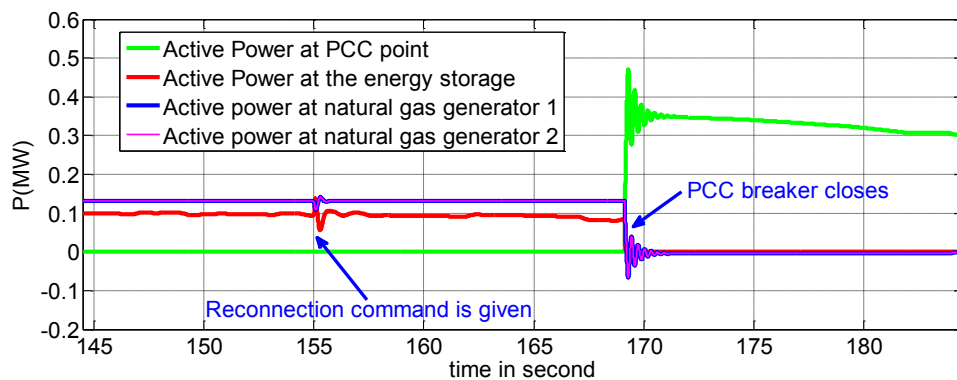


Figure 4-9 Active power at PCC terminal, energy storage device, natural gas generator 1, and natural gas generator during reconnection event; when natural droop control method is applied to Fort Sill microgrid in island mode.

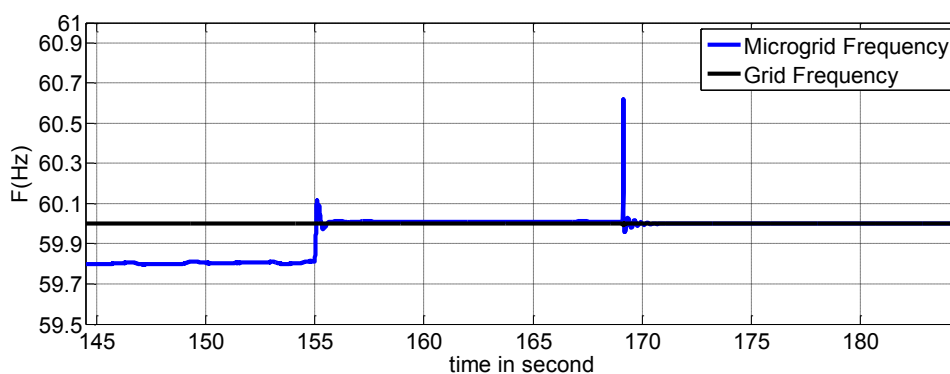


Figure 4-10. Microgrid frequency and grid frequency during reconnection event; when natural droop control method is applied to Fort Sill microgrid in island mode.

Figure 4-11 to shows the simulation results, when microgrid operates in case 3(Energy storage and both natural gas generators provides power) and reconnection

command is given. As shown in figure 18(a), PCC breaker closes as soon as the reconnection command is given. The natural gas generator's power brought back to zero before they got disconnected.

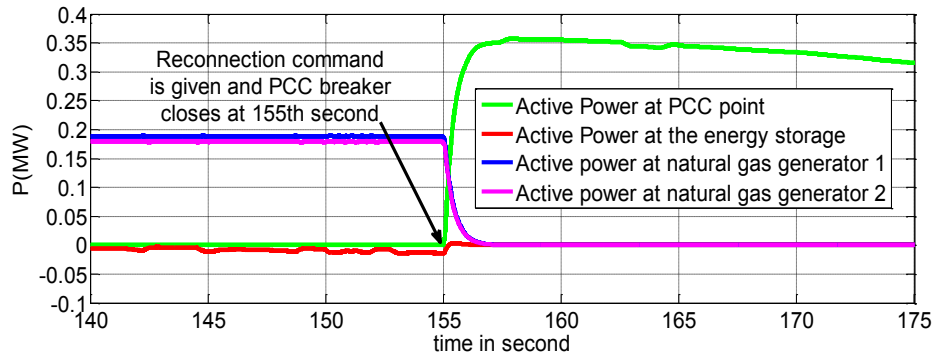


Figure 4-11. Active power at PCC terminal, energy storage device, natural gas generator 1 and 2 at the time of reconnection event; when VDC method is applied to Fort Sill Microgrid.

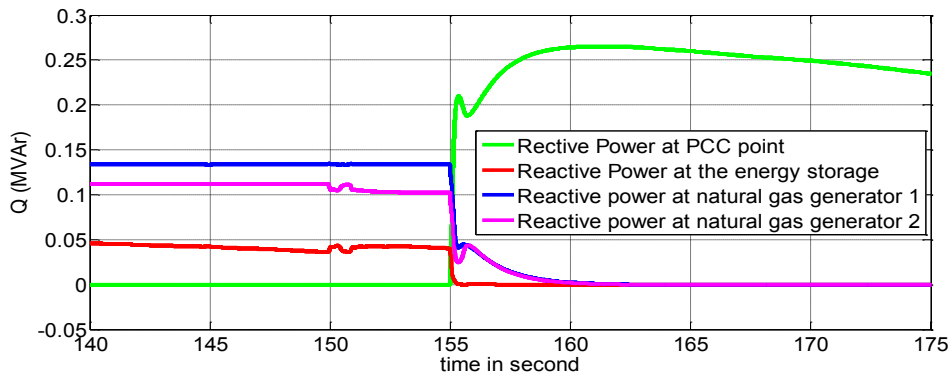


Figure 4-12. Reactive power at PCC terminal, energy storage device, natural gas generator 1 and 2 at the time of reconnection event; when VDC method is applied to Fort Sill Microgrid.

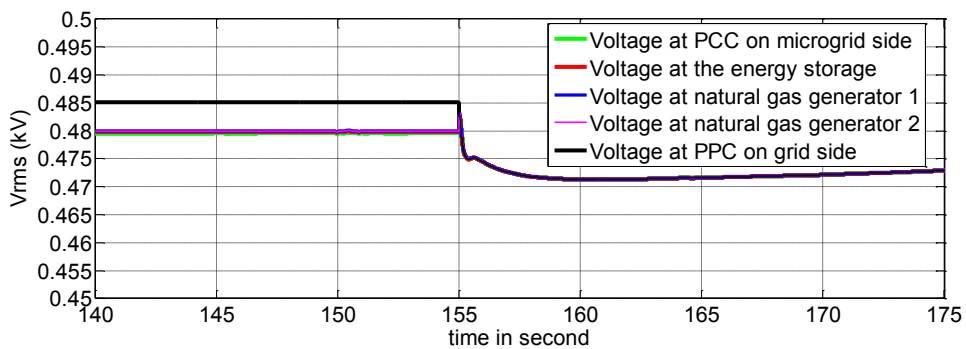


Figure 4-13. . Voltage at PCC terminal, energy storage device, natural gas generator 1 and 2 at the time of reconnection event; when VDC method is applied to Fort Sill Microgrid.

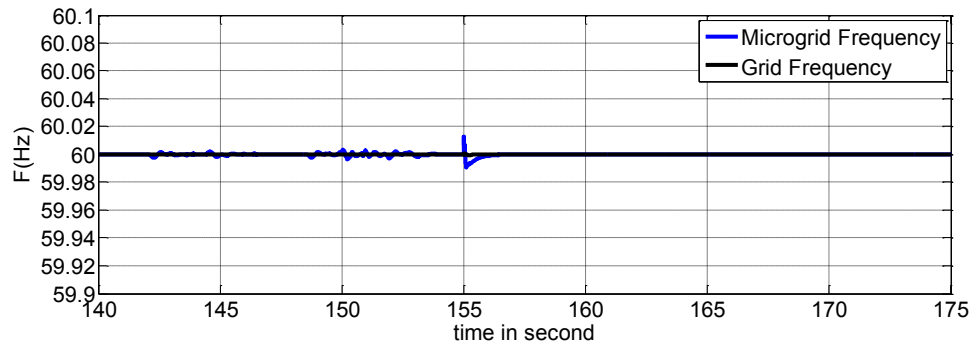


Figure 4-14. Microgrid frequency and grid frequency during reconnection event; when VDC method is applied to Fort Sill Microgrid.

Chapter 5 State Space Modeling and Stability

Analysis of Fort Sill Microgrid

In traditional large power system, frequency can be maintained by inertia of large synchronous generators, while the voltage can be maintained by maintaining reactive power. The major sources of reactive power are synchronous generator, synchronous condenser and capacitor banks. The regulating transformer also contributes to regulate the system voltage. In a microgrid, large numbers of inverters are integrated with renewables and energy storage. Hence, during island mode of operation, microgrid has small inertia or it may not have any inertia if none of synchronous generator is connected. Depending on structure of microgrid and sources connected into the microgrid, the stability aspect differs.

In conventional power system, stability analysis is well established and for the different frequency ranges of possible concern there are models which include the appropriate features. However, detailed generalized dynamic model for microgrid are not available. Previous dynamic analysis of microgrid system considered inverters as an ideal source, which is not appropriate to study the stability of the microgrid and are not useful to analyze the robustness of microgrid controls.

The state space model of voltage mode inverter, current mode inverter, natural gas generator, and transmission line/cable has been derived in this chapter. The detail state space model of fort sill microgrid has been derived for all three cases of VDC method describe in chapter 3. The stability analysis of a microgrid can be done in different scenario. The developed model can be used to design controllers of the microgrid, for example governor and excitation systems of synchronous generators, active and reactive power controller of current mode inverters and also voltage and frequency

controller for voltage mode inverter. The developed state space model is also used for optimization of controller parameters.

5.1 State space modelling of Current Mode Inverter

The schematic diagram of current mode inverter is shown in Figure 5-1.

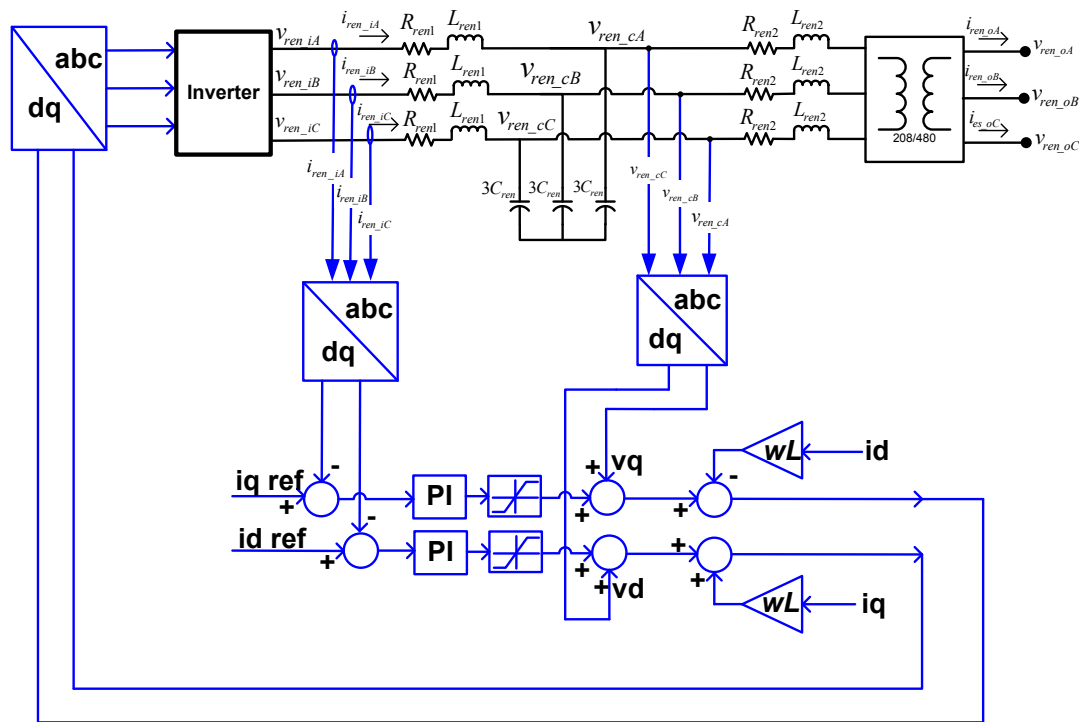


Figure 5-1 Schematic diagram of current mode inverter

The current mode inverter has been utilized in renewable energy applications mainly with solar PV and full conversion topology of wind energy system. The delta capacitor from actual inverter in LCL filter can be represented into equivalent wye connected capacitor where, the capacitor in wye connection is three time than the capacitor in delta connection. Since, in studied microgrid model, renewable energy resources utilize current mode of operation, the notation used for mathematical equations are for renewable resources. The dynamics of the inverter LCL filter are represented by following equations.

$$L_{ren1} \frac{d}{dt} (i_{ren_iA}) = -R_{ren1} i_{ren_iA} - v_{ren_cA} + v_{ren_iA} \quad (5-1)$$

$$L_{ren1} \frac{d}{dt} (i_{ren_iB}) = -R_{ren1} i_{ren_iB} - v_{ren_cB} + v_{ren_iB} \quad (5-2)$$

$$L_{ren1} \frac{d}{dt} (i_{ren_iC}) = -R_{ren1} i_{ren_iC} - v_{ren_cC} + v_{ren_iC} \quad (5-3)$$

$$\frac{d}{dt} (v_{ren_cA}) = \frac{1}{3C_{ren}} (i_{ren_iA}) - \frac{1}{3C_{ren}} \left(\frac{N_s}{N_p} \right) (i_{ren_oA}) \quad (5-4)$$

$$\frac{d}{dt} (v_{ren_cB}) = \frac{1}{3C_{ren}} (i_{ren_iB}) - \frac{1}{3C_{ren}} \left(\frac{N_s}{N_p} \right) (i_{ren_oB}) \quad (5-5)$$

$$\frac{d}{dt} (v_{ren_cC}) = \frac{1}{3C_{ren}} (i_{ren_iC}) - \frac{1}{3C_{ren}} \left(\frac{N_s}{N_p} \right) (i_{ren_oC}) \quad (5-6)$$

$$L_{ren2} \frac{d}{dt} (i_{ren_oA}) = -R_{ren2} i_{ren_oA} + \left(\frac{N_p}{N_s} \right) v_{ren_cA} - \left(\frac{N_p}{N_s} \right)^2 v_{ren_oA} \quad (5-7)$$

$$L_{ren2} \frac{d}{dt} (i_{ren_oB}) = -R_{ren2} i_{ren_oB} + \left(\frac{N_p}{N_s} \right) v_{ren_cB} - \left(\frac{N_p}{N_s} \right)^2 v_{ren_oB} \quad (5-8)$$

$$L_{ren2} \frac{d}{dt} (i_{ren_oC}) = -R_{ren2} i_{ren_oC} + \left(\frac{N_p}{N_s} \right) v_{ren_cC} - \left(\frac{N_p}{N_s} \right)^2 v_{ren_oC} \quad (5-9)$$

The above equations can be written into space phasor domain as follows.

$$\frac{d}{dt} (\vec{i}_{ren_i}) = -\frac{R_{ren1}}{L_{ren1}} \vec{i}_{ren_i} - \frac{1}{L_{ren1}} \vec{v}_{ren_c} + \frac{1}{L_{ren1}} \vec{v}_{ren_i} \quad (5-10)$$

$$\frac{d}{dt} (\vec{v}_{ren_c}) = \frac{1}{3C_{ren}} (\vec{i}_{ren_i}) - \frac{1}{3C_{ren}} \left(\frac{N_s}{N_p} \right) (\vec{i}_{ren_o}) \quad (5-11)$$

$$\frac{d}{dt}(\vec{i}_{ren_o}) = -\frac{R_{ren2}}{L_{ren2}}\vec{i}_{ren_o} + \frac{1}{L_{ren2}}\vec{v}_{ren_c} - \frac{1}{L_{ren2}}\vec{v}_{ren_o} \quad (5-12)$$

The above space phasor equations can be express into d-q reference frame. In order to transform them into d-q frame, the voltages and currents space phasor can be substituted by following equations.

$$\vec{v}_{ren_i} = v_{ren_idq} e^{j\varepsilon(t)} \quad (5-13)$$

$$\vec{v}_{ren_o} = v_{ren_odq} e^{j\varepsilon(t)} \quad (5-14)$$

$$\vec{i}_{ren_i} = i_{ren_idq} e^{j\varepsilon(t)} \quad (5-15)$$

$$\vec{i}_{ren_o} = i_{ren_odq} e^{j\varepsilon(t)} \quad (5-16)$$

$$\vec{v}_{ren_c} = v_{ren_cdq} e^{j\varepsilon(t)} \quad (5-17)$$

After substituting the voltages and currents space phasor and decomposing the system equations into real and imaginary components, the dynamics equations into d-q reference can be written as follows.

$$\frac{d}{dt}(i_{ren_id}) = \omega_0 i_{ren_iq} - \frac{R_{ren1}}{L_{ren1}} i_{ren_id} - \frac{1}{L_{ren1}} v_{ren_cd} + \frac{1}{L_{ren1}} v_{ren_id} \quad (5-18)$$

$$\frac{d}{dt}(i_{ren_iq}) = -\omega_0 i_{ren_id} - \frac{R_{ren1}}{L_{ren1}} i_{ren_iq} - \frac{1}{L_{ren1}} v_{ren_cq} + \frac{1}{L_{ren1}} v_{ren_iq} \quad (5-19)$$

$$\frac{d}{dt}(v_{ren_cd}) = \omega_0 v_{ren_cq} + \frac{1}{3C_{ren}}(i_{ren_id}) - \frac{1}{3C_{ren}} \left(\frac{N_s}{N_p} \right) (i_{ren_od}) \quad (5-20)$$

$$\frac{d}{dt}(v_{ren_cq}) = -\omega_0 v_{ren_cd} + \frac{1}{3C_{ren}}(i_{ren_iq}) - \frac{1}{3C_{ren}} \left(\frac{N_s}{N_p} \right) (i_{ren_q}) \quad (5-21)$$

$$\frac{d}{dt}(i_{ren_od}) = \omega_0 i_{ren_oq} - \frac{R_{ren2}}{L_{ren2}} i_{ren_od} + \frac{1}{L_{ren2}} \left(\frac{N_p}{N_s} \right) v_{ren_cd} - \frac{1}{L_{ren2}} \left(\frac{N_p}{N_s} \right)^2 v_{ren_od} \quad (5-22)$$

$$\frac{d}{dt}(i_{ren_oq}) = -\omega_0 i_{ren_od} - \frac{R_{ren2}}{L_{ren2}} i_{ren_oq} + \frac{1}{L_{ren2}} \left(\frac{N_p}{N_s} \right) v_{ren_cq} - \frac{1}{L_{ren2}} \left(\frac{N_p}{N_s} \right)^2 v_{ren_oq} \quad (5-23)$$

The control of current mode VSC system is based on d-q reference frame. The mathematical derivation of the current controller is derived below to represent them into the state space equations. The inverter inputs, v_{ren_id} and v_{ren_iq} are given by equations.

$$v_{ren_id}(t) = \frac{V_{DC}}{2} m_d(t) \quad (5-24)$$

$$v_{ren_iq}(t) = \frac{V_{DC}}{2} m_q(t) \quad (5-25)$$

Where, $m_d(t)$ and $m_q(t)$ are the modulation signals and they are given by following equations.

$$m_d = \frac{2}{V_{DC}} (u_d - L_{ren1} \omega_0 i_{ren_iq} + v_{ren_cd}) \quad (5-26)$$

$$m_q = \frac{2}{V_{DC}} (u_q + L_{ren1} \omega_0 i_{ren_id} + v_{ren_cq}) \quad (5-27)$$

By replacing $m_d(t)$ and $m_q(t)$ from equations (5-26) and (5-27) into equations (5-24) and (5-25), the inverter voltage can be written as follows.

$$v_{ren_id}(t) = u_d - L_{ren1} \omega_0 i_{ren_iq} + v_{ren_cd} \quad (5-28)$$

$$v_{ren_iq}(t) = u_q + L_{ren1} \omega_0 i_{ren_id} + v_{ren_cq} \quad (5-29)$$

The control signal u_d and u_q are signal coming from the PI controller, which control the reference current and given by the following equations.

$$u_d = K_{renid} X_{rend_int} + K_{renpd} i_{dref} - K_{renpd} i_{ren_id} \quad (5-30)$$

Where, X_{rend_int} is the internal state of PI controller and is represented by following equation.

$$X_{rend_int} = \int (i_{dref} - i_{ren_id}) dt \quad (5-31)$$

The differential equation of internal state can be represented by equation (5-32).

$$\frac{d}{dt}(X_{rend_int}) = i_{dref} - i_{ren_id} \quad (5-32)$$

Similarly for second PI controller the state space equation can be written as follows.

$$\frac{d}{dt}(X_{renq_int}) = i_{qref} - i_{ren_iq} \quad (5-33)$$

$$u_q = K_{reniq} X_{renq_int} + K_{renpq} i_{qref} - K_{renpq} i_{ren_iq} \quad (5-34)$$

By replacing control signal v_{ren_id} and v_{ren_iq} into equation into equations (5-18) and (5-19), the new equations can be written as follows.

$$\frac{d}{dt}(i_{ren_id}) = -\frac{R_{ren1}}{L_{ren1}} i_{ren_id} + \frac{1}{L_{ren1}} u_d \quad (5-35)$$

$$\frac{d}{dt}(i_{ren_iq}) = -\frac{R_{ren1}}{L_{ren1}} i_{ren_iq} + \frac{1}{L_{ren1}} u_q \quad (5-36)$$

By replacing control signal u_d and u_q into equation (5-35) and (5-36), new set of equation can be derived. The complete close loop state space differential equations of current mode inverter can be rewritten as follows.

$$\frac{d}{dt}(i_{ren_id}) = -\frac{(R_{ren1} + K_{renpd})}{L_{ren1}} i_{ren_id} + \frac{K_{renpd}}{L_{ren1}} i_{dref} + \frac{K_{renid}}{L_{ren1}} X_{rend_int} \quad (5-37)$$

$$\frac{d}{dt}(i_{ren_iq}) = -\frac{(R_{ren1} + K_{renpq})}{L_{ren1}} i_{ren_iq} + \frac{K_{renpq}}{L_{ren1}} i_{qref} + \frac{K_{reniq}}{L_{ren1}} X_{renq_int} \quad (5-38)$$

$$\frac{d}{dt}(X_{rend_int}) = i_{dref} - i_{ren_id} \quad (5-39)$$

$$\frac{d}{dt}(X_{renq_int}) = i_{qref} - i_{ren_iq} \quad (5-40)$$

$$\frac{d}{dt}(v_{ren_cd}) = \omega_0 v_{ren_cq} + \frac{1}{3C_{ren}}(i_{ren_id}) - \frac{1}{3C_{ren}}\left(\frac{N_s}{N_p}\right)(i_{ren_od}) \quad (5-41)$$

$$\frac{d}{dt}(v_{ren_cq}) = -\omega_0 v_{ren_cd} + \frac{1}{3C_{ren}}(i_{ren_iq}) - \frac{1}{3C_{ren}}\left(\frac{N_s}{N_p}\right)(i_{ren_q}) \quad (5-42)$$

$$\frac{d}{dt}(i_{ren_od}) = \omega_0 i_{ren_oq} - \frac{R_{ren2}}{L_{ren2}} i_{ren_od} + \frac{1}{L_{ren2}}\left(\frac{N_p}{N_s}\right)v_{ren_cd} - \frac{1}{L_{ren2}}\left(\frac{N_p}{N_s}\right)^2 v_{ren_od} \quad (5-43)$$

$$\frac{d}{dt}(i_{ren_oq}) = -\omega_0 i_{ren_od} - \frac{R_{ren2}}{L_{ren2}} i_{ren_oq} + \frac{1}{L_{ren2}}\left(\frac{N_p}{N_s}\right)v_{ren_cq} - \frac{1}{L_{ren2}}\left(\frac{N_p}{N_s}\right)^2 v_{ren_oq} \quad (5-44)$$

From equations (5-37) to (5-44), the state space model of current mode inverter for small perturbation can be written as follows.

$$\begin{aligned} \begin{bmatrix} \dot{X}_{ren} \end{bmatrix}_{8 \times 1} &= \begin{bmatrix} A_{ren} \end{bmatrix}_{8 \times 8} * \begin{bmatrix} X_{ren} \end{bmatrix}_{8 \times 1} + \begin{bmatrix} A_{ren_cable} \end{bmatrix}_{8 \times 4} * \begin{bmatrix} X_{cable} \end{bmatrix}_{4 \times 1} \\ &+ \begin{bmatrix} B_{ren} \end{bmatrix}_{8 \times 2} * \begin{bmatrix} U_{ren} \end{bmatrix}_{2 \times 1} \end{aligned} \quad (5-45)$$

Where,

$$X_{ren} = \begin{bmatrix} \Delta i_{ren_id} & \Delta i_{ren_iq} & \Delta X_{rend_int} & \Delta X_{renq_int} & \Delta v_{ren_cd} & \Delta v_{ren_cq} & \Delta i_{ren_od} & \Delta i_{ren_oq} \end{bmatrix}$$

$$X_{cable} = \begin{bmatrix} \Delta v_{ren_od} & \Delta v_{ren_oq} & \Delta i_{cable_d} & \Delta i_{cable_q} \end{bmatrix}$$

$$U_{ren} = \begin{bmatrix} \Delta i_{dref} & \Delta i_{qref} \end{bmatrix}$$

$$A_{ren} = \begin{bmatrix} -\left(\frac{R_{ren1} + K_{renpd}}{L_{ren1}}\right) & 0 & \frac{K_{renid}}{L_{ren1}} & 0 & 0 & 0 & 0 & 0 \\ 0 & -\left(\frac{R_{ren1} + K_{renpq}}{L_{ren1}}\right) & 0 & \frac{K_{reniq}}{L_{ren1}} & 0 & 0 & 0 & 0 \\ -1 & 0 & 0 & 0 & 0 & 0 & 0 & 0 \\ 0 & -1 & 0 & 0 & 0 & 0 & 0 & 0 \\ \frac{1}{3C_{ren}} & 0 & 0 & 0 & 0 & \omega_0 & -\left(\frac{N_s}{N_p}\right)\frac{1}{3C_{ren}} & 0 \\ 0 & \frac{1}{3C_{ren}} & 0 & 0 & -\omega_0 & 0 & 0 & -\left(\frac{N_s}{N_p}\right)\frac{1}{3C_{ren}} \\ 0 & 0 & 0 & 0 & \frac{1}{L_{ren2}}\left(\frac{N_p}{N_s}\right) & 0 & -\frac{R_{ren2}}{L_{ren2}} & \omega_0 \\ 0 & 0 & 0 & 0 & 0 & \frac{1}{L_{ren2}}\left(\frac{N_p}{N_s}\right) & -\omega_0 & -\frac{R_{ren2}}{L_{ren2}} \end{bmatrix}$$

$$A_{ren_cable} = \begin{bmatrix} 0 & 0 & 0 & 0 & 0 & 0 \\ 0 & 0 & 0 & 0 & 0 & 0 \\ 0 & 0 & 0 & 0 & 0 & 0 \\ 0 & 0 & 0 & 0 & 0 & 0 \\ 0 & 0 & 0 & 0 & 0 & 0 \\ 0 & 0 & 0 & 0 & 0 & 0 \\ -\left(\frac{N_p}{N_s}\right)^2 \frac{1}{L_{ren2}} & 0 & 0 & 0 & 0 & 0 \\ 0 & -\left(\frac{N_p}{N_s}\right)^2 \frac{1}{L_{ren2}} & 0 & 0 & 0 & 0 \end{bmatrix} \quad B_{ren} = \begin{bmatrix} \frac{K_{renpd}}{L_{ren1}} & 0 \\ 0 & \frac{K_{renpq}}{L_{ren1}} \\ 1 & 0 \\ 0 & 1 \\ 0 & 0 \\ 0 & 0 \\ 0 & 0 \\ 0 & 0 \end{bmatrix}$$

The LCL parameters of inverter are given below in Table 5-1.

Table 5-1. LCL filter parameters of current mode inverter.

R_{ren1}	0.2 m Ω
L_{ren1}	120 μ H
R_{ren2}	0.12 m Ω
L_{ren2}	18 μ H
C_{ren}	230 μ F

In the derived state space equations for current mode inverter, K_{renpd} , K_{renpq} , K_{renid} , K_{reniq} are the control parameters. The most common reason of stability issue in a microgrid is the feedback controller. The control parameters selected are as follows. $K_{renpd} = K_{renpq} = 0.01$ and $K_{renid} = K_{reniq} = 0.5$.

Figure 5-2 shows the poles and zeros map of current mode inverter state space model. For selected control parameters, the poles and zeros of the state space model of current mode inverters are on the left half plane, which ensures that the current mode inverter is stable.

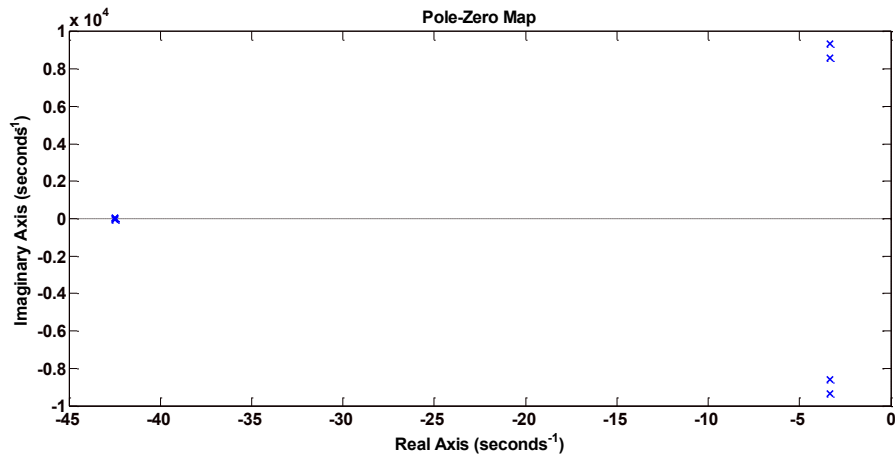


Figure 5-2. Poles and zeros map of current mode inverter state space model.

The step response of from i_{dref} to i_{ren_id} and i_{qref} to i_{ren_iq} reference are shown in Figure 5-3 and Figure 5-4 respectively. For selected control parameters, the settling time in both step responses are 75 millisecond.

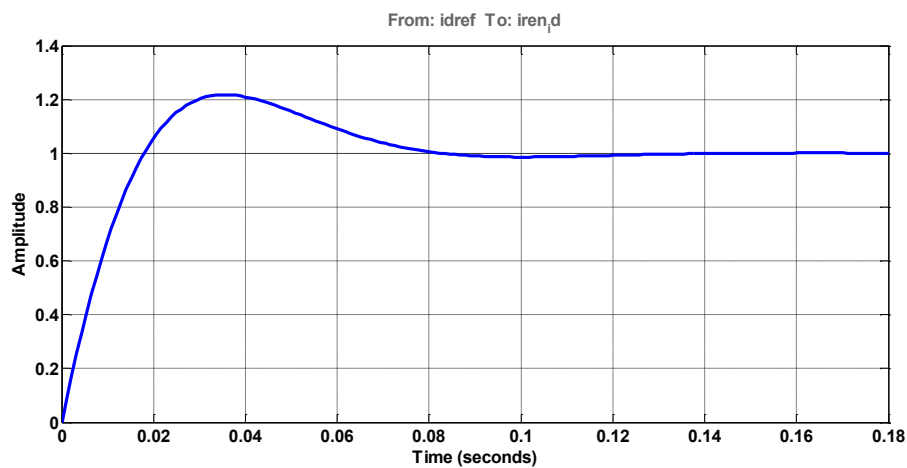


Figure 5-3. Step response from i_{dref} to i_{ren_id}

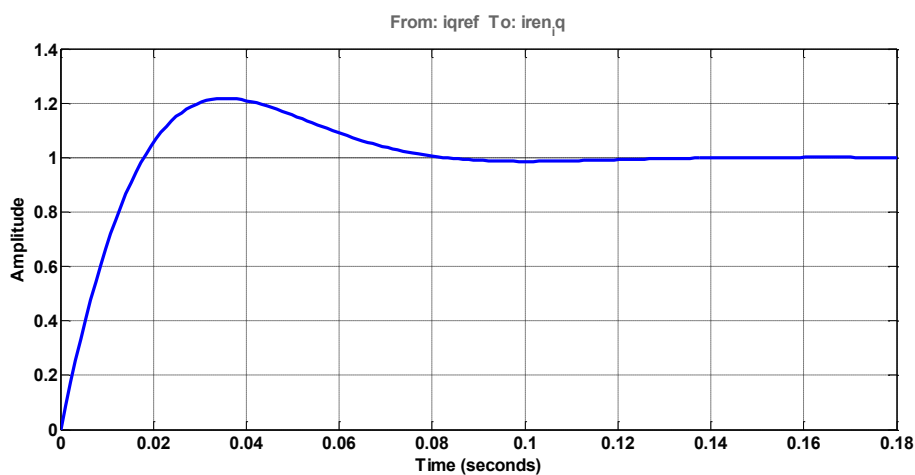


Figure 5-4. Step response from i_{dref} to i_{ren_id}

5.2 State space modeling of Voltage Mode Inverter

In studied microgrid model, only energy storage is utilized voltage mode of operation, the notation used are for energy storage inverter. In actual system the capacitors in LCL filter are connected in delta configuration. In order to make the modeling easy, the capacitors are converted to wye configuration. However, the equivalent capacitance in wye configuration is three times the capacitance in delta configuration. The schematic diagram of voltage mode energy storage system is shown in

Figure 5-5, which is used to derive the state space model of voltage mode inverter.

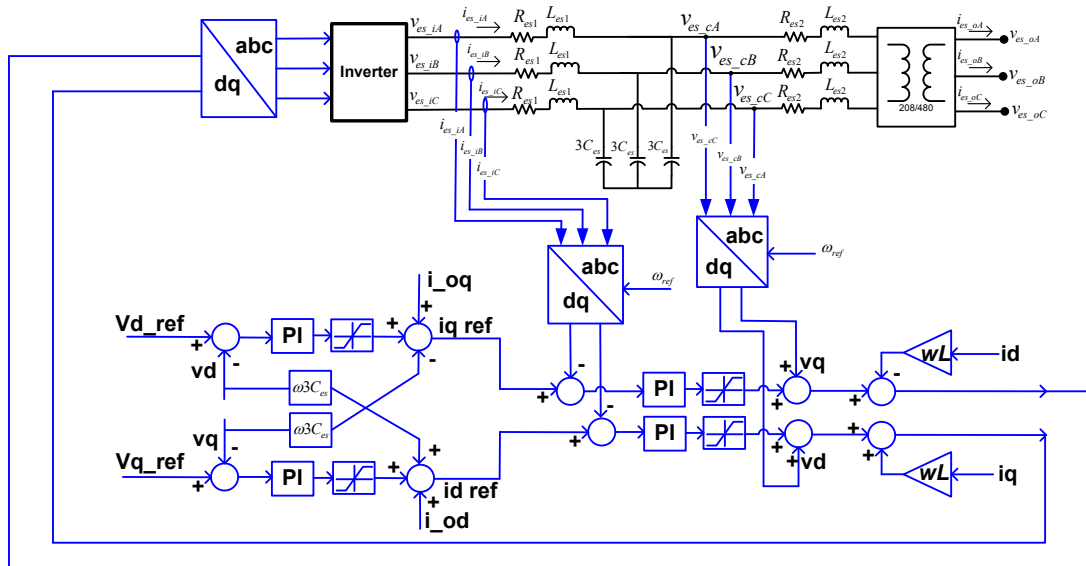


Figure 5-5. Schematic diagram of voltage mode inverter.

The dynamics of the three phase LCL filter with transformer are described by following equations.

$$L_{es1} \frac{d}{dt} (i_{es_iA}) = -R_{es1} i_{es_iA} - v_{es_cA} + v_{es_iA} \quad (5-46)$$

$$L_{es1} \frac{d}{dt} (i_{es_iB}) = -R_{es1} i_{es_iB} - v_{es_cB} + v_{es_iB} \quad (5-47)$$

$$L_{es1} \frac{d}{dt} (i_{es_iC}) = -R_{es1} i_{es_iC} - v_{es_cC} + v_{es_iC} \quad (5-48)$$

$$\frac{d}{dt} (v_{es_cA}) = \frac{1}{3C_{es}} (i_{es_iA}) - \frac{1}{3C_{es}} \left(\frac{N_s}{N_p} \right) (i_{es_oA}) \quad (5-49)$$

$$\frac{d}{dt} (v_{es_cB}) = \frac{1}{3C_{es}} (i_{es_iB}) - \frac{1}{3C_{es}} \left(\frac{N_s}{N_p} \right) (i_{es_oB}) \quad (5-50)$$

$$\frac{d}{dt} (v_{es_cC}) = \frac{1}{3C_{es}} (i_{es_iC}) - \frac{1}{3C_{es}} \left(\frac{N_s}{N_p} \right) (i_{es_oC}) \quad (5-51)$$

$$L_{es2} \frac{d}{dt} (i_{es_oA}) = -R_{es2} i_{es_oA} + \left(\frac{N_p}{N_s} \right) v_{es_cA} - \left(\frac{N_p}{N_s} \right)^2 v_{es_oA} \quad (5-52)$$

$$L_{es2} \frac{d}{dt} (i_{es_oB}) = -R_{es2} i_{es_oB} + \left(\frac{N_p}{N_s} \right) v_{es_cB} - \left(\frac{N_p}{N_s} \right)^2 v_{es_oB} \quad (5-53)$$

$$L_{es2} \frac{d}{dt} (i_{es_oC}) = -R_{es2} i_{es_oC} + \left(\frac{N_p}{N_s} \right) v_{es_cC} - \left(\frac{N_p}{N_s} \right)^2 v_{es_oC} \quad (5-54)$$

The equations in space phasor domain can be written from above equations (5-46) to (5-54) as follows.

$$\frac{d}{dt} (\vec{i}_{es_i}) = -\frac{R_{es1}}{L_{es1}} \vec{i}_{es_i} - \frac{1}{L_{es1}} \vec{v}_{es_c} + \frac{1}{L_{es1}} \vec{v}_{es_i} \quad (5-55)$$

$$\frac{d}{dt} (\vec{v}_{es_c}) = \frac{1}{3C_{es}} (\vec{i}_{es_i}) - \frac{1}{3C_{es}} \left(\frac{N_s}{N_p} \right) (\vec{i}_{es_o}) \quad (5-56)$$

$$\frac{d}{dt} (\vec{i}_{es_o}) = -\frac{R_{es2}}{L_{es2}} \vec{i}_{es_o} + \frac{1}{L_{es2}} \left(\frac{N_p}{N_s} \right) \vec{v}_{es_c} - \frac{1}{L_{es2}} \left(\frac{N_p}{N_s} \right)^2 \vec{v}_{es_o} \quad (5-57)$$

The above space phasor equations can be express into d-q reference frame as follows.

$$\frac{d}{dt}(i_{es_id}) = \omega_0 i_{es_iq} - \frac{R_{es1}}{L_{es1}} i_{es_id} - \frac{1}{L_{es1}} v_{es_cd} + \frac{1}{L_{es1}} v_{es_id} \quad (5-58)$$

$$\frac{d}{dt}(i_{es_iq}) = -\omega_0 i_{es_id} - \frac{R_{es1}}{L_{es1}} i_{es_iq} - \frac{1}{L_{es1}} v_{es_cq} + \frac{1}{L_{es1}} v_{es_iq} \quad (5-59)$$

$$\frac{d}{dt}(v_{es_cd}) = \omega_0 v_{es_cq} + \frac{1}{3C_{es}}(i_{es_id}) - \frac{1}{3C_{es}} \left(\frac{N_s}{N_p} \right) (i_{es_od}) \quad (5-60)$$

$$\frac{d}{dt}(v_{es_cq}) = -\omega_0 v_{es_cd} + \frac{1}{3C_{es}}(i_{es_iq}) - \frac{1}{3C_{es}} \left(\frac{N_s}{N_p} \right) (i_{es_q}) \quad (5-61)$$

$$\frac{d}{dt}(i_{es_od}) = \omega_0 i_{es_oq} - \frac{R_{es2}}{L_{es2}} i_{es_od} + \frac{1}{L_{es2}} \left(\frac{N_p}{N_s} \right) v_{es_cd} - \frac{1}{L_{es2}} \left(\frac{N_p}{N_s} \right)^2 v_{es_od} \quad (5-62)$$

$$\frac{d}{dt}(i_{es_oq}) = -\omega_0 i_{es_od} - \frac{R_{es2}}{L_{es2}} i_{es_oq} + \frac{1}{L_{es2}} \left(\frac{N_p}{N_s} \right) v_{es_cq} - \frac{1}{L_{es2}} \left(\frac{N_p}{N_s} \right)^2 v_{es_oq} \quad (5-63)$$

The voltage V_d is controlled by i_{dref} and V_q is controlled by i_{qref} . The current controlled loop equations can be derived as follows.

$$\frac{d}{dt}(i_{es_id}) = -\frac{(R_{es1} + K_{espld})}{L_{es1}} i_{es_id} + \frac{K_{espld}}{L_{es1}} i_{dref} + \frac{K_{esild}}{L_{es1}} X_{esd1_int} \quad (5-64)$$

$$\frac{d}{dt}(i_{es_iq}) = -\frac{(R_{es1} + K_{esplq})}{L_{es1}} i_{es_iq} + \frac{K_{esplq}}{L_{es1}} i_{qref} + \frac{K_{esilq}}{L_{es1}} X_{esq1_int} \quad (5-65)$$

$$\frac{d}{dt}(X_{esd1_int}) = i_{dref} - i_{es_id} \quad (5-66)$$

$$\frac{d}{dt}(X_{esq1_int}) = i_{qref} - i_{es_iq} \quad (5-67)$$

$$\frac{d}{dt}(v_{es_cd}) = \omega_0 v_{es_cq} + \frac{1}{3C_{es}}(i_{es_id}) - \frac{1}{3C_{es}} \left(\frac{N_s}{N_p} \right) (i_{es_od}) \quad (5-68)$$

$$\frac{d}{dt}(v_{es_cq}) = -\omega_0 v_{es_cd} + \frac{1}{3C_{es}}(i_{es_iq}) - \frac{1}{3C_{es}}\left(\frac{N_s}{N_p}\right)(i_{es_q}) \quad (5-69)$$

$$\frac{d}{dt}(i_{es_od}) = \omega_0 i_{es_oq} - \frac{R_{es2}}{L_{es2}} i_{es_od} + \frac{1}{L_{es2}}\left(\frac{N_p}{N_s}\right)v_{es_cd} - \frac{1}{L_{es2}}\left(\frac{N_p}{N_s}\right)^2 v_{es_od} \quad (5-70)$$

$$\frac{d}{dt}(i_{es_oq}) = -\omega_0 i_{es_od} - \frac{R_{es2}}{L_{es2}} i_{es_oq} + \frac{1}{L_{es2}}\left(\frac{N_p}{N_s}\right)v_{es_cq} - \frac{1}{L_{es2}}\left(\frac{N_p}{N_s}\right)^2 v_{es_oq} \quad (5-71)$$

The current references are derived as follows.

$$i_{dref} = u_d - \omega_0(3 * C_{es})v_{es_cq} + i_{es_od} \quad (5-72)$$

$$i_{qref} = u_q + \omega_0(3 * C_{es})v_{es_cq} + i_{es_oq} \quad (5-73)$$

$$u_d = K_{esid2}X_{esd2_int} + K_{espd2}v_{dref} - K_{espd2}v_{es_cd} \quad (5-74)$$

$$u_q = K_{esiq2}X_{esq2_int} + K_{esq2}v_{qref} - K_{esq2}v_{es_cq} \quad (5-75)$$

$$\frac{d}{dt}(X_{esd2_int}) = v_{dref} - v_{es_cd} \quad (5-76)$$

$$\frac{d}{dt}(X_{esq2_int}) = v_{qref} - v_{es_cq} \quad (5-77)$$

$$i_{dref} = K_{esid2}X_{esd2_int} + K_{espd2}v_{dref} - K_{espd2}v_{es_cd} - \omega_0(3 * C_{es})v_{es_cq} + i_{es_od} \quad (5-78)$$

$$i_{qref} = K_{esiq2}X_{esq2_int} + K_{esq2}v_{qref} - K_{esq2}v_{es_cq} + \omega_0(3 * C_{es})v_{es_cq} + i_{es_oq} \quad (5-79)$$

By replacing the i_{dref} and i_{qref} from into above equations, the complete set of first order differential equation can be written as follows.

$$\begin{aligned} \frac{d}{dt}(i_{es_id}) = & -\frac{(R_{es1} + K_{esp1d})}{L_{es1}}i_{es_id} - \frac{K_{esp1d} * K_{esp2d}}{L_{es1}}v_{es_cd} - \frac{K_{esp1d} * \omega_0(3 * C_{es})}{L_{es1}}v_{es_cq} \\ & + \frac{K_{esid1d}}{L_{es1}}X_{esd1_int} + \frac{K_{esp1d} * K_{esid2}}{L_{es1}}X_{esd2_int} + \frac{K_{esp1d}}{L_{es1}}i_{es_od} + \frac{K_{esp1d} * K_{esp2d}}{L_{es1}}v_{dref} \end{aligned} \quad (5-80)$$

$$\begin{aligned} \frac{d}{dt}(i_{es_iq}) = & -\frac{(R_{es1} + K_{esplq})}{L_{es1}} i_{es_iq} - \frac{K_{esplq} * K_{esp2q}}{L_{es1}} v_{es_cq} + \frac{K_{esplq} * \omega_0 (3 * C_{es})}{L_{es1}} v_{es_cd} \\ & + \frac{K_{es1lq}}{L_{es1}} X_{esq1_int} + \frac{K_{esplq} * K_{esiq2}}{L_{es1}} X_{esq2_int} + \frac{K_{esplq}}{L_{es1}} i_{es_oq} + \frac{K_{esplq} * K_{esp2q}}{L_{es1}} v_{qref} \end{aligned} \quad (5-81)$$

$$\frac{d}{dt}(v_{es_cd}) = \omega_0 v_{es_cq} + \frac{1}{3C_{es}} (i_{es_id}) - \frac{1}{3C_{es}} \left(\frac{N_s}{N_p} \right) (i_{es_od}) \quad (5-82)$$

$$\frac{d}{dt}(v_{es_cq}) = -\omega_0 v_{es_cd} + \frac{1}{3C_{es}} (i_{es_iq}) - \frac{1}{3C_{es}} \left(\frac{N_s}{N_p} \right) (i_{es_oq}) \quad (5-83)$$

$$\begin{aligned} \frac{d}{dt}(X_{esd1_int}) = & K_{esid2} X_{esd2_int} + K_{esp2d} v_{dref} - K_{esp2d} v_{es_cd} \\ & - \omega_0 (3 * C_{es}) v_{es_cq} + i_{es_od} - i_{es_id} \end{aligned} \quad (5-84)$$

$$\begin{aligned} \frac{d}{dt}(X_{esq1_int}) = & K_{esiq2} X_{esq2_int} + K_{espq2} v_{qref} - K_{espq2} v_{es_cq} \\ & + \omega_0 (3 * C_{es}) v_{es_cq} + i_{es_oq} - i_{es_iq} \end{aligned} \quad (5-85)$$

$$\frac{d}{dt}(X_{esd2_int}) = v_{dref} - v_{es_cd} \quad (5-86)$$

$$\frac{d}{dt}(X_{esq2_int}) = v_{qref} - v_{es_cq} \quad (5-87)$$

$$\frac{d}{dt}(i_{es_od}) = \omega_0 i_{es_oq} - \frac{R_{es2}}{L_{es2}} i_{es_od} + \frac{1}{L_{es2}} \left(\frac{N_p}{N_s} \right) v_{es_cd} - \frac{1}{L_{es2}} \left(\frac{N_p}{N_s} \right)^2 v_{es_od} \quad (5-88)$$

$$\frac{d}{dt}(i_{es_oq}) = -\omega_0 i_{es_od} - \frac{R_{es2}}{L_{es2}} i_{es_oq} + \frac{1}{L_{es2}} \left(\frac{N_p}{N_s} \right) v_{es_cq} - \frac{1}{L_{es2}} \left(\frac{N_p}{N_s} \right)^2 v_{es_oq} \quad (5-89)$$

The complete state space model of energy storage is written as follows.

$$\frac{d}{dt} [X_{es}]_{10 \times 1} = [A_{es}]_{10 \times 10} [X_{es}]_{10 \times 1} + [A_{es_cable}]_{10 \times 4} [X_{cable}]_{4 \times 1} + [B_{es}]_{10 \times 2} [U_{es}]_{2 \times 1} \quad (5-90)$$

Where,

$$X_{es} = [\Delta i_{es_id} \quad \Delta i_{es_iq} \quad \Delta v_{es_cd} \quad \Delta v_{es_cq} \quad \Delta X_{esd1_int} \quad \Delta X_{esq1_int} \quad \Delta X_{esd2_int} \quad \Delta X_{esq1_int} \quad \Delta i_{es_od} \quad \Delta i_{es_oq}]$$

$$X_{cable} = [\Delta v_{es_od} \quad \Delta v_{es_oq} \quad \Delta i_{cable_d} \quad \Delta i_{cable_q}]$$

$$U_{ren} = [\Delta v_{dref} \quad \Delta v_{qref}]$$

$$A_{es} = \begin{bmatrix} -\left(\frac{R_{es1} + K_{esp1d}}{L_{es1}}\right) & 0 & -\left(\frac{K_{esp1d} * K_{esp2d}}{L_{es1}}\right) & \frac{K_{esp1d} * \omega_0 * 3C_{es}}{L_{es1}} & \frac{K_{esi1d}}{L_{es1}} & 0 & \frac{K_{esp1d} * K_{esi2d}}{L_{es1}} & 0 & \frac{K_{esp1d}}{L_{es1}} & 0 \\ 0 & -\left(\frac{R_{es1} + K_{esp1q}}{L_{es1}}\right) & \frac{K_{esp1q} * \omega_0 * 3C_{es}}{L_{es1}} & -\left(\frac{K_{esp1q} * K_{esp2q}}{L_{es1}}\right) & 0 & \frac{K_{esi1q}}{L_{es1}} & 0 & \frac{K_{esp1q} * K_{esi2q}}{L_{es1}} & 0 & \frac{K_{esp1q}}{L_{es1}} \\ \frac{1}{3C_{es}} & 0 & 0 & \omega_0 & 0 & 0 & 0 & 0 & -\left(\frac{N_s}{N_p}\right) * \left(\frac{1}{3 * C_{es}}\right) & 0 \\ 0 & \frac{1}{3C_{es}} & -\omega_0 & 0 & 0 & 0 & 0 & 0 & 0 & -\left(\frac{N_s}{N_p}\right) * \left(\frac{1}{3 * C_{es}}\right) \\ -1 & 0 & -K_{esp2d} & -\omega_0 * 3C_{es} & 0 & 0 & K_{esi2d} & 0 & 1 & 0 \\ 0 & -1 & \omega_0 * 3C_{es} & -K_{esp2q} & 0 & 0 & 0 & K_{esi2q} & 0 & 1 \\ 0 & 0 & -1 & 0 & 0 & 0 & 0 & 0 & 0 & 0 \\ 0 & 0 & 0 & -1 & 0 & 0 & 0 & 0 & 0 & 0 \\ 0 & 0 & \frac{1}{L_{es2}} \left(\frac{N_p}{N_s}\right) & 0 & 0 & 0 & 0 & 0 & -\left(\frac{R_{es2}}{L_{es2}}\right) & \omega_0 \\ 0 & 0 & 0 & \frac{1}{L_{es2}} \left(\frac{N_p}{N_s}\right) & 0 & 0 & 0 & 0 & -\omega_0 & -\left(\frac{R_{es2}}{L_{es2}}\right) \end{bmatrix}$$

$$A_{es_cable} = \begin{bmatrix} 0 & 0 \\ 0 & 0 \\ 0 & 0 \\ 0 & 0 \\ 0 & 0 \\ 0 & 0 \\ 0 & 0 \\ 0 & 0 \\ 0 & 0 \\ -\left(\frac{N_p}{N_s}\right)^2 \frac{1}{L_{es2}} & 0 \\ 0 & -\left(\frac{N_p}{N_s}\right)^2 \frac{1}{L_{es2}} & 0 & 0 & 0 & 0 & 0 & 0 & 0 & 0 & 0 & 0 & 0 & 0 & 0 & 0 & 0 & 0 & 0 & 0 & 0 \end{bmatrix}$$

$$B_{es} = \begin{bmatrix} \frac{K_{esp1d} * K_{esp2d}}{L_{es1}} & 0 \\ 0 & \frac{K_{esp1q} * K_{esp2q}}{L_{es1}} \\ 0 & 0 \\ 0 & 0 \\ 0 & 0 \\ K_{esp2d} & 0 \\ 0 & K_{esp2q} \\ 1 & 0 \\ 0 & 1 \\ 0 & 0 \\ 0 & 0 \end{bmatrix}$$

The LCL parameters of inverter are given below in Table 5-2.

Table 5-2. LCL filter parameters of voltage mode inverter.

R_{es1}	0.2 m Ω
L_{es1}	120 μ H
R_{es2}	0.12 m Ω
L_{es2}	18 μ H
C_{ren}	230 μ F

In the derived state space equations for voltage mode inverter, K_{espd1} , K_{espq1} , K_{renid1} , K_{reniq1} , K_{espd2} , K_{espq2} , K_{esid2} , K_{esiq2} are the control parameters. In proposed control system, it is very important to choose these parameters appropriately to ensure the microgrid stability in any load conditions. The control parameters selected are as follows. $K_{espd1} = K_{espq1} = 0.04$, $K_{renid1} = K_{reniq1} = 10$, $K_{espd2} = K_{espq2} = 0.13$ and $K_{esid2} = K_{esiq2} = 3$.

Figure 5-6 shows the poles and zeros map of voltage mode inverter state space model. For selected control parameters, the poles and zeros of the state space model of voltage mode inverters are on the left half plane, which ensures that the voltage mode inverter is stable.

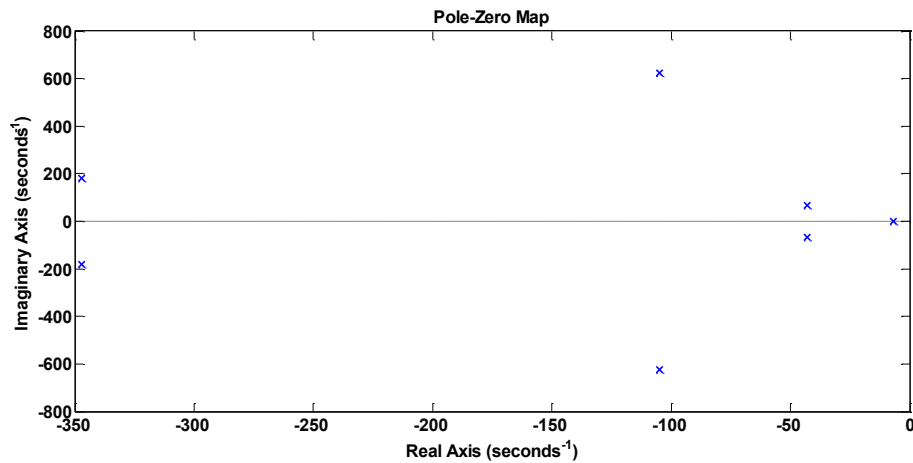


Figure 5-6. Poles and zeros map of voltage mode inverter state space model.

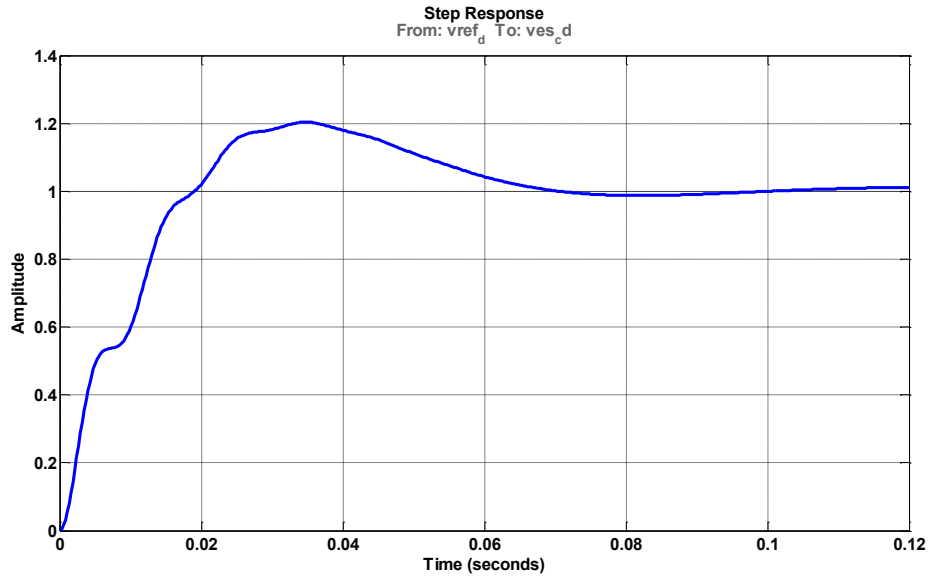


Figure 5-7. Step response from v_{dref} to ves_{cd}

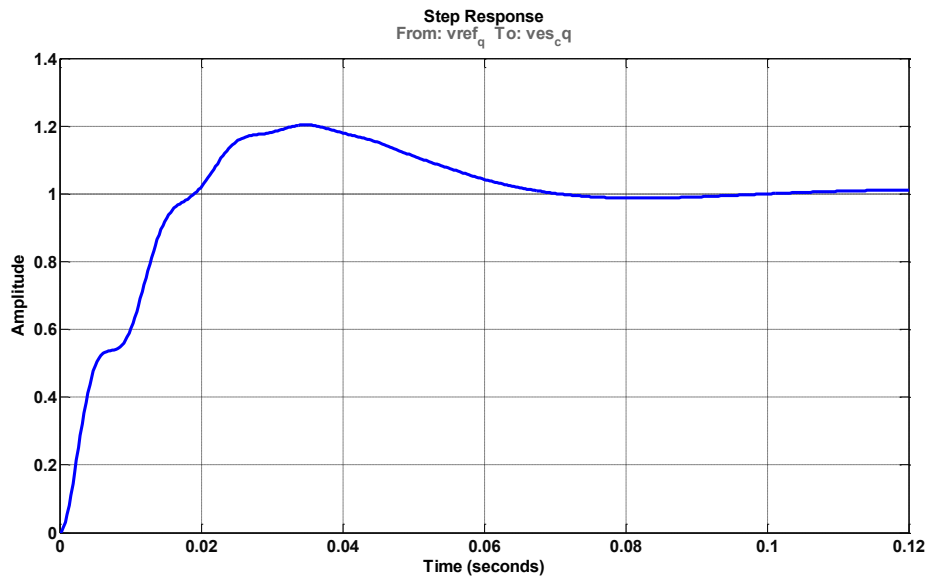


Figure 5-8. Step response from v_{qref} to ves_{cq}

5.3 Natural gas generator state space modelling

Natural gas generator performs vital role in microgrid when SOC of energy storage system is not enough and renewable resources do not generate enough power to supply microgrid load. When natural gas generator is synchronized and connected to microgrid, the stability of the microgrid is crucial due to different time responses of generators and energy storage system. Hence natural gas generator is very important to taken into consideration for stability studies. In this section, the state space model of natural gas generator is derived.

5.3.1 Mechanical system state space modeling

The equations of central importance in stability analysis are rotational inertia equations describing the effect of unbalance between the electromagnetic torque and the mechanical torque of synchronous machine. These equations are called swing equations, which are given by (5-91) and (5-92).

$$J \frac{d\omega_r}{dt} = T_m - T_e \quad (5-91)$$

Where,

T_m = mechanical torque in N-m

T_e = electromagnetic torque

J = combined moment of inertia of generator and turbine, kg-m²

ω_r = angular velocity of the rotor, mechanical radian/second

$$\frac{d\delta}{dt} = \omega_r - \omega_0 = \Delta\omega_r \quad (5-92)$$

The equation can be normalized in terms of per unit inertia constant H, which is given by equation (5-93).

$$H = \frac{1}{2} J \frac{\omega_{0m}^2}{VA_{base}} \quad (5-93)$$

Where,

ω_{0m} = Rated angular velocity in mechanical radian/second

From equation (5-93) the following equation can be written

$$J = 2H \frac{VA_{base}}{\omega_{0m}^2} \quad (5-94)$$

From equations (5-91) and (5-94), the per-unit equation can be derived as follows.

$$2H \frac{VA_{base}}{\omega_{0m}^2} \frac{d\omega_r}{dt} = T_m - T_e$$

$$2H \frac{d}{dt} \left(\frac{\omega_r}{\omega_{0m}} \right) = \frac{T_m - T_e}{\frac{VA_{base}}{\omega_{0m}}}$$

$$2H \frac{d\bar{\omega}_r}{dt} = \bar{T}_m - \bar{T}_e \quad (5-95)$$

The rotor angle in per unit is given by equation (5-96).

$$\frac{d\delta}{dt} = \omega_o \Delta \bar{\omega}_r \quad (5-96)$$

The swing equations in per unit can be linearized and represented as a set of first order differential equations, which are given by equations (5-97) and (5-98).

$$\frac{d\Delta \bar{\omega}_r}{dt} = \frac{1}{2H} \Delta \bar{T}_m - \frac{1}{2H} \Delta \bar{T}_e \quad (5-97)$$

$$\frac{d\Delta \delta}{dt} = \omega_o \Delta \bar{\omega}_r \quad (5-98)$$

It is desired to add the dynamics of natural gas engine, governor, fuel value and control system into the mathematical modeling to accurately study the behavior of natural gas generator. The complete mechanical systems is shown in Figure 5-9.

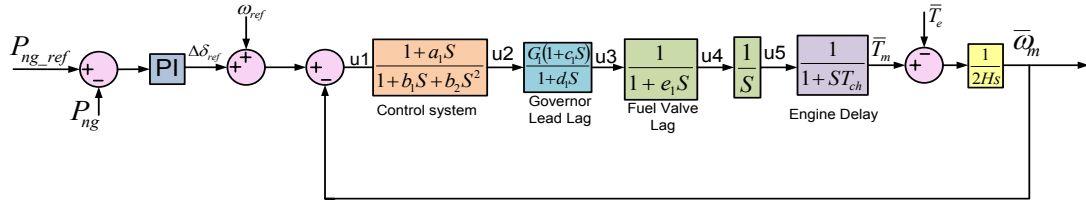


Figure 5-9. The complete mechanical system

The natural gas generator operates in power control mode. In order to increase the power output, the mechanical torque has to be increased.

The speed reference for governor system is $\omega_{ref} + \Delta\delta_{ref}$, where ω_{ref} is the speed reference and $\Delta\delta_{ref}$ is received from the PI controller to control the reference power.

$$\Delta\delta_{ref} = K_{i_Png} X_{Png_int} + K_{p_Png} P_{ng_ref} - K_{p_Png} P_{ng} \quad (5-99)$$

Where, X_{Png_int} is the internal state of PI controller and is represented by following equation.

$$X_{png_int} = \int (P_{ng_ref} - P_{ng}) dt \quad (5-100)$$

The differential equation of internal state can be represented by following equation.

$$\frac{d}{dt} (X_{Png_int}) = P_{ng_ref} - P_{ng} \quad (5-101)$$

For small perturbation, the equation (5-101) can be written as follows.

$$\frac{d}{dt} (\Delta X_{Png_int}) = \Delta P_{ng_ref} - \Delta P_{ng} \quad (5-102)$$

Active power output of natural gas generator is given by following equation.

$$P_{ng} = e_{ng_od} i_{ng_od} + e_{ng_oq} i_{ng_oq} \quad (5-103)$$

After linearizing the above equation, linearized equation can be written as follows.

$$\Delta P_{ng} = E_{ng_od} \Delta i_{ng_od} + I_{ng_od} \Delta e_{ng_od} + E_{ng_oq} \Delta i_{ng_oq} + \Delta e_{ng_oq} I_{ng_oq} \quad (5-104)$$

By replacing ΔP_{ng} from equation (5-104) into equation (5-102), the new equation can be written as follows.

$$\frac{d}{dt}(\Delta X_{Png_int}) = \Delta P_{ng_ref} - E_{ng_od} \Delta i_{ng_od} - I_{ng_od} \Delta e_{ng_od} - E_{ng_oq} \Delta i_{ng_oq} - \Delta e_{ng_oq} I_{ng_oq} \quad (5-105)$$

The input signal to the governor control system is given by following equation.

$$u_1 = \omega_{ref} + K_{i_Png} X_{Png_int} + K_{p_Png} P_{ng_ref} - K_{p_Png} P_{ng} - \omega_r \quad (5-106)$$

The transfer function of the control system is given by following equations.

$$\frac{u_2}{u_1} = \frac{1 + a_1 s}{1 + b_1 s + b_2 s^2} * \frac{x_{c1}}{x_{c1}} \quad (5-107)$$

The states of the control system are $x_{c1} = x_{c1}$ and $x_{c2} = \dot{x}_{c1}$. The state space equations for control system can be written as follows.

$$\frac{d}{dt}(x_{c2}) = -\frac{1}{b_2} x_{c1} - \frac{b_1}{b_2} x_{c2} + \frac{1}{b_2} u_1 \quad (5-108)$$

$$\frac{d}{dt}(x_{c1}) = x_{c2} \quad (5-109)$$

By replacing u_1 from equation (5-106) into equation (5-108), the new first order differential equation can be written as follows.

$$\frac{d}{dt}(x_{c2}) = -\frac{1}{b_2} x_{c1} - \frac{b_1}{b_2} x_{c2} + \frac{\omega_{ref}}{b_2} + \frac{K_{i_Png}}{b_2} X_{Png_int} + \frac{K_{p_Png}}{b_2} P_{ng_ref} - \frac{K_{p_Png}}{b_2} P_{ng} - \frac{1}{b_2} \bar{\omega}_r \quad (5-110)$$

The output equation is given by

$$u_2 = x_{c1} + a_1 x_{c2} \quad (5-111)$$

For small perturbation, equation (5-109) and (5-110) can be rewritten as follows.

$$\frac{d}{dt}(\Delta x_{c1}) = \Delta x_{c2} \quad (5-112)$$

$$\frac{d}{dt}(\Delta x_{c2}) = -\frac{1}{b_2} \Delta x_{c1} - \frac{b_1}{b_2} \Delta x_{c2} + \frac{1}{b_2} \Delta \omega_{ref} + \frac{K_{i_Png}}{b_2} \Delta X_{Png_int} + \frac{K_{p_Png}}{b_2} \Delta P_{ng_ref} - \frac{K_{p_Png}}{b_2} \Delta P_{ng} - \frac{1}{b_2} \Delta \bar{\omega}_r \quad (5-113)$$

By replacing ΔP_{ng} from equation (5-104) into equation (5-113), the equation can be rewritten as follows.

$$\begin{aligned} \frac{d}{dt}(\Delta x_{c2}) = & -\frac{1}{b_2} \Delta x_{c1} - \frac{b_1}{b_2} \Delta x_{c2} + \frac{1}{b_2} \Delta \omega_{ref} - \frac{1}{b_2} \Delta \bar{\omega}_r + \frac{K_{i_Png}}{b_2} \Delta X_{Png_int} + \frac{K_{p_Png}}{b_2} \Delta P_{ng_ref} \\ & - \frac{K_{p_Png}}{b_2} E_{ng_od} \Delta i_{ng_od} - \frac{K_{p_Png}}{b_2} I_{ng_od} \Delta e_{ng_od} - \frac{K_{p_Png}}{b_2} E_{ng_oq} \Delta i_{ng_oq} - \frac{K_{p_Png}}{b_2} \Delta e_{ng_oq} I_{ng_oq} \end{aligned} \quad (5-114)$$

The state space equation for governor lead lag can be written as follows. By multiplying both numerator and denominator by x_{g1} ,

$$\frac{u_3}{u_2} = \frac{G_1(1 + c_1 s)}{1 + d_1 s} * \frac{x_{g1}}{x_{g1}} \quad (5-115)$$

From above transfer functions, the following equation can be written.

$$u_2 = (1 + d_1 s) x_{g1} \quad (5-116)$$

$$u_2 = x_{g1} + d_1 \frac{d}{dt}(x_{g1}) \quad (5-117)$$

The states of the governor lead lag are x_{g1} and $x_{g2} = \dot{x}_{g1}$ and the state space equation can be written as follows.

$$\frac{d}{dt}(x_{g1}) = -\frac{1}{d_1} x_{g1} + \frac{1}{d_1} u_2 \quad (5-118)$$

By replacing u_2 from equation (5-111) into equation (5-118), the new equation can be written as follows.

$$\frac{d}{dt}(x_{g1}) = \frac{1}{d_1} x_{c1} + \frac{a_1}{d_1} x_{c2} - \frac{1}{d_1} x_{g1} \quad (5-119)$$

$$\frac{d}{dt}(x_{g2}) = 0 \quad (5-120)$$

The above governor lead lag differential equations can be written for small perturbation as follows.

$$\frac{d}{dt}(\Delta x_{g1}) = \frac{1}{d_1} \Delta x_{c1} + \frac{a_1}{d_1} \Delta x_{c2} - \frac{1}{d_1} \Delta x_{g1} \quad (5-121)$$

$$\frac{d}{dt}(\Delta x_{g2}) = 0 \quad (5-122)$$

Similarly, the output equation can be written as follows.

$$u_3 = G_1 x_{g1} + c_1 G_1 x_{g2} \quad (5-123)$$

The transfer function of the fuel valve lag is given by following equations.

$$\frac{u_4}{u_3} = \frac{1}{1 + e_1 s} \quad (5-124)$$

From the transfer function, the state space equation of fuel valve can be written as follows.

$$\frac{d}{dt}(u_4) = -\frac{1}{e_1} u_4 + \frac{1}{e_1} u_3 \quad (5-125)$$

By replacing u_3 from equation (5-123) into above equation (5-125), the new state space equation can be written as follows.

$$\frac{d}{dt}(u_4) = \frac{G_1}{e_1} x_{g1} + \frac{G_1 c_1}{e_1} x_{g2} - \frac{1}{e_1} u_4 \quad (5-126)$$

The integrator transfer function is given by following equation.

$$u_5 = \frac{1}{s} u_4 \quad (5-127)$$

The state space equation of the integrator can be given as follows.

$$\frac{d}{dt}(u_5) = u_4 \quad (5-128)$$

The transfer function of engine delay is given by the following equation.

$$\frac{\bar{T}_m}{u_5} = \frac{1}{1 + T_{ch} s} \quad (5-129)$$

From the transfer function the state space equation can be written as follows.

$$\frac{d}{dt}(\bar{T}_m) = -\frac{1}{T_{ch}} \bar{T}_m + \frac{1}{T_{ch}} u_5 \quad (5-130)$$

For small perturbation, the first order differential equations (5-126), (5-128) and (5-130) can be written as follows.

$$\frac{d}{dt}(\Delta u_4) = \frac{G_1}{e_1} \Delta x_{g1} + \frac{G_1 c_1}{e_1} \Delta x_{g2} - \frac{1}{e_1} \Delta u_4 \quad (5-131)$$

$$\frac{d}{dt}(\Delta u_5) = \Delta u_4 \quad (5-132)$$

$$\frac{d}{dt}(\Delta \bar{T}_m) = -\frac{1}{T_{ch}} \Delta \bar{T}_m + \frac{1}{T_{ch}} \Delta u_5 \quad (5-133)$$

The mechanical torque into the swing equation is determined from the mechanical system described above. However, it is necessary to feed electromagnetic torque into the swing equation for complete system. By assuming the speed constant the electrical power is equal to electromagnetic torque in per unit. Hence the electromagnetic torque is given by following equation.

$$\bar{T}_e = P_{ng} = e_{ng_od} i_{ng_od} + e_{ng_oq} i_{ng_oq} \quad (5-134)$$

By linearizing above equation, the small perturbation equation can be written as follows.

$$\Delta T_{ng} = E_{ng_od} \Delta i_{ng_od} + I_{ng_od} \Delta e_{ng_od} + E_{ng_oq} \Delta i_{ng_oq} + \Delta e_{ng_oq} I_{ng_oq} \quad (5-135)$$

By replacing ΔT_{ng} from equation (5-135) into swing equation (5-97), new first order differential equations can be derived, which is given by following equation.

$$\begin{aligned} \frac{d\Delta \bar{\omega}_r}{dt} &= \frac{1}{2H} \Delta \bar{T}_m - \frac{E_{ng_od}}{2H} \Delta i_{ng_od} \\ &- \frac{I_{ng_od}}{2H} \Delta e_{ng_od} - \frac{E_{ng_oq}}{2H} \Delta i_{ng_oq} - \frac{I_{ng_oq}}{2H} \Delta e_{ng_oq} \end{aligned} \quad (5-136)$$

$$\frac{d\Delta \delta}{dt} = \omega_o \Delta \bar{\omega}_r \quad (5-137)$$

$$A_{mech_stator} = \begin{bmatrix} -E_{ng_od} & -E_{ng_oq} \\ 0 & 0 \\ -\frac{K_{p_Png}}{b_2} E_{ng_od} & -\frac{K_{p_Png}}{b_2} E_{ng_oq} \\ 0 & 0 \\ 0 & 0 \\ 0 & 0 \\ 0 & 0 \\ 0 & 0 \\ -\frac{E_{ng_od}}{2H} & -\frac{E_{ng_oq}}{2H} \\ 0 & 0 \end{bmatrix}$$

$$A_{mech_cable} = \begin{bmatrix} -I_{ng_od} & -I_{ng_oq} \\ 0 & 0 \\ -\frac{K_{p_Png}}{b_2} I_{ng_od} & -\frac{K_{p_Png}}{b_2} I_{ng_oq} \\ 0 & 0 \\ 0 & 0 \\ 0 & 0 \\ 0 & 0 \\ 0 & 0 \\ -\frac{I_{ng_od}}{2H} & -\frac{I_{ng_oq}}{2H} \\ 0 & 0 \end{bmatrix}$$

$$B_{mech} = \begin{bmatrix} 1 & 0 & 0 & 0 \\ 0 & 0 & 0 & 0 \\ \frac{K_{p_Png}}{b_2} & \frac{1}{b_2} & 0 & 0 \\ 0 & 0 & 0 & 0 \\ 0 & 0 & 0 & 0 \\ 0 & 0 & 0 & 0 \\ 0 & 0 & 0 & 0 \\ 0 & 0 & 0 & 0 \\ 0 & 0 & 0 & 0 \\ 0 & 0 & 0 & 0 \end{bmatrix}$$

The selected parameters for mechanical system are given in Table 5-3.

Table 5-3. Parameters of mechanical system of natural gas generator.

a_1	0.45
b_1	0.02
b_2	0.002
G_1	1
c_1	0.25
d_1	0.009
e_1	0.0384
T_{ch}	0.025

To analyze the stability of the mechanical system, state space model is analyzed.

From state space model, pole-zero map is derived, which is shown in Figure 5-10.

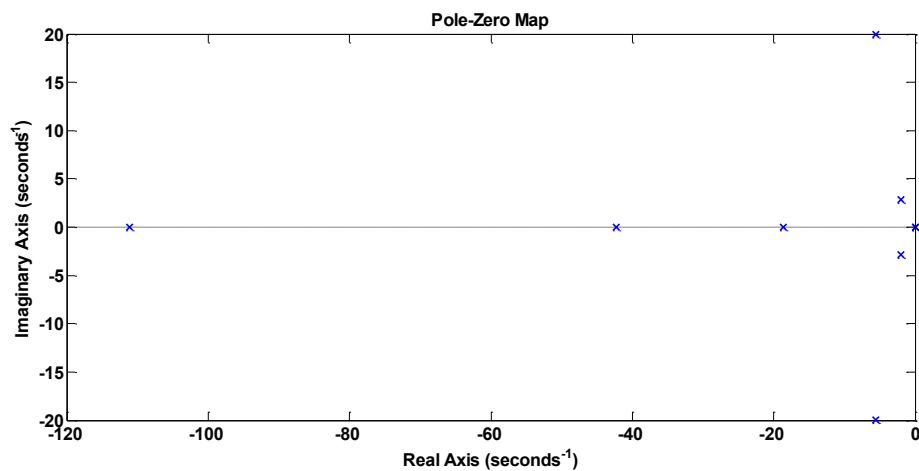


Figure 5-10. Poles and zeros map of mechanical system of natural gas generator.

The poles and zeros of mechanical system are in the left half plane which ensure the stability of the mechanical system. The step response from ω_{dref} to ω is shown in Figure 5-11 and the settling time of step responses is 2.19 second. The higher settling time is due to the mechanical inertia.

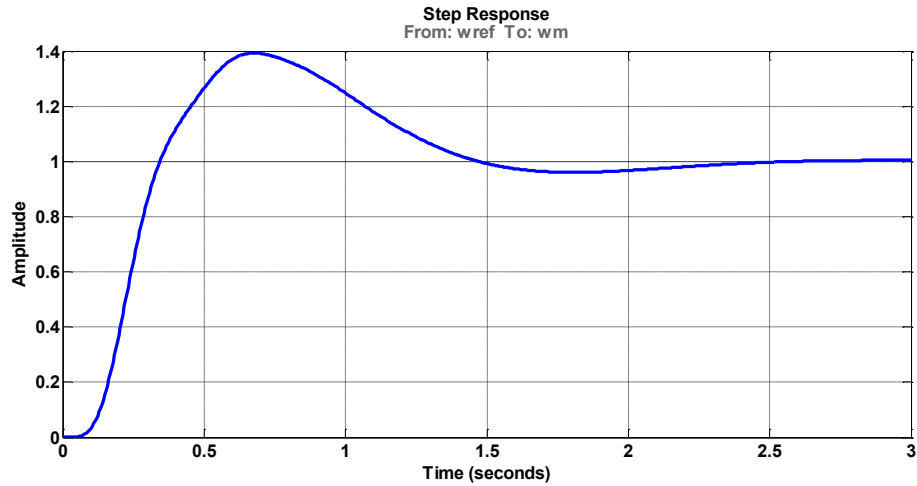


Figure 5-11. Step response from ω_{dref} to ω .

5.3.2 Exciter state space modeling

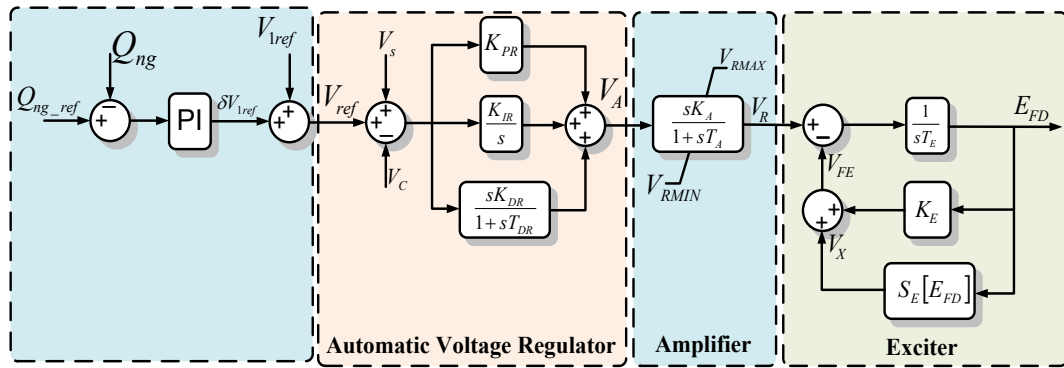


Figure 5-12. Block diagram of excitation system

The complete block diagram of excitation system is shown in Figure 5-12. From the block diagram it is observed that the voltage reference for AVR system is $\delta V_{1ref} + V_{1ref}$, where the V_{1ref} voltage reference and δV_{1ref} is received from the PI controller to control the reference reactive power. The state space equation of PI controller and output of PI is given by following equations.

$$\delta V_{1ref} = K_{Qng_i} X_{Qng_int} + K_{Qng_d} Q_{ng_ref} - K_{Qng_d} Q_{ng} \tag{5-139}$$

Where, X_{Qng_int} is an internal state of PI controller

$$\frac{d}{dt}(X_{Q_{ng_int}}) = Q_{ng_ref} - Q_{ng} \quad (5-140)$$

$$V_{ref} = V_{1ref} + \delta V_{1ref} \quad (5-141)$$

$$V_{ref} = V_{1ref} + K_{Q_{ng_i}} X_{Q_{ng_int}} + K_{Q_{ng_d}} Q_{ng_ref} - K_{Q_{ng_d}} Q_{ng} \quad (5-142)$$

Equation (5-140) can be written in small perturbation as follows.

$$\frac{d}{dt}(\Delta X_{Q_{ng_int}}) = \Delta Q_{ng_ref} - \Delta Q_{ng} \quad (5-143)$$

Active power output of natural gas generator is given by following equation.

$$Q_{ng} = e_{ng_od} i_{ng_oq} + e_{ng_oq} i_{ng_od} \quad (5-144)$$

After linearizing the above equation, linearized equation can be written as follows.

$$\Delta Q_{ng} = E_{ng_od} \Delta i_{ng_oq} + I_{ng_oq} \Delta e_{ng_od} + E_{ng_oq} \Delta i_{ng_od} + \Delta e_{ng_oq} I_{ng_od} \quad (5-145)$$

By replacing ΔQ_{ng} into equation (5-159), the new equation can be written as follows.

$$\begin{aligned} \frac{d}{dt}(\Delta X_{Q_{ng_int}}) = & \Delta Q_{ng_ref} - E_{ng_od} \Delta i_{ng_oq} - I_{ng_oq} \Delta e_{ng_od} \\ & - E_{ng_oq} \Delta i_{ng_od} - \Delta e_{ng_oq} I_{ng_od} \end{aligned} \quad (5-146)$$

The transfer function of AVR system is given by following equation.

$$\frac{V_A}{V_{ref} - V_c} = K_{PR} + \frac{K_{IR}}{s} + \frac{sK_{DR}}{1 + sT_{DR}} \quad (5-147)$$

$$\frac{V_A}{V_{ref} - V_c} = \frac{(K_{PR} T_{DR} + K_{DR})s^2 + (K_{PR} + K_{IR} T_{DR})s + K_{IR}}{s + s^2 T_{DR}} \quad (5-148)$$

By multiplying the numerator and denominator by x_{a1} , two equation can be written as follows.

$$V_A = (K_{PR} T_{DR} + K_{DR})s^2 * x_{a1} + (K_{PR} + K_{IR} T_{DR})s * x_{a1} + K_{IR} * x_{a1} \quad (5-149)$$

$$V_{ref} - V_c = s * x_{a1} + T_{DR} s^2 * x_{a1} \quad (5-150)$$

The states of the AVR system are x_{a1} , $x_{a2} = \dot{x}_{a1}$ and $x_{a3} = \dot{x}_{a2}$. By replacing V_{ref} The first order differential and output equations can be written as follows.

$$\frac{d}{dt}(x_{a1}) = x_{a2} \quad (5-151)$$

$$\frac{d}{dt}(x_{a2}) = -\frac{1}{T_{DR}}x_{a2} - \frac{1}{T_{DR}}V_c + \frac{1}{T_{DR}}V_{1ref} + \frac{K_{Qng-i}}{T_{DR}}X_{Qng-int} + \frac{K_{Qng-d}}{T_{DR}}Q_{ng-ref} - \frac{K_{Qng-d}}{T_{DR}}Q_{ng} \quad (5-152)$$

$$\frac{d}{dt}(x_{a3}) = 0 \quad (5-153)$$

$$V_A = (K_{PR}T_{DR} + K_{DR})x_{a3} + (K_{PR} + K_{IR}T_{DR})x_{a2} + K_{IR}x_{a1} \quad (5-154)$$

For small perturbation, differential equation (5-151), (5-152) and (5-153) can be written as follows.

$$\frac{d}{dt}(\Delta x_{a1}) = \Delta x_{a2} \quad (5-155)$$

$$\begin{aligned} \frac{d}{dt}(\Delta x_{a2}) = & -\frac{1}{T_{DR}}\Delta x_{a2} - \frac{1}{T_{DR}}\Delta V_c + \frac{1}{T_{DR}}\Delta V_{1ref} \\ & + \frac{K_{Qng-i}}{T_{DR}}\Delta X_{Qng-int} + \frac{K_{Qng-d}}{T_{DR}}\Delta Q_{ng-ref} - \frac{K_{Qng-d}}{T_{DR}}\Delta Q_{ng} \end{aligned} \quad (5-156)$$

$$\frac{d}{dt}(\Delta x_{a3}) = 0 \quad (5-157)$$

By replacing ΔQ_{ng} into equation (5-156), the new equation can be written as follows.

$$\begin{aligned} \frac{d}{dt}(\Delta x_{a2}) = & -\frac{1}{T_{DR}}\Delta x_{a2} - \frac{1}{T_{DR}}\Delta V_c + \frac{1}{T_{DR}}\Delta V_{1ref} \\ & + \frac{K_{Qng-i}}{T_{DR}}\Delta X_{Qng-int} + \frac{K_{Qng-d}}{T_{DR}}\Delta Q_{ng-ref} - \frac{K_{Qng-d}}{T_{DR}}E_{ng-od}\Delta i_{ng-oq} \\ & - \frac{K_{Qng-d}}{T_{DR}}I_{ng-oq}\Delta e_{ng-od} - \frac{K_{Qng-d}}{T_{DR}}E_{ng-oq}\Delta i_{ng-od} - \frac{K_{Qng-d}}{T_{DR}}\Delta e_{ng-oq}I_{ng-od} \end{aligned} \quad (5-158)$$

The transfer function of the amplifier is given by following equation.

$$\frac{V_R}{V_A} = \frac{K_A}{1 + sT_A} \quad (5-159)$$

By replacing V_A from equation (5-154) into equation (5-159), the first order differential and output equations can be written as follows.

$$\frac{d}{dt}(V_R) = \frac{K_A K_{IR}}{T_A} x_{a1} + \frac{K_A (K_{PR} + K_{IR} T_{DR})}{T_A} x_{a2} + \frac{K_A (K_{PR} T_{DR} + K_{DR})}{T_A} x_{a3} - \frac{1}{T_A} V_R \quad (5-160)$$

For small perturbation, differential equations (5-160) can be written as follows.

$$\frac{d}{dt}(\Delta V_R) = \frac{K_A K_{IR}}{T_A} \Delta x_{a1} + \frac{K_A (K_{PR} + K_{IR} T_{DR})}{T_A} \Delta x_{a2} + \frac{K_A (K_{PR} T_{DR} + K_{DR})}{T_A} \Delta x_{a3} - \frac{1}{T_A} \Delta V_R \quad (5-161)$$

The transfer function of the exciter is given by following equation.

$$\frac{E_{FD}}{V_R} = \frac{K_E}{1 + sT_E} \quad (5-162)$$

The first order differential equation can be derived as follows.

$$\frac{d}{dt}(E_{FD}) = \frac{K_E}{T_E} V_R - \frac{1}{T_E} E_{FD} \quad (5-163)$$

For small perturbation, differential equation (5-163) can be written as follows.

$$\frac{d}{dt}(\Delta E_{FD}) = \frac{K_E}{T_E} \Delta V_R - \frac{1}{T_E} \Delta E_{FD} \quad (5-164)$$

Now, the open circuit transfer function of the generator field is given by equation as follows.

$$\frac{V_c}{E_{FD}} = \frac{1}{1 + sT'_{do}} \quad (5-165)$$

Where,

$$T'_{do} = \frac{L_{ad} + L_{fd}}{R_{fd}}$$

From equation, the first order differential equation can be given as follows.

$$\frac{d}{dt}(V_c) = -\frac{1}{T'_{d0}}V_c + \frac{1}{T'_{d0}}E_{FD} \quad (5-166)$$

For small perturbation, for the above first order differential equation can be written as follows.

$$\frac{d}{dt}(\Delta V_c) = -\frac{1}{T'_{d0}}\Delta V_c + \frac{1}{T'_{d0}}\Delta E_{FD} \quad (5-167)$$

From above small perturbation equations, the state space equation for exciter system can be written as follows.

$$\begin{aligned} \frac{d}{dt}[X_{exciter}]_{7 \times 1} &= [A_{exciter}]_{7 \times 7} * [X_{exciter}]_{7 \times 1} + [A_{exciter_stator}]_{7 \times 2} * [X_{stator}]_{2 \times 2} \\ &+ [A_{exciter_cable}]_{7 \times 2} * [X_{cable}]_{7 \times 2} + [B_{exciter}]_{7 \times 2} * [U_{exciter}]_{2 \times 2} \end{aligned} \quad (5-168)$$

Where,

$$X_{exciter} = [\Delta X_{Qng_int} \quad \Delta x_{a1} \quad \Delta x_{a2} \quad \Delta x_{a3} \quad \Delta V_R \quad \Delta E_{FD} \quad \Delta V_c]$$

$$X_{stator} = [\Delta i_{ng_od} \quad \Delta i_{ng_oq}]$$

$$X_{cable} = [\Delta v_{ng_od} \quad \Delta v_{ng_oq} \quad \Delta i_{cable_d} \quad \Delta i_{cable_q}]$$

$$U_{exciter} = [\Delta Q_{ng_ref} \quad \Delta V_{ref}]$$

$$A_{exciter} = \begin{bmatrix} 0 & 0 & 0 & 0 & 0 & 0 & 0 \\ 0 & 0 & 1 & 0 & 0 & 0 & 0 \\ \frac{K_{Qng_d}}{T_{DR}} & 0 & -\frac{1}{T_{DR}} & 0 & 0 & 0 & 0 \\ 0 & 0 & 0 & 0 & 0 & 0 & 0 \\ 0 & \frac{K_A K_{IR}}{T_A} & \frac{K_A (K_{PR} + K_{IR} T_{DR})}{T_A} & \frac{K_A (K_{PR} T_{DR} + K_{DR})}{T_A} & -\frac{1}{T_A} & 0 & 0 \\ 0 & 0 & 0 & 0 & \frac{K_E}{T_E} & -\frac{1}{T_E} & 0 \\ 0 & 0 & 0 & 0 & 0 & \frac{1}{T'_{do}} & -\frac{1}{T'_{do}} \end{bmatrix}$$

$$A_{exciter_stator} = \begin{bmatrix} -E_{ng_oq} & -E_{ng_od} \\ 0 & 0 \\ \frac{K_{p_Qng} * E_{ng_oq}}{T_{DR}} & \frac{K_{p_Qng} * E_{ng_od}}{T_{DR}} \\ 0 & 0 \\ 0 & 0 \\ 0 & 0 \\ 0 & 0 \end{bmatrix}$$

$$A_{exciter_cable} = \begin{bmatrix} -I_{ng_oq} & -I_{ng_od} \\ 0 & 0 \\ -\frac{K_{Qng_d}}{T_{DR}} I_{ng_oq} & -\frac{K_{Qng_d}}{T_{DR}} I_{ng_od} \\ 0 & 0 \\ 0 & 0 \\ 0 & 0 \\ 0 & 0 \end{bmatrix} \quad B_{exciter} = \begin{bmatrix} 1 & 0 \\ 0 & 0 \\ \frac{K_{Qng_d}}{T_{DR}} & \frac{1}{T_{DR}} \\ 0 & 0 \\ 0 & 0 \\ 0 & 0 \\ 0 & 0 \end{bmatrix}$$

The selected parameters for electrical system are given in Table 5-3.

Table 5-4. Parameters of excitation system of natural gas generator.

TDR	0.002011
KDR	1.266049
KIR	2.270138
KPR	1.0129
KA	1.0
TA	0.1
KE	1.0
TE	0.5
Tdo'	1.6

To analyze the stability of the exciter system, pole-zero map is derived from state space model, which is shown in Figure 5-15. The poles and zeros of mechanical system are in the left half plane which ensure the stability of the mechanical system.

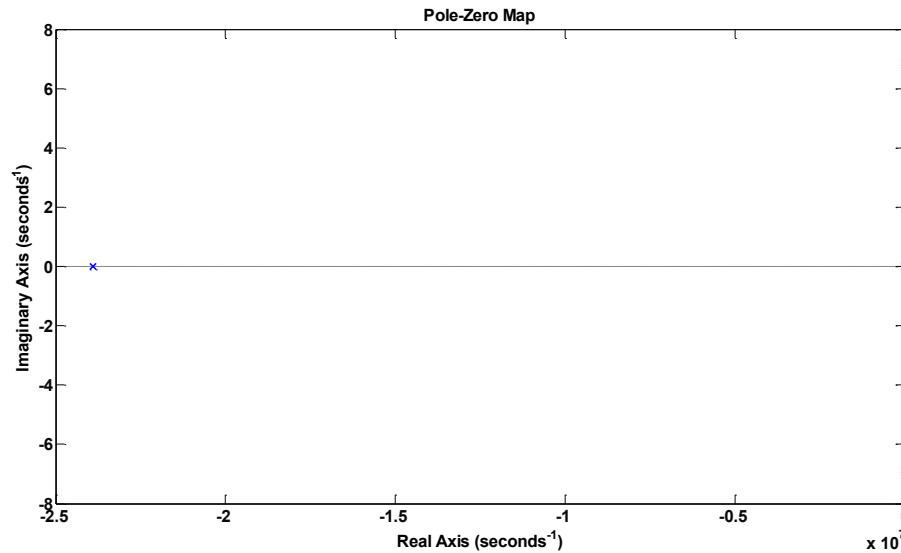


Figure 5-13. Poles and zeros map of excitation system of natural gas generator.

The step response from V_{cref} to V_c is shown in Figure 5-11 and the settling time of step responses is 0.7 second.

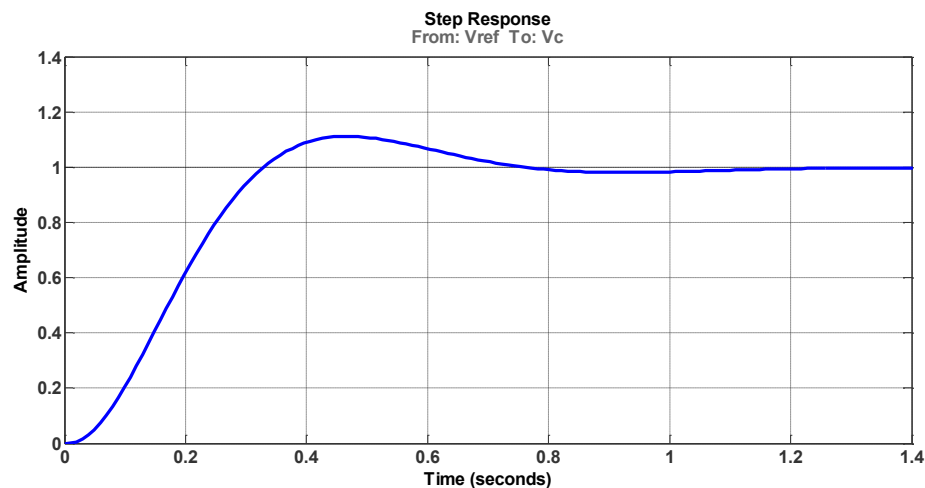


Figure 5-14. Step response from V_{dref} to V_{cref} .

5.3.3 Synchronous generator representation

The voltages behind the stator reactance in d-q reference can be written as follows.

$$e_{ng_id} = V_c \sin(\delta) \quad (5-169)$$

$$e_{ng_iq} = V_c \cos(\delta) \quad (5-170)$$

After linearization, for small perturbation, the voltages can be written as follows.

$$\Delta e_{ng_id} = \sin \delta_0 \Delta V_c + V_{c0} \cos \delta_0 \Delta \delta \quad (5-171)$$

$$\Delta e_{ng_iq} = \cos \delta_0 \Delta V_c + V_{c0} \sin \delta_0 \Delta \delta \quad (5-172)$$

Since, the natural gas generator is in per unit, the generator terminal voltage must be represent into per unit.

The differential stator voltage equations in d-q reference frame can be written as

$$\frac{d}{dt} \begin{pmatrix} i_{ng_od} \\ i_{base} \end{pmatrix} = -\omega_0 \frac{i_{ng_oq}}{i_{base}} - \frac{R_a}{L_d} \frac{i_{ng_od}}{i_{base}} + \frac{1}{L_d} e_{ng_id} + \frac{1}{L_d} \frac{e_{ng_od}}{e_{base}} \quad (5-173)$$

$$\frac{d}{dt} \begin{pmatrix} i_{ng_oq} \\ i_{base} \end{pmatrix} = \omega_0 \frac{i_{ng_od}}{i_{base}} - \frac{R_a}{L_q} \frac{i_{ng_oq}}{i_{base}} + \frac{1}{L_q} e_{ng_iq} + \frac{1}{L_q} \frac{e_{ng_oq}}{e_{base}} \quad (5-174)$$

For small perturbation, the above equations can be written as follows.

$$\frac{d}{dt} (\Delta i_{ng_od}) = -\omega_0 \Delta i_{ng_oq} - \frac{R_a}{L_d} \Delta i_{ng_od} + \frac{i_{base}}{L_d} \Delta e_{ng_id} + \frac{1}{L_d} * \frac{i_{base}}{e_{base}} \Delta e_{ng_od} \quad (5-175)$$

$$\frac{d}{dt} (\Delta i_{ng_oq}) = \omega_0 \Delta i_{ng_od} - \frac{R_a}{L_q} \Delta i_{ng_oq} + \frac{i_{base}}{L_q} \Delta e_{ng_iq} + \frac{1}{L_q} \frac{i_{base}}{e_{base}} \Delta e_{ng_oq} \quad (5-176)$$

From the above first order differential equations of stator and state space equations of mechanical system and exciter system, the complete state space equation of natural gas generator can be written as follows.

$$\begin{aligned} \frac{d}{dt} [X_{ng}]_{19 \times 1} &= [A_{ng}]_{19 \times 19} * [X_{ng}]_{19 \times 1} \\ &+ [A_{ng_cable}]_{19 \times 4} * [X_{cable}]_{2 \times 2} + [B_{ng}]_{10 \times 4} * [U_{ng}]_{10 \times 4} \end{aligned} \quad (5-177)$$

Where,

$$X_{ng} = \begin{bmatrix} [X_{mech}]_{10 \times 1} \\ [X_{exciter}]_{7 \times 1} \\ [X_{stator}]_{2 \times 1} \end{bmatrix}$$

$$X_{mech} = [\Delta X_{png_int} \quad \Delta x_{c1} \quad \Delta x_{c2} \quad \Delta x_{g1} \quad \Delta x_{g2} \quad \Delta u_4 \quad \Delta u_5 \quad \Delta T_m \quad \Delta \omega_r \quad \Delta \delta]$$

$$X_{exciter} = [\Delta X_{Qng_int} \quad \Delta x_{a1} \quad \Delta x_{a2} \quad \Delta x_{a3} \quad \Delta V_R \quad \Delta E_{FD} \quad \Delta V_c]$$

$$X_{stator} = [\Delta i_{ng_od} \quad \Delta i_{ng_oq}]$$

$$X_{cable} = [\Delta v_{ng_od} \quad \Delta v_{ng_oq} \quad \Delta i_{cable_d} \quad \Delta i_{cable_q}]$$

$$U_{ng} = \begin{bmatrix} [U_{mech}]_{2 \times 1} \\ [U_{exciter}]_{2 \times 1} \end{bmatrix}$$

$$U_{mech} = [\Delta P_{ng_ref} \quad \Delta \omega_{ref}] , \quad U_{exciter} = [\Delta Q_{ng_ref} \quad \Delta V_{ref}]$$

$$A_{ng} = \begin{bmatrix} [A_{mech}]_{10 \times 10} & [0]_{10 \times 7} & [A_{mech_stator}]_{10 \times 2} \\ [0]_{7 \times 10} & [A_{exciter}]_{7 \times 7} & [A_{exciter_stator}]_{7 \times 2} \\ [A_{stator_mech}]_{2 \times 10} & [A_{stator_exciter}]_{2 \times 7} & [A_{stator}]_{2 \times 2} \end{bmatrix}$$

$$A_{ng_cable} = \begin{bmatrix} [A_{mech_cable}]_{10 \times 2} \\ [A_{exciter_cable}]_{7 \times 2} \\ [A_{stator_cable}]_{2 \times 2} \end{bmatrix} , \quad B_{ng} = \begin{bmatrix} [B_{mech}]_{10 \times 2} \\ [B_{exciter}]_{7 \times 2} \\ [0]_{2 \times 2} \end{bmatrix}$$

$$A_{mech} = \begin{bmatrix} 0 & 0 & 0 & 0 & 0 & 0 & 0 & 0 & 0 & 0 \\ 0 & 0 & 1 & 0 & 0 & 0 & 0 & 0 & 0 & 0 \\ \frac{K_{i_Png}}{b_2} & -\frac{1}{b_2} & -\frac{b_1}{b_2} & 0 & 0 & 0 & 0 & 0 & 0 & 0 \\ 0 & \frac{1}{d_1} & \frac{a_1}{d_1} & -\frac{1}{d_1} & 0 & 0 & 0 & 0 & 0 & 0 \\ 0 & 0 & 0 & 0 & 0 & 0 & 0 & 0 & 0 & 0 \\ 0 & 0 & 0 & \frac{G_1}{e_1} & \frac{G_1 c_1}{e_1} & -\frac{1}{e_1} & 0 & 0 & 0 & 0 \\ 0 & 0 & 0 & 0 & 0 & 1 & 0 & 0 & 0 & 0 \\ 0 & 0 & 0 & 0 & 0 & 0 & \frac{1}{T_{ch}} & -\frac{1}{T_{ch}} & 0 & 0 \\ 0 & 0 & 0 & 0 & 0 & 0 & 0 & \frac{1}{2H} & 0 & 0 \\ 0 & 0 & 0 & 0 & 0 & 0 & 0 & 0 & \omega_0 & 0 \end{bmatrix}$$

$$A_{mech_stator} = \begin{bmatrix} -E_{ng_od} & -E_{ng_oq} \\ 0 & 0 \\ -\frac{K_{p_Png}}{b_2} E_{ng_od} & -\frac{K_{p_Png}}{b_2} E_{ng_oq} \\ 0 & 0 \\ 0 & 0 \\ 0 & 0 \\ 0 & 0 \\ 0 & 0 \\ -\frac{E_{ng_od}}{2H} & -\frac{E_{ng_oq}}{2H} \\ 0 & 0 \end{bmatrix}$$

$$A_{mech_cable} = \begin{bmatrix} -I_{ng_od} & -I_{ng_oq} \\ 0 & 0 \\ -\frac{K_{p_Png}}{b_2} I_{ng_od} & -\frac{K_{p_Png}}{b_2} I_{ng_oq} \\ 0 & 0 \\ 0 & 0 \\ 0 & 0 \\ 0 & 0 \\ -\frac{I_{ng_od}}{2H} & -\frac{I_{ng_oq}}{2H} \\ 0 & 0 \end{bmatrix}$$

$$A_{exciter} = \begin{bmatrix} 0 & 0 & 0 & 0 & 0 & 0 & 0 \\ 0 & 0 & 1 & 0 & 0 & 0 & 0 \\ \frac{K_{Qng_d}}{T_{DR}} & 0 & -\frac{1}{T_{DR}} & 0 & 0 & 0 & 0 \\ 0 & 0 & 0 & 0 & 0 & 0 & 0 \\ 0 & \frac{K_A K_{IR}}{T_A} & \frac{K_A (K_{PR} + K_{IR} T_{DR})}{T_A} & \frac{K_A (K_{PR} T_{DR} + K_{DR})}{T_A} & -\frac{1}{T_A} & 0 & 0 \\ 0 & 0 & 0 & 0 & \frac{K_E}{T_E} & -\frac{1}{T_E} & 0 \\ 0 & 0 & 0 & 0 & 0 & \frac{1}{T'_{do}} & -\frac{1}{T'_{do}} \end{bmatrix}$$

$$A_{exciter_stator} = \begin{bmatrix} -E_{ng_oq} & -E_{ng_od} \\ 0 & 0 \\ -\frac{K_{p_Qng} * E_{ng_oq}}{T_{DR}} & -\frac{K_{p_Qng} * E_{ng_od}}{T_{DR}} \\ 0 & 0 \\ 0 & 0 \\ 0 & 0 \end{bmatrix}$$

$$A_{exciter_cable} = \begin{bmatrix} -I_{ng_oq} & -I_{ng_od} \\ 0 & 0 \\ -\frac{K_{Qng_d}}{T_{DR}} I_{ng_oq} & -\frac{K_{Qng_d}}{T_{DR}} I_{ng_od} \\ 0 & 0 \\ 0 & 0 \\ 0 & 0 \\ 0 & 0 \end{bmatrix}$$

$$A_{stator} = \begin{bmatrix} -\left(\frac{R_a}{L_d}\right) & -\omega_0 \\ \omega_0 & -\left(\frac{R_a}{L_q}\right) \end{bmatrix}$$

$$A_{stator_mech} = \begin{bmatrix} 0 & 0 & 0 & 0 & 0 & 0 & 0 & 0 & 0 & \frac{V_{c0} \cos(\delta_0)}{L_d} \\ 0 & 0 & 0 & 0 & 0 & 0 & 0 & 0 & 0 & \frac{V_{c0} \sin(\delta_0)}{L_q} \end{bmatrix}$$

$$A_{stator_exciter} = \begin{bmatrix} 0 & 0 & 0 & 0 & 0 & 0 & \frac{\sin(\delta_0)}{L_d} \\ 0 & 0 & 0 & 0 & 0 & 0 & \frac{\cos(\delta_0)}{L_q} \end{bmatrix}$$

$$A_{stator_cable} = \begin{bmatrix} \frac{1}{L_d} & 0 & 0 & 0 \\ 0 & \frac{1}{L_q} & 0 & 0 \end{bmatrix}$$

$$B_{mech} = \begin{bmatrix} 1 & 0 & 0 & 0 \\ 0 & 0 & 0 & 0 \\ \frac{K_{p_Png}}{b_2} & \frac{1}{b_2} & 0 & 0 \\ 0 & 0 & 0 & 0 \\ 0 & 0 & 0 & 0 \\ 0 & 0 & 0 & 0 \\ 0 & 0 & 0 & 0 \\ 0 & 0 & 0 & 0 \\ 0 & 0 & 0 & 0 \\ 0 & 0 & 0 & 0 \end{bmatrix}$$

$$B_{exciter} = \begin{bmatrix} 1 & 0 \\ 0 & 0 \\ \frac{K_{Qng_d}}{T_{DR}} & \frac{1}{T_{DR}} \\ 0 & 0 \\ 0 & 0 \\ 0 & 0 \\ 0 & 0 \end{bmatrix}$$

5.4 State space modeling of transmission line/Cable

A transmission line or a cable in a power system can be represented by parameters lumped in a PI section, which is shown in Figure 5-15.

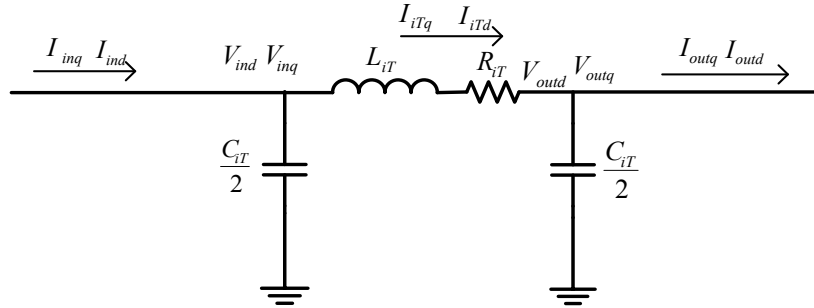


Figure 5-15. Equivalent PI representation of transmission line/Cable

The lumped parameters in a PI section L_{iT} , R_{iT} and C_{iT} for cable number iT are specified as positive and zero sequence parameters that take into account the inductive and capacitive coupling between the three phase conductors. The parameters lumped into PI section can be determined by following equations (5-178), (5-179) and (5-180).

$$R_{iT} = \left(\frac{(2R_1 + R_0)}{3} \right) * l \quad (5-178)$$

$$L_{iT} = \left(\frac{(2L_1 + L_0)}{3} \right) * l \quad (5-179)$$

$$C_{iT} = C_1 * l \quad (5-180)$$

Where, R_0 , L_0 are zero sequence resistance and inductance of the cable per mile and R_1 , L_1 and C_1 are positive sequence resistance, inductance and capacitance of the cable per mile. The length of the cable is represented by l . From Figure 5-15, the dynamics of the cable in d-q reference frame can be represented as follows.

$$\frac{d}{dt}(v_{ind}) = \omega_0 v_{inq} + \frac{2}{C_{iT}}(i_{ind}) - \frac{2}{C_{iT}}(i_{iTd}) \quad (5-181)$$

$$\frac{d}{dt}(v_{inq}) = -\omega_0 v_{ind} + \frac{2}{C_{iT}}(i_{inq}) - \frac{2}{C_{iT}}(i_{iTq}) \quad (5-182)$$

$$\frac{d}{dt}(i_{iTd}) = \omega_0 i_{iTq} - \frac{R_{iT}}{L_{iT}} i_{iTd} - \frac{1}{L_{iT}} v_{outd} + \frac{1}{L_{iT}} v_{ind} \quad (5-183)$$

$$\frac{d}{dt}(i_{iTq}) = -\omega_0 i_{iTd} - \frac{R_{iT}}{L_{iT}} i_{iTq} - \frac{1}{L_{iT}} v_{outq} + \frac{1}{L_{iT}} v_{inq} \quad (5-184)$$

$$\frac{d}{dt}(v_{outd}) = \omega_0 v_{outq} + \frac{2}{C_{iT}}(i_{Td}) - \frac{2}{C_{iT}}(i_{outd}) \quad (5-185)$$

$$\frac{d}{dt}(v_{outq}) = -\omega_0 v_{outd} + \frac{2}{C_{iT}}(i_{Tq}) - \frac{2}{C_{iT}}(i_{outq}) \quad (5-186)$$

From equations (5-181) to (5-186), the complete state space model of cable can be written as follows.

$$\dot{X}_{iT} = A_{iT} * X_{iT} + B_{iT} * U_{iT} \quad (5-187)$$

Where, i is the cable/transmission line number.

$$X_{iT} = \begin{bmatrix} v_{ind} & v_{inq} & i_{iTd} & i_{iTq} & v_{outd} & v_{outq} \end{bmatrix}$$

$$U_{iT} = \begin{bmatrix} i_{ind} & i_{inq} & i_{outd} & i_{outq} \end{bmatrix}$$

$$A_{iT1} = \begin{bmatrix} 0 & \omega_0 & -\frac{2}{C_{iT}} & 0 & 0 & 0 \\ -\omega_0 & 0 & 0 & -\frac{2}{C_{iT}} & 0 & 0 \\ \frac{1}{L_{iT}} & 0 & \frac{R_{iT}}{L_{iT}} & \omega_0 & -\frac{1}{L_{iT}} & 0 \\ 0 & \frac{1}{L_{iT}} & -\omega_0 & \frac{R_{iT}}{L_{iT}} & 0 & -\frac{1}{L_{iT}} \\ 0 & 0 & \frac{2}{C_{iT}} & 0 & 0 & \omega_0 \\ 0 & 0 & 0 & \frac{2}{C_{iT}} & -\omega_0 & 0 \end{bmatrix}$$

$$, B_{iT} = \begin{bmatrix} \frac{2}{C_{iT}} & 0 & 0 & 0 \\ 0 & \frac{2}{C_{iT}} & 0 & 0 \\ 0 & 0 & 0 & 0 \\ 0 & 0 & 0 & 0 \\ 0 & 0 & -\frac{2}{C_{iT}} & 0 \\ 0 & 0 & 0 & -\frac{2}{C_{iT}} \end{bmatrix}$$

In most of power system, the cable/transmission lines are in cascaded connection in order to form power system. In studied microgrid system, the current is flowing through multiple cables. Hence it is required to find the coupling between two cables in state space modeling. The cascaded connection of nominal PI section circuits of cable/transmission lines are represented by Figure 5-16

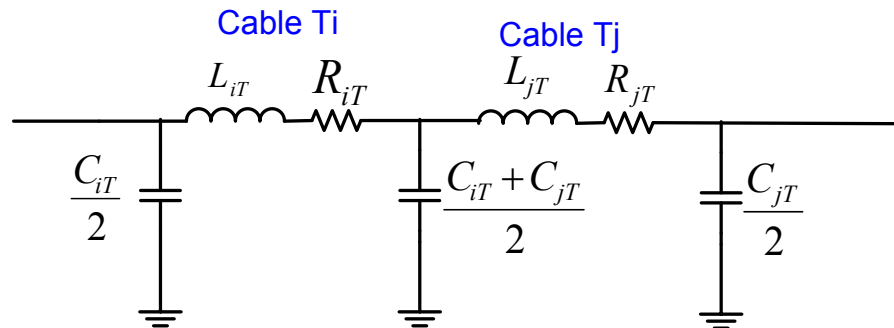


Figure 5-16. Cascaded transmission line/cable representation.

For cascaded transmission lines/cables, the voltage at node of connection is depends on both cable. The node equation in d-q reference frame can be written as follows.

$$\frac{d}{dt}(v_{ijd}) = \omega_0 v_{ijq} + \frac{2}{C_i + C_j}(i_{iTd}) - \frac{2}{C_{iT} + C_{jT}}(i_{jTd}) \quad (5-188)$$

$$\frac{d}{dt}(v_{ijq}) = -\omega_0 v_{ijq} + \frac{2}{C_{iT} + C_{jT}}(i_{jTq}) - \frac{2}{C_{iT} + C_{jT}}(i_{ijq}) \tag{5-189}$$

Equations (5-190) and (5-191) are generalized equations, where more than two cables are connected to same node. These equations are very important for writing the state space equations for entire microgrid.

$$\frac{d}{dt}(v_{ijTd}) = \omega_0 v_{ijTd} + \frac{2}{(l_i * C_i) + (l_1 * C_1) + \dots + (l_j * C_j)}(i_{iTd}) - \frac{2}{(l_i * C_i) + (l_1 * C_1) + \dots + (l_j * C_j)}(i_{1Td} + i_{2Td} + \dots + i_{jTd}) \tag{5-190}$$

$$\frac{d}{dt}(v_{ijTq}) = -\omega_0 v_{ijTq} + \frac{2}{(l_i * C_i) + (l_1 * C_1) + \dots + (l_j * C_j)}(i_{iTq}) - \frac{2}{(l_i * C_i) + (l_1 * C_1) + \dots + (l_j * C_j)}(i_{1Tq} + i_{2Tq} + \dots + i_{jTq}) \tag{5-191}$$

The complete line configuration of the fort sill microgrid system is shown in Figure 5-17.

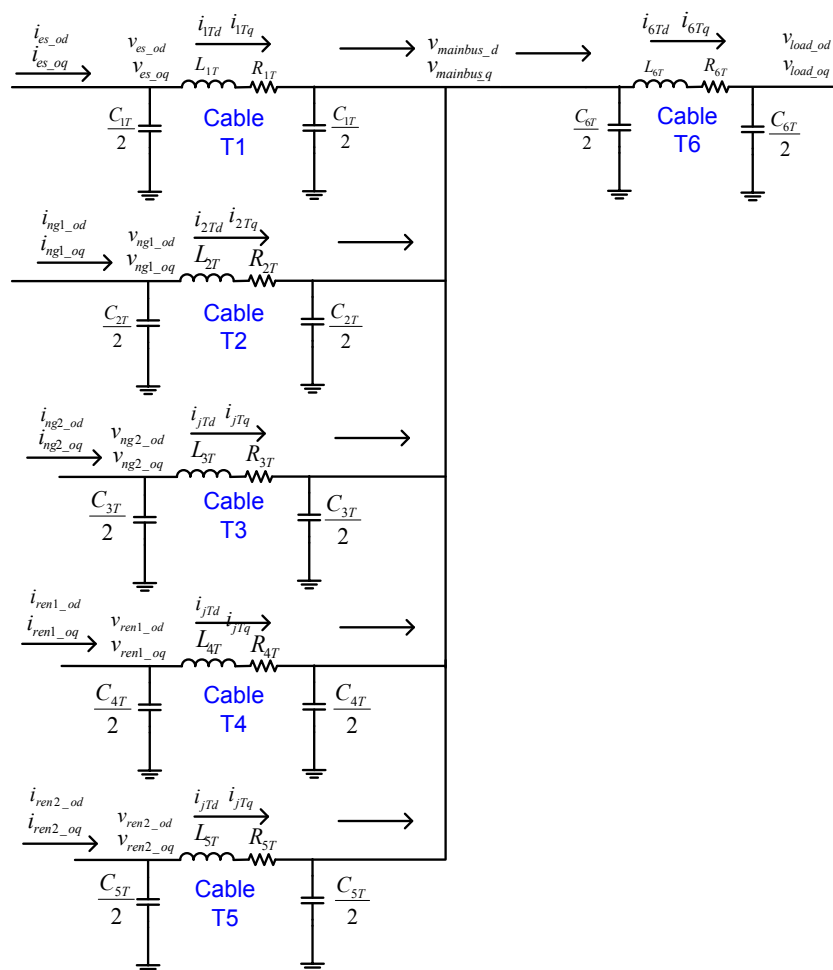


Figure 5-17. Line configuration of the fort Sill microgrid system.

From above discussion and from Figure 5-17, the complete state space model of the microgrid line configuration for small perturbation can be derived as below.

$$\dot{X}_T = [A_T] * [X_T] + [A_{T_sources}] * [X_{sources}] + [B_T] * [U_{load}] \quad (5-192)$$

Where,

$$X_T = \begin{bmatrix} [\Delta X_{1T}]_{4 \times 1} \\ [\Delta X_{2T}]_{4 \times 1} \\ [\Delta X_{3T}]_{4 \times 1} \\ [\Delta X_{4T}]_{4 \times 1} \\ [\Delta X_{5T}]_{4 \times 1} \\ [\Delta X_{mainbus}]_{2 \times 1} \\ [\Delta X_{6T}]_{4 \times 1} \end{bmatrix}, \quad X_{source} = \begin{bmatrix} [\Delta X_{es}]_{10 \times 1} \\ [\Delta X_{ng1}]_{9 \times 1} \\ [\Delta X_{ng2}]_{9 \times 1} \\ [\Delta X_{ren1}]_{8 \times 1} \\ [\Delta X_{ren2}]_{8 \times 1} \end{bmatrix}, \quad U_{load} = \begin{bmatrix} \Delta i_{load_d} \\ \Delta i_{load_q} \end{bmatrix},$$

$$X_{1T} = \begin{bmatrix} \Delta v_{es_od} \\ \Delta v_{es_oq} \\ \Delta i_{1Td} \\ \Delta i_{1Tq} \end{bmatrix}, \quad X_{2T} = \begin{bmatrix} \Delta v_{ng1_od} \\ \Delta v_{ng2_oq} \\ \Delta i_{2Td} \\ \Delta i_{2Tq} \end{bmatrix}, \quad X_{3T} = \begin{bmatrix} \Delta v_{ng2_od} \\ \Delta v_{ng2_oq} \\ \Delta i_{3Td} \\ \Delta i_{3Tq} \end{bmatrix},$$

$$X_{4T} = \begin{bmatrix} \Delta v_{ren1_od} \\ \Delta v_{ren1_oq} \\ \Delta i_{4Td} \\ \Delta i_{4Tq} \end{bmatrix}, \quad X_{5T} = \begin{bmatrix} \Delta v_{ren2_od} \\ \Delta v_{ren2_oq} \\ \Delta i_{5Td} \\ \Delta i_{5Tq} \end{bmatrix}, \quad X_{6T} = \begin{bmatrix} \Delta i_{6Td} \\ \Delta i_{6Tq} \\ \Delta v_{load_d} \\ \Delta i_{load_q} \end{bmatrix},$$

$$X_{mainbus} = \begin{bmatrix} \Delta V_{mainbus_d} \\ \Delta V_{mainbus_q} \end{bmatrix}$$

$$A_T = \begin{bmatrix} [A_{1T}]_{4 \times 4} & [0]_{4 \times 4} & [0]_{4 \times 4} & [0]_{4 \times 4} & [0]_{4 \times 4} & [A_{1T_mainbus}]_{4 \times 2} & [0]_{4 \times 4} \\ [0]_{4 \times 4} & [A_{2T}]_{4 \times 4} & [0]_{4 \times 4} & [0]_{4 \times 4} & [0]_{4 \times 4} & [A_{2T_mainbus}]_{4 \times 2} & [0]_{4 \times 4} \\ [0]_{4 \times 4} & [0]_{4 \times 4} & [A_{3T}]_{4 \times 4} & [0]_{4 \times 4} & [0]_{4 \times 4} & [A_{3T_mainbus}]_{4 \times 2} & [0]_{4 \times 4} \\ [0]_{4 \times 4} & [0]_{4 \times 4} & [0]_{4 \times 4} & [A_{4T}]_{4 \times 4} & [0]_{4 \times 4} & [A_{4T_mainbus}]_{4 \times 2} & [0]_{4 \times 4} \\ [0]_{4 \times 4} & [0]_{4 \times 4} & [0]_{4 \times 4} & [0]_{4 \times 4} & [A_{5T}]_{4 \times 4} & [A_{5T_mainbus}]_{4 \times 2} & [0]_{4 \times 4} \\ [A_n]_{2 \times 4} & [A_n]_{2 \times 4} & [A_n]_{2 \times 4} & [A_n]_{2 \times 4} & [A_n]_{2 \times 4} & [A_{mainbus}]_{2 \times 2} & [A_{mainbus_6T}]_{2 \times 4} \\ [0]_{4 \times 4} & [0]_{4 \times 4} & [0]_{4 \times 4} & [0]_{4 \times 4} & [0]_{4 \times 4} & [A_{6T_mainbus}]_{4 \times 2} & [A_{6T}]_{4 \times 4} \end{bmatrix}$$

$$A_{iT} = \begin{bmatrix} 0 & \omega_0 & -\frac{2}{C_{iT}} & 0 \\ -\omega_0 & 0 & 0 & -\frac{2}{C_{iT}} \\ \frac{1}{L_{iT}} & 0 & -\frac{R_{iT}}{L_{iT}} & \omega_0 \\ 0 & \frac{1}{L_{iT}} & -\omega_0 & -\frac{R_{iT}}{L_{iT}} \end{bmatrix} \text{ and } A_{6T} = \begin{bmatrix} -\frac{1}{L_{6T}} & 0 & 0 & 0 \\ 0 & -\frac{1}{L_{6T}} & 0 & 0 \\ \frac{2}{C_{6T}} & 0 & \omega_0 & 0 \\ 0 & \frac{2}{C_{6T}} & 0 & -\omega_0 \end{bmatrix}$$

Where, i is from 1 to 5.

$$A_{mainbus} = \begin{bmatrix} 0 & \omega_0 & -2/\sum_{i=1}^7 C_i & 0 \\ -\omega_0 & 0 & 0 & -2/\sum_{i=1}^7 C_i \end{bmatrix}$$

$$A_n = \begin{bmatrix} 0 & 0 & -2/\sum_{i=1}^7 C_i & 0 \\ 0 & 0 & 0 & -2/\sum_{i=1}^7 C_i \end{bmatrix}$$

$$A_{mainus_6T} = \begin{bmatrix} 2/\sum_{i=1}^7 C_i & 0 & 0 & 0 \\ 0 & 2/\sum_{i=1}^7 C_i & 0 & 0 \end{bmatrix}$$

$$A_{iT_mainbus} = \begin{bmatrix} 0 & 0 \\ 0 & 0 \\ -\frac{1}{L_{iT}} & 0 \\ 0 & -\frac{1}{L_{iT}} \end{bmatrix} \text{ Where, i is from 1 to 5.}$$

$$A_{mainbus_6T} = \begin{bmatrix} 1 & 0 \\ L_{6T} & \\ 0 & \frac{1}{L_{6T}} \\ 0 & 0 \\ 0 & 0 \end{bmatrix}$$

$$A_{T_sources} = \begin{bmatrix} [A_{1T_es}]_{4 \times 10} & [0]_{4 \times 19} & [0]_{4 \times 19} & [0]_{4 \times 8} & [0]_{4 \times 8} \\ [0]_{4 \times 10} & [A_{2T_ng1}]_{4 \times 19} & [0]_{4 \times 19} & [0]_{4 \times 8} & [0]_{4 \times 8} \\ [0]_{4 \times 10} & [0]_{4 \times 19} & [A_{3T_ng2}]_{4 \times 19} & [0]_{4 \times 8} & [0]_{4 \times 8} \\ [0]_{4 \times 10} & [0]_{4 \times 19} & [0]_{4 \times 19} & [A_{4T_ren1}]_{4 \times 8} & [0]_{4 \times 8} \\ [0]_{4 \times 10} & [0]_{4 \times 19} & [0]_{4 \times 19} & [0]_{4 \times 8} & [A_{5T_ren2}]_{4 \times 8} \\ [0]_{4 \times 10} & [0]_{4 \times 19} & [0]_{4 \times 19} & [0]_{4 \times 8} & [0]_{4 \times 8} \\ [0]_{4 \times 10} & [0]_{4 \times 19} & [0]_{4 \times 19} & [0]_{4 \times 8} & [0]_{4 \times 8} \end{bmatrix}$$

$$A_{1T_es} = \begin{bmatrix} [0]_{4 \times 8} & [A_{iTs}]_{4 \times 2} \end{bmatrix}$$

$$A_{2T_ng1} = \begin{bmatrix} [0]_{4 \times 17} & [A_{iTs}]_{4 \times 2} \end{bmatrix}$$

$$A_{3T_ng2} = \begin{bmatrix} [0]_{4 \times 17} & [A_{iTs}]_{4 \times 2} \end{bmatrix}$$

$$A_{4T_ren1} = \begin{bmatrix} [0]_{4 \times 6} & [A_{iTs}]_{4 \times 2} \end{bmatrix}$$

$$A_{5T_ren2} = \begin{bmatrix} [0]_{4 \times 6} & [A_{iTs}]_{4 \times 2} \end{bmatrix}$$

$$A_{iTs} = \begin{bmatrix} \frac{2}{C_{iT}} & 0 \\ 0 & \frac{2}{C_{iT}} \\ 0 & 0 \\ 0 & 0 \end{bmatrix}$$

Where,

$$B_T = \begin{bmatrix} [0]_{4 \times 1} \\ [0]_{4 \times 1} \\ [0]_{4 \times 1} \\ [0]_{4 \times 1} \\ [0]_{2 \times 1} \\ [0]_{4 \times 1} \\ [B_{load}]_{4 \times 1} \end{bmatrix} \quad \text{Where,} \quad B_{load} = \begin{bmatrix} 0 & 0 \\ 0 & 0 \\ \frac{2}{C_{6T}} & 0 \\ 0 & \frac{2}{C_{6T}} \end{bmatrix}$$

5.5 Microgrid state space modeling

The state space models of all microgrid components are derived into sections 5.1 to 5.4. These derived microgrid components are used to build the complete microgrid state space model, which can be used for all different cases of VDC method. The complete derived state space model is given below.

$$\begin{aligned} \dot{X}_{\mu grid} &= A_{\mu grid} * X_{\mu grid} + B_{\mu grid} * U_{\mu grid} \\ Y_{\mu grid} &= C_{\mu grid} * X_{\mu grid} + D_{\mu grid} * U_{\mu grid} \end{aligned} \quad (5-193)$$

Where,

$$X_{\mu grid} = \begin{bmatrix} [\Delta X_{es}]_{10 \times 1} \\ [\Delta X_{ng1}]_{19 \times 1} \\ [\Delta X_{ng2}]_{19 \times 1} \\ [\Delta X_{ren1}]_{8 \times 1} \\ [\Delta X_{ren2}]_{8 \times 1} \\ [\Delta X_{1T}]_{4 \times 1} \\ [\Delta X_{2T}]_{4 \times 1} \\ [\Delta X_{3T}]_{4 \times 1} \\ [\Delta X_{4T}]_{4 \times 1} \\ [\Delta X_{5T}]_{4 \times 1} \\ [\Delta X_{mainbus}]_{2 \times 1} \\ [\Delta X_{6T}]_{4 \times 1} \end{bmatrix} \quad U_{\mu grid} = \begin{bmatrix} [\Delta U_{es}]_{2 \times 1} \\ [\Delta U_{ng1}]_{4 \times 1} \\ [\Delta U_{ng2}]_{4 \times 1} \\ [\Delta U_{ren1}]_{2 \times 1} \\ [\Delta U_{ren2}]_{2 \times 1} \\ [\Delta U_{load}]_{2 \times 1} \end{bmatrix},$$

$$Y_{\mu grid} = X_{\mu grid}$$

$$C_{\mu grid} = [I]_{90 \times 90}$$

$$D_{\mu grid} = [0]_{90 \times 90}$$

$$A_{ignd} = \begin{bmatrix} [A_{es}]_{0 \times 10} & [0]_{0 \times 19} & [0]_{0 \times 19} & [0]_{0 \times 8} & [0]_{0 \times 8} & [A_{es_T1}]_{0 \times 4} & [0]_{0 \times 4} & [0]_{0 \times 4} & [0]_{0 \times 4} & [0]_{0 \times 4} & [0]_{0 \times 2} & [0]_{0 \times 4} \\ [0]_{19 \times 10} & [A_{ng1}]_{9 \times 19} & [0]_{9 \times 19} & [0]_{9 \times 8} & [0]_{9 \times 8} & [0]_{19 \times 4} & [A_{ng1_T2}]_{9 \times 4} & [0]_{9 \times 4} & [0]_{9 \times 4} & [0]_{9 \times 4} & [0]_{9 \times 2} & [0]_{9 \times 4} \\ [0]_{19 \times 10} & [0]_{9 \times 19} & [A_{ng2}]_{9 \times 19} & [0]_{9 \times 8} & [0]_{9 \times 8} & [0]_{19 \times 4} & [0]_{9 \times 4} & [A_{ng2_T3}]_{9 \times 4} & [0]_{9 \times 4} & [0]_{9 \times 4} & [0]_{9 \times 2} & [0]_{9 \times 4} \\ [0]_{8 \times 10} & [0]_{8 \times 19} & [0]_{8 \times 19} & [A_{ren1}]_{8 \times 8} & [0]_{8 \times 8} & [0]_{8 \times 4} & [0]_{8 \times 4} & [0]_{8 \times 4} & [A_{ren1_T4}]_{8 \times 4} & [0]_{8 \times 4} & [0]_{8 \times 2} & [0]_{8 \times 4} \\ [0]_{8 \times 10} & [0]_{8 \times 19} & [0]_{8 \times 19} & [0]_{8 \times 8} & [A_{ren2}]_{8 \times 8} & [0]_{8 \times 4} & [0]_{8 \times 4} & [0]_{8 \times 4} & [0]_{8 \times 4} & [A_{ren2_T5}]_{8 \times 4} & [0]_{8 \times 2} & [0]_{8 \times 4} \\ [A_{T1_es}]_{4 \times 10} & [0]_{4 \times 19} & [0]_{4 \times 19} & [0]_{4 \times 8} & [0]_{4 \times 8} & [A_{T1}]_{4 \times 4} & [0]_{4 \times 4} & [0]_{4 \times 4} & [0]_{4 \times 4} & [0]_{4 \times 4} & [A_{T1_mainbus}]_{4 \times 2} & [0]_{4 \times 4} \\ [0]_{4 \times 10} & [A_{T2_ng1}]_{4 \times 19} & [0]_{4 \times 19} & [0]_{4 \times 8} & [0]_{4 \times 8} & [0]_{4 \times 4} & [A_{T2}]_{4 \times 4} & [0]_{4 \times 4} & [0]_{4 \times 4} & [0]_{4 \times 4} & [A_{T2_mainbus}]_{4 \times 2} & [0]_{4 \times 4} \\ [0]_{4 \times 10} & [0]_{4 \times 19} & [A_{T3_ng2}]_{4 \times 19} & [0]_{4 \times 8} & [0]_{4 \times 8} & [0]_{4 \times 4} & [0]_{4 \times 4} & [A_{T3}]_{4 \times 4} & [0]_{4 \times 4} & [0]_{4 \times 4} & [A_{T3_mainbus}]_{4 \times 2} & [0]_{4 \times 4} \\ [0]_{4 \times 10} & [0]_{4 \times 19} & [0]_{4 \times 19} & [A_{T4_ren1}]_{4 \times 8} & [0]_{4 \times 8} & [0]_{4 \times 4} & [0]_{4 \times 4} & [0]_{4 \times 4} & [A_{T4}]_{4 \times 4} & [0]_{4 \times 4} & [A_{T4_mainbus}]_{4 \times 2} & [0]_{4 \times 4} \\ [0]_{4 \times 10} & [0]_{4 \times 19} & [0]_{4 \times 19} & [0]_{4 \times 8} & [A_{T5_ren2}]_{4 \times 8} & [0]_{4 \times 4} & [0]_{4 \times 4} & [0]_{4 \times 4} & [0]_{4 \times 4} & [A_{T5}]_{4 \times 4} & [A_{T5_mainbus}]_{4 \times 2} & [0]_{4 \times 4} \\ [0]_{2 \times 10} & [0]_{2 \times 19} & [0]_{2 \times 19} & [0]_{2 \times 8} & [0]_{2 \times 8} & [A_n]_{2 \times 4} & [A_n]_{2 \times 4} & [A_n]_{2 \times 4} & [A_n]_{2 \times 4} & [A_n]_{2 \times 4} & [A_{mainbus}]_{2 \times 2} & [0]_{2 \times 4} \\ [0]_{4 \times 10} & [0]_{4 \times 19} & [0]_{4 \times 19} & [0]_{4 \times 8} & [0]_{4 \times 8} & [0]_{4 \times 4} & [0]_{4 \times 4} & [0]_{4 \times 4} & [0]_{4 \times 4} & [0]_{4 \times 4} & [A_{T6_main}]_{4 \times 2} & [A_{T6}]_{4 \times 4} \end{bmatrix}$$

$$B_{\mu grid} = \begin{bmatrix} [B_{es}]_{10 \times 2} & [0]_{10 \times 4} & [0]_{10 \times 4} & [0]_{10 \times 2} & [0]_{10 \times 2} & [0]_{10 \times 2} \\ [0]_{19 \times 2} & [B_{ng1}]_{19 \times 4} & [0]_{19 \times 4} & [0]_{19 \times 2} & [0]_{19 \times 2} & [0]_{19 \times 2} \\ [0]_{19 \times 2} & [0]_{19 \times 4} & [B_{ng2}]_{19 \times 4} & [0]_{19 \times 2} & [0]_{19 \times 2} & [0]_{19 \times 2} \\ [0]_{8 \times 2} & [0]_{8 \times 4} & [0]_{8 \times 4} & [B_{ren1}]_{8 \times 2} & [0]_{8 \times 2} & [0]_{8 \times 2} \\ [0]_{8 \times 2} & [0]_{8 \times 4} & [0]_{8 \times 4} & [0]_{8 \times 2} & [B_{ren2}]_{8 \times 2} & [0]_{8 \times 2} \\ [0]_{4 \times 2} & [0]_{4 \times 4} & [0]_{4 \times 4} & [0]_{4 \times 2} & [0]_{4 \times 2} & [0]_{4 \times 2} \\ [0]_{4 \times 2} & [0]_{4 \times 4} & [0]_{4 \times 4} & [0]_{4 \times 2} & [0]_{4 \times 2} & [0]_{4 \times 2} \\ [0]_{4 \times 2} & [0]_{4 \times 4} & [0]_{4 \times 4} & [0]_{4 \times 2} & [0]_{4 \times 2} & [0]_{4 \times 2} \\ [0]_{4 \times 2} & [0]_{4 \times 4} & [0]_{4 \times 4} & [0]_{4 \times 2} & [0]_{4 \times 2} & [0]_{4 \times 2} \\ [0]_{4 \times 2} & [0]_{4 \times 4} & [0]_{4 \times 4} & [0]_{4 \times 2} & [0]_{4 \times 2} & [0]_{4 \times 2} \\ [0]_{2 \times 2} & [0]_{2 \times 4} & [0]_{2 \times 4} & [0]_{2 \times 2} & [0]_{2 \times 2} & [0]_{2 \times 2} \\ [0]_{4 \times 2} & [0]_{4 \times 4} & [0]_{4 \times 4} & [0]_{4 \times 2} & [0]_{4 \times 2} & [B_{load}]_{4 \times 2} \end{bmatrix}$$

In the above state space model, when the source is connected, the associated matrix is multiplied by 1 and if the source is disconnected the associated matrix is multiplied by 0. For example, in case 1 when natural gas generator 1 is disconnected, the matrix A_{ng1} , B_{ng1} and A_{ng1_T2} are multiplied by zero.

5.6 Stability Analysis for Proposed VDC method.

The stability of nonlinear system is given by the poles and zeros of the characteristic equation. When the poles and zeros have negative real parts, the system is asymptotically stable. When at least one of the poles and zeros have a positive real part, the system is unstable. In the proposed VDC method, the microgrid is operated in different mode of operation. In mode 1, only energy storage provides power to the system. In mode 2, energy storage and natural gas generator provides power to the system and in mode 3, energy storage and both generators provides power to the system. The power output of the renewables are intermittent. So it has to be consider during stability analysis. In this section, all different scenarios are consider and pole-zero map has been plotted.

Case 1: Only energy storage is connected into microgrid. The renewables and both natural gas generators are assume to be disconnected from the system. For selected control parameters, the pole-zero map has been plotted as shown in Figure 5-18.

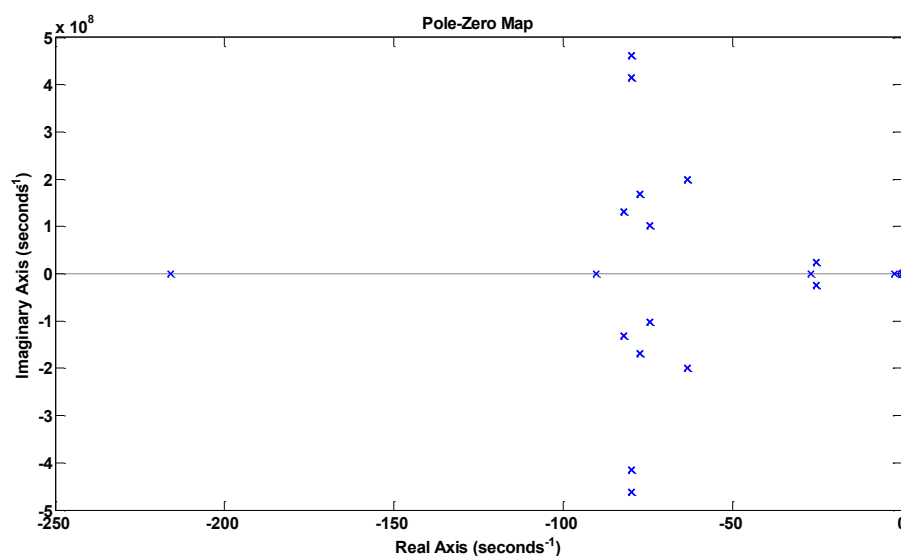


Figure 5-18. Pole-zero map for microgrid, when only energy storage is connected.

All the poles and zeros are in the left half plane. Hence, the microgrid operation is stable while renewable and generators are disconnected and only energy storage provides power.

Case 2: In this case, energy storage and solar PV are connected into microgrid. However, both generators and wind turbine are not connected to the microgrid. Figure 5-19 shows the pole-zero map and confirms the stable operation of microgrid. Few poles are relocated and few poles are added due to connection of solar PV.

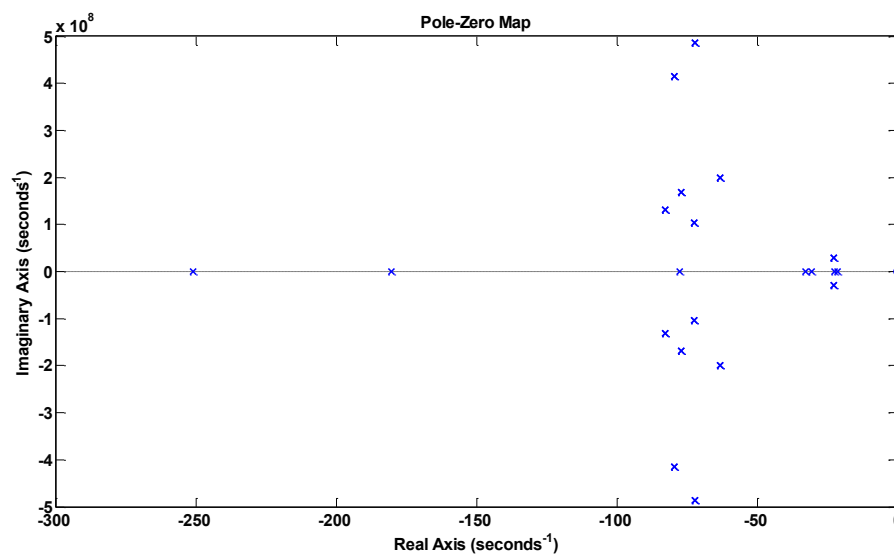


Figure 5-19. Pole-zero map for microgrid, when energy storage and solar PV are connected.

Case 3: In this case, energy storage, renewables and natural gas generator 1 are connected. This is mode 1 of unit commitment algorithm. Figure 5-20 shows the pole-zero map and confirms the stable operation of microgrid. Few poles are relocated and few poles are added due to the connection of wind turbine.

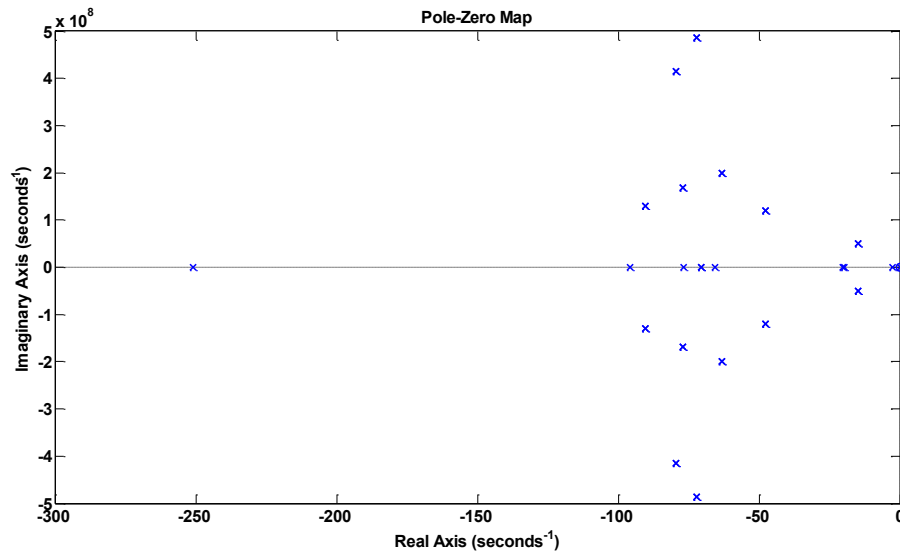


Figure 5-20. Pole-zero map for microgrid, when energy storage and renewables are connected.

Case 4: In this case, energy storage, solar PV, wind turbine and both generators are connected. This is mode 2 of unit commitment algorithm. Figure 5-21 shows the pole-zero map and confirms the stable operation of microgrid.

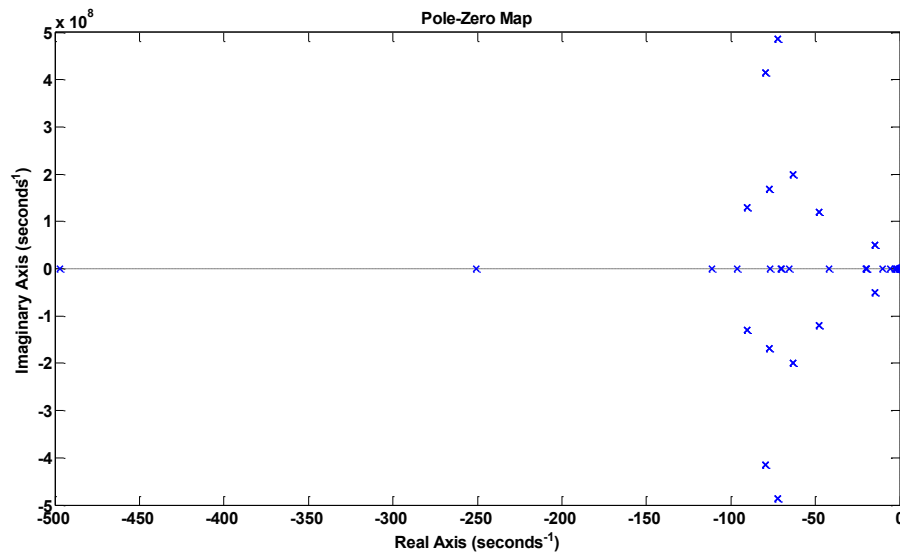


Figure 5-21. Pole-zero map for microgrid, when energy storage, renewables and generator 1 are connected.

Case 5: In this case, energy storage, solar PV and wind turbine are connected. This is mode 3 of unit commitment algorithm. Figure 5-22 shows the pole-zero map and confirms the stable operation of microgrid.

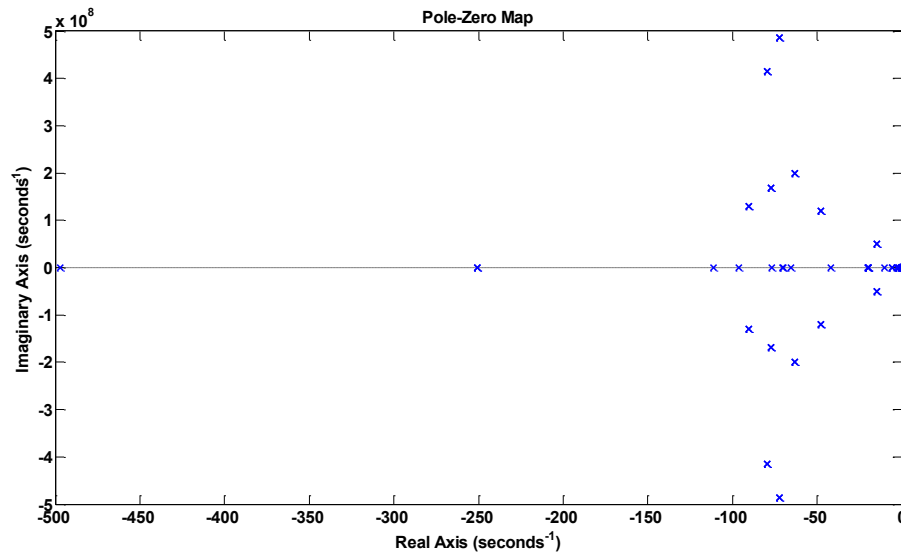


Figure 5-22. Pole-zero map for microgrid, when energy storage, renewables and both natural gas generators are connected.

In all different possible scenarios of VDC method, poles and zeros are remain in left half plane. Hence, the microgrid is stable.

Chapter 6 Modified Control Technique for CO₂ Reduction, Improve Efficiency and Power Quality in a Microgrid

6.1 Introduction

In this chapter, energy resources management technique is proposed to improve power quality indexes, reduce CO₂ emission, and improve energy efficiency. Modified IEEE 34 bus system is used to model a microgrid in an island mode. The DRs and load profile have been added into the standard IEEE 34 system and four cases have been studied. In base case, two large natural gas generators are connected to the energy network. In case 2, in addition to the generators, energy network is highly penetrated with renewables. In case 3, energy storages are added at the point of interconnection (POI) of each renewable sources are added to the system examined in case 2 and the proposed modified control technique is applied.

In the simulation, the CO₂ emissions, associated with the combustion of fossil fuels, are calculated for 24 hours load profile. Quality index is calculated based on critical load outages. If the voltage and frequency do not meet the requirements for the critical load, the load is assumed to be off line. The critical load outage time, in a first approximation, can be associated with System Average Interruption Duration Index (SAIDI), which is used by the utility companies to evaluate the power quality and system reliability.

Simulation results for all three cases have been presented. CO₂ emission, efficiency and power quality indexes were calculated. Simulation results for all three cases have

been presented. CO₂ emission, efficiency and power quality indexes were calculated and compared in order to verify the proposed energy management technique.

6.2 Renewables and Energy storage system sizing

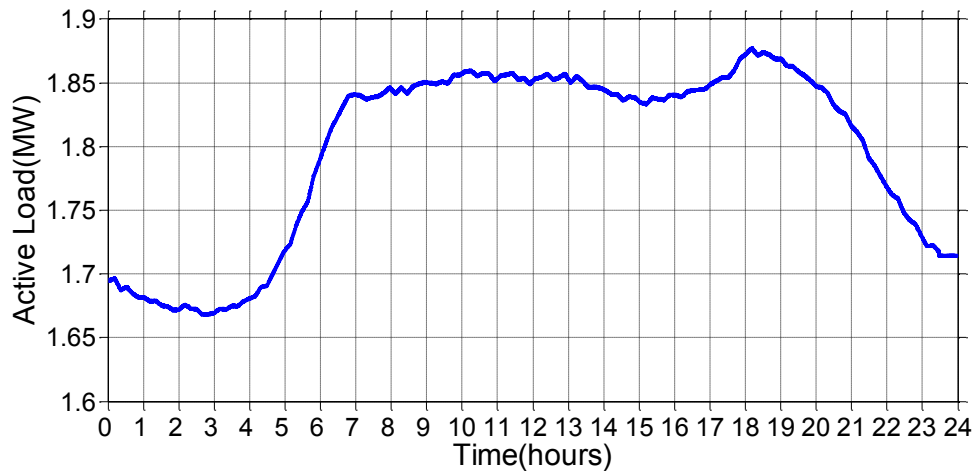


Figure 6-1. Active load profile of small island energy network

The load power profile for 24 hours is shown in Figure 6-1. As shown in the figure, peak load of the system is around 1.9 MW. The system has significant line losses due to long lines. In base case, to meet the total load and losses requirement two generators, each rated at 1.5 MVA are added into the system model. Each generator is assumed to have 0.8 power factor and reactive power capability. Hence, the 2.4 MW of total power from the generators can meet the total load requirement including losses. Based on the NREL reports, 30% of total electricity will be generated from renewable resources by 2030. Hence, two 0.5 MW wind turbines and one 0.25 MW of solar PV have been integrated into the system model and this scenario is considered as a case 2.

The energy storage systems were integrated with renewables in order to deal with the intermittency issues. The energy storage should provide an additional resource to help system frequency management. It charges or discharges on a minute to minute basis to help maintain system frequency at 60 Hz. It provides energy for a short duration during sudden increase in loads until the natural gas generator can be brought online.

The assumption is made that large wind and solar PV farms have the output power which will not change more than 45% of its rated capacity at any instance. Hence, 565

kW should be minimum charging/discharging power capacity of energy storage system, which is 45% of total renewable resources capacity.

A natural gas generator will operate and provide power to the system only if the load on the generator is above the limit determined by its lowest allowable efficiency. As a result, in cases when the power generation requirement from the natural gas generators drops below its minimum operating limits, the energy storage system should be able to provide that minimum power requirement so that the natural gas generators can be off line. In the studied small island system, each generator has 20% minimum power requirement. The energy storage should be able to provide that amount of power, which is at least 600 kW or 20% for each 1.2 MW generator. So the total power capacity for energy storage system should be 1.165 MW.

To integrate large amount of renewables into Puerto Rico power system, the Puerto Rico Electric Power Authority (PREPA) has established minimum technical requirements (MTR) for the interconnection of renewables into a small island system. According to MTR, frequency response and ramp rate control are two major requirements and they dictate the energy capacity for the energy storage systems.

The energy storage system utilized for frequency support requirements should have energy capacity equivalent to 9.5 minute at 10% of total rated renewable energy systems power. Hence, the minimum storage capacity for the purpose of frequency support for 1.25 MW of renewables is:

Storage Capacity for frequency regulation =

$$\frac{0.10 * 1.25 MW * 9.5}{60} = 19.79 kWh$$

Based on the MTR, the power ramp rate of renewable energy sources should not be more than 10% of the rated capacity per minute at its Point of Interconnection (POI). This means that each renewable has to incorporate some amount of energy storage. As

an example, for the 500kW wind turbine connected to the bus 848, the necessary amount of storage for the ramp rate limiting will be:

$$\frac{500kW * 10 \text{ min}}{2 * 60 \text{ min/ h}} = 41.67kWh$$

In the modeled system, we have the total 1.25 MW of renewables. In the worst case, the power could change from 1.25 MW to 0 MW, the energy storage at the POI of each renewable should pick up the change and should limit the ramp to 125 kW per minute. As a result, it takes 10 minutes to ramp down the power, from 1.25MW to zero. The minimum total energy storage requirement for the entire system for the ramp rate limiting is 104.16 kWh. The total minimum size of energy storage for ramp rate control and frequency support for the entire system will be 123.95 kWh. In case 4, to applied virtual droop control method, a 250 kW, 500 kWhr ZBB energy storage has been added at bus 800.

6.3 Control Algorithm

In islanded microgrid, the stability of microgrid frequency is a key for an overall energy network's stability. Small frequency deviation indicates the changes in power and can lead to load shedding. Large power loss events deviates the frequency to great extent and main objective of a grid operator is to minimize the power loss event. Hence, the Puerto Rico Electric Power Authority (PREPA) has established technical requirements for interconnection of renewables with energy network. In MTR, specifically, the requirements for managing sudden changes of power output called "Ramp Rate Control" and mandate a minimum amount of power to respond to grid frequency changes called "Frequency Response" are very important. In addition, voltage control is an essential part of MTR requirement. To meet MTR requirements, ramp rate and frequency support control have been implemented. Based on the frequency deviation and change in the power output of renewable energy systems, the power command references for the integrated energy storage systems are calculated.

Frequency response is not limited by ramp rate control and is decoupled from the ramp rate control. Frequency response is continuous in operation even during ramp rate event, unless the ramp rate event requires its frequency response resources to use for ramp rate control. The renewable energy facility should be able to simultaneously meet both requirements, as long as the ramp rate event does not require the frequency response resources to use with the ramp rate requirement. If the ramp rate control uses all the available resources, the frequency response control will not be in effect during this specific period of time. The part of energy storage system utilized for frequency response control shall have a storage capacity equivalent to 9.5 minutes of the 10% AC contracted capacity. This includes 9 minutes of full participation and one minute ramp down complying with the ramp rate requirement. For small frequency deviation (less

than 0.3 Hz), the renewable energy facility response should be proportional to the frequency deviation, based on the specified 5% droop characteristic. For small frequency deviation, the frequency response should follow the ramp rate. The maximum allowable dead band for frequency response is 0.02%. For large frequency deviations (greater than 0.3 Hz), the renewable energy facility shall provide an immediate real power of at least 10% of AC power contracted capacity. The time response should not be more than 1 second. If the frequency deviation stays above 0.3 Hz, the renewable energy facility should be able to provide 10% of AC contracted power for at least 9 minutes and after that, the real power primary response should decrease at a 10% per minute ramp rate. If the energy available for regulation is drained the frequency response control shall be restored in a time less than 10 minutes after restoration of the frequency to within the frequency control dead band.

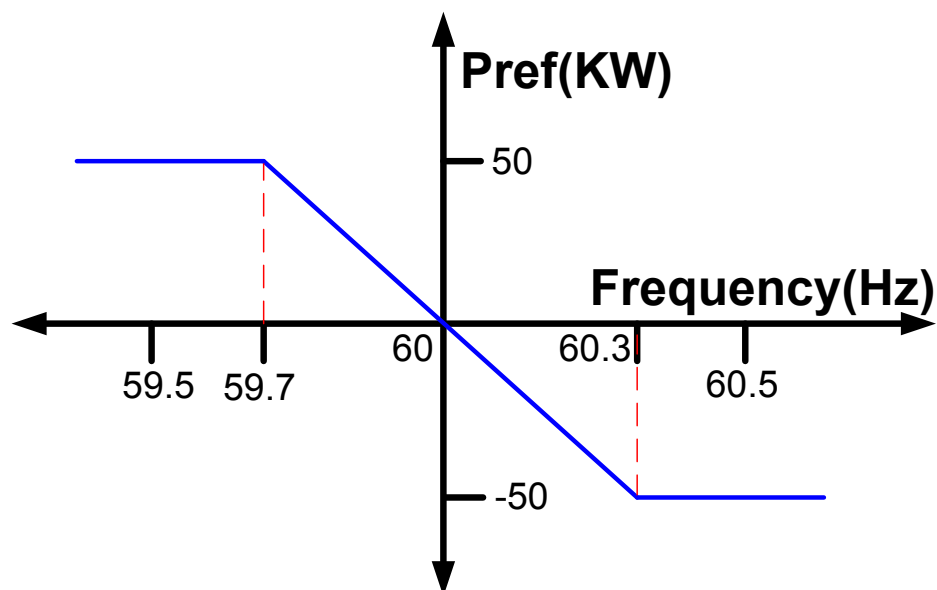


Figure 6-2. Predefined droop curve for frequency support power reference for solar PV energy storage system versus the system frequency

As an example for the 250 kW solar PV facility, for small frequency deviation, less than 0.3 Hz, the frequency support power reference is calculated based on the predefined

droop curve, as shown in Figure 6-2. However, for large frequency deviation, greater than 0.3 Hz, the energy storage system will provide immediate 50 kW support.

Ramp rate control is required to smoothly transits from one output level to another. The solar PV or wind facility should be able to control the rate of change of power output during some circumstances such as, (1) increase in renewable energy facility power output (2) decrease in renewable energy facility power output (3) rate of increase of power when a curtailment of power is released (4) rate of decrease in power when curtailment limit is engaged. According to PREPA requirement, the rate of change of power output at renewable energy facility should not be greater than 10% of AC contracted capacity per minute. This ramp rate limit is applied to both increase and decrease of power output. The 10% tolerance shall be applied to ramp rate control. The energy storage system utilized for ramp rate control requirement shall have a minimum nominal capacity of 20% of AC contracted capacity and for at least one minute, a minimum effective storage capacity of 30% of AC contracted capacity. If case of ramp rate control resource is not sufficient, the frequency response control resource will be used to the extent of its full nominal 10% capacity and 15% effective capacity.

As an example for the 250 kW PV facility the power at POI should not change more than 25 kW per minute. In simulated model, the 24 hours load profile is scaled down to 2400 seconds, which means that 1 real time minute is equal to 1.667 simulation seconds. As a result, the simulation ramp rate has to be scaled to 15 kW per simulation second.

The solar PV energy storage controller will store the last measurement of the solar PV output power. It will be compared with the current power measurement and the ramp rate and its direction will be calculated. Based on this information, the power reference for the integrated energy storage is calculated as follows:

$$P_{RR_CMD} = \left(P_{pv_current} - P_{pv_previous} + P_{RR_previousCMD} \right) + (RR_{sign} * 15kW) \quad (6-1)$$

Where,

P_{RR_CMD} = Power Command to control the ramp rate at Point of Interconnection

$P_{pv_current}$ = present power measurement

$P_{pv_previous}$ = Previous power measurement

RR_{sign} = Ramp rate direction

In addition to the frequency support and the ramp rate control, the voltage support is also provided using integrated energy storage system. According to MTR, renewable energy facility should have the reactive power capability to meet +/- 0.85 power factor range, which is the maximum MVar capability corresponding to maximum MW output. This reactive power capability should be persistent throughout the complete range of operation of the renewable facility. The reactive power injection/absorption should follow the droop characteristics, which should be adjustable from 0 to 10%. The SCADA system should be able to adjust the percentage of the droop curve and voltage set point at POI of renewable facility.

In order to provide the voltage support, the POI voltage is measured and the reactive power command for the integrated energy storage is calculated based on the following equation.

$$Q_{cmd} = \left(\frac{0.687}{\left(\frac{\%droop}{200} \right) * V_{set}} \right) * V_{dev} \quad (6-2)$$

Where, $V_{dev} = V_{set} - V_{POI}$

6.4 Results

As discussed earlier, four cases have been simulated. For all four cases, total fuel consumption, CO₂ emission, system energy efficiency and power quality index SAIDI have been calculated.

Case 1:

In base case, two large traditional natural gas generators each rated at 1.5 MW have been integrated into small island energy network. In addition, the 24 hours load profile, shown earlier in Figure 6-1, has been applied. The natural gas generators are operated in droop mode and the droop curve shown as shown in Figure 6-3 has been used for both generators.

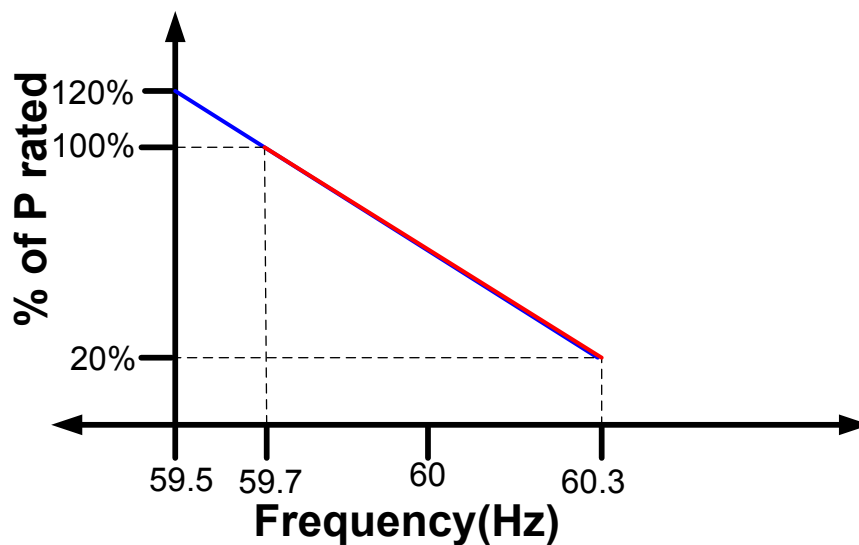


Figure 6-3. Droop curve for 1.5 MW natural gas generator.

Figure 6-4 shows the typical efficiency curve for synchronous generator and natural gas engine. Based on the efficiency curve, if the natural gas generator is operated between 20% and 100 % of the rated load, acceptable operating efficiency can be achieved. The generator can be overloaded by 20% for short periods of time without compromising the acceptable efficiency. As a result, the droop curve for 1.5 MW generator is shown in Figure 6-3. The blue section of the droop curve represents the

overload region of the generator and the red section represents the operating region with acceptable efficiency. If the load drops below 20% the generator should be turned off.

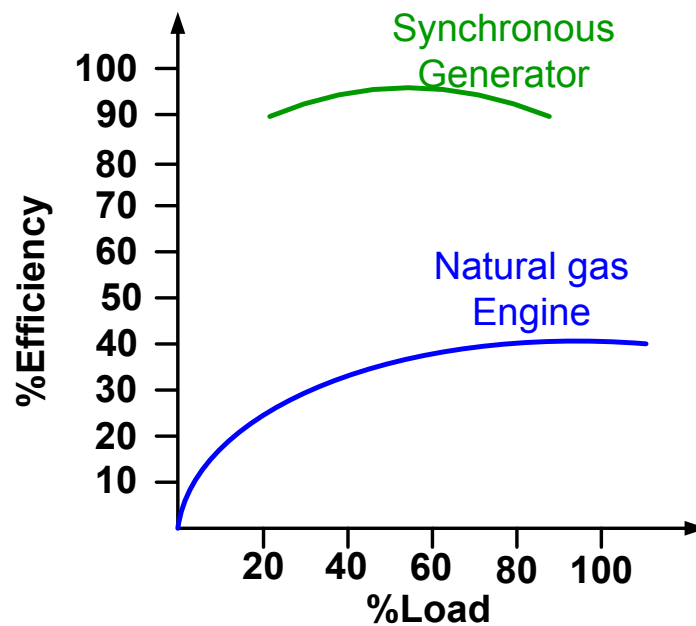


Figure 6-4. Typical load v/s efficiency curve

The operating range of system frequency is 59.5 Hz to 60.5 Hz. As shown in Figure 6-5, the energy network frequency remains within the operating range. Figure 6-6 shows the active power output of natural gas generators in base case.

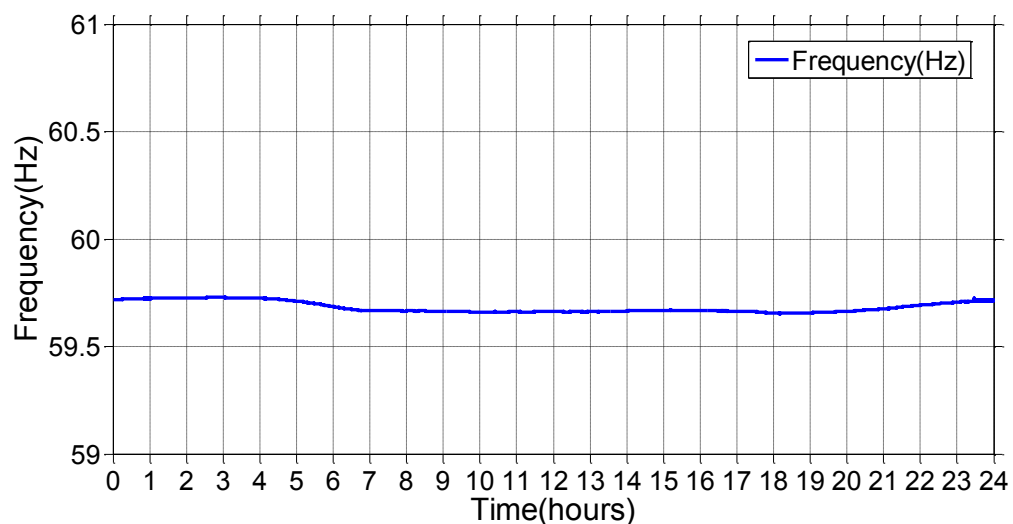


Figure 6-5. Energy network frequency; case1.

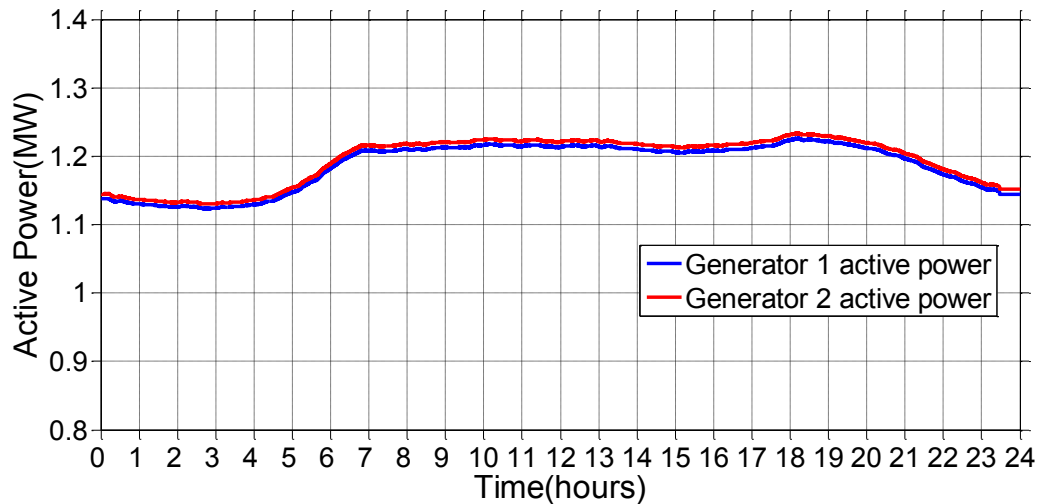


Figure 6-6. Active power output of generator 1 and 2; case1.

Figure 6-7 shows the reactive power output of natural gas generators. Since generator 2 is located near voltage regulator 2, the reactive power output of generator 2 is less compared to the generator 1.

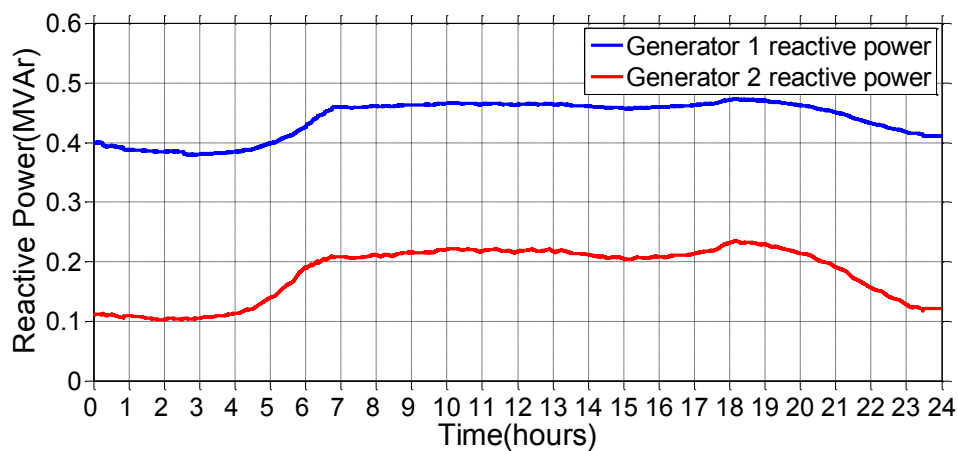


Figure 6-7. Reactive power output of generator 1 and 2; case1.

The operating range of the voltage is between 0.9 and 1.1 per unit. Figure 6-8 shows the generators terminal voltages while operating the small island energy system in base case. As generators are large and the system has two regulators, the voltages at generator terminals as well as at critical loads are maintained.

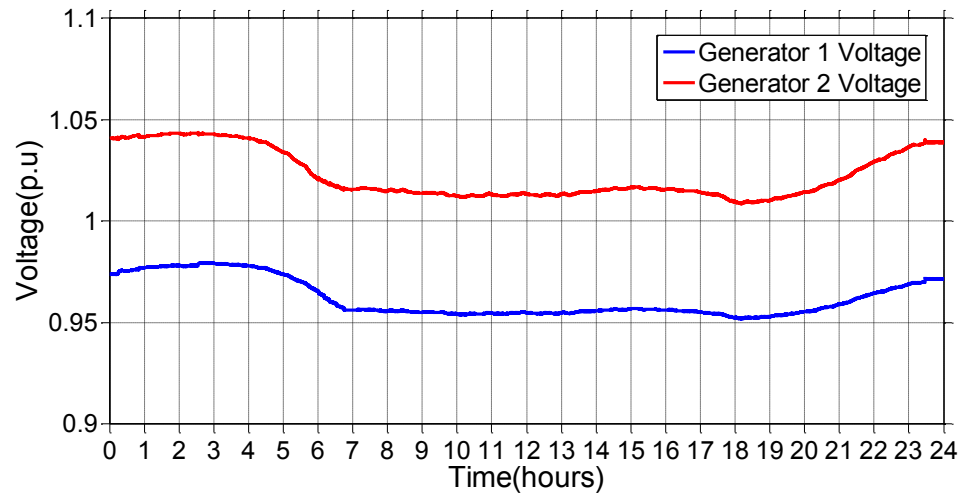


Figure 6-8. Voltage output of generator 1 and 2; case 1.

The overall energy efficiency of energy network in base case is 25%. The total fuel consumption by natural gas generators is 4478 gallons and total CO₂ emission is 3,02,400 pounds. The calculated power quality index SAIDI is 0 hours per day for base case.

Case 2:

In the case 2, in addition to two 1.5 MW generators, two 0.5 MW wind turbines and one 0.25 MW solar PV have been added at buses 828, 848 and 890 respectively. The 24 hours wind speed data and irradiation data from Milwaukee area have been used for renewables. Figure 6-9 shows the active power output of both generators, both wind turbines and solar PV.

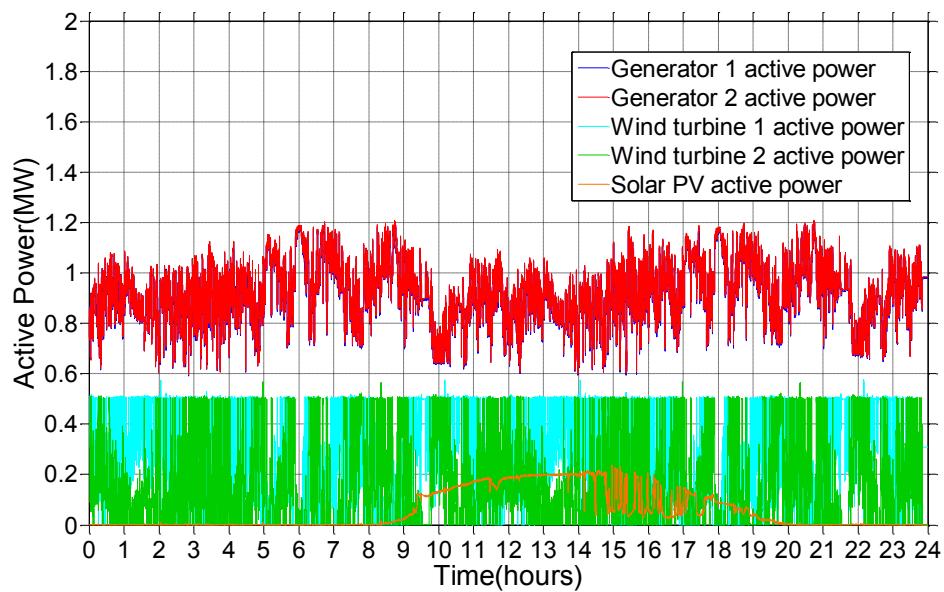


Figure 6-9. Active power output of generator 1, generator 2, wind turbine 1, wind turbine 2 and solar PV; case2.

Figure 6-10 shows the frequency of the energy network while Figure 6-11 shows the generators terminal voltages. Due to sudden drop or rise in renewable power output, the system frequency and critical loads voltages violate the specified limits.

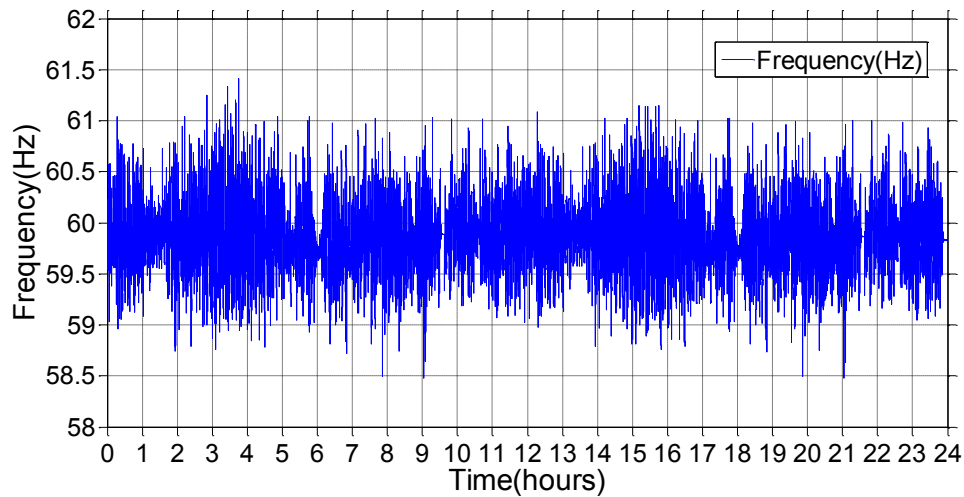


Figure 6-10. Energy network frequency; case2.

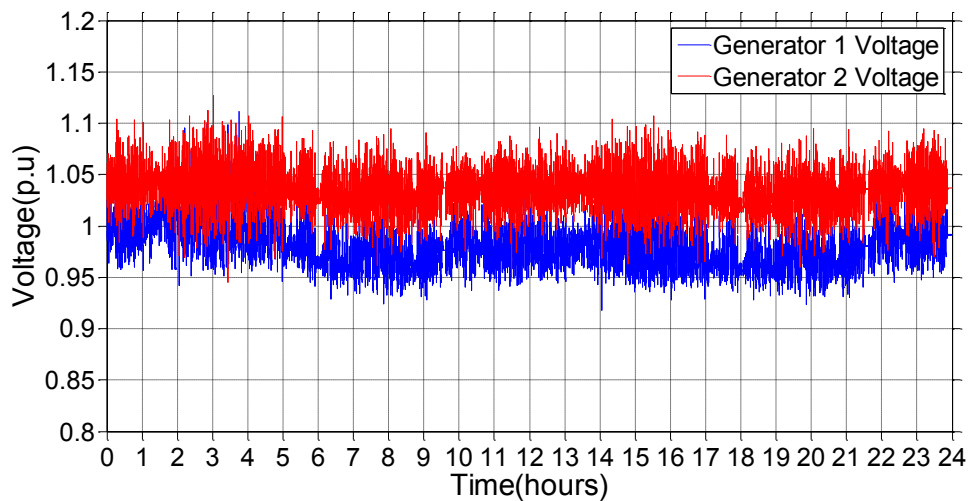


Figure 6-11. Voltage output of generator 1 and 2; case 2.

Due to voltage fluctuation, the reactive power output of both generators also fluctuates. Figure 6-12 shows the reactive power of both generators when renewables are integrated.

After including renewable energy systems, the overall energy efficiency of energy network in case 2 is 32.82%. The total fuel consumption by generators is 3576 gallons while total CO₂ emission is 2,21,137 pounds. The calculated power quality index SAIDI is 27.23 hours per year.

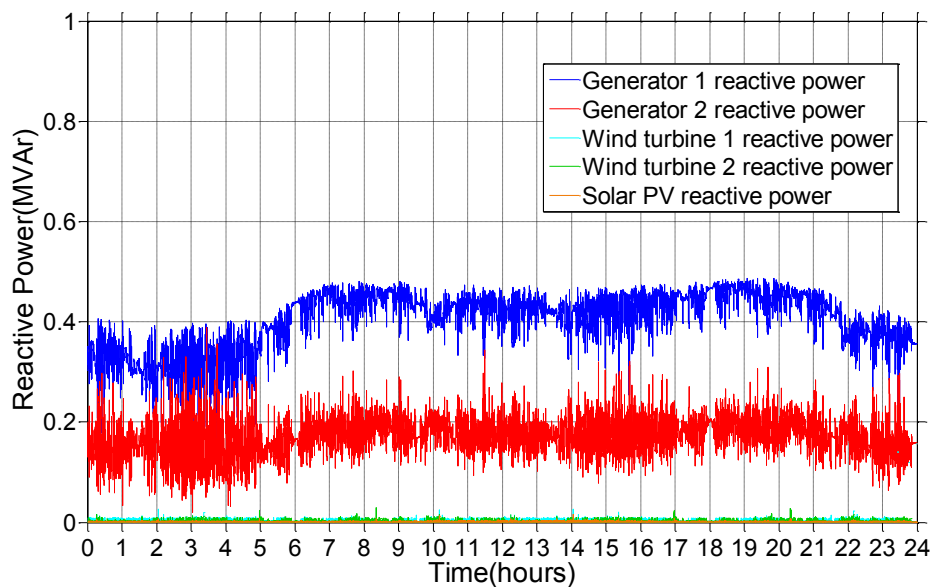


Figure 6-12. Reactive power output of generator 1, generator 2, wind turbine 1, wind turbine 2 and solar PV; case2.

By adding renewable energy systems into energy network, the energy efficiency is improved by 7.82 % and fuel consumption is reduced by 902 gallons. In addition, CO₂ emission is reduced by 81,263 pounds. However, the power quality SAIDI is degraded by 27.23 hours per year.

Case 3:

In case 3, the energy storage systems have been integrated with renewable energy systems and the proposed technique has been applied to the energy management. Figure 6-13 shows the active power output of both generators.

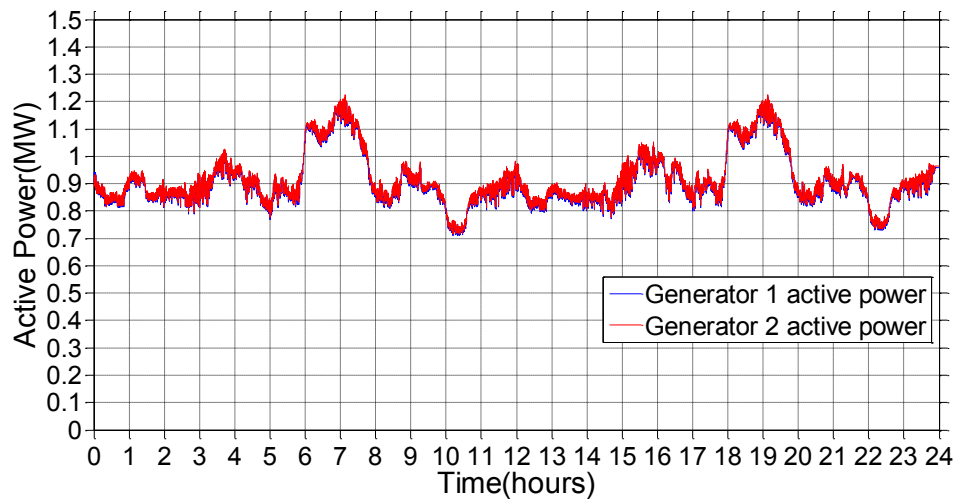


Figure 6-13. Active power output of generator 1 and 2; case3.

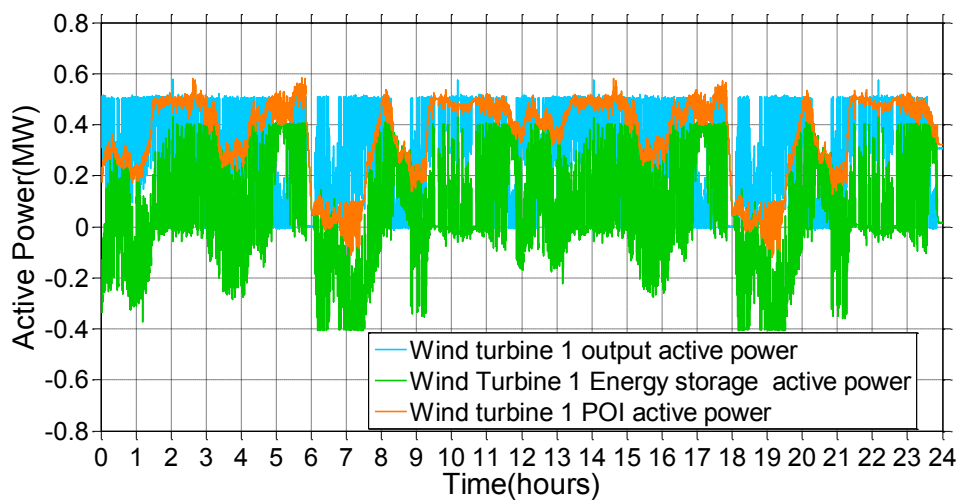


Figure 6-14. Active power output of wind turbine 1, active power of associate energy storage system and active power at POI of wind turbine 1.

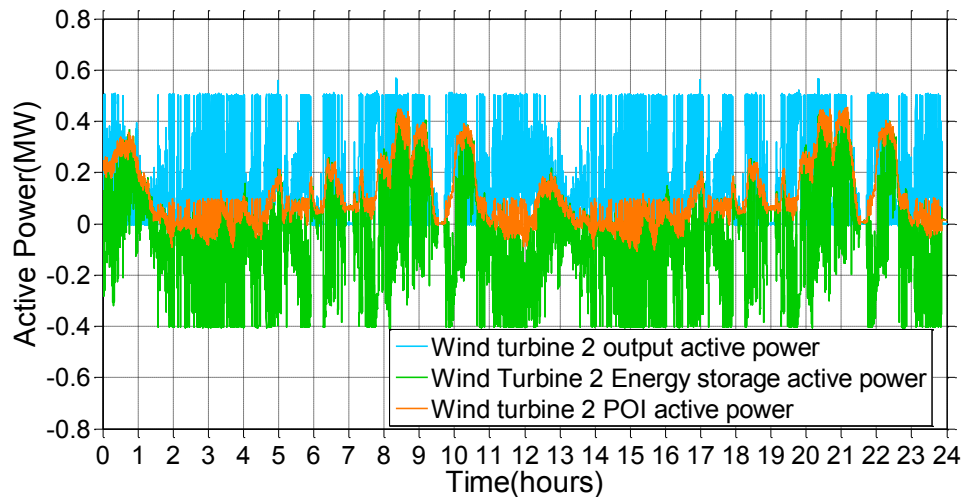


Figure 6-15. Active power output of wind turbine 2, active power of associate energy storage system and active power at POI of wind turbine 2.

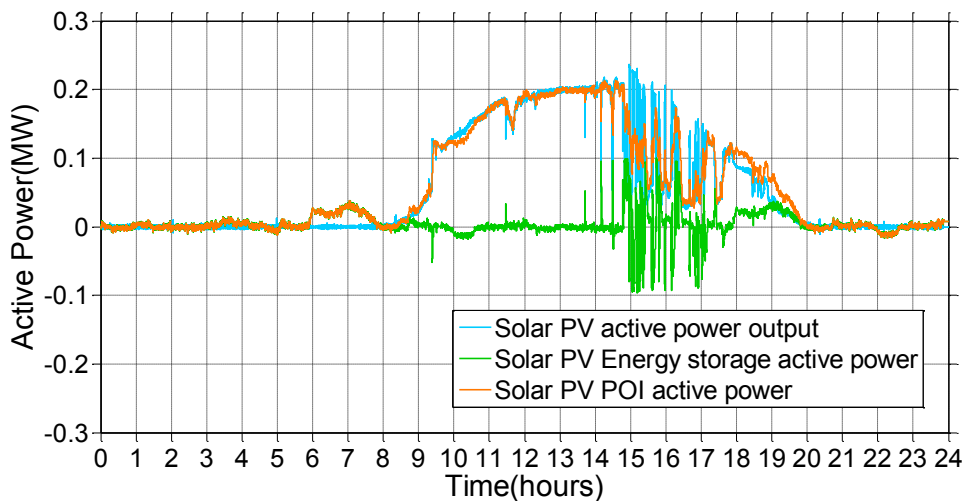


Figure 6-16. Active power output of solar PV, active power of associate energy storage system and active power at POI of solar PV.

Figure 6-14 to Figure 6-16 shows the active power output of renewable energy systems, active power of associated energy storage system and active power at POI of renewable system. The effect of sudden drop or rise in renewable power output at POI is decreased by integrated energy storage systems. The change in active power at POI is regulated to maintain at most 10% per minute ramp rate. In addition, the frequency support is also provided by energy storage system. As shown in Figure 6-17, the system frequency is regulated between 59.5 and 60.5 Hz. However in some cases, frequency crosses the specified limit as a result of huge fluctuations in renewable energy systems

power output, sampling rate of power measurement and scaling of the simulation time. In any case, breaker did not tripped because the frequency transients do not last more than 0.16 second.

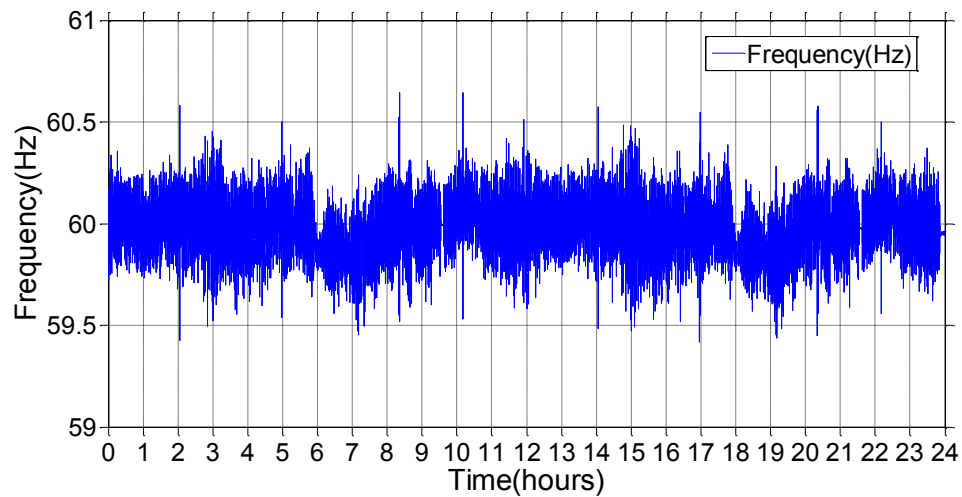


Figure 6-17. Energy network frequency; case3.

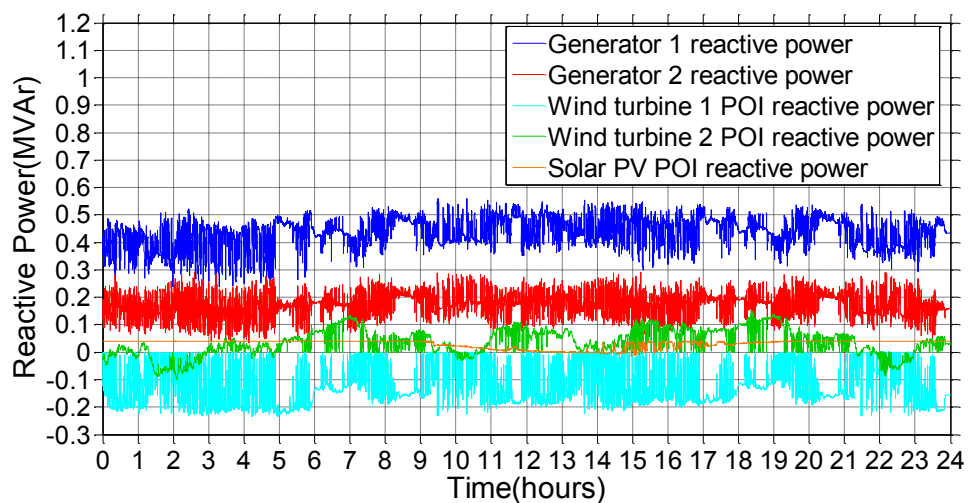


Figure 6-18. Reactive power at generator 1, generator 2, wind turbine 1 POI, wind turbine 2 POI and solar PV POI; case3.

In addition, voltage support is also provided by the integrated energy storage systems. Figure 6-18 shows the reactive power at generators and at POIs of renewable energy systems. Figure 6-19 shows the terminal voltage of generators.

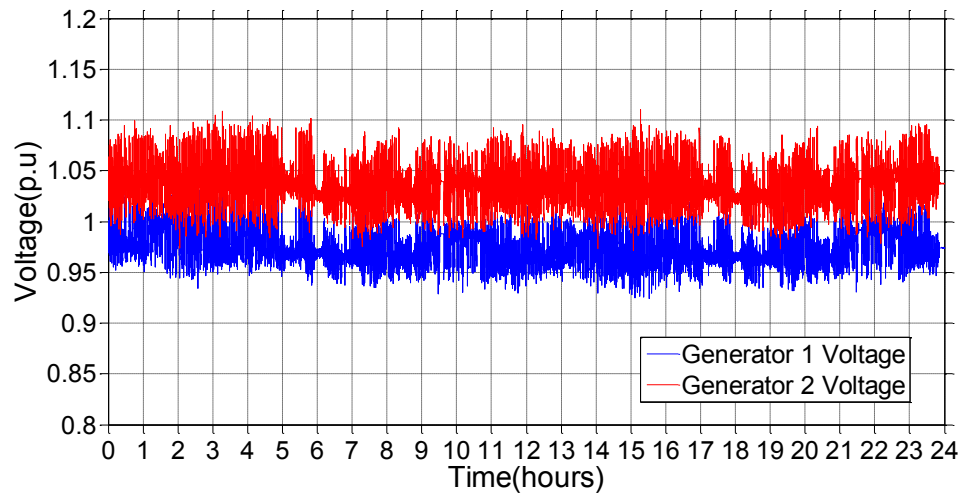


Figure 6-19. Voltage at generator 1, generator 2; case3.

The energy efficiency of energy network in case 3 is 33.35%. The total fuel consumption by generators is 3539 gallons and total CO₂ emission is 2,17,310 pounds. The calculated power quality index SAIDI is 0.073 hours per year.

By integrating energy storage systems with renewable energy systems, the energy efficiency is improved by 8.35 % compare to base case. Moreover, the fuel consumption is reduced by 939 gallons and CO₂ emission is reduced by 85,090 pounds. While as compare to case 2, the power quality index SAIDI is improved by 27.157 hours per year.

Chapter 7 Conclusion

In this dissertation, the detail modeling of microgrid and its components are presented. The virtual droop control method is proposed and introduced to manage microgrids in various operating modes. The proposed method is applied to the Fort Sill microgrid. It regulates the microgrid voltage and frequency more tightly than the natural droop control technique. The unit commitment algorithm is proposed to improve system efficiency, to reduce carbon dioxide emission and also to reduce fuel consumption.

The proposed virtual droop control framework enables the microgrid management using small size of energy storage. It also operates the fossil based generators at near rated power to increase their operating efficiency. The technique to operate microgrid without communication is also presented. Detailed analysis for intentional islanding, unintentional islanding and reconnected are presented.

The simulation results for 24 hours load, solar PV radiation and wind profiles are presented for Fort Sill microgrid system. The simulation results of virtual droop control method are compared with the results from natural droop control. The fuel consumptions of natural gas generator for 24 hours are also calculated for both natural droop control and proposed VDC method and are compared. The results for proposed technique to operate microgrid without communication are also presented. The experimental results are also presented to verify the proposed method. The state space model has been developed for the Fort Sill microgrid and the stability analysis has been done to verify stability of a microgrid in all possible scenarios of proposed VDC method.

A modified control technique is proposed to regulate voltage and frequency for high penetration of renewable energy, which can be used with VDC framework. The technique allows the improvement of efficiency and power quality indexes for critical loads while reducing CO₂ emissions. Three different cases were studied and simulated. The CO₂ emission, efficiency and power quality indexes have been calculated and compared for all three cases in order to verify the performance of the proposed control technique.

References

- [1] T. Lorde, K. Waithe and B. Francis, "The importance of electrical energy for economic growth in Barbados," *Energy Econ*, vol. 32, pp. 1411-1420, 2010.
- [2] E.A. Hudson and D.W. Jorgenson, "US energy policy and economic growth, 1975-2000," *The Bell Journal of Economics and Management Science*, pp. 461-514, 1974.
- [3] D.W. Jorgenson, "The role of energy in productivity growth," *The Energy Journal*, pp. 11-26, 1984.
- [4] D.I. Stern, "Energy and economic growth in the USA: a multivariate approach," *Energy Econ*, vol. 15, pp. 137-150, 1993.
- [5] F. Bressand, D. Farrell, P. Haas, F. Morin, S. Nyquist, J. Remes, S. Roemer, M. Rogers, J. Rosenfeld and J. Woetzel, "Curbing global energy demand growth: the energy productivity opportunity," McKinsey Global Institute, 2007.
- [6] Y. Abdildin, "Multiattribute utility functions for the deep borehole filter restoration problem," *Multiattribute Utility Functions for the Deep Borehole Filter Restoration Problem*, 2014.
- [7] S. Shafiee and E. Topal, "When will fossil fuel reserves be diminished?" *Energy Policy*, vol. 37, pp. 181-189, 2009.
- [8] O. Tahvonen and S. Salo, "Economic growth and transitions between renewable and nonrenewable energy resources," *Eur.Econ.Rev.*, vol. 45, pp. 1379-1398, 2001.
- [9] W.P. Nel and C.J. Cooper, "Implications of fossil fuel constraints on economic growth and global warming," *Energy Policy*, vol. 37, pp. 166-180, 2009.
- [10] G. Marland, T.A. Boden, R.J. Andres, A. Brenkert and C. Johnston, "Global, regional, and national fossil fuel CO₂ emissions," *Trends: A Compendium of Data on Global Change*, pp. 34-43, 2003.
- [11] J. Hansen, M. Sato, R. Ruedy, A. Lacis and V. Oinas, "Global warming in the twenty-first century: an alternative scenario," *Proc.Natl.Acad.Sci.U.S.A.*, vol. 97, pp. 9875-9880, Aug 29. 2000.
- [12] T. Degner, J. Schmid and P. Strauss, "Distributed Generation with High Penetration of Renewable Energy Sources," *Final Public Report of Dispower Project*, ISBN 3-00-016584-3, March 2006.
- [13] Anonymous "U.S. Wind Industry: Market Update," *American Wind Energy Association*(Available at [Https://Www.Awea.Org/](https://www.awea.org/)), .

- [14] Anonymous "20% Wind Energy by 2030. Increasing Wind Energy's Contribution to U.S. Electricity Supply," U.S. Department of Energy, vol. (available at <http://www.nrel.gov/>), July 2008.
- [15] Anonymous "Solar market insight report," Solar Energy Industries Association, 2014.
- [16] Anonymous "2013 report card for America's infrastructure," American Council of Civil Engineers (Available at <Http://Www.Infrastructurereportcard.Org/>), .
- [17] G. Joos, "Distribution System Design Topologies and Communications," in Workshop on Future of Smart Distribution Grids with Distributed Energy Resources, McGill University Canada, 2002.
- [18] D. Cao, D. Pudjianto, S. Grenard, G. Strbac, A. Martikainen, S. Kärkkäinen and J. Farin, "Costs and Benefits of DG Connections to Grid System," 2006.
- [19] C. Marnay, H. Asano, S. Papathanassiou and G. Strbac, "Policymaking for microgrids," *Power and Energy Magazine*, IEEE, vol. 6, pp. 66-77, 2008.
- [20] C. Abbey, D. Cornforth, N. Hatziaargyriou, K. Hirose, A. Kwasinski, E. Kyriakides, G. Platt, L. Reyes and S. Suryanarayanan, "Powering Through the Storm: Microgrids Operation for More Efficient Disaster Recovery," *Power and Energy Magazine*, IEEE, vol. 12, pp. 67-76, 2014.
- [21] R. Masiello and S. Venkata, "Microgrids: There May Be One in Your Future [Guest Editorial]," *Power and Energy Magazine*, IEEE, vol. 11, pp. 14-93, 2013.
- [22] H. Jiayi, J. Chuanwen and X. Rong, "A review on distributed energy resources and MicroGrid," *Renewable and Sustainable Energy Reviews*, vol. 12, pp. 2472-2483, 2008.
- [23] T. Ackermann, G. Andersson and L. Söder, "Distributed generation: a definition," *Electr.Power Syst.Res.*, vol. 57, pp. 195-204, 2001.
- [24] C. Bayliss, C.R. Bayliss and B.J. Hardy, *Transmission and distribution electrical engineering*, Elsevier, 2012, .
- [25] A. Ipakchi and F. Albuyeh, "Grid of the future," *Power and Energy Magazine*, IEEE, vol. 7, pp. 52-62, 2009.
- [26] R. Cossent, T. Gómez and P. Frías, "Towards a future with large penetration of distributed generation: Is the current regulation of electricity distribution ready? Regulatory recommendations under a European perspective," *Energy Policy*, vol. 37, pp. 1145-1155, 2009.
- [27] T. Ackermann, G. Andersson and L. Söder, "Distributed generation: a definition," *Electr.Power Syst.Res.*, vol. 57, pp. 195-204, 2001.

- [28] R.H. Lasseter, "Microgrids," in Power Engineering Society Winter Meeting, 2002. IEEE, pp. 305-308, 2002.
- [29] R.H. Lasseter and P. Paigi, "Microgrid: a conceptual solution," in Power Electronics Specialists Conference, 2004. PESC 04. 2004 IEEE 35th Annual, pp. 4285-4290 Vol.6, 2004.
- [30] S. Van Broekhoven, N. Judson, J. Galvin and J. Marqusee, "Leading the Charge: Microgrids for Domestic Military Installations," Power and Energy Magazine, IEEE, vol. 11, pp. 40-45, 2013.
- [31] P. Agrawal, "Overview of DOE microgrid activities," in Symposium on Microgrid, Montreal, June, 2006.
- [32] R.L. Dohn, "The business case for microgrids," White Paper Siemens, 2011.
- [33] F. Blaabjerg, Z. Chen and S.B. Kjaer, "Power electronics as efficient interface in dispersed power generation systems," Power Electronics, IEEE Transactions On, vol. 19, pp. 1184-1194, 2004.
- [34] Anonymous "DOE Microgrid workshop report," US Department of Energy., Aug. 2011.
- [35] P. Asmus, "Why microgrids are inevitable and why smart utilities should plan accordingly," Distributed Energy Magazine, pp. 44-47, Sep.-Oct. 2011.
- [36] Q. Fu, A. Solanki, L.F. Montoya, A. Nasiri, V. Bhavaraju, T. Abdallah and D. Yu, "Generation capacity design for a microgrid for measurable power quality indexes," in Innovative Smart Grid Technologies (ISGT), 2012 IEEE PES, pp. 1-6, 2012.
- [37] A. Kwasinski, "Microgrids role in powering critical loads during extrem events," 2011.
- [38] R. Lasseter, A. Akhil, C. Marnay, J. Stephens, J. Dagle, R. Guttromson, A.S. Meliopoulos, R. Yinger and J. Eto, "Integration of distributed energy resources. The CERTS Microgrid Concept," Lawrence Berkeley National Laboratory, 2002.
- [39] P. Asmus, "Why Microgrids Are Moving into the Mainstream: Improving the efficiency of the larger power grid." Electrification Magazine, IEEE, vol. 2, pp. 12-19, 2014.
- [40] E. Markey and A. Waxman, "Electric grid vulnerability: Industry responses reveal security gaps," .
- [41] D. Barr, C. Carr and E. Putnam, "Microgrid effects and opportunities for Utilities," Techbrief, 2013.
- [42] J. Eto, R. Lasseter, B. Schenkman, J. Stevens, D. Klapp, H. Volkommer, E. Linton, H. Hurtado and J. Roy, "Overview of the CERTS Microgrid laboratory

- Test Bed," in Integration of Wide-Scale Renewable Resources Into the Power Delivery System, 2009 CIGRE/IEEE PES Joint Symposium, pp. 1-1, 2009.
- [43] C. Marnay, N. DeForest and J. Lai, "A green prison: The Santa Rita Jail campus microgrid," in Power and Energy Society General Meeting, 2012 IEEE, pp. 1-2, 2012.
- [44] J. Stamp, "The SPIDERS project - Smart Power Infrastructure Demonstration for Energy Reliability and Security at US military facilities," in Innovative Smart Grid Technologies (ISGT), 2012 IEEE PES, pp. 1-1, 2012.
- [45] Anonymous "US Army Installation Management Energy Portfolio," Oct 15, 2012.
- [46] Anonymous "NJ Transist annual report," 2013.
- [47] S. Bossart, "Renewable and distributed systems integration demonstration projects," in EPRI Smart Grid Demonstration Advisory Meeting. <http://www.smartgrid.epri.com/doc/15%20DOE%20RDSI%20Project%20Update.pdf>, 2009.
- [48] W.J. Barich, B.L. Dessing and A.B. Harley, "A case analysis of energy savings performance contract projects and photovoltaic energy at Fort Bliss, El Paso, Texas," 2006.
- [49] J. Kelly and D.V. Dollen, "The Illinois Institute of Technology's Perfect Power System Prototype," Grid-Intercop, Nov 2007 Albuquerque, NM.
- [50] A.P.A. Ling, "Towards Sustainable Energy Systems Through Deploying Smart Grids: The Japanese Case," in Smart Grid Applications and Developments, Springer, 2014, pp. 239-258.
- [51] S. Oser, "Presentation on Energy Independence Districts (EID's)," March 2008.
- [52] F. Cleveland, "California DR Integration Projects: San Diego and Marin County," December 2008.
- [53] M. Smith and D. Ton, "Key Connections: The US Department of Energy's Microgrid Initiative," Power and Energy Magazine, IEEE, vol. 11, pp. 22-27, 2013.
- [54] C. Edge, "Clean Energy Trends 2009," March) URL: <Http://Www.Cleanedge.Com/Reports/Pdf/Trends2009.Pdf>, 2009.
- [55] J. Parks, "Smart grid implementation in Sacramento," August 2012.
- [56] P. Piagi and R.H. Lasseter, "Autonomous control of microgrids," in Power Engineering Society General Meeting, 2006. IEEE, pp. 8 pp., 2006.

- [57] Jaehong Kim, J.M. Guerrero, P. Rodriguez, R. Teodorescu and Kwanghee Nam, "Mode Adaptive Droop Control With Virtual Output Impedances for an Inverter-Based Flexible AC Microgrid," *Power Electronics, IEEE Transactions On*, vol. 26, pp. 689-701, 2011.
- [58] R. Majumder, A. Ghosh, G. Ledwich and F. Zare, "Angle droop versus frequency droop in a voltage source converter based autonomous microgrid," in *Power & Energy Society General Meeting, 2009. PES '09. IEEE*, pp. 1-8, 2009.
- [59] Y.A.-I. Mohamed and A. Radwan, "Hierarchical Control System for Robust Microgrid Operation and Seamless Mode Transfer in Active Distribution Systems," *Smart Grid, IEEE Transactions On*, vol. 2, pp. 352-362, 2011.
- [60] Chun-xia Dou and Bin Liu, "Multi-Agent Based Hierarchical Hybrid Control for Smart Microgrid," *Smart Grid, IEEE Transactions On*, vol. 4, pp. 771-778, 2013.
- [61] P.M. Anderson and A.A. Fouad, *Power system control and stability*, John Wiley & Sons, 2008, .
- [62] S.B. Crary, *Power system stability*, J. Wiley, 1947, .
- [63] E.W. Kimbark, *Power system stability*, John Wiley & Sons, 1995, .
- [64] P. Kundur, N.J. Balu and M.G. Lauby, *Power system stability and control*, McGraw-hill New York, 1994, .
- [65] V. Bhavaraju, A. Nasiri and Q. Fu, "Multi-Inverter Controls and Management of Energy Storage for Microgrid Islanding," *The Electricity Journal*, vol. 25, pp. 36-44, 10. 2012.
- [66] F. Katiraei, M. Iravani and P. Lehn, "Small-signal dynamic model of a micro-grid including conventional and electronically interfaced distributed resources," *IET Generation, Transmission & Distribution*, vol. 1, pp. 369-378, 2007.
- [67] N. Hatziargyriou, H. Asano, R. Iravani and C. Marnay, "Microgrids," *Power and Energy Magazine, IEEE*, vol. 5, pp. 78-94, 2007.
- [68] F. Katiraei, R. Iravani, N. Hatziargyriou and A. Dimeas, "Microgrids management," *Power and Energy Magazine, IEEE*, vol. 6, pp. 54-65, 2008.
- [69] R. Dugan and W. Kersting, "Induction machine test case for the 34-bus test feeder-description," in *Power Engineering Society General Meeting, 2006. IEEE*, pp. 4 pp., 2006.
- [70] W. Kersting, "Radial distribution test feeders," *Power Systems, IEEE Transactions On*, vol. 6, pp. 975-985, 1991.
- [71] Z. Zhou, "Induction machine test case for the 34-bus test feeder: a wind turbine time-domain model," in *2006 IEEE Power Engineering Society General Meeting, 2006*.

- [72] A.L. Sheldrake, Handbook of electrical engineering: for practitioners in the oil, gas and petrochemical industry, Wiley, 2003, .
- [73] I. Canay, "Causes of discrepancies on calculation of rotor quantities and exact equivalent diagrams of the synchronous machine," Power Apparatus and Systems, IEEE Transactions On, pp. 1114-1120, 1969.
- [74] D. Lee, D. Baker and K. Bess, "IEEE recommended practice for excitation system models for power system stability studies," Energy Development and Power Generation Committee of Power Engineering Society, 1992.
- [75] "IEEE Guide for Identification, Testing, and Evaluation of the Dynamic Performance of Excitation Control Systems," IEEE Std 421.2-1990, pp. 1-44, 1990.
- [76] "IEEE Standard Definitions for Excitation Systems for Synchronous Machines," IEEE Std 421.1-2007 (Revision of IEEE Std 421.1-1986), pp. 1-33, 2007.
- [77] K. Kim and R.C. Schaefer, "Tuning a PID controller for a digital excitation control system," Industry Applications, IEEE Transactions On, vol. 41, pp. 485-492, 2005.
- [78] K. Yeager and J. Willis, "Modeling of emergency natural gas generators in an 800 megawatt nuclear power plant," Energy Conversion, IEEE Transactions On, vol. 8, pp. 433-441, 1993.
- [79] E. De Jaeger, N. Janssens, B. Malfliet and F. Van De Meulebroeke, "Hydro turbine model for system dynamic studies," Power Systems, IEEE Transactions On, vol. 9, pp. 1709-1715, 1994.
- [80] M.H. Rashid, Power electronics handbook, Academic Pr, 2001, .
- [81] P. Bimbhra, Power electronics, Khanna Publishers, 2012, .
- [82] D.W. Hart, Power electronics, Tata McGraw-Hill Education, 2011, .
- [83] B.K. Bose, Power electronics and motor drives: advances and trends, Academic press, 2010, .
- [84] N. Mohan, Power electronics: a first course, Wiley, 2012, .
- [85] A. Yazdani and R. Iravani, Voltage-sourced converters in power systems: modeling, control, and applications, John Wiley & Sons, 2010, .
- [86] E. Twining and D.G. Holmes, "Grid current regulation of a three-phase voltage source inverter with an LCL input filter," Power Electronics, IEEE Transactions On, vol. 18, pp. 888-895, 2003.
- [87] A.K. Sahoo, A. Shahani, K. Basu and N. Mohan, "LCL filter design for grid-connected inverters by analytical estimation of PWM ripple voltage," in Applied

Power Electronics Conference and Exposition (APEC), 2014 Twenty-Ninth Annual IEEE, pp. 1281-1286, 2014.

- [88] F. Blaabjerg, M. Liserre and K. Ma, "Power electronics converters for wind turbine systems," *Industry Applications, IEEE Transactions On*, vol. 48, pp. 708-719, 2012.
- [89] P.M. Ivry, M.J. Rawa, D. Thomas and M. Sumner, "Power quality of a voltage source converter in a smart grid," in *PowerTech (POWERTECH), 2013 IEEE Grenoble*, pp. 1-6, 2013.
- [90] A. Yazdani, "Control of an islanded distributed energy resource unit with load compensating feed-forward," in *Power and Energy Society General Meeting- Conversion and Delivery of Electrical Energy in the 21st Century, 2008 IEEE*, pp. 1-7, 2008.
- [91] Anonymous "Bottling electricity: Storage as a strategic tool for managing variability and capacity concerns in the modern grid," *Electrical Advisory Committee*, december 2008.
- [92] C. Narula, "Final Report on Economic analysis of deploying used batteries in power systems," *Oak Ridge National Laboratory*, June 2011.
- [93] A. Hamidi, L. Weber and A. Nasiri, "EV charging station integrating renewable energy and second-life battery," in *Renewable Energy Research and Applications (ICRERA), 2013 International Conference on*, pp. 1217-1221, 2013.
- [94] E. Manla, A. Nasiri, C.H. Rentel and M. Hughes, "Modeling of zinc bromide energy storage for vehicular applications," *Industrial Electronics, IEEE Transactions On*, vol. 57, pp. 624-632, 2010.
- [95] O. Tremblay, L. Dessaint and A. Dekkiche, "A generic battery model for the dynamic simulation of hybrid electric vehicles," in *Vehicle Power and Propulsion Conference, 2007. VPPC 2007. IEEE*, pp. 284-289, 2007.
- [96] A. Esmaili and A. Nasiri, "Energy storage for short-term and long-term wind energy support," in *IECON 2010-36th Annual Conference on IEEE Industrial Electronics Society*, pp. 3281-3286, 2010.
- [97] K. Clark, N.W. Miller and J.J. Sanchez-Gasca, "Modeling of GE wind turbine-generators for grid studies," *General Electric International, Technical Report*, 2010.
- [98] N.W. Miller, W.W. Price and J.J. Sanchez-Gasca, "Dynamic modeling of GE 1.5 and 3.6 wind turbine-generators," *GE-Power Systems Energy Consulting*, 2003.
- [99] Zhenhong Guo and Liuchen Chang, "Two-phase converter used for wind turbine PMSG generation system," in *Electrical and Computer Engineering, 2008. CCECE 2008. Canadian Conference on*, pp. 001255-001258, 2008.

- [100] R. Pena, J. Clare and G. Asher, "Doubly fed induction generator using back-to-back PWM converters and its application to variable-speed wind-energy generation," IEE Proceedings-Electric Power Applications, vol. 143, pp. 231-241, 1996.
- [101] L. Mihet-Popa, F. Blaabjerg and I. Boldea, "Wind turbine Generator modeling and Simulation where rotational speed is the controlled variable," Industry Applications, IEEE Transactions On, vol. 40, pp. 3-10, 2004.
- [102] A. Miller, E. Muljadi and D.S. Zinger, "A variable speed wind turbine power control," Energy Conversion, IEEE Transactions On, vol. 12, pp. 181-186, 1997.
- [103] D. Sahu, "Maximum power extraction for direct driven variable speed wind turbine system using PMSG and fixed pitch angle," in Control Computing Communication & Materials (ICCCCM), 2013 International Conference on, pp. 1-7, 2013.
- [104] A. Solanki, L.F. Montoya, Q. Fu, A. Nasiri, V. Bhavaraju, T. Abdallah and D. Yu, "Managing intermittent renewables in a microgrid," in Innovative Smart Grid Technologies (ISGT), 2012 IEEE PES, pp. 1-6, 2012.
- [105] E. Muljadi, M. Singh and V. Gevorgian, "PSCAD modules representing PV generator," Technical Report, NREL, August 2013.
- [106] S.A. Rahman and R.K. Varma, "PSCAD/EMTDC model of a 3-phase grid connected photovoltaic solar system," in North American Power Symposium (NAPS), 2011, pp. 1-7, 2011.
- [107] A. Kalbat, "PSCAD simulation of grid-tied photovoltaic systems and Total Harmonic Distortion analysis," in Electric Power and Energy Conversion Systems (EPECS), 2013 3rd International Conference on, pp. 1-6, 2013.
- [108] A.D. Rajapakse and D. Muthumuni, "Simulation tools for photovoltaic system grid integration studies," in Electrical Power & Energy Conference (EPEC), 2009 IEEE, pp. 1-5, 2009.
- [109] Q. Fu, A. Nasiri, V. Bhavaraju, A. Solanki, T. Abdallah and D.C. Yu, "Transition Management of Microgrids With High Penetration of Renewable Energy," 2014.

CURRICULUM VITAE

Ashishkumar Solanki

Place of Birth: Gujarat, India

Education:

- Bachelor of Engineering, Sardar Patel University, Gujarat, India, May 2007
Major: Electrical Engineering
- Masters of Science, Gannon University, Erie, Pennsylvania, December 2008
Major: Electrical Engineering

Doctorate Dissertation Title: Virtual droop control framework and stability analysis for microgrid with high penetration of renewables

Work experience:

Research Intern (June 2014-December 2014)

Corporate Research and Technology, Eaton Corporation, Menomonee Falls, WI.

Responsibilities:

- Developed a ramp rate control algorithm and voltage, frequency support algorithm for solar PV system using energy storage inverter based on PREPA minimum technical requirement.
- Proposed and developed microgrid stability controller to ensure the microgrid stability based on Jacobian matrix.
- Developed co-simulation between PSCAD and CYME using python programming to utilize the capability of CYME for real time control and for optimization of energy network.
- Extensively work on distributed power system emulator (DPSe) to test control algorithm, communication latency and also to enable hardware in loop capability.

Research Intern (June 2013-August 2013)

Corporate Research and Technology, Eaton Corporation, Menomonee Falls, WI.

Responsibilities:

- Testing of 250 kW, 56 kWh Li-Ion Altairnano power battery system and 250 kW SMAX inverter for microgrid application.
- Testing of 100 kW natural gas generator and 125 kW diesel generator in isochronous and droop mode.
- Testing of parallel operation of battery inverter and generators for microgrid application.

- Extensively worked on communication between SEL 849 Schweitzer relay used for load measurement, inverter and battery system using Modbus TCP/IP.

Research Assistant

(January 2012-December 2014)

University of Wisconsin Milwaukee, Milwaukee, WI.

Responsibilities:

- Proposed and developed virtual droop control method for microgrid power management and voltage and frequency control.
- Established a control method to manage microgrid during communication sabotage.
- Proposed and developed power curtailment for integration of high penetration of renewables in distributed system.
- Developed detailed PSCAD simulation model of the microgrid for US Army Fort Sill microgrid project collaborated with Eaton Corporation.
- Developed mathematical state space model of Fort Sill microgrid for stability analysis and to design controls of system components.
- Developed voltage and current mode inverter models for different power ratings.
- Developed complete simulation model for diesel generators and natural gas generators and verified with in housed test results.
- Worked on islanding and reconnection schemes for microgrids.

Research and Development Intern

(May 2010- September 2010)

TAPCO, Milwaukee, USA

Responsibilities:

- Software development for temperature measurement, PWM, duty cycle, solar PV and battery power management using ATMEL microcontroller and STK600 development tool.
- Designed and developed control and power circuit for LED based flashing Sign.

Teaching Assistant

(September 2010-December 2010)

University of Wisconsin Milwaukee, Milwaukee, WI.

Responsibilities

- Designed and taught conceptual lab experiments for components such as resistors, capacitors, inductors, sensors, transistors and op-amps.
- Assisted students to use debugging tools such as oscilloscope, multi-meter, LCR meter, function generator and pulse generator.

Teaching Assistant

(January 2008- December 2008)

Gannon University, Erie, PA.

Responsibilities:

- Setup experiments on single and three phase AC/DC controlled rectifier, buck and boost converters.

- Trained students with Cadence PSPICE simulation software for power electronics converters.
- Designed assignments and simulation projects.

PUBLICATIONS

- **A. Solanki**, L. F. Montoya, Q. Fu, A. Nasiri, V. Bhavaraju, and D. Yu, “Managing Intermittent Renewables in a Microgrid”, in Proc. 2012 IEEE PES Conference on Innovative Smart Grid Technologies, Washington D.C.
- **A. Solanki**, A. Nasiri and V. Bhavaraju, “A New Control Method of Power Management,” In Proc. 2013 International Conference on Renewable Energy Research and Applications(ICRERA), Madrid, Spain.
- **A. Solanki**, A. Nasiri, V. Bhavaraju, Y. Familiant and Q. Fu, “A New Framework for Microgrid Management: Virtual Droop Control” submitted in IEEE Transaction on Smart Grid.
- **A. Solanki**, A. Nasiri, V. Bhavaraju, Y. Familiant B. Novakovic and Q. Fu, “Modified Control and Effective Energy Storage Sizing for Efficiency and Power Quality Improvement; CO2 and Cost Reduction, in an Island Energy Network” ,” In Proc. 2014 International Conference on Renewable Energy Research and Applications(ICRERA), Milwaukee, Wisconsin.
- **A. Solanki**, Q. Fu, V. Bhavaraju, Y. Familiant, B. Novakovic and G. Herman, White paper on “Utility Scale PV Design for Puerto Rico”, 2014.
- Q. Fu, **A. Solanki**, L. F. Montoya, A. Nasiri, V. Bhavaraju, and D. Yu, “Generation Capacity Design for a Microgrid for Measurable Power Quality Indexes”, in Proc. 2012 IEEE PES Conference on Innovative Smart Grid Technologies, Washington D.C.
- Q. Fu, **A. Solanki**, L. F. Montoya, A. Nasiri, V. Bhavaraju, and D. Yu, “Microgrid Generation Capacity Design With Renewables and Energy Storage Addressing Power Quality and surety”, IEEE Transaction On Smart Grid, vol. 3, no. 4, pp. 2019-2027, 2012.
- Q. Fu, **A. Solanki**, A. Nasiri, V. Bhavaraju, T. Abdallah, and D. Yu, " Transition Management of Microgrid with High Penetration of Renewable Energy" accepted for IEEE Transactions on Smart Grid, 2013.